4D seismic reservoir characterization, integrated with geo-mechanical modelling

Proefschrift

ter verkrijging van de graad van doctor
aan de Technische Universiteit Delft,
op gezag van de Rector Magnificus prof. dr. ir. J.T. Fokkema,
voorzitter van het College voor Promoties,
in het openbaar te verdedigen,
op donderdag 10 december 2009 om 12:30 uur

door

Petar Vladov ANGELOV

Master of Applied Geophysics,
"Mining and Geology" University, Sofia, Bulgaria

geboren te Pernik, Bulgarije

Dit proefschrift is goedgekeurd door de promotoren:

Prof. dr. ir. R.J. Arts
Prof. dr. ir. C.P.A. Wapenaar

Samenstelling promotiecommissie:

Rector Magnificus	voorzitter
Prof. dr. ir. R.J. Arts,	Technische Universiteit Delft, promotor
Prof. dr. ir. C.P.A. Wapenaar,	Technische Universiteit Delft, promotor
Prof. dr. M. Landrø,	NTNU, Trondheim, Noorwegen
Prof. dr. S.M. Luthi,	Technische Universiteit Delft
Prof. dr. W.A. Mulder,	Technische Universiteit Delft
Dr. P.J.F. Verbeek,	Nederlandse Aardoile Maatschappij BV
Dr. ir. P.R. Mesdag,	Fugro-Jason BV

ISBN 978-90-9024985-8

SUPPORT
The research reported in this thesis was financially supported by the Dutch Technology Foundation STW, applied science division of NWO and the Tehnology Program of the Ministry of Economic Affairs (grant DAR.5763)
The results of geo-mechanical modelling and time-shift analysis of the Shearwater filed are published in this thesis with the permission of XOM, BP and Shell U.K. Limited.

Cover: Measured differential time-shifts in a depleting gas reservoir (Figure 7.31) together with the geo-mechanical model of the reservoir (Figure 5.22) and the time-lapse changes in the vertical stress calculated from the measured time-shifts and the results of the geo-mechanical modelling (Figure 7.38).

Printed in The Netherlands by Sieca Repro Delft

4D seismic reservoir characterization, integrated with geo-mechanical modelling

Petar Vladov Angelov

November 25, 2009

Summary

4D seismic reservoir characterization, integrated with geo-mechanical modelling

Hydrocarbon production induces time-lapse changes in the seismic attributes (travel time and amplitude) both at the level of the producing reservoir and in the surrounding rock. The detected time-lapse changes in the seismic are induced from the changes in the petrophysical properties of the rock, i.e. (visco-)elastic constants as a consequence of saturation, porosity, and stress-strain changes, and by direct changes in the layer-thickness due to compaction or elongation. Usually the production effects in the surrounding rock and the effect of changes in the layer thickness are neglected, which can lead to misinterpretation of the recorded time-lapse information.

In this study we have first investigated how large each of these effects can be and what factors have the main influence. To this end we have developed different synthetic models, for which the parameters have been based on a real field cases. In more detail we adopted the following steps to investigate the time-lapse changes in the stress field both in the reservoir and in the surrounding rock for different scenarios.

- We developed a petrophysical model of hydrocarbon-saturated sandstone reservoir, based on the Hertz-Mindlin contact theory, to investi-

gate the time-lapse changes in the seismic parameters (velocities and density) following from 4D changes in the rock parameters. The influence of the different rock properties and environmental conditions (pore pressure, water saturation and porosity) on the seismic parameters inside the reservoir has been investigated. As expected it was demonstrated that the hydrocarbon substitution by water causes an increase in the aforementioned seismic parameters, whereas an increase in the porosity and pore pressure will decrease the values of these parameters.

- We developed three different geo-mechanical models based on the North Sea reservoirs and ran several scenarios with each of the models to understand the development of the stress and strain fields as result of production.

  [1] The first model consisted of a 2D layer-cake model and has been used to investigate the stress distribution and vertical strain in the reservoir and in the surrounding rocks. We observed that the distribution of the stress changes in the surrounding rock depends on the elastic properties of the reservoir and surrounding media and is linked to the lateral boundaries between the reservoir and the surrounding rock.

  [2] The second model was also a layer cake model, but now with parameters and layering based on the gas field Shearwater. This model has also been used to investigate the effect of offset on the development of the time-shifts.

  [3] The third and final model considered of a 2D model now also with the geometry of the gas field Shearwater. In that model we ran several scenarios changing the shape and the depleting segments of the reservoir in order to investigate their influence on the stress distribution and vertical strain.

  Overall we concluded that the main factors influencing the changes in the stress distribution and vertical displacement in a depleting gas reservoir are: 1) the distribution and the magnitude of the pressure drop in the reservoir, 2) the geometrical shape of the reservoir and the

overlaying rocks, 3) the presence of faults, and 4) the elastic properties of the layers.

We investigated the time-shift variation as a function of offset using the second geo-mechanical model. We created synthetic time-lapse seismic data for a simple 2D model. This was done by combining the results of the geo-mechanical modelling with the time-shifts representative for the Shearwater data, given in the literature. We measured the time-shifts from the synthetic 4D data for different stacks in order to find the optimal value of signal-to-noise ratio without violating the requirement for vertical travel paths. From the case study we concluded that the near offset partial stack (500-1300 m) can be used in the real data example to give reliable results of the measured time-shifts.

As a second step in this study we introduced a new workflow in order to separate the effect of the changes in petrophysical properties and environmental conditions in the surrounding and reservoir rock and the physical displacement of the layers. The proposed workflow has been applied to the Shearwater 4D seismic data. The following steps have been taken:

- We measured the time-shifts using 4D data from the Shearwater field. The differences in the two-way travel time at the main reflectors were estimated and stabilized using vertical stacks of estimated time-shifts around the interfaces in order to reduce the effect of multiple reflections. Further the time-shifts are smoothed using a lateral median filter to remove the effect of the outliers, and time-shifts horizontal maps are produced for each of the main reflectors.

- We calculated the differential time-shifts in each of the geological layers using the relative ratio between the measured time-shifts at the top and at the bottom of the layers. We used the results from the 2D geo-mechanical modelling (vertical strain) to remove the time-shifts caused by changes in the displacement of the layers. We observed that the calculated differential time-shifts follow accurately the modelled changes in the stress field for the seismic 2D line which corresponds to the geo-mechanical model.

We concluded that the results of geo-mechanical modelling can be effectively used to eliminate the effect of displacement from the measured time-

shifts. The resulting time-shifts are thus induced by changes in the seismic velocity. Furthermore, the changes in the seismic velocity are consequence of changes in the petrophysical properties and environmental conditions. This allows us to use the calculated differential time-shifts to map directly the changes in the stress field. In the Shearwater field the effect of physical displacement appeared to be negligibly small for the selected 2D line, where the geo-mechanical modelling has been applied. Furthermore, we demonstrated that the calculated changes in the seismic velocity follow accurately the modelled stress field variations. We used the inverse relation ship between the modelled stress changes and the calculated time-shifts (induced by velocity changes) to define the changes in the vertical stress over the entire field. We conclude that the stress changes in and around a depleting hydrocarbon reservoir will always induced changes in the seismic velocity. As demonstrated in this example the correlation between the two allows an estimation of changes in the petrophysical properties and in the environmental conditions from observed velocity changes.

Samenvatting

4D seismische karakterisering van reservoirs, geïntegreerd met geomechanische modellering

De productie van koolwaterstoffen induceert temporele veranderingen in de seismische attributen (looptijd en amplitude), zowel in het reservoir als in het omringende pakket gesteenten. De waargenomen veranderingen in met de tijd herhaalde seismiek worden veroorzaakt door de veranderingen in de petrofysische eigenschappen van het gesteente, d.w.z. in (visco-) elastische constanten, als gevolg van saturatie-, porositeits- en spannings-vervormings veranderingen, en door rechtstreekse veranderingen in de laagdikte door compactie of rek. Meestal worden de effecten van productie in het omliggende gesteentepakket en van veranderingen in de laagdikte verwaarloosd. Dit kan leiden tot misinterpretatie van de informatie in met de tijd herhaalde seismiek.

In deze studie hebben we eerst onderzocht hoe groot de uitwerking van elk van deze effecten kan zijn en wat de effecten met de grootste invloed zijn. Hiervoor hebben we verschillende synthetische modellen ontwikkeld, met parameters gekozen naar voorbeelden uit het veld. Wij hebben onderstaande stappen gemaakt om de temporele veranderingen in het spanningsveld zowel in het reservoir als in het omringende gesteentepakket te onderzoeken met

verschillende scenario tests.

- Uitgaande van de Hertz-Mindlin contact theorie hebben we een petrofysisch model ontwikkeld van een koolwaterstof-verzadigd zandsteen reservoir, om de temporele veranderingen van de seismische parameters (snelheden en dichtheid) als gevolg van 4D veranderingen in gesteenteparameters te onderzoeken. De invloed van verschillende gesteente-eigenschappen en omgevingsomstandigheden (poriedruk, watersaturatie en porositeit) op de seismische parameters in het reservoir zijn onderzocht. Zoals verwacht werd aangetoond dat het vervangen van koolwaterstoffen door water tot een verhoging van de eerder genoemde seismische parameters leidt, terwijl een verhoging van de porositeit en poriedruk de waarden van deze seismische parameters laten dalen.

- We hebben drie verschillende geomechanische modellen ontwikkeld, gebaseerd op Noordzee reservoirs, en met elk van de modellen verschillende scenario's doorlopen om begrip te krijgen van het spannings- en vervormingsverloop als gevolg van productie.

  [1] Het eerste model is een 2D gelaagd model dat is gebruikt om de verdeling van spanning en verticale vervorming in het reservoir en in de omringende gesteenten te onderzoeken. We namen waar dat de verdeling van de spanningsveranderingen in het omliggende gesteentepakket afhangt van de elastische eigenschappen van het reservoir en omliggende media en gekoppeld is aan de zij-grenzen tussen het reservoir en het omliggende gesteentepakket.

  [2] Het tweede model was eveneens een gelaagd model, maar in dit geval met parameters en gelaagdheid gebaseerd op het gasveld Shearwater, waarvoor ook seismische velddata beschikbaar waren. Dit model is tevens gebruikt voor onderzoek naar het effect van bron-ontvanger afstand op de ontwikkeling van looptijdverschillen.

  [3] Het derde en laatste model was een 2D model waarin ook de geometrie van het Shearwater gasveld werd meegenomen. In dat model hebben we verschillende scenario's doorlopen, waarbij we

die de vorm en de producerende segmenten van het reservoir veranderden, om hun invloed op de spanningsverdeling en verticale vervorming te onderzoeken.

Uit deze modelleringsstudie hebben we de algemene conclusie getrokken dat de hoofdfactoren die de spanningsdistributie en de verticale vervorming in een producerend gasreservoir be?nvloeden, als volgt zijn: 1) de verdeling en grootte van de drukval in het reservoir, 2) de vorm van het reservoir en van het bovenliggende gesteentepakket, 3) de aanwezigheid van breuken, en 4) de elastische eigenschappen van de lagen.

Wij hebben de verandering van looptijdverschillen met bron-ontvanger afstand onderzocht met behulp van het tweede geomechanische model. We creëerden synthetische, in de tijd herhaalde seismische data voor dit model door de resultaten van de geomechanische modellering te combineren met looptijdverschillen die representatief zijn voor de Shearwater data, verkregen uit de literatuur. Wij maten de looptijdverschillen op van de synthetische 4D data voor verschillende bron-ontvanger intervallen om de optimale signaal-ruis verhouding te vinden, zonder afbreuk te doen aan de eis van verticale straalpaden. Uit deze praktijkgerichte studie hebben wij geconcludeerd dat de korte bron-ontvanger afstanden (500-1300 m) gebuikt kunnen worden in het veldvoorbeeld om tot betrouwbare resultaten van de gemeten looptijdverschillen te komen.

Als een tweede stap in dit onderzoek hebben we een nieuw werkplan opgezet om het effect van de veranderingen in petrofysische eigenschappen en omgevingsomstandigheden in het omringende pakket gesteenten en in het reservoir te scheiden van de compactie van de lagen. Dit werkplan is toegepast op de 4D seismische Shearwater data. De volgende stappen zijn uitgevoerd:

- Vaststellen van de looptijdverschillen uit de 4D seismische data van het Shearwater veld. De looptijdverschillen zijn op de belangrijkste reflectoren geschat en gestabiliseerd door gebruik te maken van verticale sommaties van geschatte tijdverschillen rond de laaggrenzen, dit om het effect van meervoudige reflecties te verminderen. Verder zijn de looptijdverschillen met behulp van een lateraal mediaan filter

gemiddeld om uitschieters te verwijderen. De looptijdverschillen zijn in kaart gebracht langs de belangrijkste reflectoren.

- Berekenen van de relatieve looptijdverschillen in iedere geologische laag, gebruik makend van de relatieve verhouding tussen de gemeten looptijdverschillen aan de bovenkant en aan de onderkant van de lagen. De resultaten van de 2D geomechanische modellering (verticale vervorming) zijn gebruikt om de looptijdverschillen veroorzaakt door verplaatsing van de lagen te verwijderen. We namen waar dat de berekende relatieve looptijdverschillen nauwkeurig de gemodelleerde veranderingen volgden in het spanningsveld voor de 2D seismische lijn die overeenkomt met het geomechanische model.

Onze conclusie hieruit is dat de resultaten van geomechanisch modelleren doeltreffend gebruikt kunnen worden om de gemeten seismische looptijdverschillen te corrigeren voor de effecten van fysieke verplaatsing. De resulterende looptijdverschillen zijn dus gerelateerd aan de veranderingen in de seismische snelheden ten gevolge van veranderingen in de petrofysische eigenschappen en omgevingsomstandigheden. Dit biedt ons de kans gebruik te maken van de berekende relatieve looptijdverschillen om rechtstreeks de veranderingen in het spanningsveld in kaart te brengen. In het Shearwater veld bleek het effect van fysieke verplaatsing voor de geselecteerde 2D lijn, waar de geomechanische modellering is toegepast, verwaarloosbaar klein te zijn. Verder hebben we aangetoond dat de berekende veranderingen in de seismische snelheden nauwgezet de gemodelleerde spanningsvariaties volgen. We hebben de inverse relatie tussen de gemodelleerde spanningsveranderingen en de berekende looptijdverschillen (geïnduceerd door snelheidsveranderingen) gebruikt om veranderingen in de verticale spanning over het gehele veld te beschrijven. In het algemeen zullen de spanningsveranderingen in en rondom een producerend koolwaterstof reservoir altijd veranderingen zullen veroorzaken in de akoestische snelheid. Zoals aangetoond in dit voorbeeld maakt de correlatie tussen deze twee variabelen maakt het mogelijk veranderingen in de petrofysische eigenschappen en in de omgevingsomstandigheden te schatten uit waargenomen snelsheidsveranderingen.

List of abbreviations and symbols

λ, μ	The Lamé coefficients
e	Strain
e_v	Volumetric strain
e_{zz}	Vertical strain
ν	The Poisson ratio
ν_{res}	The Poisson ratio in the reservoir rock
ν_{sur}	The Poisson ratio in the rock surrounding the reservoir
ϕ	Porosity
ϕ_0	Critical porosity
ρ	Density
ρ_{res}	Density in the reservoir rock
ρ_{sur}	Density in the rock surrounding the reservoir

ρ_G	The saturation density
ρ'	The pseudo density
σ	Stress
σ_{eff}	Effective stress
$\overline{\sigma'}$	Mean effective stress
Δ	Time-lapse changes in seismic or rock propeties
Δt	Time-shifts
$\Delta t'$	Time-shifts induced by changes in the stress field
$\Delta t''$	Time-shifts induced by changes in the vertical strain
Δs	Area where the force is applied
γ	Stress arching
γ_x	Horizontal stress arching
γ_z	Vertical stress arching
2D	Two-dimensional
3D	Three-dimensional
4D	Four-dimensional, also known as time-lapse
A	Seismic Amplitude
AVO	Amplitude variation with offset
C	In the Hertz-Mindlin contact theory - number of contacts per grain
C_{ij}	Coefficient of the stiffness matrix
CO_2	Carbon dioxide

CMP	Common mid point
DMO	Dip moveout
du	Displacement
E	The Young modulus
E_{res}	The Young modulus in the reservoir rock
E_{sur}	The Young modulus in the rock surrounding the reservoir
f_i	External force
F	Force per unit area
FEM	Finite Element Method
G	Shear modulus
G_{eff}	Effective Shear modulus calculated using the Hashin-Strickman bounds
G_{HM}	Shear modulus calculated using the Hertz-Mindlin contact theory
JGW	Jason Geoscience Workbench
HPHT	High-pressure, high-temperature
K	Bulk modulus
K_{eff}	Effective Bulk modulus calculated using the Hashin-Strickman bounds
K_{fr}	The Bulk modulus of the dry rock
K_{HM}	Bulk modulus calculated using the Hertz-Mindlin contact theory
L	Length

$\mathbf{n}$	Normal vector
NMO	Normal moveout
p	Pore pressure
p_h	Hydrostatic pressure
PSDM	Pre-stack depth migration
$\dot{q}$	Stress distribution connected to the source
QC	Quality control
R	Factor translating the vertical strain into time-lapse changes in the acoustic velocity
R_G	Gas-to-oil ratio
RMS	Root mean square
S	Salinity
S_{ij}	Coefficient of the compliance matrix
T	Two-way travel time in Chapters 5,6 and 7
T	Temperature in Chapter 3
$\mathbf{T}$	Traction
Sw	Water saturation
t	Time-thickness
TWT	Two-way travel time
TLSRM	Time-lapse seismic reservoir monitoring
v	Particle velocity
V_P	P-wave velocity

V_S	S-wave velocity
u_z	Vertical displacement
Z	Depth-thickness

Contents

1

Introduction

1.1 History

One of the key instruments for the characterization of hydrocarbon reservoirs is seismic data analysis. In the early 1990's the concept of time-lapse seismic data were introduced. Initially time-lapse data, (also known as 4D data), were used qualitatively to mark hydrocarbon migration fronts. This has led to remarkable success of infill drilling in by-passed zones. During the 1990's the quality of the 4D seismic method has dramatically increased due to improved acquisition and processing of the data. This enabled a more quantitative approach, where instead of hydrocarbon migration fronts, fluid saturation and pore pressure could be estimated from the seismic data, e.g., Tura and Lumley [1999], Landrø [2001] and Meadows [2001]. Up to then, only changes in the reservoir were considered. More recently, clear changes in seismic attributes were observed above and below high-pressure, high-temperature (HPHT) reservoirs (e.g. Guilbot and Smith [2002], Hatchell et al. [2003]). In general, these changes are relatively small but they tend to build up over large zones. These effects are described as geo-mechanical effects (e.g. Kenter et al. [1996] and Settari [2002], Hatchell et al. [2003]), i.e.,

stress-strain induced time-shifts in the overburden. In order to predict the changes in the stress field and layer thickness, as well as the variations in the overburden and underburden, the use of geo-mechanical forward modeling is recommended. Guilbot and Smith [2002] monitored the time shift in the Ekofisk field as an effect of physical, vertical, displacement (compaction), using a constrained tomographic method. According to their method, a time shift of 7 ms at the top of the reservoir and 12-16 ms shift below the reservoir level has been observed after 10 years of production, i.e., between 1989 and 1999. In order to predict stress and strain changes, related to the time shifts observed in the time-lapse seismic data, Hatchell et al. [2003] implemented results from geo-mechanical modeling. The latter work presents a good correlation of predicted vertical strain and monitored time shifts. Hatchell and Bourne [2005] used geomechanical modelling together with a stress-strain dependent seismic velocity to compute the time lapse changes in travel time in the overburden and at the reservoir level. Considering a number of experimental investigations and observations worldwide, and applying a linear strain-velocity relation, they reported a good agreement between real data and synthetic modeling. Carcione [2006] employed calibrated petro-elastic models in order to obtain the changes in velocity and thickness of the reservoir and in the overburden rocks, by using the time-lapse variations in the seismic attributes (travel time). Staples et al. [2007a] investigated the variations in the two-way travel time at the HPHT North Sea gas reservoir - Shearwater. Further, they applied the strain-velocity relation suggested by Hatchell and Bourne [2005] to calculate the changes in the P-wave velocity as a result of production.

1.2 Changes in rock properties induced by hydrocarbon production

A rock can be considered as a frame of mineral grains with open pore space between the mineral particles. In reservoir rocks, the pore space is generally filled up either with water/brine or hydrocarbons (i.e., oil or gas). Seismic data are sensitive to the bulk modulus and density of a rock (i.e. grains and pore fluid). These rock properties depend on a number of parameters and events such as : compaction, consolidation, age, cementation, texture,

porosity, lithology, pore shape, viscosity, density, saturation, temperature, and effective stress. The different parameters are strongly dependent on each other. When changing one property at the time, other parameters will be affected. Production will immediately influence the saturation/gas-density of the rock and the pore pressure. As a consequence, changes in the bulk and shear modulus and in the density are expected. Variations in the pore pressure over time might also lead to changes in the porosity (compaction or elongation), again influencing the bulk modulus and density. For a better understanding of the production process and the 4D changes of the rock properties, it is useful to make a synthetic simulation, using a forward rock-physics and geo-mechanical model. There are two approaches to link both the variations in the rock parameters over time with the 4D changes in the seismic attributes (amplitude and travel time):

[1] The common and generally accepted approach is to perform laboratory experiments to predict the time-lapse changes of one or several rock properties as a result of hydrocarbon production at the reservoir level. The experimental results from the laboratory tests are analyzed and models are developed. Two of the major issues in using such models derived from laboratory experiments are up-scaling and the need of representative cores. Nes et al. [2000] studied the reliability of core data as an input parameter for the reservoir characterization. One of the problems in using core data is to compensate for the core damage effects which are induced by the unloading of the sample. Another problem is to thoroughly represent the in situ conditions in the laboratory during the lab test.

[2] An alternative approach, which can help in studying the changes of the rock physics properties, is to use of an estimated relations between time-lapse seismic data and rock physics properties. These relations can be predicted using the rock physics theory (effective elastic media and granular media) or based on the real-data observations (empirical relations). The changes in the rock parameters will influence the elastic properties of the rock and consequently will affect the seismic signal. By monitoring the time-lapse changes in the seismic data (travel time and amplitude), one can invert for the changes in the elastic properties and environmental conditions.

1.3 Is 4D seismics able to detect variations in rock properties induced by production?

The major question to answer is which of the rock properties can be detected by time-lapse seismic data. Wang and Nur [2000] reported an overview of the physical basis of the feasibility of time-lapse seismic reservoir monitoring (TLSRM). If the changes in the reservoir seismic properties are large enough, time-lapse seismic data can successfully map changes in: fluid distributions, pressure/fluid fronts and changes in the temperature. Favorable candidates for TLSRM according to Wang [2002a] are:

[1] Shallow reservoirs with low effective stress are showing large effects on pressure and on pore fluid;

[2] Rocks with low frame bulk modulus, as unconsolidated or poorly consolidated rocks or rocks with open; fractures.

[3] High contrast in pore fluid compressibility of the saturating fluids. substitution.

In addition to influencing the reservoir properties and parameters, the overburden can also significantly influence the possibility for detection of these properties from the seismic repeated surveys. Several authors observed and reported 4D changes in the seismic attributes in the overburden layers:

- Johnston et al. [1998] presented case study of the Fulmar Field and evaluated the potential of the 4D seismic to detect the pressure changes and fluid substitution in the reservoir. The authors applied two different techniques to investigate the 4D changes in the seismic properties: 1) the direct hydrocarbon indicators a mapped and recognized on the time-lapse changes in the seismic attributes, 2) The time-lapse difference in the acoustic impedance is estimated. Furthermore, Johnston et al. [1998] used petrophysical models to calculate the time-lapse changes in the acoustic impedance using results from a flow simulator (pressure and water saturation). Johnston et al. [1998] claimed to monitor a good overall agreement between the calculated and actual impedance changes. With their case study Johnston et al. [1998] demonstrated that the results of the time-lapse seismic can be interpreted in terms of 4D changes in the reservoir properties.

- Vidal et al. [2002] applied a flow simulation of an oil reservoir to obtain the saturation and pore pressure changes in time. The pore pressure was used as input to the geo-mechanical model in order to calculate the mean effective stress field. Both the effective stress and the saturations are then used in combination with a petro-elastic model to simulate the repeated seismic data. This study was further elaborated by Vidal-Gilbert et al. [2005] and Vidal-Gilbert and Tisseau [2006].

- Arts et al. [2004b] and Arts et al. [2004a] used the 4D changes in the seismic data to investigate and monitor the CO_2 migration in Spleiner field. The results of the seismic interpretation were presented, supported by synthetic seismic modelling and reservoir flow simulation of the migrating CO_2. Next, Arts et al. [2004b] used the seismic interpretation to construct a reservoir flow simulation model. They used this model to simulate the injection process and to "predicted" distribution of the CO_2 at the times of the monitoring seismic surveys. Arts et al. [2004b] used the distribution to generate synthetic seismic and compared them directly to the seismic field data. Arts et al. [2004b] claimed that the satisfactory match increases the confidence in a correct understanding of the fluid flow in the reservoir. Arts et al. [2008] comprised the whole 10 years time-lapse study of the CO_2 injection effect on the 4D seismic in Spleiner. They also included the results of 4D gravity study, where the results are used to estimate the density and temperature of the injected CO_2.

- A good guide how to build and use the geo-mechanical modelling in order to link the changes in rock physics properties to the changes in seismic attributes, are the publications of Kenter et al. [2004] and Molenaar et al. [2004]. From their modelling it can be observed that the modeled stress changes are mapping quite accurately the observed time shifts in the real-data examples.

- Stammeijer et al. [2004] studied the time-lapse seismic effect in a depleting gas field. The geo-mechanical modeling shows that in this latter case, the changes in time shifts will occur not only in the reservoir, but also in the rock, bounding the reservoir, which will be the effect of stress and strain alterations, induced by the production itself.

Stammeijer et al. [2004] reported that in some cases the changes in the two way travel time over time in the overburden can be comparable and even larger than the time-shifts at the reservoir level.

- Hatchell et al. [2005] observed less subsidence at the surface than at the top of the reservoir which means that the overburden has been stretched. Based on these observations, Hatchell and Bourne [2005] proposed forward models of time-lapse time shifts, constructed from stress/strain dependent seismic velocities. The stress and strain values are computed using geo-mechanical models. Based on actual time-shift observations, various velocity stress/strain models were tested to see which agreed best with the data. Based on observations of time-lapse seismic data from several locations around the world, Hatchell and Bourne [2005] found that a simple linear model relating the relative changes in the seismic velocity with vertical normal strain works well in the their case-studies. Their observations also show that the velocity-strain dependence is larger for rock elongation than for rock contraction.

- Røste et al. [2005], independently from Hatchell and Bourne [2005], introduced a method to distinguish between the changes in the seismic velocity and layer thickness induced by compaction. In the proposed method, Røste et al. [2005] demonstrated that the effect of layer compaction on the rock properties (porosity and permeability) on the seismic velocity can be found using linear relation between the relative changes in the seismic velocity and the vertical strain. In addition to the proposed Hatchell and Bourne [2005] approach Røste et al. [2006] investigated the lateral changes in the seismic velocity by utilizing the zero-offset and the offset dependent time-shifts. Røste et al. [2005] also presented that the stress-velocity relationship will also changes laterally dependent on the changes in the petrophysical properties of the rock.

- Holt et al. [2005] elaborate on the ability to recognize the correlate the stress induced time-lapse changes in the seismic data with the petrophysical measurements of stress velocity. Holt et al. [2005] incorporate nonlinear elasticity in the petrophysical model in order to ob-

tain stress sensitivity which will match accurately the stress-velocity changes in the field. Holt et al. [2005] demonstrated that the time-lapse changes in the seismic velocity depends on three stress-dependent factors: 1)changes in porosity with stress, 2)existence of sharp grain contacts and 3)presence of generation of cracks/fractures.

- Staples et al. [2007a] converted the results of the geo-mechanical modelling to synthetic seismic time-shifts by adapting the Hatchell and Bourne [2005] approach and compared the results with the measured time-shifts from the real 4D data. Staples et al. [2007a] investigated the changes in the travel time in each of the overburden layers separately and presented good correlation between the measured and calculated time-shifts. Hatchell and Bourne [2005] also explained the changes in time-shifts with the time-lapse changes in seismic velocity induced by 4D changes in the rock properties.

- Landrø and Amundsen [2009] suggested a simple method to estimate the relation between the relative changes in the seismic velocity and vertical strain using the analytical expression for the 4D changes in the gravity filed and measured time-shifts. Landrø and Amundsen [2009] used the 4D changes in the gravity to calculate the vertical stain at the top of the reservoir.

A step further will be to look quantitatively into changes in the reservoir as a result of production or fluid migration. The seismic changes are a result of all combined rock physical properties variations (both in the reservoir and in the bounding layers). Is it possible to distinguish the various changes, resulting from different rock properties, by using the data information from repeated seismic surveys? One of the ways to quantify the variations in the different rock physics properties, for instance a changes in pore pressure and changes in saturation, is by exploiting the fact that the seismic attributes will be affected differently by both of these changes. Landrø [2001] used the rock modelling in order to investigate how the changes in pore pressure will affect the seismic amplitude (intercept and gradient). Meadows [2001] elaborated Landrø's method by using the seismic impedance, rather than intercept and gradient information. Further in his research, Landrø [2002] proposed to reduce the uncertainties from the direct inversion of the rock

physics properties from time-lapse changes in the amplitude, by including the time-shifts information in the inversion process. Considering the fact that density will remain unchanged after pure stress effects, it will be possible to quantify the pressure and saturation effects. Note, that this is possible only when the compaction effect is negligible. A comprehensive summary, regarding the qualification and quantification of the rock properties by using TLSRM, can be found in Avseth et al. [2005].

1.4 Objective of the research

Considering the previous discussion in section 1.3, under favorable conditions 4D seismics apparently offers the opportunity to detect and moreover quantify time-lapse changes in rock physical properties. The work flow used in this thesis to detect and quantify such changes is depicted in Figure 1.1. The main objective of this research is to investigate how geo-mechanical modelling can improve reservoir characterization from time-lapse seismic data. The reservoir characterization is improved by including the geo-mechanical modelling (work-flow in Figure 1.1). The production effects on the two-way travel time both in the overburden and at the reservoir layer are explained with time-lapse changes in the effective stress and reservoir compaction. In our case study we assumed that the effect of fluid migration inside the reservoir is negligible and the time-lapse effects are induced from the changes in the pressure filed.
Two models with different complexities in geometry are developed to reach the objectives:

- A relatively simple box-model representative for a North Sea oil reservoir. The effect of the time-lapse changes in the overburden on the TLSRM is investigated.

- A more complex model representative for a real North Sea gas reservoir. The model structure is built using the interpreted time horizons. 4D seismic production data (Shearwater field) are used together with geo-mechanical modelling to explain the time-lapse changes observed as a result of reservoir depletion. The relation between the time-lapse changes in the real data examples and the result of the geo-mechanical modelling (stress/strain) is presented.

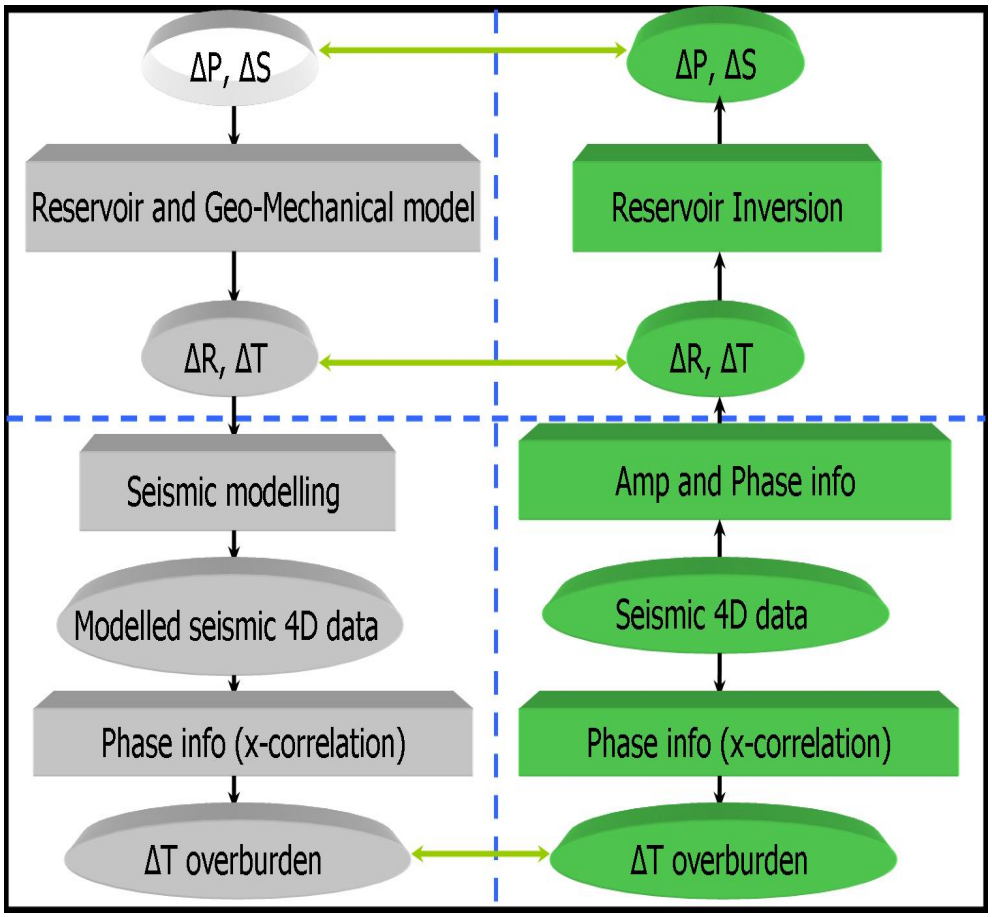

Figure 1.1: *The work flow used in the thesis: the left section presents the forward problem; the right section depicts the rock properties inversion from the time-lapse data (ΔP, ΔS : changes in pore pressure and water saturation ; ΔR, ΔT : changes in reflection amplitude and travel time). In the forward problem time-lapse changes in the environmental conditions and rock properties are simulated using flow simulator and geo-mechanical modelling. These 4D changes are used to modelled production related synthetics time-lapse data and to measured the synthetic time-shifts. The synthetic time-shifts are used to understand the measured time-shifts from the real 4D data in the inverse modelling. Further, the time-shifts measured from the real data are used to invert the variations in the rock properties and environmental conditions as result of production.*

1.5 Outline

Chapter 1 gives an overview of time-lapse reservoir characterization. The influence of the rock physics properties on the repeated seismic data and the possibility to qualify and even quantify the changes in the solid and fluid properties is indicated with several examples from the literature. The assumption that production induced changes in the overburden can be neglected is questioned here and examples of non-negligible effects are discussed. In this thesis a method is proposed to quantify these effects by using geomechanical modelling.
In **Chapter 2** the physical framework of geo-mechanical and seismic modelling is given. The fundamental concepts of strain and stress must be well understood, prior to building the model and studying the elastic properties of the rocks. In order to map the time-lapse changes in the seismic data, resulting from the geo-mechanical changes, the theoretical and physical aspects of both modelling approaches are compared. The constitutive equations, applied for both models, are further discussed. Finally the interrelation between the results from the geo-mechanical forward modelling and variations in the seismic data is presented. This relation is used to predict the 4D changes in the rock physics properties.
Chapter 3 discusses the effect of pore pressure and saturation changes, investigated by building a rock physics model of a hydrocarbon reservoir. This model was built using analytical models, available from literature. The model consists of two separate parts corresponding to the dry rock and pore fluid. The solid phase was built, using the model suggested by Mavko et al. [1998], which is a model of poor consolidated sandstones, where the contacting cement is separated from the grain boundaries. The alterations, relevant to the fluid phase of the model, were derived using the analytical solution for a mixture of brine and live oil, given by Wang [2001]. The Gassmann low frequency theory, see Mavko et al. [1998], was used to couple the solid and fluid parts in saturated rock.
Geo-mechanical modelling allows to monitor the changes in a stress/strain field as result of production at the reservoir level. The first Section of **Chapter 4** illustrates different analytical and numerical approaches from the literature. In the second section of this chapter, the stress regimes in the subsurface are discussed together with the general concepts of stress and strain devel-

opment for hydrocarbon reservoirs. The analytical solutions, given in this section, will help to understand the obtained time-lapse changes as a product of the geo-mechanical modelling (stress arching, stress changes, displacement).
Further, **Chapter 5** presents the development of two types of models. For the first model, an analytical solution of the reservoir modeling was used (**Chapter 3**) to set up the elastic properties of the model. For the second model, well log data obtained from a North Sea reservoir were used.
Chapter 6 describes the forward synthetic seismic modelling, by using the results from **Chapter 5**. Time-lapse changes in the seismic properties occurred as a result from production at the reservoir level. The changes over time in the two-way travel time were observed. The measured time-shifts as a function of offset are used for the feasibility study of the real data example. The inverse problem, depicted in Fig.1.1. (right section) is discussed in **Chapter 7**. The time shifts are obtained from the North Sea gas reservoir time-lapse seismic data. Geo-mechanical modeling is performed to understand the changes in the stress and strain field as a result of production and to explain the monitored 4D effects in the seismic data examples. The stress changes are inverted from the repeated seismic surveys by using the computed relation between the measured time-shifts and the results of the geo-mechanical modelling.
Finally, **Chapter 8** comprises an overview of the initial objectives, the experimental procedures and modeling approaches to reach the main goals of this research and the conclusions from this work. Additionally, some recommendations for future research, related to the findings of the thesis, are presented.

2

Fundamental physical concepts

In this chapter the relation between geo-mechanical and seismic modelling is explained. Geo-mechanical modelling simulates the time-lapse changes in the stress and strain field as a result of production at the reservoir level. The challenge is to find the relation between changes in the rock mechanics and seismic properties, which will help to solve the forward problem, i.e., the calculation of the 4D seismic changes induced by the stress-strain variations. In Section 2.1 of this chapter the basic concepts of the elastic theory and geo-mechanical modelling are presented. In Section 2.2 the wave equation in elastic media is presented. Finally in Section 2.3 the coupling between geo-mechanics and seismic data is discussed.

2.1 Strain and stress - geo-mechanical modelling

Stress is defined as a force per surface area through which the force is acting, as shown in Figure 2.1. In the left part of a body with a small element on the surface is shown. The external traction $\mathbf{T}$ represents the force per unit

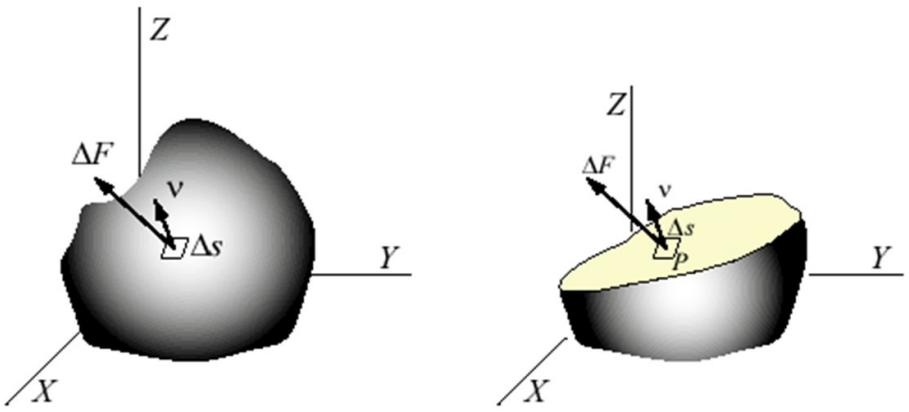

Figure 2.1: *Left - force acting on the body surface, Right - force acting inside a solid (adapted from Mulders [2003]).*

area acting at a given location on the body's surface. Traction $\mathbf{T}$ is a bound vector, which means $\mathbf{T}$ cannot slide along its line of action or translate to another location and keep the same meaning. A traction vector cannot be fully described unless both the force and the surface where the force acts on has been specified. Given both $\Delta\mathbf{F}$ and Δs, the traction $\mathbf{T}$ can be defined as:

$$\mathbf{T} = \lim_{\Delta s \to 0} \frac{\Delta \mathbf{F}}{\Delta s} = \frac{d\mathbf{F}}{ds}. \tag{2.1}$$

The internal traction within a solid (see the right part of Figure 2.1) can be defined in a similar way. Surface tractions would appear on the exposed surface, similar in form to the external tractions applied to the body's exterior surface. Stress therefore can be interpreted as internal tractions that act on a defined internal plane. Surface tractions, or stresses acting on an internal datum plane, are typically decomposed into three mutually orthogonal components. One component is normal to the surface and represents normal stress. The other two components are tangential to the surface and represent shear stresses (see Figure 2.2). The stress state at point P (Figure 2.2) can be

represented with an infinite small cube with three stress components on each side of the cube.

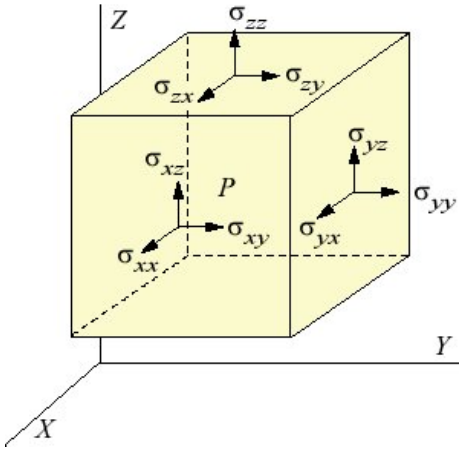

Figure 2.2: *Components of stress vectors on coordinate planes (adapted from Mulders [2003]).*

If the body is under static equilibrium, then the state of stress can be represented with nine components from three sides of the cube. These nine components can be organized in one matrix:

$$\begin{pmatrix} \sigma_{xx} & \sigma_{xy} & \sigma_{xz} \\ \sigma_{yx} & \sigma_{yy} & \sigma_{yz} \\ \sigma_{zx} & \sigma_{zy} & \sigma_{zz}, \end{pmatrix} \tag{2.2}$$

where shear stress as mirrored across the diagonal of the matrix $\sigma_{ij} = \sigma_{ji}$ are identical as a result of static equilibrium. The matrix in equation 2.2 is known as the stress tensor. The traction on a plane with normal vector $\mathbf{n}$ is related to the stress tensor via $\mathbf{T} = \sigma\mathbf{n}$. Consider a bar with initial length L which is stretched to a length L' (Figure 2.3). The strain measure e, a dimensionless ratio, is defined as the ratio of elongation with respect to the original length,

$$e = \frac{L' - L}{L}. \tag{2.3}$$

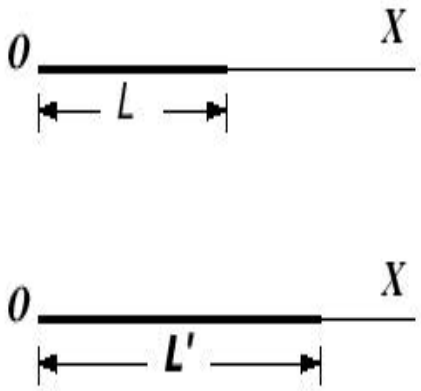

Figure 2.3: *1D Strain (adapted from Mulders [2003]).*

The above strain measure is defined in a global sense. The strain at each point may vary dramatically if the bar's elastic modulus or cross-sectional area changes. To track down the strain at each point, further refinement in the definition is needed. Consider an arbitrary point P in the bar, which has a position vector x, and its infinitesimal neighbor $x + dx$ (Figure 2.4). Point P shifts to P', which has a position vector x', after the stretch. In the meantime, the small "step" dx is stretched to dx'. The strain can hence be rewritten as,

$$e = \frac{dx' - dx}{dx} = \frac{du}{dx}, \tag{2.4}$$

where du is denoted to the displacement. The components of strain for a solid like in the Figure 2.2 can be organized in a matrix similar to the stress tensor (Equation 2.2):

$$\begin{pmatrix} e_{xx} & e_{xy} & e_{xz} \\ e_{yx} & e_{yy} & e_{yz} \\ e_{zx} & e_{zy} & e_{zz}, \end{pmatrix} \tag{2.5}$$

the strain (e) will be further defined in Equation 2.12.

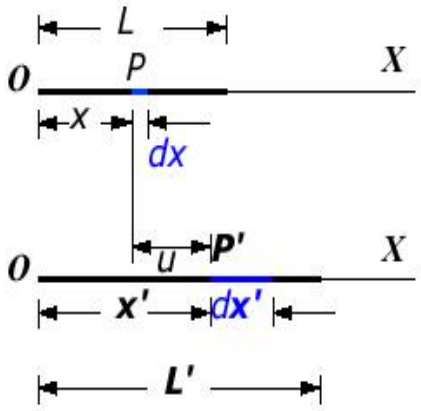

Figure 2.4: *Strain at specific point (adapted from Mulders [2003]).*

The so called constitutive equations in mechanics are characterizing the behavior of specific materials. The stress and strain tensors describe the state of a material. The relationship between internal stress and internal strain can be expressed as a constitutive equation (Tiğrek [2004]). The mechanical behavior of real materials is very diverse and complex and it would be impossible to formulate equations which are capable of determining the stress in a body under all circumstances (Spencer [2004]). The aim is to establish equations which describe the most important features of the behavior of the material in a given situation. Such equations could be regarded as defining ideal materials. It is unlikely that any real material will conform exactly to any such mathematical model, but if the ideal material is well chosen its

behavior may give an excellent approximation to that of the real material which it models (Spencer [2004]). One ideal model is based on the assumption of a linear relation between stress and strain which will lead to a linear constitutive equation. The common effect of different strain histories will be equal to the sum of the effects of the individual strain histories. For a locally reacting material the internal stress at a certain fixed position can be related entirely to the strain history of that local material (Tiğrek [2004]). Materials following the same constitutive equations are building one rheological class. Depending on the material properties and stress/strain relation the rheological classes can be elasticity, plasticity, or viscosity. In our case study we will discuss only the case of elasticity. Elastic behavior is characterized by the following two conditions: (1) the stress in a material is a unique function of strain, and (2) the material has the property of complete recovery to a "natural" shape upon removal of applied forces (Mase and Mase [1999]). The behavior of a material can be elastic or not elastic (inelastic), see Figure 2.5, where the elastic behavior may be linear or nonlinear. Elastic behavior means that applied stress leads to a strain, which is reversible when the stress is removed. Linear elasticity implies that the relationship between stress and strain is linear, which is correct only in the case of small strains, or small stress increments. The particular material and the particular state of stress under consideration determine what is "small". Most rock mechanics applications are based on linear elasticity, although it is well established that most sedimentary rocks exhibit non-linear behavior, plasticity, and even time dependent deformation (creep). However, the linear elasticity is simple, and the parameters required can be estimated from log data and standard laboratory tests. The rocks in the upper lithosphere can be considered elastic for loads with a duration that is short when compared with the age of the Earth (Ranalli [1995]). This gives us the ability to consider elasticity as the most important rheological class in geo-mechanical modelling (Tiğrek [2004]). Robert Hooke (1660) showed that linear elasticity can be mathematically expressed as:

$$F = -ku, \tag{2.6}$$

where F is the applied force, u is the deformation of the elastic body subjected to the force F and k is the force constant. In three dimensional case

the link between stress and strain is given with the stiffness matrix which has 81 components. Due to the symmetry of the stress tensor, strain tensor, and stiffness tensor, only 21 elastic coefficients are independent. Cauchy used the Voigt notation to generalize Hooke's law to three dimensional elastic bodies and stated that the 6 components of stress are linearly related to the 6 components of strain, according to

$$\begin{pmatrix} e_{xx} \\ e_{yy} \\ e_{zz} \\ e_{yz} \\ e_{zx} \\ e_{xy} \end{pmatrix} = \begin{pmatrix} S_{11} & S_{12} & S_{13} & S_{14} & S_{15} & S_{16} \\ S_{21} & S_{22} & S_{23} & S_{24} & S_{25} & S_{26} \\ S_{31} & S_{32} & S_{33} & S_{34} & S_{35} & S_{36} \\ S_{41} & S_{42} & S_{43} & S_{44} & S_{45} & S_{46} \\ S_{51} & S_{52} & S_{53} & S_{54} & S_{55} & S_{56} \\ S_{61} & S_{62} & S_{63} & S_{64} & S_{65} & S_{66} \end{pmatrix} \begin{pmatrix} \sigma_{xx} \\ \sigma_{yy} \\ \sigma_{zz} \\ \sigma_{yz} \\ \sigma_{zx} \\ \sigma_{xy} \end{pmatrix}, \tag{2.7}$$

$$\begin{pmatrix} \sigma_{xx} \\ \sigma_{yy} \\ \sigma_{zz} \\ \sigma_{yz} \\ \sigma_{zx} \\ \sigma_{xy} \end{pmatrix} = \begin{pmatrix} C_{11} & C_{12} & C_{13} & C_{14} & C_{15} & C_{16} \\ C_{21} & C_{22} & C_{23} & C_{24} & C_{25} & C_{26} \\ C_{31} & C_{32} & C_{33} & C_{34} & C_{35} & C_{36} \\ C_{41} & C_{42} & C_{43} & C_{44} & C_{45} & C_{46} \\ C_{51} & C_{52} & C_{53} & C_{54} & C_{55} & C_{56} \\ C_{61} & C_{62} & C_{63} & C_{64} & C_{65} & C_{66} \end{pmatrix} \begin{pmatrix} e_{xx} \\ e_{yy} \\ e_{zz} \\ e_{yz} \\ e_{zx} \\ e_{xy} \end{pmatrix}, \tag{2.8}$$

where C are the coefficients of the stiffness matrix and S the coefficients of the compliance matrix. The stiffness and compliance matrices of a solid, isotropic and lineraly elastic material have only 2 independent variables (i.e. elastic constants),

$$\begin{pmatrix} e_{xx} \\ e_{yy} \\ e_{zz} \\ e_{yz} \\ e_{zx} \\ e_{xy} \end{pmatrix} = \frac{1}{E} \begin{pmatrix} 1 & -\nu & -\nu & 0 & 0 & 0 \\ -\nu & 1 & -\nu & 0 & 0 & 0 \\ -\nu & -\nu & 1 & 0 & 0 & 0 \\ 0 & 0 & 0 & 1+\nu & 0 & 0 \\ 0 & 0 & 0 & 0 & 1+\nu & 0 \\ 0 & 0 & 0 & 0 & 0 & 1+\nu \end{pmatrix} \begin{pmatrix} \sigma_{xx} \\ \sigma_{yy} \\ \sigma_{zz} \\ \sigma_{yz} \\ \sigma_{zx} \\ \sigma_{xy} \end{pmatrix}, \tag{2.9}$$

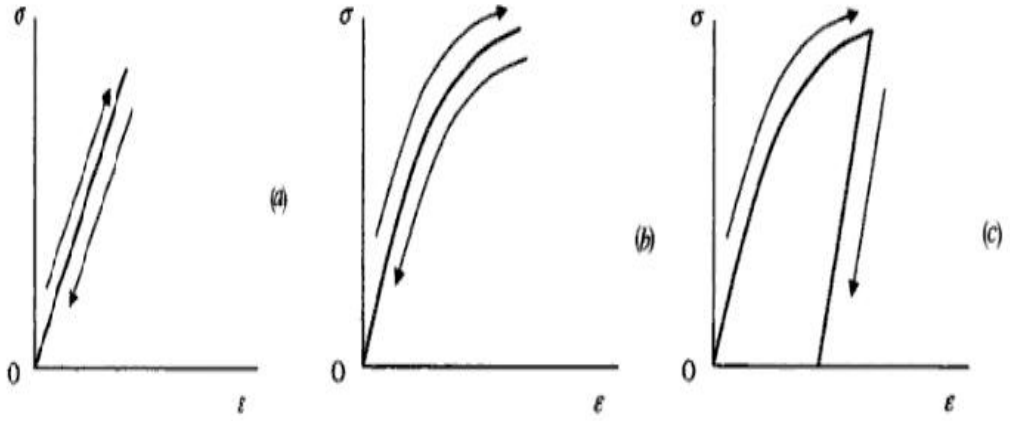

Figure 2.5: *Uniaxial loading-unloading stress curves for (a) linear elastic, (b) nonlinear elastic and (c) inelastic behavior, Mase and Mase [1999]*

where E is the Young modulus and ν is the Poisson ratio, Charlez [1991]. Young's modulus and Poisson's ratio can be determined from the uniaxial stress ($\sigma_{xx} = \sigma_{yy} = 0$). Using this condition from Equation 2.9 follows:

$$\begin{aligned} \sigma_{zz} &= E e_{zz}, \\ e_{xx} &= e_{yy} = -\nu e_{zz}. \end{aligned} \tag{2.10}$$

From Equation 2.10 follows that the Young's modulus represents the stiffness of a material, i.e. the resistance against compression under uniaxial loading conditions, where as the Poisson ratio is giving the ratio between lateral expansion and longitudinal contraction, (Mulders [2003]). The Young modulus and the Poisson ratio can be related with two other important elastic parameters: 1) the bulk modulus (the inverse of the compressibility) and 2) the shear modulus, which is the relation between shear stress and shear strain. Suppose that an isotropic solid is subjected to hydrostatic pressure p_h, in such a case all the shear stresses will be zero and the normal stresses will be uniform ($\sigma_{xx} = \sigma_{yy} = \sigma_{zz} = -p_h$). The relation between hydrostatic stress and volumetric strain ($e_v = e_{xx} + e_{yy} + e_{zz}$) can be expressed as

$$\begin{aligned} -p_h &= Ke_v, \\ K &= E/3(1-2\nu), \end{aligned} \tag{2.11}$$

where K is the bulk modulus. Let us consider a "pure shearing", the relation between shear strains and shear stresses in Equation 2.9 can be presented as

$$\begin{aligned} e_{yz} &= \frac{\sigma_{yz}}{2G}, \\ e_{zx} &= \frac{\sigma_{zx}}{2G}, \\ e_{xy} &= \frac{\sigma_{xy}}{2G}, \end{aligned} \tag{2.12}$$

with $G = E/2(1+\nu)$ known as the shear modulus. The different elastic stiffness parameters E, ν, K, and G are not independent. In an isotropic material, there are only 2 independent stiffness parameters, so we may choose to work with any pair of elastic parameters that we would like. In seismic wave propagation the so-called Lamé coefficients λ and μ are used. Equation 2.9 can be presented with Lamé's parameters:

$$\sigma_{ij} = \lambda e_{kk}\delta_{ij} + 2\mu e_{ij}, \tag{2.13}$$

where Einstein's summation convention applies to repeated subscripts, and

$$\lambda = \frac{E\nu}{(1+\nu)(1-2\nu)}, \tag{2.14}$$

$$\mu = \frac{E}{2(1+\nu)}. \tag{2.15}$$

Equation 2.13 can be used in both the geo-mechanical model and in the seismic model, (Tiğrek [2004]). It is conjectured that the values in the two models are different but related through the static state of stress and that the static and dynamic elastic parameters depend in the same way on the static

state of stress. This conjecture is experimentally validated in Tiğrek [2004]. Comparing Equation 2.15 with Equation 2.12 we can see that $\mu = G$. In terms of the strain tensor, Equation 2.13 can be written as

$$e_{ij} = \frac{1}{E}((1+\nu)\sigma_{ij} - \nu\sigma_{kk}\delta_{ij}). \tag{2.16}$$

The Equation 2.13 and 2.16 are valid for an inhomogeneous, isotropic, solid material, (Mulders [2003]). They apply to perfectly elastic and isotropic solids and can be used for geo-mechanical modelling. For finite motion the equation of motion in continuous media is given from Aki and Richards [2002] in form of

$$\frac{\partial \sigma_{ji}}{\partial x_j} + f_i = \rho \frac{\partial^2 u_i}{\partial t^2}, \tag{2.17}$$

where f_i is the external force. For elastic homogeneous bodies this equation can be rewritten using Hooke's law and the expression for strain

$$e_{ij} = \frac{1}{2}(\partial_j u_i + \partial_i u_j), \tag{2.18}$$

$$(\lambda + \mu)\partial_i \partial_j u_j + \mu \nabla^2 u_i + f_i = \rho \frac{\partial^2 u_i}{\partial t^2}. \tag{2.19}$$

For geo-mechanical modelling the right hand side of Equation 2.17, representing the acceleration, can be taken as zero (Tiğrek [2004])

$$\frac{\partial \sigma_{ji}}{\partial x_j} + f_i = 0. \tag{2.20}$$

This is the equation of equilibrium. Similar to this Equation 2.19 also can be written as:

$$(\lambda + \mu)\partial_i \partial_j u_j + \mu \nabla^2 u_i + f_i = 0, \tag{2.21}$$

which is the equation of equilibrium for the displacement.

2.2 Seismic wave equation

The linearized form of equation of motion for the elastic wave field is coming from Equation 2.17, where the velocity is used instead of displacement (Wapenaar and Berkhout [1989]) :

$$\frac{\partial \sigma_{ij}}{\partial x_j} + f_i = \rho \frac{\partial v_i}{\partial t}. \tag{2.22}$$

To find the elastic wave equation we need to define the constitutive equation which is coming from Hooke's law (Wapenaar and Berkhout [1989])

$$\frac{\partial \sigma_{ij}}{\partial t} - c_{ijkl} \frac{\partial v_k}{\partial x_l} = -\dot{q_{ij}}, \tag{2.23}$$

where $\dot{q}_{ij}$ represents the stress distribution connected to the source. The equation for elastic wave propagation follows by differentiating both sides of Equation 2.22 with respect to time and substituting the stress velocity relation into the result

$$\rho \frac{\partial^2 v_i}{\partial t^2} - \frac{\partial}{\partial x_j}(c_{ijkl} \frac{\partial v_k}{\partial x_l}) = \frac{\partial f_i}{\partial t} - \frac{\partial \dot{q}_{ij}}{\partial x_j}. \tag{2.24}$$

This equation is describing wave propagation in inhomogeneous and anisotropic solids. In case of inhomogeneous, isotropic, media Equation 2.24 can be simplified using Equation 2.13, valid for both geo-mechanical and seismic modelling, to

$$\rho \frac{\partial^2 v_i}{\partial t^2} - \frac{\partial}{\partial x_i}\left(\lambda \frac{\partial v_k}{\partial x_k}\right) - \frac{\partial}{\partial x_j}\left[\mu\left(\frac{\partial v_i}{\partial x_j} + \frac{\partial v_j}{\partial x_i}\right)\right] = \frac{\partial f_i}{\partial t} - \frac{\partial \dot{q}_{ij}}{\partial x_j}. \tag{2.25}$$

The seismic velocities are related to the Lamé parameters through (Sheriff [2002]):

$$V_p = \sqrt{\frac{\lambda + 2\mu}{\rho}}, \quad V_s = \sqrt{\frac{\mu}{\rho}}, \tag{2.26}$$

where V_p is the P-wave velocity and V_s denotes the S-wave velocity. The elastic parameters in the Equation 2.25 are not the same as the ones given in Equation 2.21. The static state of stress is common to both models as given in Equation 2.13. In seismic modelling the stress is related to the small strains, and the corresponding stiffness matrix is called the dynamic stiffness matrix, that includes dynamic elastic parameters. In a geo-mechanical model, the same term is related to the larger strains as a result of plate movements, rifting, overburden pressure, etc. Here, naturally, lower values will come out for the elements of the stiffness matrix and this can be called the static stiffness matrix. A static stiffness matrix includes the static elastic parameters. The dynamic elastic parameters are different from the static ones, however they can be presented as a function of stress, and are related throughout the static state of stress (Tiğrek [2004]).

2.3 Interrelation between geo-mechanical modelling and seismic data

Seismic velocities and bulk densities may change as a result of production. This is illustrated in Figure 2.6. The left part of Figure 2.6 represents the compacted reservoir. Seismic velocity decreased in the overburden due to elongation, whereas the pressure depletion increased the seismic velocity in the reservoir. The slight velocity increase, observed in the side-burden, can be explained by a stress redistribution phenomenon known as stress arching (Stammeijer et al. [2004]). The right hand side of Figure 2.6 depicts the cumulative time-shift, measured at the vertical line, through the center of the reservoir. The time-lapse variations in the two-way travel time are directly affected by the changes in the seismic velocity and layer thickness. The forward modelling, applied to predict the changes into dynamic elastic properties (seismic velocity and density), used in this research is similar to the work flow proposed by Vidal-Gilbert and Tisseau [2006] and Kawar et al. [2003]. The approach is outlined in Figure 2.7. Using the empirical relation between the seismic velocity and the vertical strain,

$$\Delta V_p/V_p = -Re_{zz}, \tag{2.27}$$

introduced by Hatchell et al. [2005], it is possible to present the changes in

the seismic velocity as a function of the vertical strain. The dimensionless R coefficients represents the effect of compaction on the changes in the seismic velocity affected from the changes in the effective stress and porosity of the rock. The R coefficient will also depend on the elastic properties of the building rock. Note that Røste et al. [2005], independently from Hatchell and Bourne [2005] proposed similar approach to calculate the changes in the seismic velocity using the measured vertical strain. In their approach Røste et al. [2005] denoted the linear coefficient with α instead with R. Hatchell et al. [2005] demonstrated that under favorable conditions, i.e. good repeatability, low noise level, etc., it is possible to detect the changes in the two-way travel time and seismic amplitude from the time-lapse seismic data. Further more the results of the 4D seismic (amplitude and travel time) are used to validate the predicted velocity from the geo-mechanical modelling. Landrø and Stammeijer [2004] demonstrated that the link between geo-mechanics and seismic attributes, for small changes in acoustic velocity, can be presented as

$$\Delta t/t = \Delta Z/Z - \Delta V_p/V_p, \tag{2.28}$$

where Z denotes the depth-thickness, t is the time-thickness and V_p is the acoustic velocity in the specific interval. Equation 2.27 and 2.28 can be combined to predict the time-shift (Staples et al. [2007a]). The adopted from Staples et al. [2007a] to the two-way travel time is presented below:

$$\Delta t(Z) = 2\int_0^Z (1+R)\frac{e_{zz}}{V_p}dZ. \tag{2.29}$$

Using Equation 2.29 the changes in the seismic velocity, predicted from the geo-mechanical modelling, are calibrated using the time-shift derived from the 4D data. Also, the calibrated changes in velocity are compared with the results from the analytical model of the reservoir. The petro-elastic model is adjusted to fit the real data observations and used to invert the changes in the rock parameters from the time-lapse information.

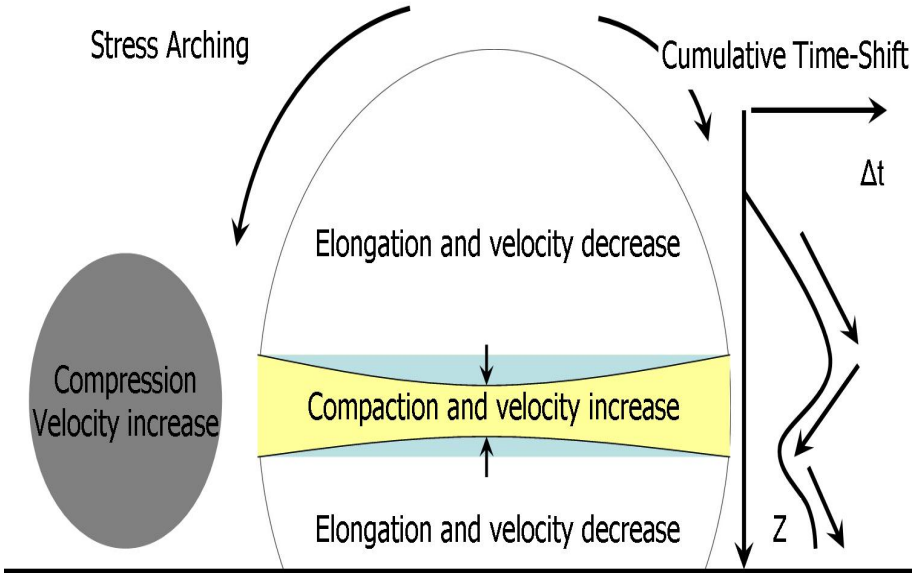

Figure 2.6: *Time-lapse changes in the seismic velocity induced from the compaction of the hydrocarbon reservoir and the changes of the stress field as a result of hydrocarbon production, Staples et al. [2007a].*

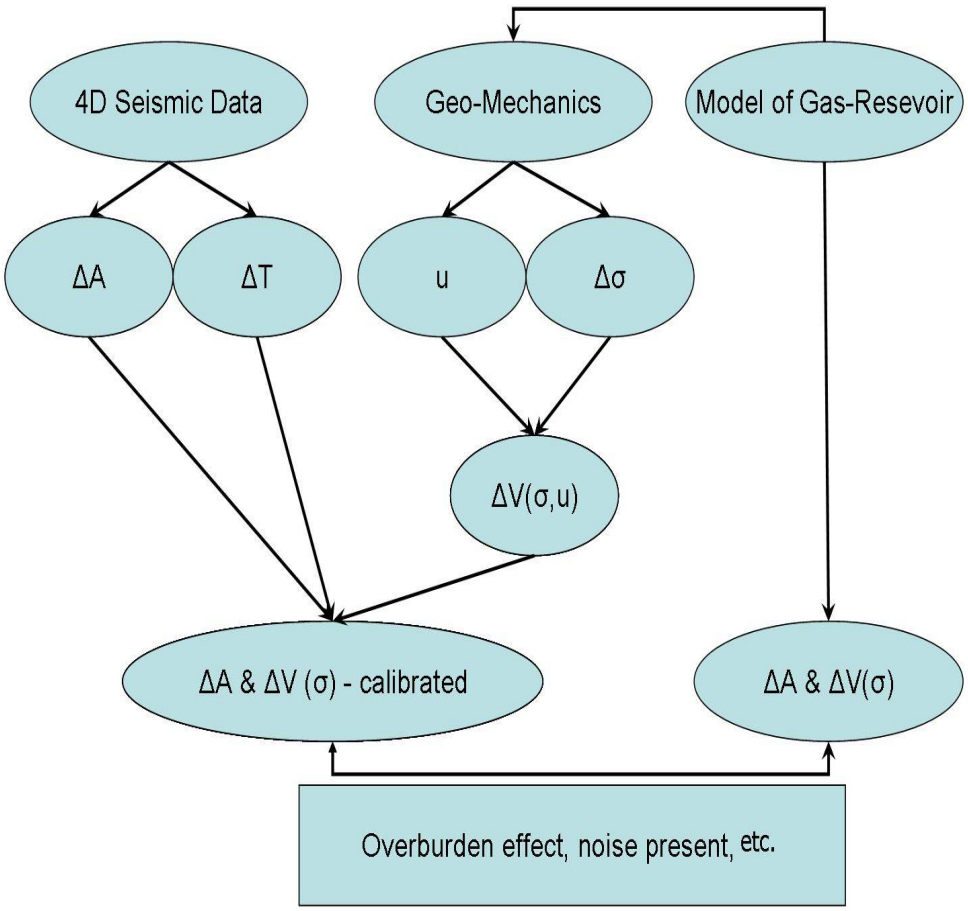

Figure 2.7: *Work flow used in the forward modelling, where ΔA and ΔT denote the changes of seismic properties (amplitude and travel time). ΔV and ΔA are, respectively, the time-lapse changes of seismic velocity and seismic amplitude. Geo-mechanical properties displacement and stress are denoted with u and σ.*

3

Simulation of production induced effects on seismic parameters. Petrophysical model of an oil reservoir

This chapter describes the effect of time-lapse changes in rock physics parameters on the seismic velocities and density. An analytical North Sea oil-reservoir model is built in order to investigate this effect. The estimated relations between the rock physics and seismic parameters are used in the 4D seismic analysis for pore pressure and water saturation quantification. In Section 3.1 a general overview of the effect of the time-lapse changes in the rock parameters on the seismic velocities and density is presented. Additionally the technical risk of the 4D project, based on the representative examples from the literature, is assessed. The general production processes and their effects on the time-lapse seismic are discussed. The reservoir model is separated in two parts: 1) Solid rock given in Section 3.2, and 2) Fluid part presented in Section 3.3. The effect of variations in the petrophysical prop-

erties on the elastic properties of the solid/fluid is presented separately for each of those parts. The combined effect of changes of the elastic properties of the solid and fluid is discussed in Section 3.4 of this chapter.

3.1 The effect of the rock parameters on the seismic properties.

Nur [1989] pointed out some of the major reservoir properties and events, influencing the recovery of the hydrocarbon reservoirs: porosity, saturation, permeability, rock compressibility, fluid viscosity, hydrocarbon chemistry, wettability, fluid compressibility, fluid chemistry, effective stress, temperature. The variations of these properties and events are caused by two major effects: hydrocarbon production and fluid/gas injection (Figure 3.1). In the scenario sketched in Figure 3.1, the production effect occurred between Time 1 and Time 2, followed by water injection, which appeared between Time 2 and Time 3.

- During the production of the reservoir, the pore pressure drops and the water saturation increases. If the original reservoir has substantial dissolved gas and it is much more compressible than the water, than during the production the gas can evolve out of solution so that the effective GOR will increase.

- In case of injection the water saturation will increase because of the injected water. This will lead to an increase in the pore pressure (decrease in the effective stress).

The effect of various oil and/or gas production operations was given by Batzle et al. [1998], Table A.1. Generally the formation properties will be sensitive to factors including fluid composition, density, effective stress and temperature. For a successful 4D project the combined total effect of the changes of all these properties and events in the reservoir has to be large enough to be differentiated seismically at a given seismic resolution (Wang [1997]).
The analysis of the technical risk of the 4D project involves four basic steps reported by Lumley et al. [1997]:

[1] Use raw information to estimate the properties of the rocks, oil, water, gas, the seismic data and the geometry of the reservoir. This esti-

mation is necessary in order to determine the probability of success for the 4D project. Considering a number of observations worldwide, Lumley et al. [1997] established the ”ideal” properties and compared them with the real data examples from the investigated reservoir. The complete 4D fact sheet from the work of Lumley et al. [1997] is given in the **Appendix A**, Table A.2.

[2] From Table A.2 the key reservoir parameters are selected. The 4D changes of these parameters are monitored using the evaluation of the 4D seismic projects. Further the time-lapse changes are assessed, as it is presented in Table A.3.

[3] After the critical reservoir and seismic variables have been scored, they can be entered into the 4D Technical Risk Spreadsheet, Table A.4, which compresses the risk assessment to five reservoir variables and four seismic variables.

[4] Using Table A.4, the risk of the 4D project at the given field was assessed. This analysis involved three major components: Reservoir conditions, time-lapse seismic condition and combined total score.

By building the forward reservoir model to simulate temporal changes in the seismic properties, it is important to consider the results from Table A.4 and to answer the question, whether the simulated changes at the reservoir level will be detectable using the time-lapse seismic tool. According to Lumley et al. [1997] a reasonable threshold for a passing score is 60%, which means that the reservoir score must exceed 15/25, Table A.4.

3.2 The solid part of the model

In this section we used a rock physics theory to build a pertrophysical model of the solid rock. The rock physics models are mostly based on two theories:

[1] Effective elastic media; In this theory the elastic properties of the rock are presented as one conglomerate from the elastic properties of the building particles (different rocks and minerals). Some of the most famous theories are:

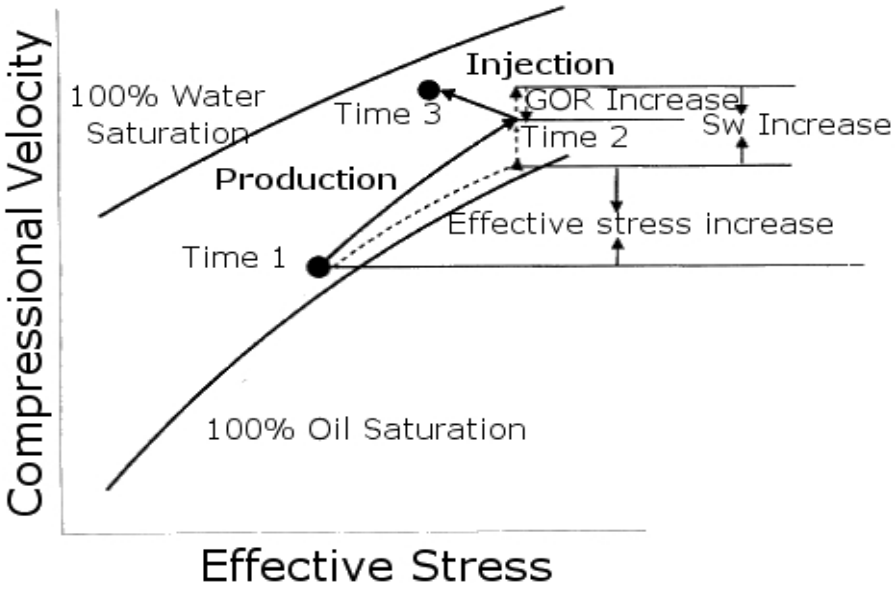

Figure 3.1: *Combined effects of oil production and water injection on the compressional velocity. As the field is produced, pore pressure drops (effective stress increases) and water saturation increases. As water is injected, pore pressure increases (effective stress decreases) and water saturation increases, Wang [1997].*

- Hashin-Shtrikman bounds; Hashin and Strickman [1963] presented a theory to predict the elastic modula of mixture of grains by knowing the constitutive modula and volumes of the different fractions. In their theory, for an isotropic, linear, elastic composite, the effective modulus of the composite will fall between determined bounds.
- Voigt, (Mavko et al. [1998]), introduced a upper bound where the effective modulus was calculated as a summation of the constitutive modula multiplied by the volume fraction. Reuss, (Mavko et al. [1998]), introduced a lower bound, where the effective modulus was calculated as the sum of the harmonics of the constitutive modula multiplied with the corresponding volume frac-

tions.

- Kuster and Toksöz [1974a] derived expressions for seismic velocities by using a long-wavelengh firs-order scattering theory. Further, Kuster and Toksöz [1974a] and later Berryman [1987] generalized their expressions for the effective bulk and shear modula for a variety of inclusion shapes.
- Xu and White [1996], show a model, mixture between clay and sand, used to predict the S-wave velocity from lithology and any pair of P-wave velocity, porosity and shale volume. The model evaluates the bulk and shear modula of the dry rock frame by a combination of the Kuster and Toksöz [1974a] theory and differential effective medium theory.

[2] Random spherical grain packing; contact model theory:

- Hertz-Mindlin model; In this model the effective bulk and shear modula are calculated using the normal compression of two identical spheres and the tangetial force which is applied afterward. This model can be used to describe the properties of the precompacted granular rocks.
- Walton [1987], assumed that the normal and shear deformation of a two-grain combination occur simultaneously. The difference from the Hertz-Mindlin model is that there is no partial slip in the contact area. The slip occurs across the whole area once applied traction exceed the friction resistance.
- The Digby model gives effective modula for a dry, random packing of identical elastic spherical particles. Neighboring particles are initially firmly bonded across small, flat, circular regions.
- Brandt [1955] model allows one to calculate the bulk modulus of randomly packed elastic spheres of identical mechanical properties having different sizes.
- Norris and Johnson [1997] and Johnson et al. [1998] developed an effective medium theory for the nonlinear elasticity of granular sphere packs.

In this research we used the suggested by Dvorkin and Nur [1996] theoretical petrophysical model, of high-porosity North Sea sandstones (Blangy et al. [1993]), representative for the Troll field to calculate the effective modula as a function of the variations in the petrophysical properties and environmental conditions. The velocities as a function of effective stress are calculated by using a modification of Hertz-Mindlin contact theory presented in Mavko et al. [1998]. The background of this theory is given in Appendix A, Section A.3. The effective elastic moduli using the Dvorkin and Nur [1996] model for the uncemented sand, for the case of critical porosity (ϕ_0), are

$$\begin{aligned} K_{HM} &= \left[\frac{C^2(1-\phi_0)^2G^2}{18\pi^2(1-\nu)^2}\sigma_{eff}\right]^{1/3}, \\ G_{HM} &= \frac{5-4\nu}{5(2-\nu)}\left[\frac{3C^2(1-\phi_0)^2G^2}{2\pi^2(1-\nu)^2}\sigma_{eff}\right]^{1/3}, \end{aligned} \tag{3.1}$$

where C is the average number of contact per grains, σ_{eff} is the effective stress, G is the grain shear modulus, and ν is the grain Poisson's ratio. To calculate the effective modulus at a different porosity, a modified Hashin-Strikman lower bound is used. Applying the Hashin-Strickman lower bound (Appendix A, Section A.3), Dvorkin and Nur [1996] calculated the uncemented sand model at different porosity levels,

$$\begin{aligned} K_{eff} &= \left[\frac{\phi/\phi_0}{K_{HM}+\frac{4}{3}G_{HM}} + \frac{1-\phi/\phi_0}{K+\frac{4}{3}G_{HM}}\right]^{-1} - \frac{4}{3}G_{HM}, \\ G_{eff} &= \left[\frac{\phi/\phi_0}{G_{HM}+\frac{G_{HM}}{6}\left(\frac{9K_{HM}+8G_{HM}}{K_{HM}+2G_{HM}}\right)} + \frac{1-\phi/\phi_0}{G+\frac{G_{HM}}{6}\left(\frac{9K_{HM}+8G_{HM}}{K_{HM}+2G_{HM}}\right)}\right]^{-1} \\ &\quad -\frac{G_{HM}}{6}\left(\frac{9K_{HM}+8G_{HM}}{K_{HM}+2G_{HM}}\right), \end{aligned} \tag{3.2}$$

where K is denoted to the grain bulk modulus. Once can easily see, that in the case of zero porosity ($\phi = 0$), the effective moduli will be equal to the moduli of the grain, and in the case case of critical porosity ($\phi = \phi_0$) the effective moduli will correspond to the K_{HM} and G_{HM}. In this thesis,

the model, based on Equation 3.2 was used : 1) the model is calibrated with the well logs and data from the real North Sea reservoir - Troll field, 2) the model is relatively simple and only the major reservoir properties, which are influencing the bulk and shear modulus of the rock, are required as input parameters, 3) a direct relation exists between the variations in the effective stress over time and the time-lapse changes in the elastic modulus, Equation 3.1. The model of the dry solid, denoted as A, and used in this chapter is the first of the three models presented in Figure 3.2 , Dvorkin and Nur [1996]. The validation of the uncemented sand model is illustrated in Figure 3.3, where the velocities measured from the log-data are plotted together with the results predicted from the reservoir modelling. The initial properties of the modeled dry rock were taken from the literature and are presented in Table 3.1. The values for density, porosity, elastic modulus and the effective stress are comparable with the average values for the North Sea reservoirs, which are given in Appendix A, Table A.2. The reservoir is shallower (around 2 km), compared to the average value given by Lumley et al. [1997] but it corresponds well to some of the observations from the Troll field, e.g. Hoversten et al. [2006] and Petterson et al. [1990]. The very low Poisson ratio (0.06) is also in agreement with the Troll field. The initial value of pore pressure is smaller compared to the average given in Appendix A, Table A.2, but the simulated pressure depletion at the reservoir level is comparable with the levels, given in the literature, see Landrø [2001].

Critical Porosity	Porosity	Contact per grain	Overburden Stress [MPa]	Pore Pressure [MPa]
0.36	0.2	9	45	20
The Poisson ratio	Density $[kg/m^3]$	Grain Bulk modulus [GPa]	Grain Shear modulus [GPa]	
0.06	2650	45	37	

Table 3.1: *Initial parameters used to model the elastic properties and density of the dry rock.*

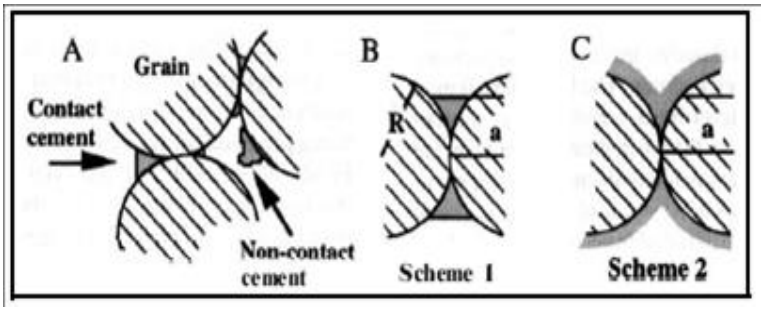

Figure 3.2: *Schematic representation of the models developed by Dvorkin and Nur [1996]. The model used in this chapter is denoted with A. A - the uncemented sand model, B and C - models using the cementation theory, Dvorkin et al. [1991] and Dvorkin et al. [1994]*

.

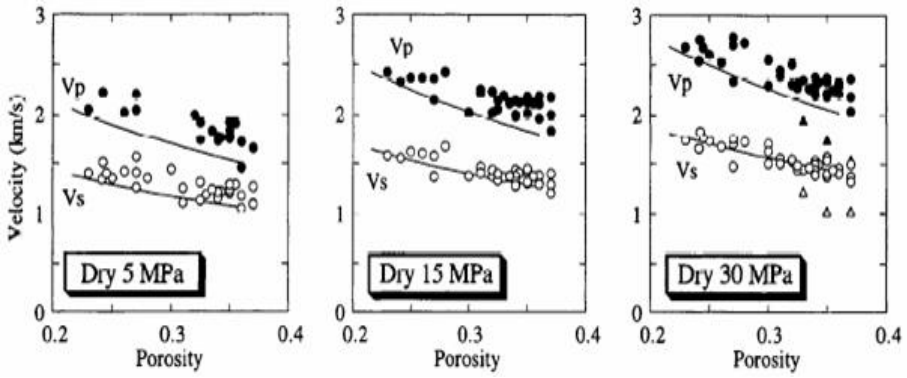

Figure 3.3: *.Dry rock velocities in the Troll samples at the effective stress of 5, 15 and 30 [MPa]. Filled symbols are for P-wave velocities, open symbols are for S-wave velocities. The solid lines are estimated with modelling. Dvorkin and Nur [1996].*

3.3 The fluid part of the model

The analytical solution published by Wang [2001] is used to simulate the effect of the 4D changes, occurring in the fluid part of the model, on the bulk modulus and the density of the two-phases fluid mixture (live oil and brine). This application is used widely in the oil industry and is based on laboratory experiments and data observations, Schoen [1996]. The density of live-oil (ρ) was calculated using the formula:

$$\begin{aligned} \rho &= \frac{\rho_G + (0.00277p - 1.71 * 10^{-7}p^3)(\rho_G - 1.15)^2 + 3.49 * 10^{-4}p}{0.972 + 3.81 * 10^{-4}(T + 17.78)^{1.175}}, \\ \rho_G &= \frac{\rho_0 + 0.0012R_G G}{B_0}, \\ B_0 &= 0.972 + 0.00038\left[2.495R_G\left(\frac{G}{\rho_0}\right)^{1/2} + T + 17.8\right]^{1.175}, \end{aligned} \tag{3.3}$$

where ρ_G is the saturation-density, p is the pore pressure, T is the temperature, ρ_0 is the reference density of the oil, R_G represents the gas-to-oil ratio and G is the gas specific gravity (relative to air). B_0 represents the volume expansion factor. The volume expansion factor is a measure of the reduction in the volume of crude oil as it is produced. B_0 is of prime importance as it relates directly to the calculation of the petroleum reserve and oil in place under stock-thank conditions. It is the ratio of reservoirs barrels of oil plus the volume of dissolved gas under reservoir pressure and temperature over stock-tank barrels of dead oil at the surface. It is possible to estimate the bulk modulus of the live-oil, using Equation 3.3 and the acoustic velocity in the oil:

$$\begin{aligned} V_{oil} &= 2096\left(\frac{\rho'}{2.6-\rho'}\right)^{1/2} - 3.7T + 4.64p \\ &\quad +0.0115\left[\left(\frac{18.33}{\rho'} - 16.97\right)^{1/2} - 1\right]Tp, \\ \rho' &= \frac{\rho_0}{(1+0.001R_G)B_0}, \\ K_{oil} &= \rho V_{oil}^2, \end{aligned} \tag{3.4}$$

where V_{oil} and K_{oil} are the acoustic velocity and bulk modulus of the live-oil respectively and ρ' is the pseudo-density. The density and the elastic modulus of the brine were calculated in order to estimate the properties of the fluid mixture. The analytical solutions suggested by Batzle and Wang [1992] used for the calculation of the properties of the brine are

$$\begin{aligned} \rho_b &= \rho_w + 0.668S + 0.44S^2 + 10^{-6}S[300p - 2400pS \\ &\quad +T(80 + 3T - 3300S - 13p + 47pS)], \\ V_b &= V_w + S(1170 - 9.6T + 0.055T^2 - 8.5 * 10^{-5}T^3 \\ &\quad +2.6p - 0.0029Tp - 0.0476p^2) + S^{1.5}(780 \\ &\quad -10p + 0.16p^2) - 1820S^2, \\ K_b &= \rho_b V_b^2, \end{aligned} \tag{3.5}$$

where the density, velocity, bulk modulus and salinity of the brine are denoted with ρ_b, V_b, K_b, and S. The density and velocity of the water (ρ_w and V_w) are found from the literature, e.g. Mavko et al. [1998], Wang [2001], Batzle and Wang [1992] and Schoen [1996]. The bulk modulus of the mixture of live-oil and brine was calculated using the Hill [1963] theory. Hill [1963] showed that when all the phases or constituents in a given composite have the same shear modulus, the effective bulk modulus can be calculated as:

$$\frac{1}{K_{eff}} = \sum_{i=1}^{n} \frac{f_i}{K_i}, \tag{3.6}$$

where K_{eff} is the effective modulus of the mixture of liquids or gases, or both, f_i and K_i are the fraction volume and the bulk modulus of the i-th constituent of the mixed fluid/gas. The density of the fluid composite was estimated

$$\rho_{fl} = (1 - S_w)\rho + S_w\rho_b, \tag{3.7}$$

where ρ_{fl} is the density of the two-liquids composite and S_w is the water saturation. The initial properties of the fluid part of the model were taken from the literature, Petterson et al. [1990], and presented in Table 3.2.

Pore Pressure [MPa]	Temperature [Celsius]	Salinity [ppm/10^6]	oil gravity [API]
20	76	0.023	38.4
Gas-to-oil ratio [l/l]	Gas gravity [API]	Water saturation %	
162	0.6	0	

Table 3.2: *Initial parameters used to model the bulk modulus and density of the composite of brine and live-oil.*

Appendix A, Table A.2 shows similar values of oil gravity and temperature, where the salinity and the pore pressure are different. The value of the pore pressure was already discussed and the value of the salinity is typical for the North Sea reservoir - Gullfaks field.

3.4 Implementing the model of the saturated rock

Next, the elastic properties of the solid-fluid mixture (saturated rock) are calculated. The value of the shear modulus can be derived from the solid

part of the model assuming it equals to G_{eff} calculated in Equation 3.2. The density is calculated assuming that the pore space is fully saturated with the fluid mixture

$$\rho_{sat} = (1 - \phi)\rho_{dry} + \phi\rho_{fl}, \tag{3.8}$$

where the density of the saturated rock is presented by ρ_{sat}, the solid and fluid densities are respectively ρ_{dry} and ρ_{fl}, and ϕ indicates the porosity in the reservoir rock. The low-frequency theory, suggested by Gassmann [1951] is applied to predict the resulting increase in effective bulk modulus on the saturated rock

$$\frac{K_{sat}}{K_0 - K_{sat}} = \frac{K_{dry}}{K_0 - K_{dry}} + \frac{K_{fl}}{\phi(K_0 - K_{fl})}, \tag{3.9}$$

where the K_{sat}, K_0, K_{dry} and K_{fl} are the bulk modulus of the saturated rock, rock-building mineral, dry rock and fluid. The Gassmann [1951] theory is valid only at sufficiently low frequency ($<$100Hz for seismic data), so that the pore pressure induced from the passing seismic wave is equilibrated through the pore space. The basic assumptions in the Gassmann [1951] theory are given in Section A.4.

Now that the model is developed, the next step is to answer the question what kind of 4D changes in the seismic attributes are expected and whether these changes could be detected in the seismic data. Similar to the Table A.3 and the Table A.4 a technical risk spread-sheet is required. An important question here is what kind of production will be simulated and which of the reservoir properties are time-variant? The parameters given in Table 3.1 and Table 3.2 are typical for North Sea reservoirs (Table A.2). A quick look at Table A.4 shows that the total score of the North Sea reservoirs is 23/45 (reservoir and seismic conditions). According to Lumley et al. [1997] the score of the reservoir conditions must be at least 60% from the ideal case (15/25) in order to obtain detectable 4D changes in the seismic data. The North Sea reservoir conditions meet the reservoir threshold (60%). Therefore it is expected that by using the initial values given in Table 3.1 and Table 3.2, it is possible to simulate the time-lapse changes, which are visible and detectable in the 4D seismic data. Using the developed reservoir model, it

is possible to simulate temporal changes in four factors influencing directly the seismic properties (effective stress, fluid properties, porosity and temperature), and to monitor the effect of these changes on the seismic velocities and density. Variations over time in the selected rock physics factors will also influence the other parameters given in Table 3.3. The effect of 4D changes in the rock properties on the seismic velocities and density is discussed in **Appendix A** (Section A.5). In general the empirical relation between seismic velocity and petro-physical properties is given by Koesoemadinata and McMechan [2001] as

$$V = a_1 + a_2\phi + a_3 C + a_4 \ln(\sigma_{eff}) + a_5 S_w + a_6 f, \qquad (3.10)$$

where V is the velocity of the saturated rock, a_2 to a_6 are the fitting coefficients for porosity(ϕ), clay content(C), the natural logarithm of effective stress(σ_{eff}), the water saturation(S_w), and frequency f - included because of the velocity dispersion as it was shown by Winkler [1985], Winkler [1986], Jones [1986], and Sams et al. [1997]). According to equation 3.10, when the changes in the petrophysical properties and environmental conditions are small (porosity, effective stress, clay content, and water saturation) they can be treated as independent variables. The used relations between the seismic velocities and petro-physical properties in equation 3.10 are linear except for the effective stress, where a logarithmic dependence is used. Koesoemadinata and McMechan [2001] showed that the relation between the compressional velocity and partial water saturation depends also on the frequency used in the laboratory measurements. From the laboratory experiments presented by equation 3.10, it follows that three of the rock parameters (effective stress, saturation, and porosity) can be considered as independent variables. This means that it is possible to investigate the effect of a single factor on the seismic velocity and/or density. Following this fact, it is also possible to quantify the changes in the effective stress, pore pressure and porosity from the time-lapse variations in the seismic data. The effect of the variations in the rock physics properties, by isotherm conditions using equations 3.2-3.9, on the seismic velocities, seismic impedances, and density is plotted in Figure 3.4. The compressional velocity is sensitive to all of the three factors, Figure 3.4 - A. The shear velocity is less influenced by the fluid substitution, Figure 3.4 - B, the variations here are a consequence of the 4D changes

in density of the saturated rock. The density is not sensitive to the small changes of pore pressure, where the porosity is not affected, Figure 3.4 - E. Seismic impedances are calculated from the velocity and density. The 4D changes in the impedances are following the time-lapse changes in the seismic velocity and density. Is it possible, using the presented analytical models of saturated rock, to quantify the changes of pore pressure, water saturation and porosity from the time-lapse changes in the seismic data? Generally the 4D marine seismic data could give information about the changes in the travel-time and in the seismic amplitude. Using the AVO (amplitude versus offset) technique it is theoretically possible to invert the variations in the seismic impedances and density from 4D amplitude information, Aki and Richards [2002], Yilmaz [2001a], and Yilmaz [2001b]. However, in practice it is difficult to obtain the value of density from the seismic amplitude. The reason for this is that the density, in the linear approximations of the Zoeppritz equation, is tied to the square of tangents of the incident angle. To distinguish the tangent from the sine, a large angle of incidence is required in order to estimate the correct value of the density. Such angles are hard to obtain for the typical depth of hydrocarbon reservoirs. From a mathematical point of view, it is possible to invert the chosen rock physics properties. The changes in the petro-physical properties will affect three independent seismic properties - travel-time, P-impedance, and S-impedance (note that the measured travel-time 4D changes have a low-frequency spectrum, where the inverted time-lapse changes in the impedances are full-bandwidth). Therefore, it will be possible to build three equations with three unknowns (pore pressure, water saturation and porosity). However, the changes in the porosity are strongly depending on the textures of the dry rock, Han et al. [1986], and it is not possible to generalize if such changes will occur and how large they will be. In this first forward modelling exercise the porosity changes will be neglected and only time-lapse changes in case of fluid substitution and pore pressure will be applied, Figure 3.5. Figure 3.6 depicts the relative changes in the seismic impedances. A good rule of thumb for seismic detection is that impedances changes between surveys should be larger than 4% (note that the effect of the noise is not included in the calculations; 20 dB signal-to-noise ratio means that the signal is 10 times stronger than the noise, i.e. 10 % of the signal is noise). From Figure 3.6 it can be concluded that the 4D changes in the P- and S-Impedance are in the same range.

The simulated variations of the rock physics properties must have their practical equivalent. Some of the general recovery processes and their effects are presented in Table A.1 and Figure 3.1:

- The depletion of the reservoir can be with weak and with strong aquifer, Batzle et al. [1998] and Dutta [1998]. In the first case the seismic impedances will increase as a result of the increase of the effective stress and the slight increase of the water saturation; in the second case the P-impedance will increase (due to water saturation), where the S-impedance will be less affected by the production process.

- In case of water injection the water flood will increase the impedances and density, but in the vicinity of the injectors the pore pressure increase will decrease the seismic properties (impedances and density).

Using the model presented in Section 3.4, the effect of water injection in the vicinity of the injector and depletion with weak aquifer support were simulated. The limitations of the rock model are discussed in Section A.6.

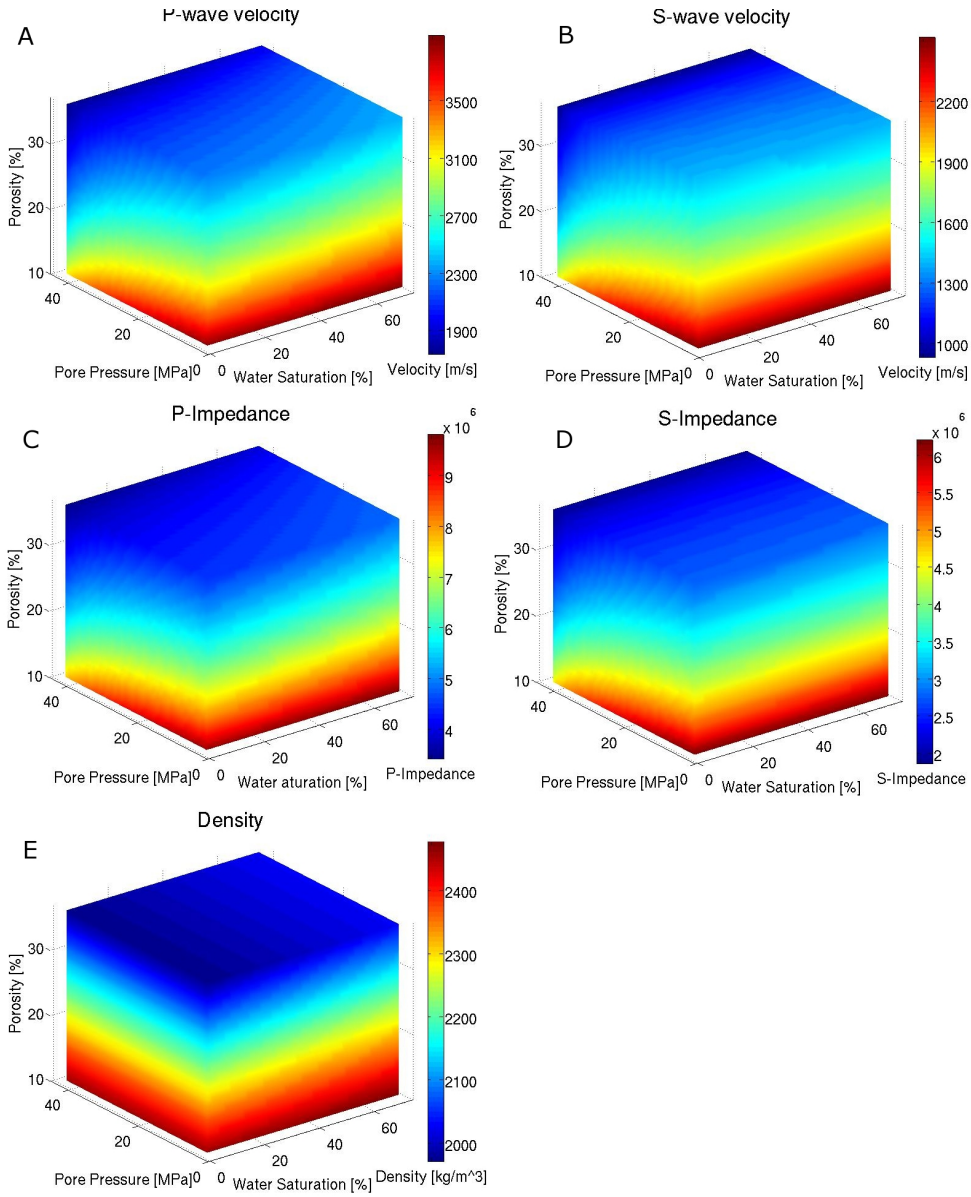

Figure 3.4: *Seismic velocities, impedances and density as a function of pore pressure, water saturation and porosity. The unit of the impedances is [m/s*kg/m^3]. The initial properties of the model are given in Table 3.1 and 3.2, (20 [MPa] pore pressure and 20 [%] water saturation).*

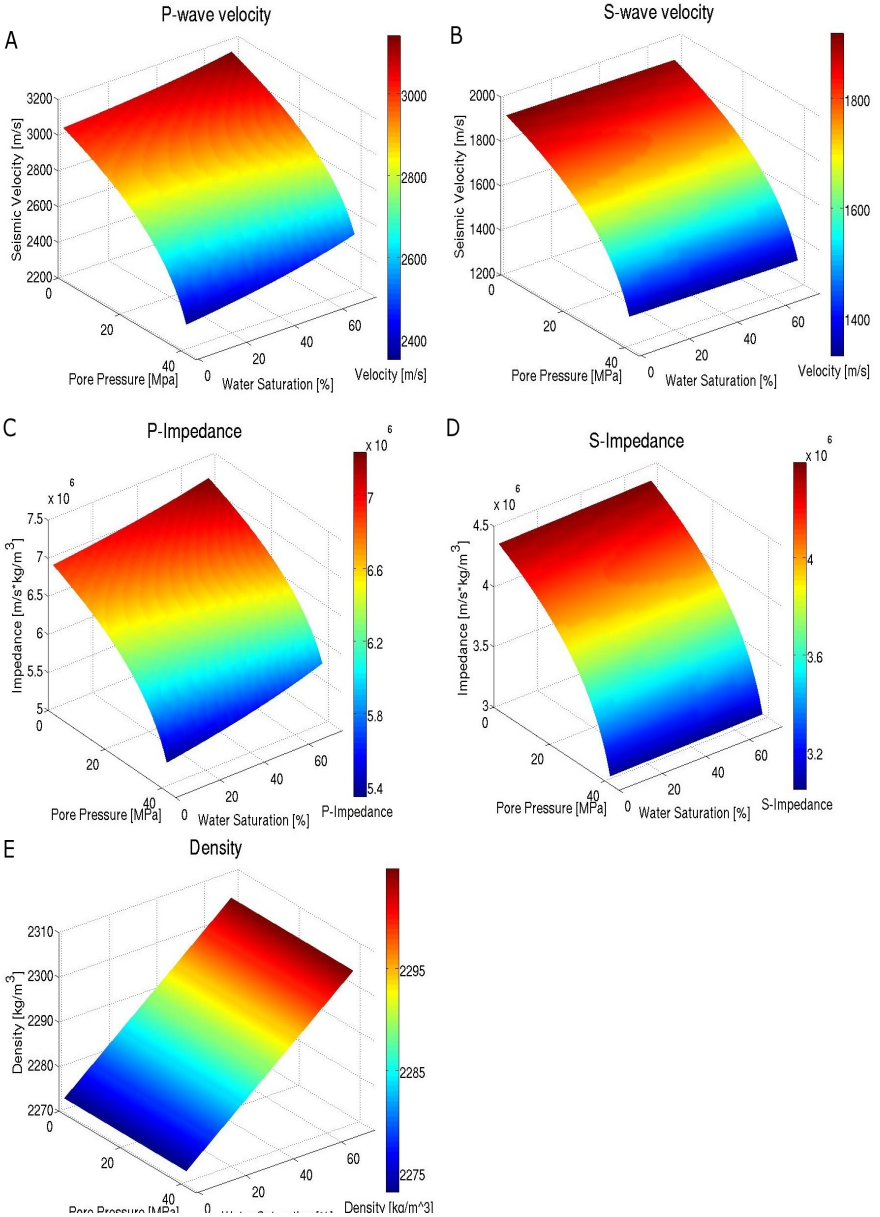

Figure 3.5: *Seismic velocities, impedances and density as a function of pore pressure and water saturation. The unit of the impedances is [m/s*kg/m^3]. The initial properties of the model are given in Table 3.1 and 3.2, (20 [MPa] pore pressure and 20 [%] water saturation).*

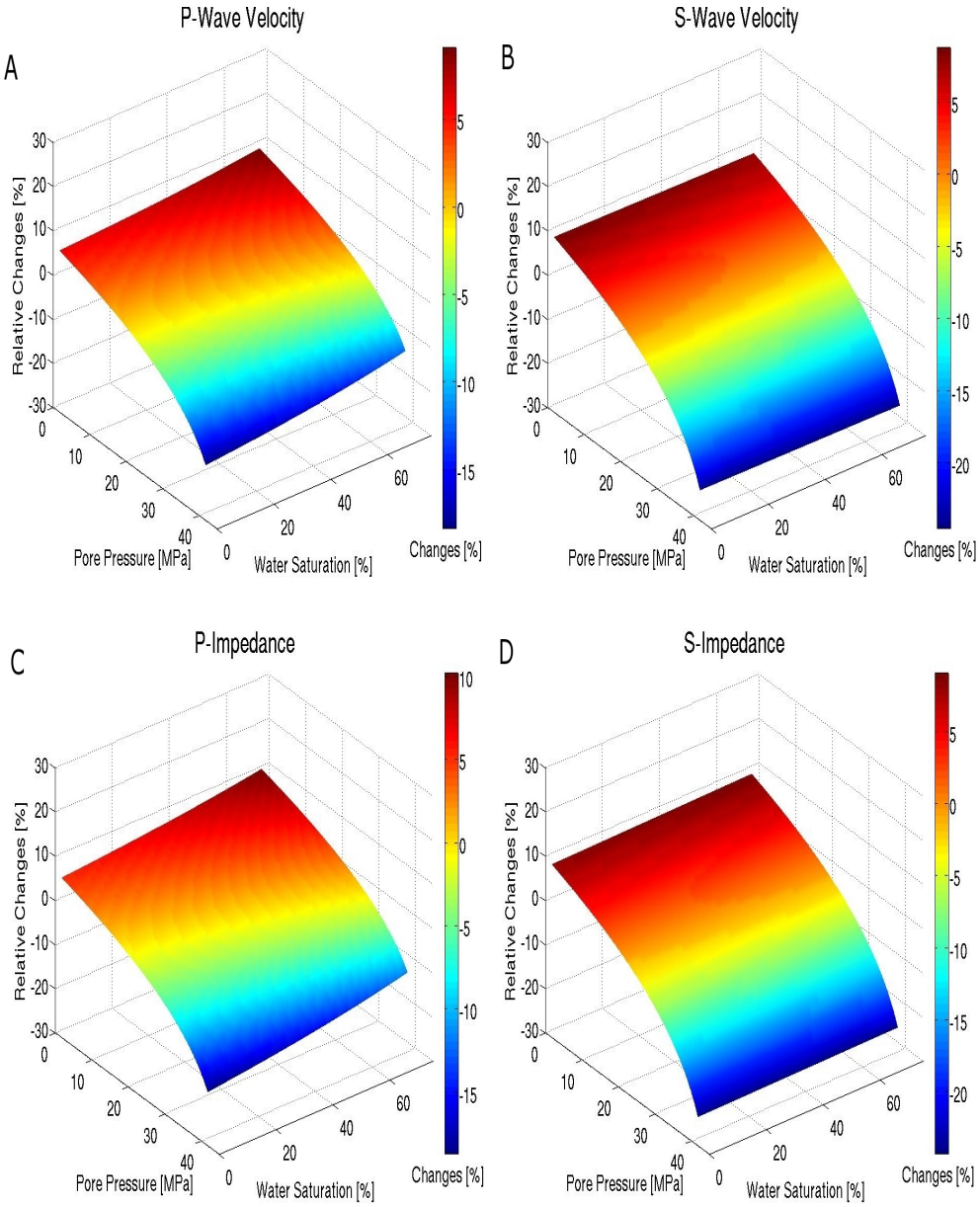

Figure 3.6: *Relative changes in the seismic velocities and impedances, induced by the 4D changes in the petrophysical properties and environmental conditions. The initial values of the rock physics properties are given in Table 3.1 and Table 3.2, (20 [MPa] pore pressure and 20 [%] water saturation).*

4

Geo-mechanical modelling; Fundamentals and theoretical background

Geo-mechanics has evolved as an interdisciplinary subject combining mainly geology and mechanics. Geo-mechanical modelling is simulating physical processes such as stress/strain behavior, heat transfer and dynamic loading in complex situations (Mulders [2003]). This technique is applied to estimate the effects of production activities on stress/strain behavior of rocks and environmental issues. For example, the deformation of mineral grains in rocks and the variations in the rock porosity are used as indicators in petroleum and gas exploration. In this thesis geo-mechanical modelling is used to simulate the pressure depletion at the reservoir level. Resulting stress and strain changes are further applied to predict the changes in the seismic velocity and density, in the reservoir as well as in the overburden, as a result of production. Section 4.1 outlines different approaches for the calculation of the geo-mechanical problem (analytical and numerical), published in the literature. Section 4.2 presents stress regimes in the subsurface and the gen-

eral concepts of stress and strain development for hydrocarbon reservoirs as result of production.

4.1 Geo-Mechanical Modelling - theoretical background

Some of the analytical solutions and case studies of the geo-mechanical behavior are presented in the historical order:

- Eshelby [1957] studied the behavior of an ellipsoidal inclusion under strain embedded in a homogeneous surrounding. In this study, Eshelby [1957] also determined the elastic state of an inclusion, showing a change in form and size.

- Geertsma [1973] and later Geertsma and van Opstal [1973] presented an analytical solution for the calculation of the displacement field and stress changes for the idealized reservoir in the form of a horizontal, circular cylinder of limited thickness.

- The extraction of pore fluids from within the crust influences the changes in the stress field and can trigger earthquakes (Yerkes and Castle [1976], Segall [1983], Pennington et al. [1986], Segall [1989], Grasso and Wittlinger [1990]). The pore pressure declines at the reservoir level causing a slight contraction of the reservoir. Because the reservoir is elastically coupled to the surrounding rocks, these contractions affect the neighboring crust and cause subsidence and horizontal contraction above the reservoir, and in some cases might trigger seismicity, Segall and Fitzgerald [1998].

- Figure 4.1 illustrates the faulting associated with fluid withdrawal. As reported by Segall [1989], in extensional environments normal faults bounding the reservoir may be developed perpendicular to the smallest horizontal principal stress. In compressional environments reverse faulting may be developed above and below the reservoir.

- Teufel et al. [1991] reported an investigation on the effect of reservoir depletion and pore pressure drawdown on the in situ stress and deformation for the “Ekofisk” Field. It was assumed that the change of

effective stress is caused by the pore pressure drawdown in the field. It was also suggested that in situ stresses are a function of the overburden load only. Evaluation of the effective stress measurements in the reservoir displayed a linear increase with production. To understand the stress path followed by the reservoir rock, additional uniaxial compression tests were carried out on reservoir rock specimens. To meet the uniaxial strain assumption, the tests were performed excluding lateral strain.

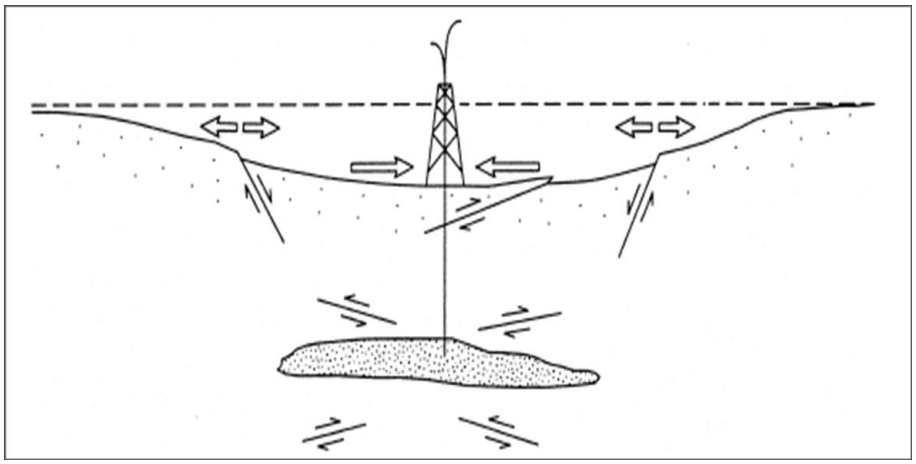

Figure 4.1: *The observed faulting associated with fluid withdrawal. Open arrows indicate horizontal strain. Normal faults develop on the field when the depleted reservoir is located in an extensional environment, whereas reverse faults develop above and below the reservoir in compressional environments, Segall [1989]*

- Using the formulation given by Geertsma [1973] and considering preliminary information for the reservoir geometry, pore pressure depletion and material properties of the rock, Segall et al. [1994] computed the subsidence and changes in the stress field. Further Segall and Fitzgerald [1998] theoretically derived the elastic response and direction of traction resulting from contraction of an ellipsoidal inhomogeneity, a reservoir, respectively, in a homogeneous isotropic and

elastic full space. Contraction of the inhomogeneity is leading to a stress field as given in Figure 4.2. The arrows indicate lateral compression above and below the reservoir and lateral extension inside and next to it. The non-constraint surface shows subsidence. Segall [1989] also calculated analytically the stress distribution in the surrounding of such a reservoir with depletion. His assumptions included a flat permeable layer of small thickness compared to the depth, the plane strain condition, impermeable properties for the surrounding (matrix) and a uniform reduction of fluid mass per unit volume in the reservoir. Regional stresses were not considered in this approach, Figure 4.3. The results presented in Figure 4.3 coincide with the observations presented in Figure 4.1.

- Rudnicki [1999] reported a model based on Eshelby [1957] to study the effect of inhomogeneity using different elastic properties for the reservoir than those of the surrounding media. Variations of several parameters, including the reservoir thickness and the Poisson's ratio of the inhomogeneity, were used. It was found that resulting stress paths are steeper for flatter reservoirs, smaller Poisson's ratios, smaller ratios of reservoir shear modulus to matrix shear modulus, and a larger Biot's constant. Rudnicki [1999] assessed the state of stress with respect to a yield or failure surface given by the Mohr-Coulomb failure criterion. The state of stability depends on the steepness of the stress path. Steep stress paths favor stability with injection and smaller stress path slopes favor stability for withdrawal. It was noted that the consideration of failure could be complicated by the presence of faults within or at the boundary of the reservoir.

- Wu et al. [1998] presented an investigation on the stress estimation in faulted regions considering a Mohr-Coulomb failure criterion on the faults. They analytically presented the effect of the fault friction angle on the ratio of the minimum to maximum principal stress as a function of the fault angle.

- Lehner [2002] calculated the changes in the stress field for a simple 2D model in plane strain condition. He used the problem from the thermoelasticity theory solved by Nowacki [1986], where the ther-

moelastic solutions are rewritten in terms of an analogous poroelastic problem.

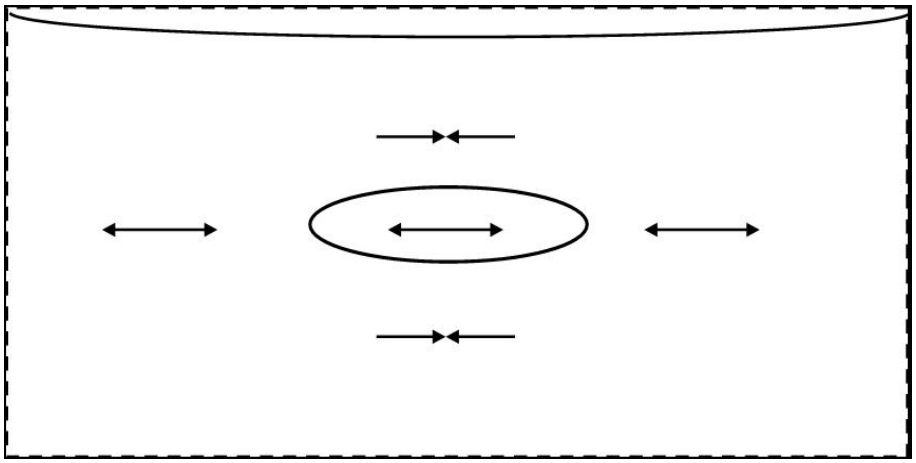

Figure 4.2: *Stress field inside and in the surrounding of an inhomogeneity undergoing contraction, Segall and Fitzgerald [1998]*

The presented analytical or "closed form" solutions are only available for simple situations. Therefore the numerical methods, e.g. Morita et al. [1989], Fokker and Orlic [2006] and Yin et al. [2007], are more popular for solving the geo-mechanical problems. With regard to the problems of geo-mechanics, the most widely used numerical models are: 1) the finite element method (FEM), 2) the discrete element method and 3) the boundary element method, Pande and Pietruszczak [1992]. The first model i.e. the FEM is used in this thesis. The FEM is implemented into finite element software DIANA developed by TNO. The way the stress regimes and the displacement are calculated, using DIANA (initial modelling), is given by Mulders [2003].

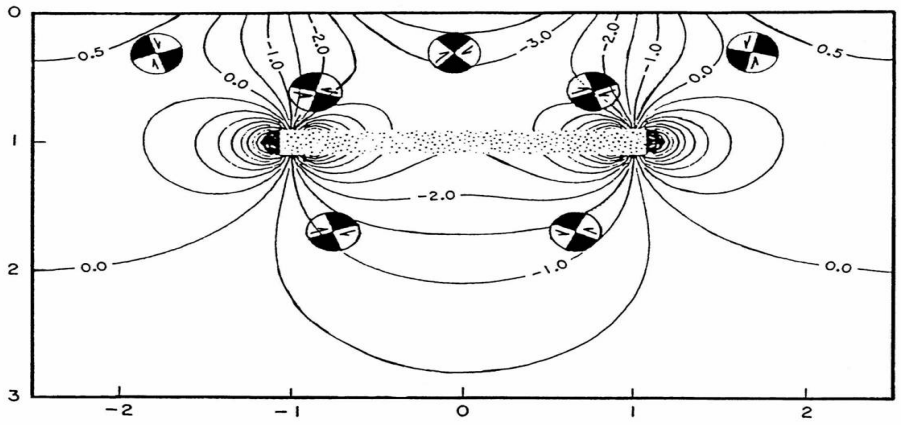

Figure 4.3: *Calculated change in horizontal, normal stress due to fluid extraction, Segall [1989]*

4.2 Stress regimes in the subsurface; General concepts of stress and strain development for hydrocarbon reservoirs

In this chapter the general concepts of stress and strain development in the hydrocarbon reservoirs are discussed. This will help to understand the results of the geo-mechanical modelling and further to ensure the correct interpretation of seismic time-lapse effects. Most of the analytical solutions, presented in this Section 4.3, are taken from "Petroleum Related Rock Mechanics" course, given by Holt in Delft, 2005.
In general the stresses in rock can be divided into initial and induced stresses. According to Amadei and Stephansson [1997] the classification of stresses in the subsurface are as plotted in Figure 4.4. The stress field in the subsurface is described by three components: 1) the vertical total stress (σ_V), 2) the maximum horizontal total stress (σ_H) and 3) the minimum horizontal total stress (σ_h). For rocks at depth, it is often assumed that gravity has a main control on the stress state, and hence the vertical stress is the principal stress.

The vertical stress is given by the weight of the overburden, i.e.,

$$\sigma_v = \int_0^z \rho(z) g_i dz, \tag{4.1}$$

where with g_i is denoted to gravity acceleration, z is the depth and $\rho(z)$ is the density as a function of depth. The horizontal stresses are to some extent also caused by gravity. In the ocean, the horizontal "stress" is equal to the vertical "stress"; simply because the ocean consists of a fluid which transmits only pressure and no shear stress. In a formation with certain rigidity (shear modulus), the gravity induced horizontal stress will be different from the vertical. We consider a very simplistic (and unrealistic!) model of a sediment, as confined from lateral (horizontal) displacement, so that $\sigma'_H = \sigma'_{11}$, and $\sigma'_h = \sigma'_{22}$, and $\sigma'_H = \sigma'_h$, and $e_h = e_{11} = e_{22} = 0$ and $\sigma'_v = \sigma'_{33}$, where the $'$ sign is in meaning of effective stress, equation 2.18 . In such a case the horizontal stress can be presented as

$$\sigma'_H \;=\; \sigma'_h = \frac{\nu}{1-\nu}\sigma'_v. \tag{4.2}$$

The weakness in the argument above is that the present stress has to be found by keeping zero lateral strain throughout geological history, through which Poissons ratio has not been constant. Thus; an equation like 4.2 has to be integrated over geological time in order to make sense. Another approach is to assume that the sedimentary rock is in a continuous failure process. If this process is in accord with Mohr-Coulombs failure criterion, then (neglecting cohesion) for a normal stress regime with the vertical stress as the largest the following applies:

$$\sigma'_h \;=\; \frac{1}{\tan^2\beta}\sigma'_v, \tag{4.3}$$

where β is the failure angle. Both models give however proportionality between horizontal and vertical effective stress, and can be summarized as

$$\sigma'_h \;=\; K_0\sigma'_v. \tag{4.4}$$

Production in the hydrocarbon reservoirs causes a reduction of the initial pore pressure and an increase of effective stress. This leads to changes in the effective stress at the reservoir level, as well as in the surrounding rocks. Depending on the reservoir geometry, the rock properties of reservoir and surrounding rock, the initial stress field, and the pore pressure development, stress concentrations and zones with relatively small stresses can develop simultaneously during hydrocarbon production in different parts of the reservoir, Mulders [2003]. The effective stress change $\Delta\sigma'$ is related to the changes in the total stress $\Delta\sigma$ and pore pressure Δp

$$\Delta\sigma' = \Delta\sigma - \alpha\Delta p, \tag{4.5}$$

where α represents the Biot's coefficient giving the relation between the volume and the pore-volume change. Similar to Mulders [2003] the change in stress/pressure is defined as the difference between the effective stress before and after the production

$$\Delta\sigma' = \Delta\sigma'_{after} - \Delta\sigma'_{before}. \tag{4.6}$$

The arching (γ), as presented by many authors e.g. Kenter et al. [1996], Settari [2002], Molenaar et al. [2004] and Vidal-Gilbert and Tisseau [2006], gives the relation between the changes in the total stress and pore pressure variations

$$\gamma = \frac{\Delta\sigma}{\Delta p}. \tag{4.7}$$

Using equations 4.5 and 4.7 the stress path in the reservoir (i.e. Schutjens et al. [2004]) can be written as

$$\begin{aligned} \gamma_v &= \frac{\Delta\sigma_v}{\Delta p}, \\ \gamma_h &= \frac{\Delta\sigma_h}{\Delta p}. \end{aligned} \tag{4.8}$$

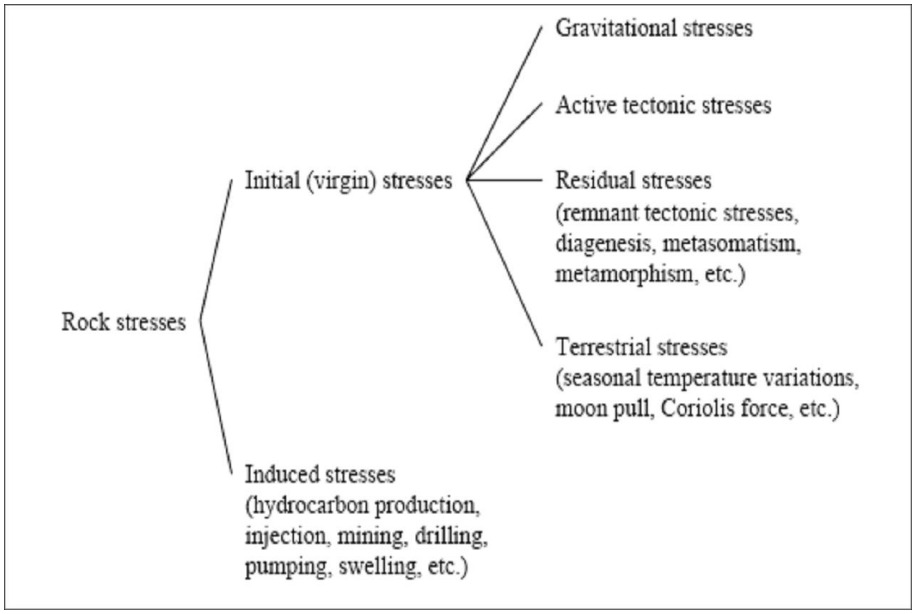

Figure 4.4: *Possible classification of rock stresses relation, Amadei and Stephansson [1997].*

Usually if the aspect ratio of the reservoir is < 1 than, $\gamma_h > \gamma_v$ at the reservoir level, thus $\Delta\sigma'_v > \Delta\sigma'_h$ (γ is always negative). In general the increase of the effective stress at the reservoir level causes reservoir compaction, Figure 4.5. The amount of subsidence depends on the compaction, and on the shielding, provided by the overburden. This is again related to the geometry and the depth vs. extent of the reservoir, and to the properties of the overburden rocks. Translating the poroelastic Hookes law to the field applications gives:

$$
\begin{aligned}
e_h &= \frac{1}{E_{fr}}\Delta\sigma'_h - \frac{\nu_{fr}}{E_{fr}}\Delta\sigma'_H - \frac{\nu_{fr}}{E_{fr}}\Delta\sigma'_v, \\
e_H &= -\frac{\nu_{fr}}{E_{fr}}\Delta\sigma'_h + \frac{1}{E_{fr}}\Delta\sigma'_H - \frac{\nu_{fr}}{E_{fr}}\Delta\sigma'_v, \\
e_v &= -\frac{\nu_{fr}}{E_{fr}}\Delta\sigma'_h - \frac{\nu_{fr}}{E_{fr}}\Delta\sigma'_H + \frac{1}{E_{fr}}\Delta\sigma'_v,
\end{aligned} \tag{4.9}
$$

where E_{fr} and ν_{fr} are the elastic parameters of the drained rock. Using equation 4.9 if $\Delta\sigma'_h = \Delta\sigma'_H$ (isotropic horizontal stress field) it is possible to present the vertical strain as a function of vertical and horizontal stresses

$$
e_v = \frac{1}{E_{fr}}\Delta\sigma'_v - \frac{2\nu_{fr}}{E_{fr}}\Delta\sigma'_h. \tag{4.10}
$$

The compaction can be calculated directly by assuming uniaxial compaction (the lateral strain is zero)

$$
\frac{\Delta Z}{Z} = \frac{\alpha(1-2\nu_{fr})(1+\nu_{fr})}{E_{fr}(1-\nu_{fr})}(-\Delta p), \tag{4.11}
$$

where,

$$
\Delta\sigma'_v = -\alpha\Delta p. \tag{4.12}
$$

Equation, 4.11 gives a direct relation between the changes in the pore pressure and the changes in the reservoir thickness. In this case the effective vertical stress changes only as a result of pore pressure change; i.e. the weight of the overburden is thought to be completely transferred to the reservoir at all times during production. However this simple assumption may give erroneous predictions of the reservoir compaction. For the more general case, equation 4.8, where the stress arching is included the compaction can be calculated

$$
\frac{\Delta Z}{Z} = \alpha\frac{(1-\gamma_v/\alpha) - 2\nu_{fr}(1-\gamma_h/\alpha)}{E_{fr}}(-\Delta p). \tag{4.13}
$$

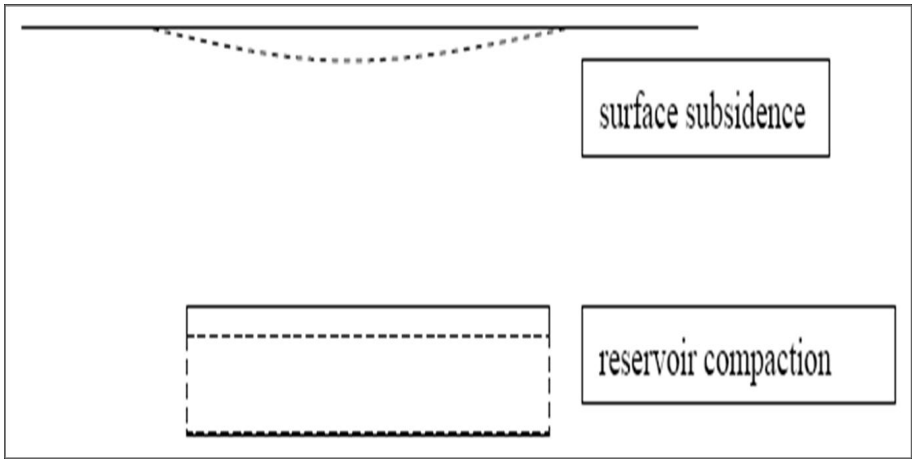

Figure 4.5: *Compaction of the reservoir and surface subsidence, caused by the depletion at the reservoir level.*

In order to find out the link between the changes in pore pressure and displacement, the next step is to calculate the stress arching coefficients. The arching effect depends on the geometry of the reservoir and on the mechanical properties of the surrounding and the reservoir rocks. Rudnicki [1999] calculated analytically the arching coefficient, where the ellipsoidal inclusion of Eshelby [1957] was used as reservoir. By changing the pore pressure within the ellipsoidal inclusion, the stress path coefficients may be computed. The resulting coefficients depend on the aspect ratio (e), and on the contrast in elastic parameters between the reservoir and its surroundings. Assuming no contrast in shear modulus between the reservoir and the surrounding rock, and a fixed Poissons ratio in the surroundings, the coefficients can be calculated for flat reservoirs using the following expressions:

$$\begin{aligned} \gamma_h &\simeq \alpha \frac{1-2\nu}{1-\nu}\left[1-\frac{\pi}{4}e\right], \\ \gamma_v &\simeq \alpha \frac{1-2\nu}{1-\nu}\left[\frac{\pi}{2}e\right]. \end{aligned} \tag{4.14}$$

By reducing the stiffness of the reservoir, arching is promoted, leading to

an increase both in γ_v and in γ_h. On the contrary, a stiff reservoir in soft surroundings will have lower stress path coefficients. The compaction of the reservoir will induce subsidence at the surface. Having the value of the compaction and subsidence it is possible to calculate the extension of the overburden as effect of production. Geertsma [1973] considered a nucleus of strain in the form of a sphere inside the reservoir (Figure 4.6). The volumetric strain of the depleting sphere is given by

$$\frac{\Delta V}{V} = \frac{\alpha}{H_{fr}} |\Delta p_f|, \tag{4.15}$$

where V denotes the volume of the sphere and H_{fr} is the compaction modulus. In case of uniaxial compaction see equation 4.11.

$$H_{fr} = \frac{E_{fr}(1-\nu_{fr})}{(1+\nu_{fr})(1-2\nu_{fr})}, \tag{4.16}$$

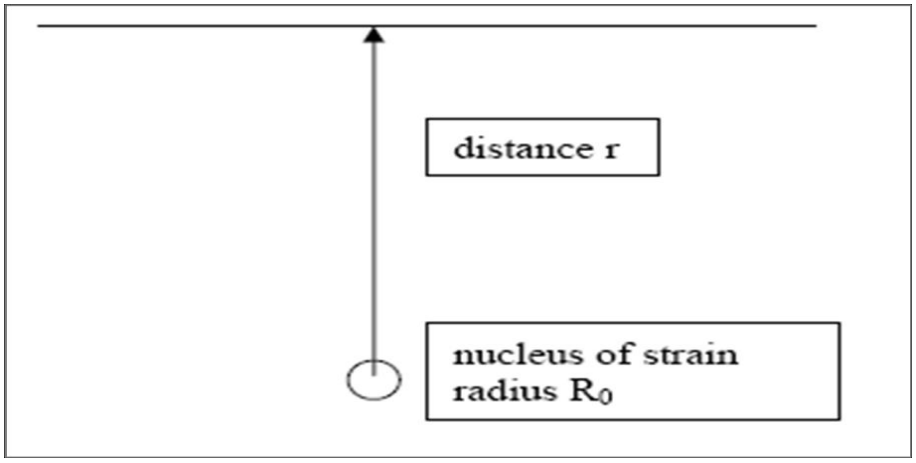

Figure 4.6: *Geometry for the determination of the displacement field around a nucleus of strain.*

The resulting (radial) displacement of the sphere will be

$$u = \frac{\alpha}{H_{fr}} \frac{V}{4\pi} |\Delta p_f| \frac{1}{r^2}, \tag{4.17}$$

where r is the radius of the sphere. Furthermore, as it was presented by Geertsma [1973] the displacement between the nucleus and the point at the surface is

$$u_r = \frac{(\alpha)(1-\nu_{fr})}{H_{fr}} \frac{V}{\pi} |\Delta p_f| \frac{1}{r^2}. \tag{4.18}$$

The displacement field is found by adding the contribution of all the nuclei, and for the situation of disk-shaped reservoir, described in Figure 4.7, at the top of the reservoir is

$$u_z(z=D) = \frac{\alpha |\Delta p_f|}{H_{fr}} h, \tag{4.19}$$

at the surface the calculated subsidence is

$$u_z(z=0) = \frac{\alpha(1-\nu_{fr})|\Delta p_f|}{H_{fr}} h(1 - \frac{D}{\sqrt{D^2+R^2}}), \tag{4.20}$$

where h, R and D are the thickness, radius and depth of the reservoir.
As demonstrated the changes in pore pressure will affect the stress field and displacement. Part of the stress change is related to stress arching, which implies that the stress state within the surrounding rock also changes. At the edge of the reservoir the vertical stress increases. The effect of arching is to shield the reservoir rock from the overburden stress. As long as arching develops, this will reduce compaction and subsidence. The highest value of compaction/subsidence is expected to occur at the center of the reservoir, where the highest stress changes in the overburden are expected at the edges of the reservoir.
Using the numerical geo-mechanical code it is possible to forward model the changes in stress and displacement as an effect of pore pressure changes.

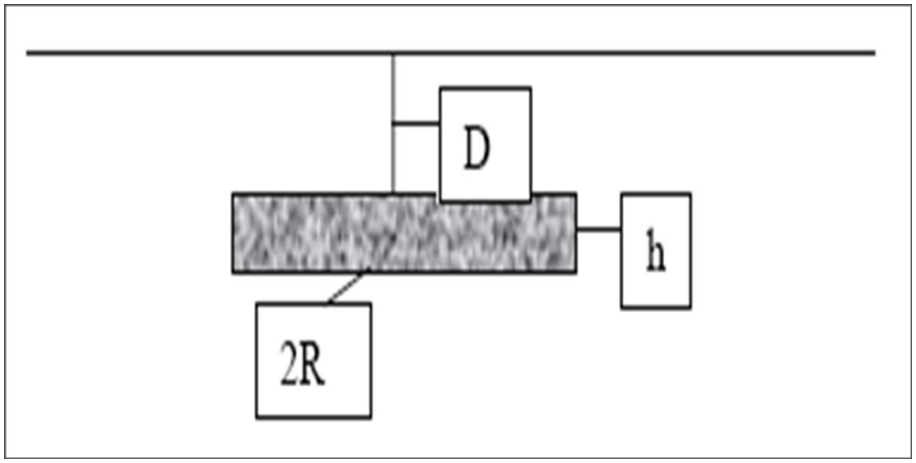

Figure 4.7: *Geometry of the disk-shaped reservoir.*

Also, knowing the changes of the effective stress and strain it is possible to calculate the changes in the elastic properties of the rock, and to predict the changes in the seismic attributes (travel time and amplitude). The application of the geo-mechanical modelling is further discussed in **Chapter 5**.

5

Investigating the effect of pore pressure changes through Geo-mechanical modelling

This chapter presents the geo-mechanical models used to simulate the pressure depletion in two different types of reservoirs. A 2D box-model of a live-oil reservoir, previously discussed in **Chapter 3**, is presented in Section 5.1. The rock physics model is applied to set up the elastic properties of the rocks inside the reservoir, where literature sources are used to determine the petro-physical properties of the surrounding media rocks. Section 5.2 presents two geo-mechanical models loosely based on a North Sea gas reservoir: 1) a model with simplified geometry, using the layer thickness as observed in a well and 2) a 2D model, using the geometry of the reservoir obtained from the interpreted horizons. Well-log information is used to set up the elastic properties of the models in Section 5.2. Further, stress/strain-velocity relations were used, for the live-oil and gas reservoir models so as to map the changes in the seismic velocities in the overburden as well as at the reservoir level due to the effect of production.

5.1 Integrating the Geo-mechnical Model with the Seismic Data using the North Sea live-oil reservoir

A 2D box-model of a North Sea oil reservoir with a simplified geometry is developed, Figure 5.1. This model is used to investigate the changes in stress field and displacement in the overburden and at the reservoir level as result of hydrocarbon production. The results of the geo-mechanical modelling were used further to predict the changes in the seismic properties over time as effect of production, using the rock physics theory (**Chapter 3**). The petrophysical model, developed in Section 3.1 was used to obtain the elastic properties of the reservoir rock for the initial time-step (before production). The overburden rocks are shales. The elastic properties of these shales are taken from the literature, i.e. Wang [2002a] and Petterson et al. [1990]. The rocks in the overburden and inside the reservoir are homogeneous and isotropic. Part of the finite element mesh used for the box-model is plotted in Figure 5.2. Six different parameterizations of the model were compiled with different values of the Young's modulus, Poisson's ratio and density in the reservoir. For each of the parameterizations, three different scenarios of depletion in the reservoir are simulated, considering a pore pressure decrease of 5, 10 and 15 MPa with respect to the initial effective stress of 25 MPa. The changes in the pore pressure are assumed constant through the entire reservoir. The elastic properties of the rocks of the six different parameterizations used in the geo-mechanical forward modelling are presented in Table 5.1. The initial value of the vertical stress is plotted in Figure 5.3. The stress is calculated in two steps: 1) equation 4.1 is used to calculate the initial vertical stress, 2) pore pressure is included at the reservoir level and the stress field is recalculated using the method described by Mulders [2003]. The initial horizontal stress is illustrated in Figure 5.4. The value of the horizontal stress is estimated using equation 4.4, where K_0, i.e. the ratio between the horizontal and vertical stress, is set up to be equal to 0.33. The stress concentration, situated on the boundary between the side-burden and the lateral edges of the reservoir, Figure 5.4, is an effect of the initial pore pressure inside the reservoir and is related to the lateral reservoir extension. The reservoir is "pushing the side-burden", and to keep the equilibrium the side-burden reacts back. To monitor the stress field in more detail at the boundary between the reservoir and the surrounding medium, as well as the

stress inside the reservoir, two observation lines are constructed (Figure 5.5).

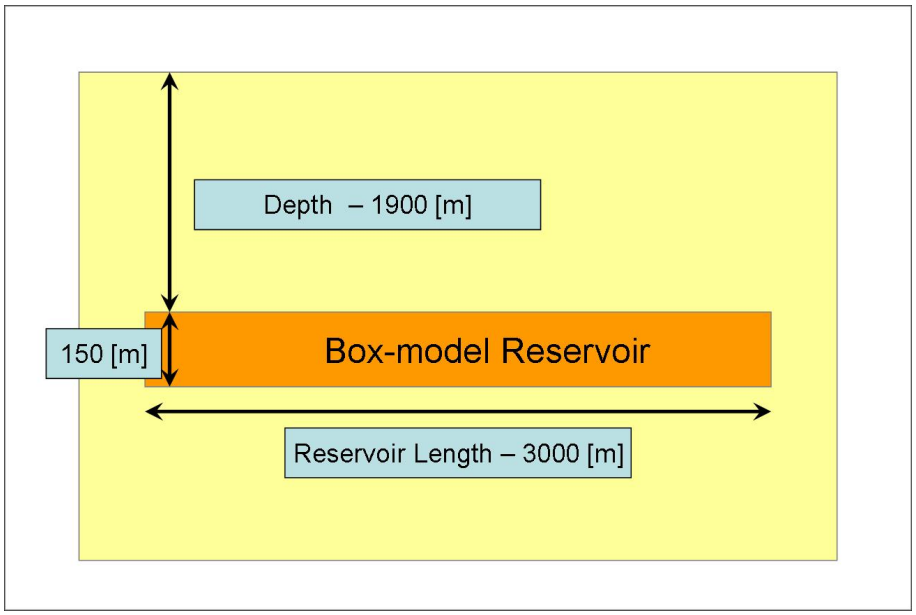

Figure 5.1: *Simple box-model of North Sea oil reservoir. The size of the model in the horizontal direction is 11000 m , where in the vertical direction the model has a size of 4000 m. The reservoir box is 150 x 3000 m, where the depth to the top of the reservoir is 1900 m.*

The horizontal monitoring line is going through the central point, inside the reservoir. It includes observation points 2 and 3, situated at the center and on the right edge of the reservoir. The vertical monitoring line is going through the center of the reservoir. The monitoring points, belonging to the vertical observation line are 1, 2 and 4, positioned at the reservoir top, middle and bottom. Figure 5.6 depicts the linear increase of the vertical stress component, corresponding to equation 4.1. As a consequence of the pore pressure increase at the reservoir level, a decrease in the effective stress is observed between points 1 and 4. The result from the horizontal monitoring line through the center of the reservoir is plotted in Figure 5.7. The effect of loading on the initial pore pressure in the reservoir is visible between

	Surrounding medium		
Elastic parameters	$E_{sur}\ GPa$	ν_{sur}	$\rho_{sur}\ kg/m^3$
	11.3	0.243	2319
	Reservoir		
Elastic parameters	$E_{res}\ GPa$	ν_{res}	$\rho_{res}\ kg/m^3$
Model 1	7.901	0.164	1962
Model 2	7.545	0.163	1943
Model 3	7.205	0.162	1923
Model 4	6.881	0.162	1903
Model 5	6.571	0.161	1884
Model 6	6.274	0.160	1864

Table 5.1: *The six different initial parameterizations of the model used in the modelling part with the elastic parameters of the reservoir and the surrounding medium, Angelov et al. [2005].*

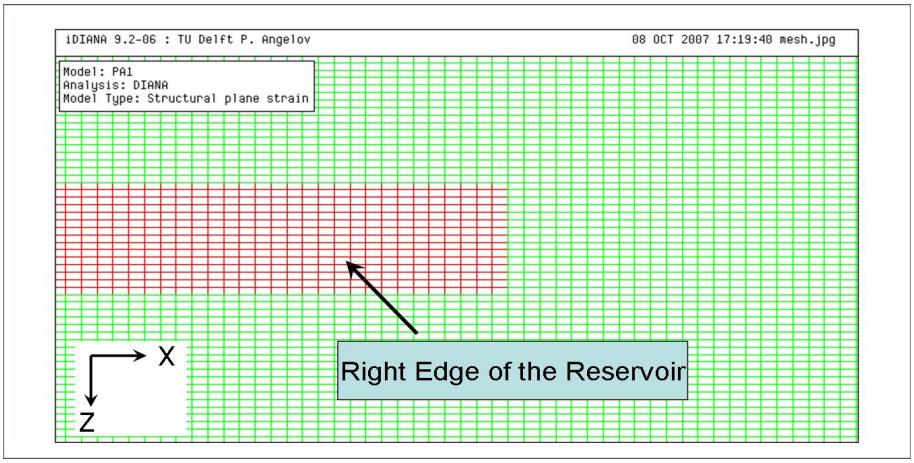

Figure 5.2: *Part of the FEM used in the Simple box-model of North Sea oil reservoir. The mesh is zoomed at the right edge of the reservoir (in red color).*

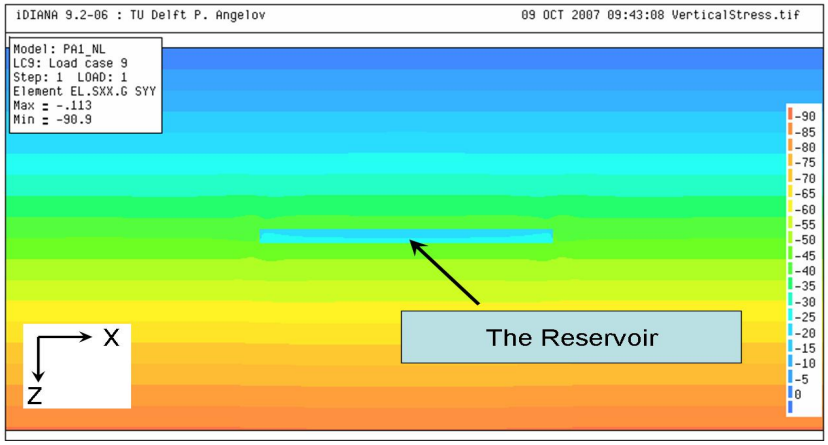

Figure 5.3: *The Vertical Stress field, around the reservoir, before the production start (Model 1 from Table 5.1). The color scale is from 10 to 80 MPa, where the stress increases from "cold" to "hot" color.*

points 2 and 3. The vertical effective stress as illustrated in Figures 5.6 and 5.7, is corresponding to the simulated load of the initial pore pressure of 20 MPa inside the reservoir. As previously discussed in Section 4.2 depletion of the reservoir (production effect) will induce changes in the stress field and displacement. These changes occur in the overburden and inside the reservoir. The variations in the effective stress throughout the reservoir are not changing laterally. The lack of lateral changes comes from the fact, that the model consists of homogenous and isotropic layers, and the values of pressure depletion are constant over the whole reservoir. The compaction of the reservoir causes stress concentration in the overburden at the edges of the reservoir (stress arching). In order to understand the stress/strain development as a result of pressure depletion, "Model 1" from Table 5.1 is investigated at first and the summary is given in Section B.1. As discussed in **Chapter 4** the stress changes depend not only on the value of pressure changes, but also on the elastic properties of the rocks, the geometry of the model, and the aspect ratio of the reservoir. This Section 5.1 presents an investigation of the stress development as a function of rock property con-

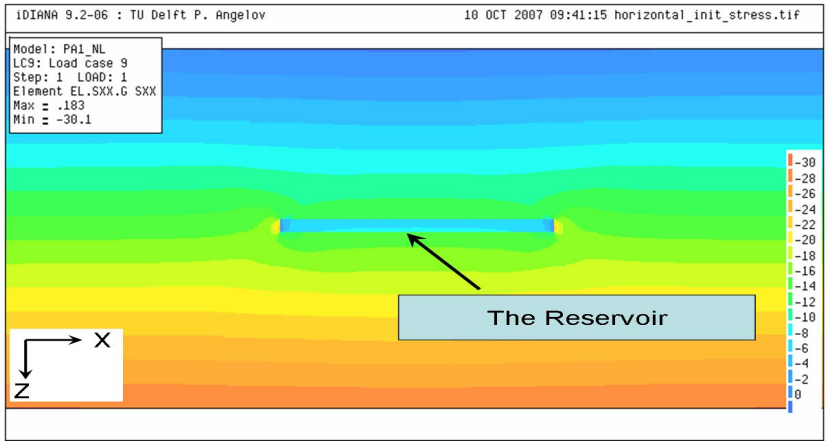

Figure 5.4: *The Horizontal Stress field, around the reservoir, before the production start (Model 1 from Table 3.7). The color scale is from 0 to 30 MPa, where the stress increases from "cold" to "hot" color.*

trast between the reservoir and the surrounding rock using the initial values from Table 5.1. The results of the six different parameterizations are illustrated in Figure 5.8. An increase in the vertical stress path (γ_z) and in the horizontal stress path γ_x, note that they are denoted as γ_v and γ_h in Equation 4.8, is observed with increasing stiffness of the reservoir rock. Larger γ values imply a smaller effective stress increase during the hydrocarbon production. In other words a tendency exists for the stresses to be arched around the relatively soft depleted reservoir (Mulders [2003]). From C and D, Figure 5.8, the most significant stress-changes, caused by changes in the elastic properties of the reservoir, are concentrated at the lateral boundaries of the reservoir. By softening the reservoir with 14%, the vertical stress variations per unit depletion at the top of the reservoir, i.e. close to the reservoir edges, are increasing with 20%. The stress-path changes, detected at the center of the reservoir are negligible. Above and below the reservoir center, the reservoir contraction results in a slight decrease of the total horizontal stress. In general the vertical and the horizontal stresses are increasing by decreasing the elastic properties of the reservoir. Parallel to the changes in the Young

modulus and density, the Poisson ratio is also influencing the stress development within the reservoir. This means that the γ_x values within the reservoir are decreasing with increasing values of ν_{res}. The larger the value of ν_{res}, i.e. the larger the bulk stiffness of the reservoir rock, the less stress is arched away to the surrounding rocks.

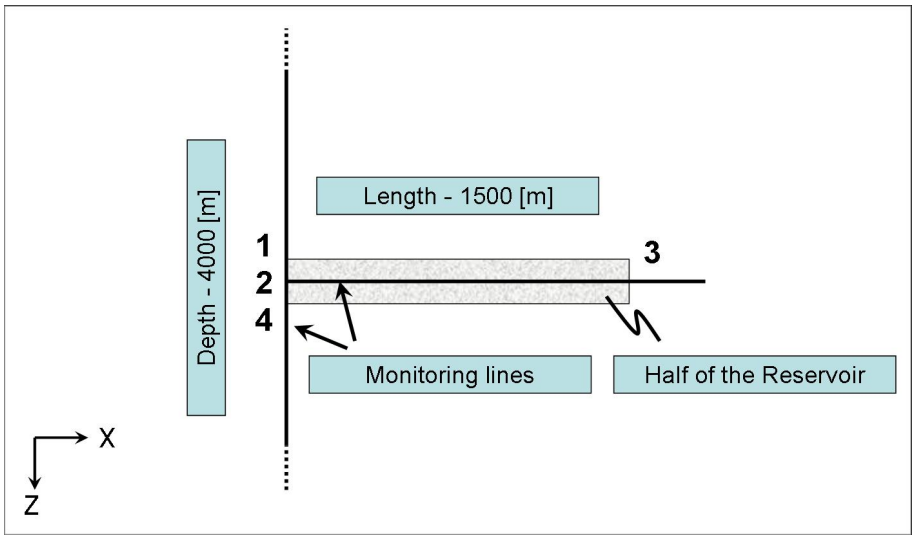

Figure 5.5: *The observation lines (vertical and horizontal) constructed to monitor the state of the vertical stress inside and at the top and the bottom of the reservoir. Only half of the reservoir is investigated, from the center to the right edge of the box-model, because of the symmetry. The stress at four observation points will be discussed, labeled with* $1, 2, 3$ *and* 4*.*

Equations 4.15 and 4.16 indicate that the reservoir compaction is also influenced by the changes in the elastic properties of the rock. Increasing the stiffness of the reservoir rock will reduce the reservoir compaction. Figure 5.9 depicts the vertical displacement, relative to the displacement in Model 1 (Table 5.1), as a function of the petrophysical properties of the reservoir rock. The vertical displacement increased with almost 30% as a result of 14% decrease in the layer stiffness. As a result of a softened reservoir rock, the overburden could easily impinge on the reservoir, so that compaction in-

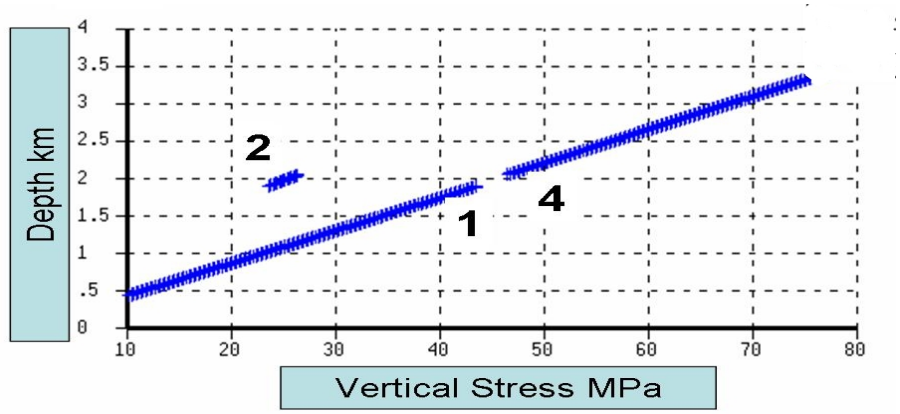

Figure 5.6: *The vertical initial stress, monitored at the vertical observation line, Figure 5.5. On the vertical axes is plotted the depth from* 0 *till* 4000 *m, and on the horizontal axes is plotted the vertical stress in MPa.*

creases.
Once the changes in stress and the compaction of the reservoir are known, it is possible to predict the changes in the elastic properties. One approach is using the rock physics theory, as discussed in **Chapter 3**. However the changes in the volumetric strain will affect both the porosity and the elastic properties of the rock, as well as the reservoir thickness, (Tura et al. [2005]). The predicted changes in seismic properties from the forward rock modelling are not sufficient for simulating the correct time-lapse changes of the seismic attributes. In this section 5.1 the approach, suggested by Hatchell et al. [2003] is applied, where the changes in the seismic properties are predicted using an empirical relation between the vertical displacement and the seismic velocity. This relation was already introduced in **Chapter 2**, Equation 2.27. Holt et al. [2005] elaborated on the relationship between the Hatchell R-factor and the stress/strain sensitivity.
If the rock behavior is such that the velocity depends essentially on the net mean stress, then using equation 2.11 (Hooke's law) the changes in the velocity are given by Holt et al. [2005]:

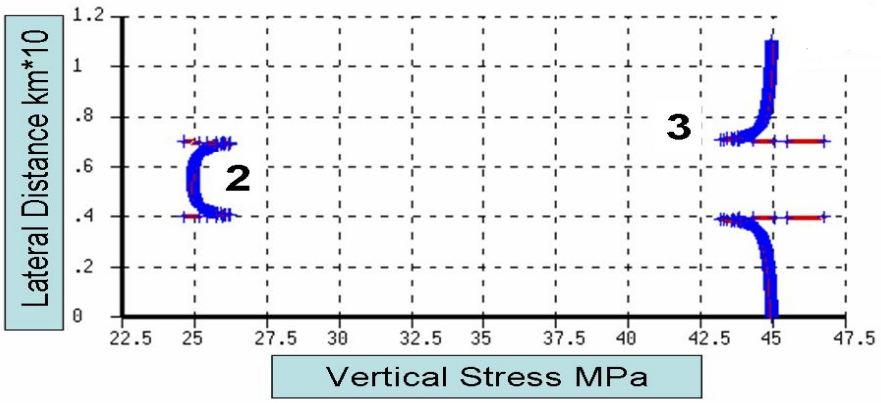

Figure 5.7: *The vertical initial stress, monitored at the horizontal observation line, Figure 5.5. On the vertical axes is plotted the lateral distance from* 0 *till* 11000 *m, and on the horizontal axes is plotted the vertical stress in MPa. The center of the reservoir lay at* 5500 *m.*

$$\frac{\Delta V}{V} = \frac{1}{V}\frac{\Delta V}{\Delta \overline{\sigma'}} K_{fr} e_v, \tag{5.1}$$

where the seismic velocity is denoted with V, K_{fr} is the bulk modulus of the dry rock, e_v is the volumetric strain and $\overline{\sigma'}$ is the mean effective stress. Therefore the R factor (**Chapter 2**) is stress dependent. Further using equation 2.27 the dimensionless parameter R can be presented as a function of stress and strain

$$R = -K_{fr}\left(\frac{1}{V}\frac{\Delta V}{\Delta \overline{\sigma'}}\right)\frac{e_v}{e_{zz}}. \tag{5.2}$$

Hence R is a function of the material and rock physics properties, and it depends also on the changes in the geometry of the reservoir. As reported by Holt et al. [2005], due to lateral variations of the stress field around a depleting reservoir, it is likely that R varies with offset and position, even if

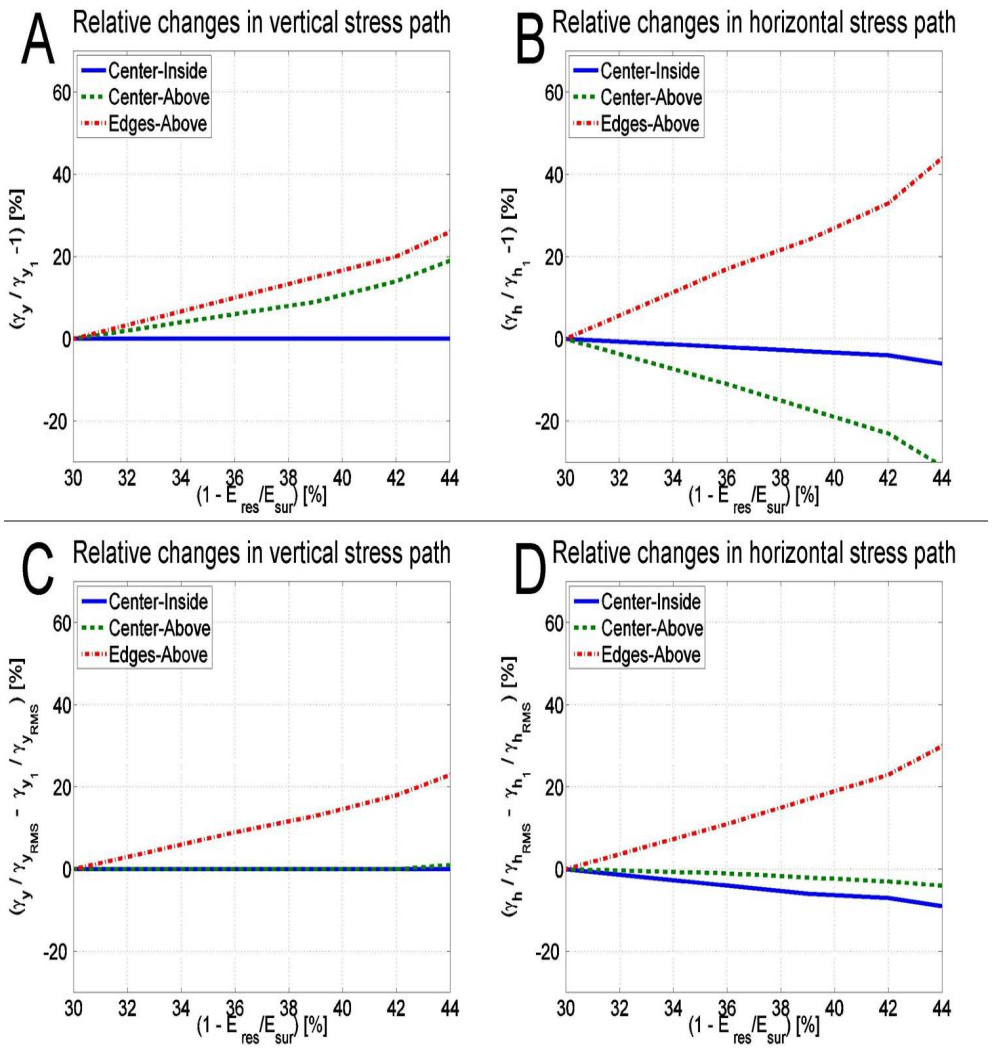

Figure 5.8: *Relative changes in γ_z and γ_x as function of the contrast between the elastic properties of the reservoir and surrounding media. A, B - changes in γ compared to the situation in Model 1, Table 5.1. C, D - changes in γ compared to the situation in Model 1, where the RMS of γ_z and γ_x values is used for normalization. The blue solid line is presenting the changes occurring at point 2, Figure 5.5. The green dashed line depict the changes at observation point just above point 1 at Figure 5.5, where the red dash-dotted line is presenting the results above point 4, near the top of the reservoir.*

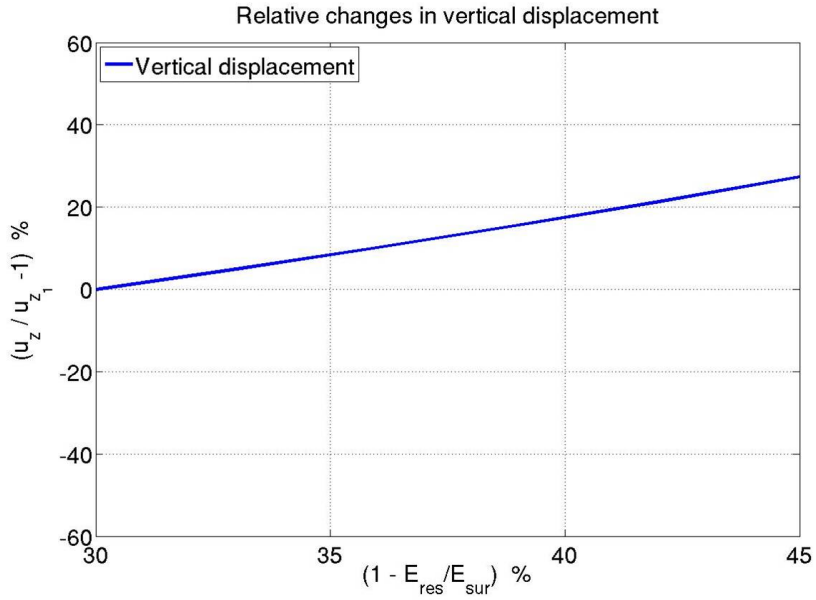

Figure 5.9: *Relative changes in the vertical displacement as function of the contrast between the elastic properties of the reservoir and surrounding media. The displacement is calculated on the top, at center of the reservoir, Figure 5.5 – observation point 1.*

the rock properties are uniform in the area. From Equation 5.2 the changes in the seismic velocity can be predicted, using either the results of the geo-mechanical forward modelling and the calculated R

$$\frac{\Delta V}{V} = -R\frac{e_{zz}}{e_v}\left(\frac{\Delta\overline{\sigma'}}{K_{fr}}\right). \tag{5.3}$$

σ', e_v and e_{zz} follow from the geo-mechanical modelling. Therefore, the dimensionless R factor can be considered as ratio between the changes in seismic velocity induced by changes in the stress filed and the vertical strain. From here, the R coefficient can be successfully used to decouple the effects of changes in stress and strain in the measured time-shifts. Further, the stress

induced time-shifts can be used to calculate the time-lapse changes in the acoustic velocity. If the time-shift ($\Delta t/t$) can be estimated from the time-lapse seismic data, then R can be calculated using the presented by Staples et al. [2007a] expression:

$$\frac{\Delta t}{t} = (1+R)e_{zz}. \tag{5.4}$$

What must be considered before building the velocity models, is the following: what kind of physical mechanism started after the reservoir depletion and how does this mechanism affect the seismic velocity in the reservoir? Table 5.2 presents the various sources of stress sensitivity in a depleting reservoir according to Holt et al. [2005]. For the case study in this section, an increase in effective stress is applied, which causes compaction of the rock and leads to an increase in the seismic velocities (Table 5.2 - second row). The effect of anisotropy on the velocity is presumed to be negligible. No fractures or cracks are present. As already demonstrated, the reservoir depletion leads to stress changes not only at the reservoir level, but also in the surrounding rock above, underneath, and on the sides of the reservoir. As reported by Goulty [1998], Holt and Fjaer [2003], and Holt et al. [2005], the wave velocities in intact shales (overburden rock) are sensitive to increasing porosity. The stress changes are affecting the seismic velocity in shales primarily through the porosity, (Holt et al. [2005]). Therefore the stress/strain changes in the overburden, caused by reservoir depletion, will influence the seismic properties of the shales. In case of pore pressure depletion, generally the value of R is set to 1 inside the reservoir, and 5 in the overburden, i.e. Hatchell and Bourne [2005], Hatchell et al. [2005], Røste et al. [2006], Staples et al. [2007a] and Hawkins et al. [2007]. Setting R to 1 in equation 5.2 and using the results from the rock physics and geo-mechanical modelling gives the changes in the seismic velocity in the order of 2 m/s for the central part of the reservoir. This result does not correspond to the calculated velocity from the Dvorkin and Nur [1996] theory (**Chapter 3**), which is around 20 m/s for the case of 2.5 MPa changes in the mean effective stress. The reason is that in the Dvorkin and Nur [1996] theory we simulated only changes in the pore pressure and did not include the changes in the petrophysical properties, for example porosity and contact per grain. To link the geo-mechanical modelling with the seismic model it is necessary to adjust the R

coefficient, using equation 5.2. This lead to an R value of 15, which is quite high but not unusual according to Staples et al. [2007b]. The relative changes in the P-velocity as a function of the mean effective stress for the center of the reservoir are plotted in Figure 5.10. The values for the seismic velocity, calculated with the R coefficient are smaller but still in the same order, compared to the results from the modelling using the rock physics theory. The R coefficient used to calculate the velocity changes in the overburden, is taken to be 5 times larger as the value used for the reservoir (Hatchell et al. [2005]). When the R value and the vertical displacement are already known, equation 2.27 is applied to predict the changes in the seismic velocity in the overburden and at the reservoir level.

Mechanism	**Controlling factor**	**Wave velocity change**	**Effect on velocity anisotropy**	**Conditions**
Porosity decrease	Increase of mean effective stress	$\Uparrow$ small effect	none	Most efficient near critical ϕ
Grain contact compression	Increase of effective stresses	$\Uparrow$	$\Downarrow$	Requires uncemented grains
closure of cracks/fractures	increase of effective stresses	$\Uparrow$	$\Downarrow$	Fractured reservoir
Generation of cracks/fractures	Reservoir stress path	$\Downarrow$	$\Uparrow$	Rock brought beyond yield onset/initially fractured rock
Decrease of pore fluid bulk modulus	Pore pressure reduction	$\Downarrow$ small effect	$\Uparrow$ small effect	Above bubble point of fluid constant amount of dissolv. gas

Table 5.2: *Various sources of in-situ stress sensitivity for velocities in a depleting reservoir, Holt et al. [2005].*

Figure 5.11 depicts the computed R coefficients used to calculate the changes in the seismic velocity at the reservoir level. The R values are constant throughout the whole reservoir, except at the lateral boundaries of the reservoir, where the higher values of the stress-path coefficient appear, Figure B.4 and B.6. A small sensitivity of the R values to the magnitude of the pressure depletion is observed, Figure 5.11, which is a consequence of the relationship between the velocity and the effective stress, see Figure 5.10. Figure

5.12, presents the time-lapse changes in the P-Velocity for Model 1 (Table 5.1) after a pressure drop of 15 MPa at the reservoir level. As expected the seismic velocity decreases in the overburden, affected by the elongation of the overburden layer, where positive time-lapse changes are observed at the reservoir level. The relative changes in the P-velocity inside the reservoir are in the order of 3% and slightly decreasing towards the reservoir edges. In the overburden rocks, the seismic velocity is decreasing with about 1%, compared to the reference case. The variations in the S-wave velocity, in the overburden and in the reservoir, are calculated using the time-lapse changes in the P-wave velocity and the Poisson ratio given in Table 5.1. In this case study the changes in density are negligible, and for simplicity are assumed to be zero.

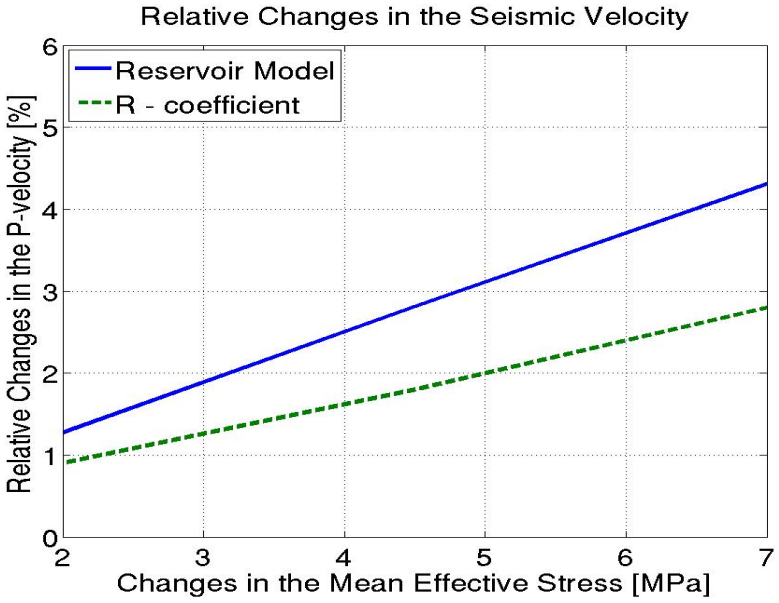

Figure 5.10: *Relative changes in the P-velocity as a function of the effective mean stress at the center of the reservoir. The variations in the seismic velocity are calculated using 1)the reservoir modelling from* ***Chapter 3*** *(the blue solid line), and 2)using the calculated R value (the dashed green line).*

Figure 5.13 depicts the relative changes in the P-wave velocity, as a function of the stiffness contrast between the reservoir and overburden rocks; $100 * (E_{sur} - E_{res})/E_{res}$, where E_{sur} and E_{res} are the Young modulus in the surrounding media and in the reservoir. The time-lapse variations in the seismic velocity depend on the R factor and the vertical displacement, equation 2.27. As observed the vertical displacement, Figure 5.13 - the green-doted line, increases with about 25%, as an effect of the 14% increase in the stiffness contrast between the reservoir and the overburden. The red-dash-dotted line, Figure 5.13, depicts the R factors calculated for the six different parameterizations, Table 5.1. As illustrated by equation 5.2, R depends on the changes in stress and displacement, and on the initial material properties of the reservoir rock. In this Section 5.1 relative small changes in the effective stress are simulated (around 7 MPa). Consequently, the variations in the R factors are determined mainly by the elastic properties of the reservoir. The stiffer the reservoir, the larger values of R are calculated. The observation of the changes in the seismic velocity, Figure 5.13 – the solid-blue line shows that the relative changes are decreasing with decreasing stiffness of the reservoir, i.e. the influence of the R factor is larger than the effect of the reservoir compaction. In conclusion it can be stated, that the seismic velocity inside the reservoir increases for all of the six parameterizations (Table 5.1) as a consequence of pressure depletion, with the largest increase occurring for the most compressible reservoir. The seismic properties in the overburden are affected directly by changes in the porosity of the overburden. The variations in the vertical stress and mean stress in the overburden are negligible (< 0.5 MPa), except near the lateral boundaries of the reservoir, Appendix B, Figure B.5 - B.6. Therefore the seismic velocity is affected by 4D changes in the petrophysical properties induced by vertical strain, like variations in the porosity and contacts per grain. Because the initial elastic properties of the surrounding media remained unchanged for all of the six models in Table 5.1, the R value used to estimate the velocity variations in the overburden is one and the same for all models. For simplicity, the R coefficient is taken to be five times larger in the overburden than in the reservoir (Model 1). The changes in the overburden velocity are plotted in Figure 5.14. The relative changes in the seismic velocity in the overburden increase with decreasing stiffness of the reservoir rock, as a result of the increase in the vertical displacement, Figure 5.9.

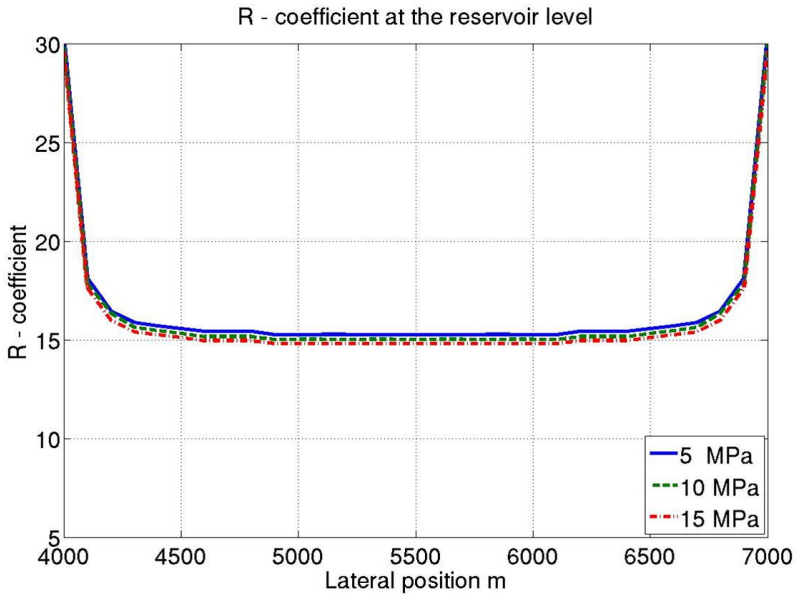

Figure 5.11: *R - coefficient, inside the reservoir (Model 1 - Table 5.1), as a function of the lateral position. The solid, dashed and dot-dashed lines are corresponding to pressure drop of 5, 10 and 15 MPa.*

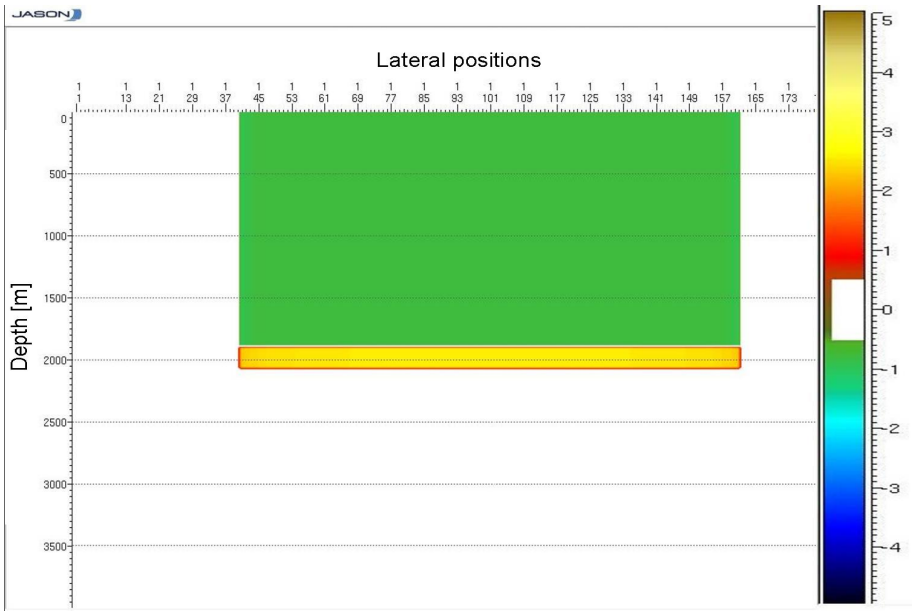

Figure 5.12: *Relative changes in the P-Velocity (Model 1 - Table 5.1) in %, in the overburden and at the reservoir level, after pressure depletion of 15 MPa. Note that the colors represents the changes in the acoustic velocity in %.*

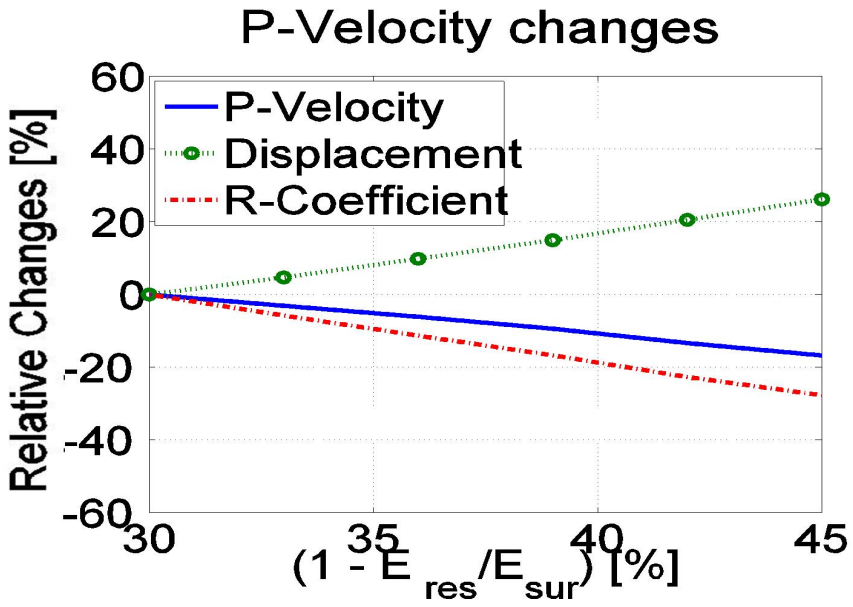

Figure 5.13: *Relative changes in the seismic velocity, vertical displacement, and R coefficient at the reservoir level (at the center of the model). Blue-solid line - P-wave velocity; green-dotted line - vertical displacement of the reservoir; red-dash-dotted line - calculated R coefficient.*

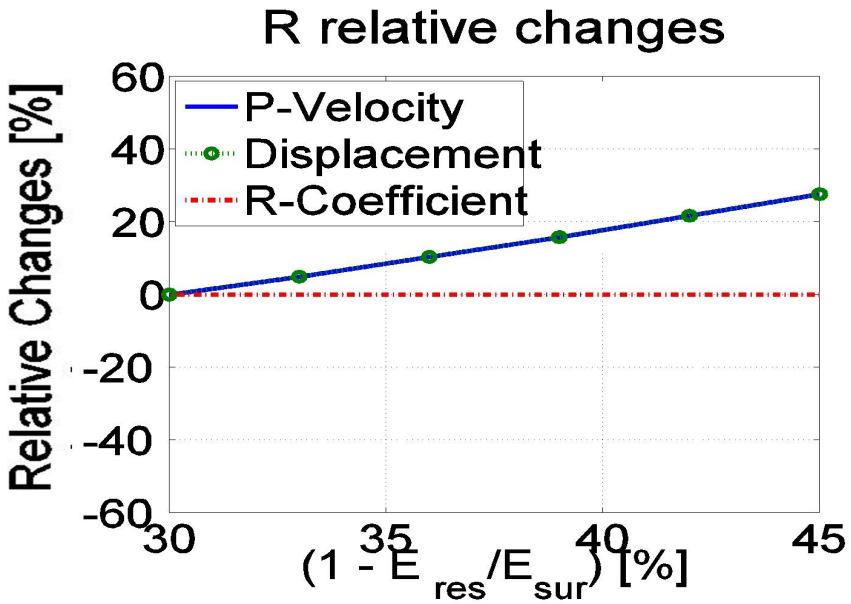

Figure 5.14: *Relative changes in the seismic velocity, vertical displacement, and R coefficient in the overburden (at the center of the model). Blue-solid line - P-wave velocity; green dotted line - vertical displacement of the reservoir; red-dash-dotted line - calculated R coefficient.*

5.2 Building the model by using real data and geo-mechanical modeling, based on the Shearwater reservoir in the North Sea

In this section, the geo-mechanical modelling is applied, using the geometry and elastic properties of Shearwater, a North Sea gas reservoir. Two models with different reservoir-geometry are developed:

[1] Section 5.2.1 introduces a box-model of the reservoir,

[2] Depth-horizons are used to build the geometry of the model presented in Section 5.2.2.

Holm et al. [2005] presented the location and the stratigraphy of the Shearwater field, see Appendix B, Figure B.7 and B.8. The Shell U.K. Limited operated Shearwater gas field, together with Total operated Elgin and Franklin are located at the central part of the North Sea, east from Aberdeen.

Model Layer	Elastic Parameters		
	E $[GPa]$	ν	ρ $[kg/m^3]$
Water Column	0.00141	0.5	1000
Claystone	2.5	0.24	2184
Chalk - Tor	26	0.26	2636
Chalk - Hod	20.5	0.26	2583
Chalk and Marl - Creta	16	0.3	2535
Organic Claystone and Marl	1.7	0.2	2506
Sandstone - Upper Fulmar - Reservoir	4.7	0.16	2147
Sandstone - Lower Fulmar - Reservoir	12.5	0.22	2355
Underburden	22.5	0.25	2600

Table 5.3: *The elastic properties of the layers, used in the geo-mechanical modelling of the Shearwater gas reservoir.*

Based on the stratigraphic column (Figure B.8), the overburden is devided into five main layers: 1) claystone material – till ~ 3600 m, 2) sandstone with

tuff and claystone – from ~ 3600 to ~ 3900 m, 3) chalk – from ~ 3900 to ~ 5600 m, 4) chalk with marl – from ~ 5600 to ~ 5900 m, and 5) organic clay between ~ 5900 and ~ 6100 m. The reservoir has an average thickness of 300 m and consists of gas/water saturated sandstones. The elastic properties of the rocks, have been derived from the well logs (Table 5.3). The pore pressure values are obtained from a flow simulator (source Shearwater).

■ 5.2.1 Box-model

Similar to Section 5.1 a simplified geometry (box-model) of the reservoir is simulated (Figure 5.15). The depth and thickness of the different layers are determined at the position of the producing well. The box-shape is employed to minimize the effects of reservoir geometry on the geo-mechanical modelling. Pressure depletion at the reservoir level is applied in five steps:

[1] initial stress, calculated using equation 4.14 and 4.17,

[2] adding of 100 MPa of initial pore-pressure in the year 2001,

[3] 22 MPa pressure depletion in 2002,

[4] 15 MPa pressure depletion in 2003,

[5] 16 MPa pressure depletion in 2004.

The pressure drop due to depletion is considered homogenous over the entire reservoir. The analysis is concentrated on the time-lapse effect between years 2002 and 2004, i.e. steps 3) and 5), corresponding to the period with the largest changes observed in the real 4D seismic data. The R coefficient is estimated directly from the time-shift observed in the real data (Staples et al. [2007a]) and the vertical displacement calculated in our model using equations 2.29.
Vertical and horizontal monitor lines are constructed in order to calculate the effect of stress path and vertical displacement, as a result of pressure depletion at the reservoir level, Figure 5.16. From Table 5.4, the reservoir has compacted with 56 cm between 2002 and 2004. From the overburden layers, the three chalk intervals (Table 5.3) vertically stretched 3 cm. The organic-clay-layer suffered a relatively small vertical elongation of 1 cm.

Interface	Depth m	Vertical Displacement m
Sea Bottom	90	0.338
Top of the Chalk - Tor	3480	0.468
Top of the Chalk - Hod	3960	0.481
Chalk and Marl - Top	4640	0.497
Organic Clay - Top	4700	0.499
Top of the Reservoir	4770	0.51
Bottom of the Reservoir	5030	-0.0466

Table 5.4: *Vertical displacement monitored using the vertical monitoring line - Figure 5.25. The observation points* 1 *and* 3 *are corresponding to the top and the bottom of the reservoir (rows six and seven).*

However since the layer thickness is only 70 m the resulting strain is relatively large. The changes in the effective stress occurred parallel to the compaction/elongation. Tables 5.5 – 5.7 show the stress paths, γ_z and γ_x, for the vertical and horizontal lines (Figure 5.16). From the stress path it can be concluded that inside the reservoir, most of the changes in the vertical effective stress came directly by the pressure changes. The variations in the horizontal stress are linked to the vertical ones (Equation 4.4).

Interface	Claystone	Chalk	Chalk and Marl	Organic Claystone	Reservoir
γ_z	≈ 0	≈ 0	≈ 0	≈ 0	≈ -1
γ_x	≈ 0	≈ -0.01	≈ 0	≈ 0	≈ -0.33

Table 5.5: *Stress path for the vertical monitoring line (Points 1–3, Figure 5.16).*

Close to the edges of the reservoir the changes in the vertical stress are decreasing, whereas the horizontal stress variations are increasing as a result of the lateral displacement of the reservoir, i.e. the side burden is impinging onto the reservoir. No or negligible stress changes are observed above the center of the reservoir. Stress concentrations are observed close to the edges just above the reservoir. These effects are the result of stress arching and

lateral displacement of the reservoir.

Lateral Position m	7200 (Reservoir)	8200	9200	9600 (Reservoir Edges)	10000	12000
γ_z	≈ -1	≈ -1	≈ -0.94	≈ -0.9	≈ -0.08	≈ 0
γ_x	≈ -0.33	≈ -0.33	≈ -0.4	$\approx -0.75 \sim\approx 0.45$	≈ 0.1	≈ 0

Table 5.6: *Stress path, for the horizontal monitoring line (Points 2-4, Figure 5.16).*

Lateral Position m	7200 (Reservoir)	8200	9200	9600 (Reservoir Edges)	10000	12000
γ_z	≈ 0	≈ 0	≈ 0.07	≈ 0	≈ -0.07	≈ 0
γ_x	≈ 0	≈ 0	≈ 0	$\approx -0.03 \sim\approx 0.03$	≈ 0	≈ 0

Table 5.7: *Stress path for the horizontal monitoring line (Points 1–5, Figure 5.16).*

Top of Interface	Chalk Tor	Chalk Hod	Chalk Marl	Organic Claystone	Reservoir	Underburden
Depth of the Interface [m]	3480	3960	4640	4700	4770	5030
Time-shift [ms]	0.4	1.1	2.9	3.1	3.5	2.5

Table 5.8: *The time-shift at the top of the layers picked from Figure 5.18.*

According to the results of the geo-mechanical modelling presented in the Tables 5.4 to 5.7, one would expect: 1) an increase in the seismic velocity inside the reservoir, caused by the increase in the effective stress and reservoir compaction, and 2) a velocity decrease in the entire overburden. The changes in the seismic velocity are depending on the elastic properties of the rocks, as well as on the magnitude of the vertical displacement. Therefore different values of the velocity changes are expected in the different overburden layers. These corresponds to the observations published in the literature, e.g.

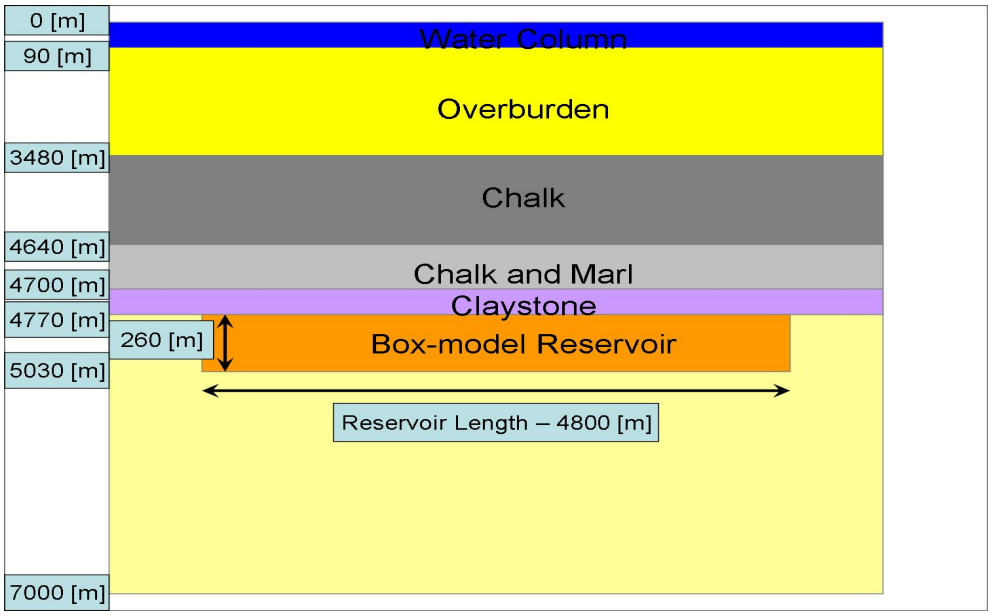

Figure 5.15: *Simple cartoon, presenting the geometry and depth of the layers included in the box-model. The depth is considered by using the well-log information.*

Hatchell and Bourne [2005], Vidal-Gilbert and Tisseau [2006] and Hawkins et al. [2007]. As already mentioned, the R factor is estimated using

$$R = \left(\frac{\Delta t}{t} - \frac{\Delta z}{z}\right) / \frac{\Delta z}{z}. \tag{5.5}$$

For the vertical monitoring line through the center of the reservoir the estimated R and the calculated time variations in the seismic velocity are given in Table 5.9. The migration velocity is used in order to calculate the reference velocity at year 2002.
The compressional R factor (2) correlates with the values proposed by Hatchell and Bourne [2005], which are between 0 and 2, and is close to the value presented by Staples et al. [2007a] – between 3 and 5. In case of elongation in the overburden, for the same gas reservoir, Hatchell and Bourne [2005]

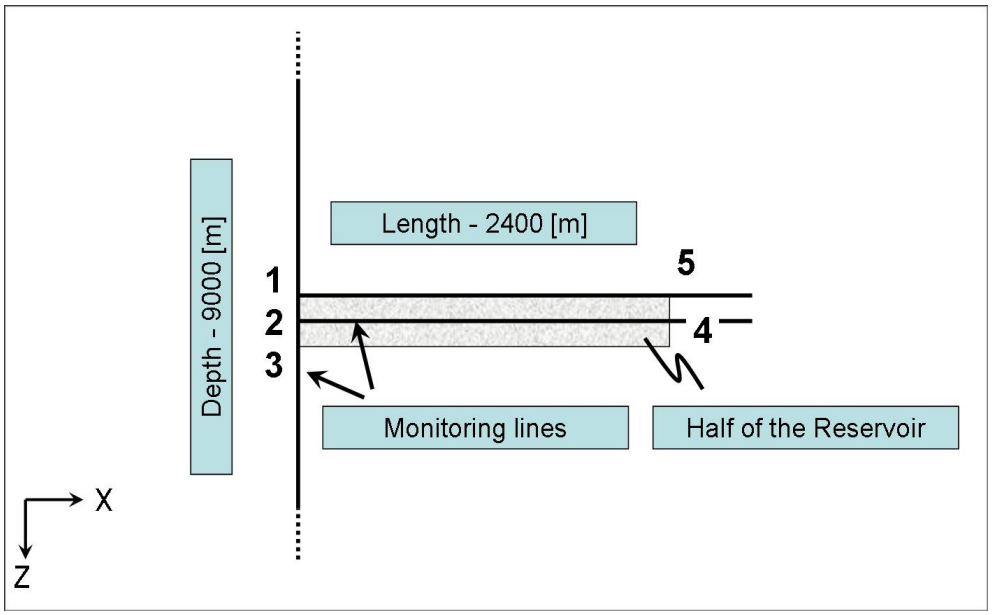

Figure 5.16: *The horizontal and vertical observation lines constructed to monitor the state of the vertical stress inside and at the top and the bottom of the reservoir. Only half of the reservoir is investigated, from center to the right edge of the box-model because of the symmetry. The stress at five observation points will be discussed, labeled with* $1, 2, 3, 4$ *and* 5.

Layer	Chalk Tor	Chalk Hod	Chalk Marl	Organic Claystone	Reservoir
R - coefficient	139	245	206	50	2
Velocity changes m/s	-19	-25	-28	-22	16

Table 5.9: *R factors and calculated time-lapse changes in the P-wave velocity, for the overburden and reservoir layers. The R coefficient is calculated for each of the layers using the time-shift and vertical displacement.*

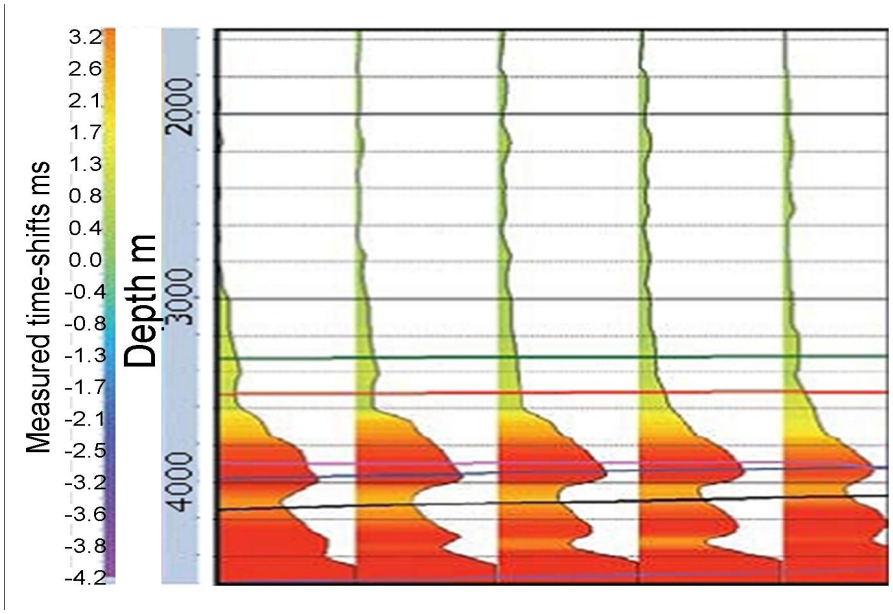

Figure 5.17: *Shearwater measured time-shifts with horizons, (Staples et al. [2007a]). The horizons are corresponding to the intervals presented in Table 5.3: 1) green - top of the chalk-tor, 2) red - top of the chalk-hod, 3) pink - top of the organic claystone, 4) blue - top of the sandstone fulmar interval, and 5) black - base of the sandstone fulmar interval.*

presented values of R between 4 and 8. In their case study, Hatchell and Bourne [2005] interpreted the whole overburden as one layer. In our case, considering the overburden as one single layer, a value of 8 for R is estimated. However, the R factor depends on the stress distribution as well as on the elastic properties of the layer (Equation 5.2). Therefore the R values are obtained for each of the overburden layers as presented in Table 5.9. The value of the R coefficient is sensitive to the errors in the measured time-shift and to the errors in the rock compressibility (Staples et al. [2007a]):

[1] The accuracy of the observed time-shift depends on the time-lapse processing and data quality.

[2] The correct estimation of the vertical displacement depends on the elastic properties of the rocks, reservoir geometry, magnitude of pressure depletion, and the finite element mesh used for the calculations.

In Figure 5.18 the possible errors in the calculation of the R coefficient are illustrated, where the results of the observed time-shifts are perturbed from 0 to 100 %. In Figure 5.19 the error in the R factor is plotted where the calculated vertical displacement is perturbed from 0 to 100 %. Finally the estimated changes in the seismic velocity, inside the reservoir and in the overburden layers, are presented in Figure 5.20. The stress changes in the three chalk layers are negligible and velocity variations are determined only from the strain. The absolute value of changes in the seismic velocity is increasing with depth (increase in the vertical strain) and is between 0.4 and 0.6 % of the initial velocity value.

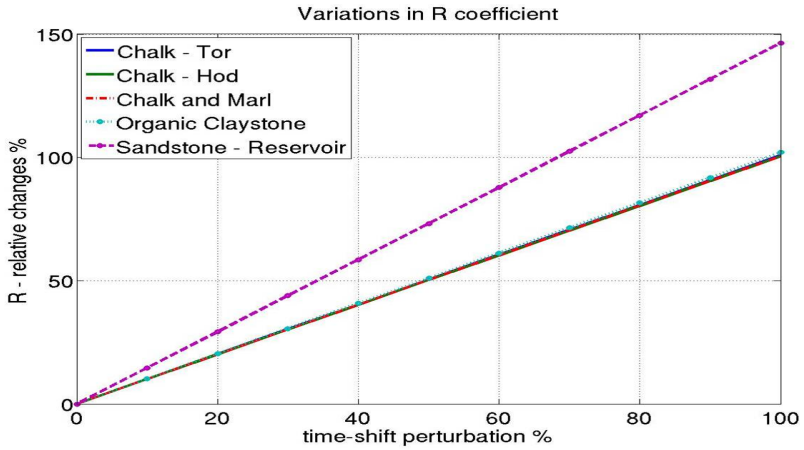

Figure 5.18: *The R coefficient as a function of the perturbations in the measured time-shift. The graphs which represent the overburden layers are on top of each other. The reason is that the vertical strain is almost one and the same in all of the overburden layers.*

In the overburden, just above the reservoir, the absolute value is around 0.7 % and decreasing from the center to the lateral boundaries of the reservoir. The

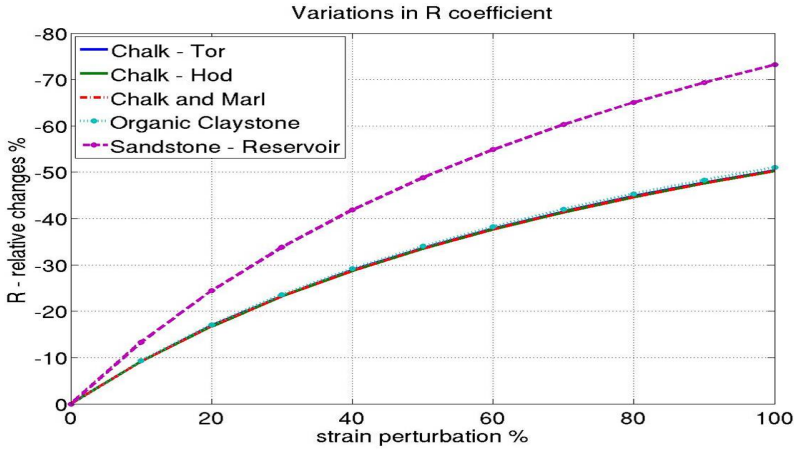

Figure 5.19: *The R coefficient as a function of the perturbations in the vertical strain - calculated with the geo-mechanical modelling. The graphs which represent the overburden layers are on top of each other. The reason is that the vertical strain is almost one and the same in all of the overburden layers.*

reason for this is the decrease of the vertical displacement above the lateral boundaries of the reservoir. Inside the reservoir, the velocity is increasing by about 0.5 %. At the lateral edges of the reservoir the time variations in the seismic velocity are slightly increasing because of the increase in the mean effective stress. The constructed velocity model is used in **Chapter 6** to simulate the time-lapse changes in the seismic attributes. Further the values of the variations in the P and S-wave velocities over time are plotted in Figure B.9 and B.10.

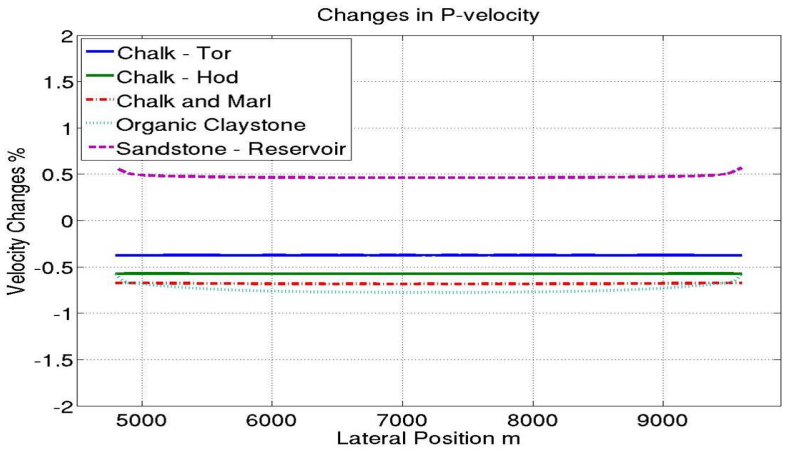

Figure 5.20: *Relative changes in the P-wave velocity.*

5.2.2 Complex - reservoir-geometry-model

For this model the geometry of a 2D section of Shearwater has been used (Figure 5.21). The geometry of the model, presented in Figure 5.21, is slightly modified to make it suitable for the finite element mesh presented in Figure 5.22.

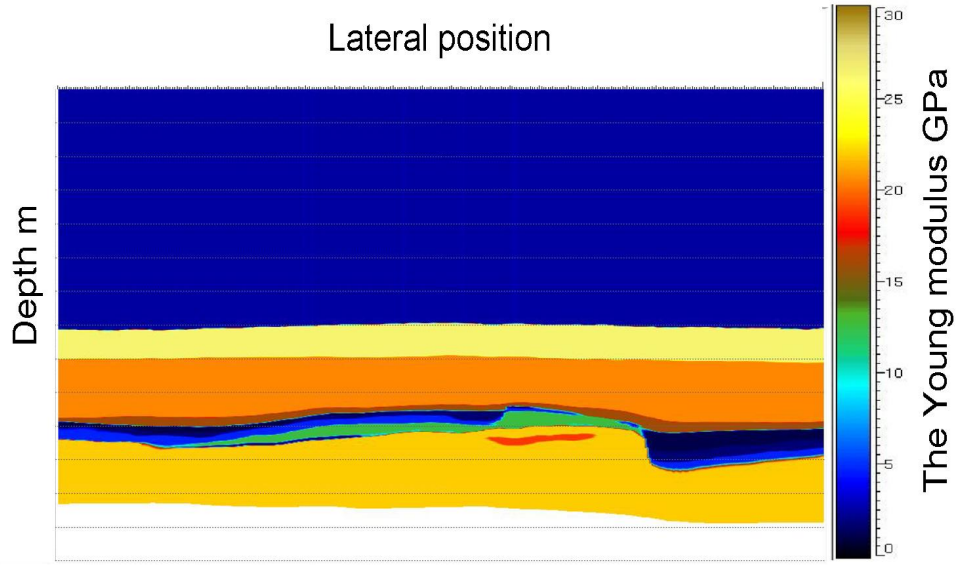

Figure 5.21: *The geometry of the 2D section with the Young modulus of the layers (source Shearwater). The unit of the color scale is GPa.*

The upper and the lower parts of the reservoir are given respectively in green and pink. Red just above the reservoir corresponds to the organic clay layer, blue to the chalk and marl. The chalk intervals - belonging to the Hod and Tor formations are colored in yellow and red. The coarser non-colored grid above the reservoir is used to build the claystone overburden layer together with the water column, where the non-colored grid below the reservoir is representing the underburden. The elastic properties denoted to the different layers are given in Table 5.3. Similar to Section 5.2.1 the pressure depletion

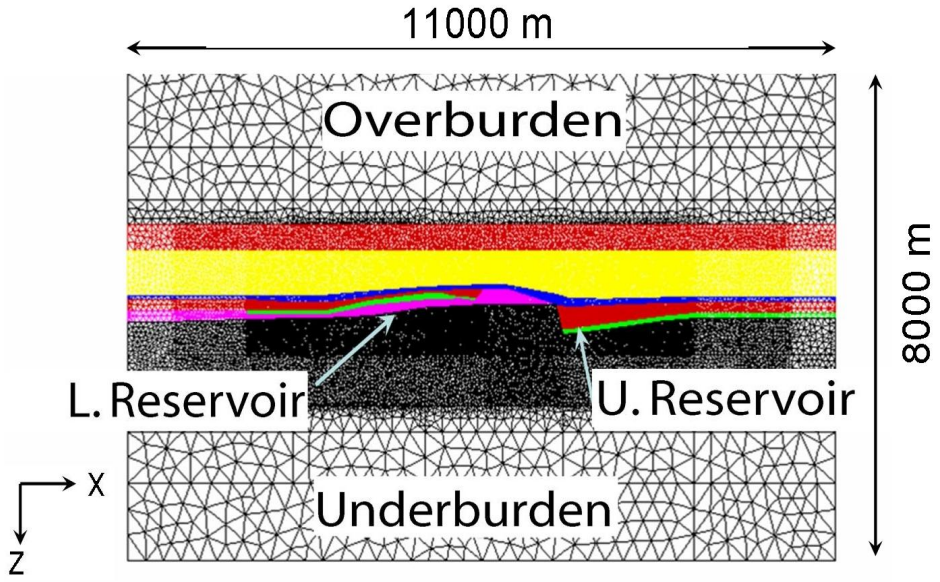

Figure 5.22: *Finite Element mesh, used in the 2D geo-mechanical modelling.*

is applied in four steps, but now based on a reservoir flow simulation and therefore no longer homogeneously distributed within the reservoir:

[1] initialization of the initial pre-production stress and overpressure at the reservoir level in the year of 2001,

[2] 13 to 22 MPa pressure depletion in 2002,

[3] 15 to 20 MPa pressure depletion in 2003,

[4] 16 to 19 MPa pressure depletion in 2004.

The calculated changes in the vertical effective stress (2002 – 2004), together with the vertical displacement (2002 – 2004) are given in Figure 5.23 and 5.24.
Time-lapse changes in the effective stress are observed through the whole model:

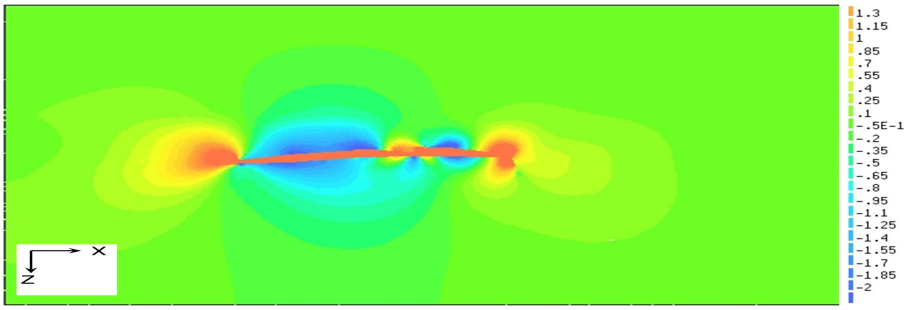

Figure 5.23: *Changes in the vertical effective stress as result of pressure depletion at the reservoir level between years of 2002 and 2004 in MPa. The "cold" colors are associated to a decrease in the effective stress, where the "hot" colors are presenting increase in the effective stress. The presented results are clipped between −2 and 2 MPa.*

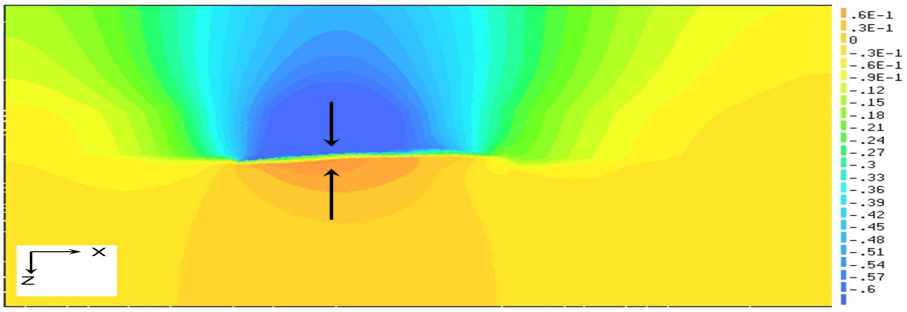

Figure 5.24: *Vertical displacement as a result of pressure depletion at the reservoir level between years 2004 and 2002 in m. The negative values of the displacement are presenting the elongation of the overburden and the reservoir compaction, where the positive values are the result of a pull-up of the underburden. The presented results are between -60 and 15 cm.*

- The positive changes in the vertical stress are calculated throughout the whole depleting part of the reservoir. The maximum value of these changes occurred near the faults (2 and 3) and the dipping event (1) (Figure B.12). The variations in the horizontal stress are plotted in Figure B.13. The stress path depends on the elastic properties of the rock and is therefore smaller in the softer upper reservoir layer than in the less compressible lower layer. Near the fault (2), quite high absolute values of the stress path are monitored because of the reservoir geometry. This region can be considered as an edge of the reservoir where the changes in the horizontal stress are reaching their maximum, see Table 5.6. The time-lapse changes in the mean effective stress are plotted in Figure B.14. The changes in the mean effective stress are a result of the changes in the vertical and horizontal stresses. There are less changes in the softer upper layer than in the harder lower interval.

- In the side-burden the vertical stress increased as a result of the stress arching (Figure B.12). As it was explained in the previous sections, the maximum value of the horizontal stress changes occurred at the lateral edges of the reservoir (Figure B.13).

- Figure B.12 illustrates how the geometry of the faults (1) and (2) increase the vertical effective stress in the overburden. This increase is caused by the fact that the organic claystone between the events (1) and (2) is acting both as overburden and side-burden of the reservoir. Further increase in the vertical stress over the top of the reservoir is monitored at the pinch-out close to fault (3). Over the central part of the reservoir, a decrease in the vertical effective stress is monitored. In the overburden, Figure B.13, the variations in the horizontal stress over time are negligible, except on the top of the reservoir near the fault (2). As was mentioned, the reason for this is that the organic claystone overburden is acting as a side-burden as well, because of the specific reservoir geometry, e.g. Table 5.7. At the upper Chalk (Chalk-Tor) interval a slight increase in the horizontal stress ($\gamma_x \approx -0.12$) is monitored. The reason for this is that the layer is pressed between the thick overburden-Clay layer and the hard Chalk-Hod interval, leading to lateral extension and thus causing an increase in the horizontal stress. In the overburden, Figure B.14, the mean effective stress de-

crease over the central part of the reservoir and the stress increase as near the faults (2) and (3) as well in the Chalk-Tor interval are monitored.

- In addition eight new models have been evaluated with different reservoir geometries, in order to investigate the effect of the faults (1) and (2) (Figure B.11) on the effective stress changes and displacement. In these models the "gap" between faults (1) and (2) is gradually closed from left to right. The results are presented in Appendix B, Figure B.15 – B.16. Removing the "gap" at the top of the reservoir, the anomalously time-lapse increase of the mean effective stress in this part of the overburden vanished and the changes in the effective stress field resembled the box-model results (Section 5.1).

Changes in the two-way travel-time as a function of changes in the physical distance and mean effective stress Pore pressure changes at the reservoir level cause variations in the stress field as well as changes in the layer thickness (Figure 5.24). The elongation of the overburden, i.e., the subsidence of the reservoir top, is monitored over the whole depleting part of the reservoir. Maximum vertical displacement is monitored over the central part of the reservoir. The R coefficient and the seismic velocity depend directly on the mean effective stress, vertical and volumetric strain, and on the elastic properties of the rock materials. The R coefficient can be calculated directly using the measured time-shift from the time-lapse seismic data and the vertical displacement as it was demonstrated in Section 5.2. However the calculation of R is depending on two factors (Table 5.10): 1) the quality of the time-lapse changes in the two-way travel time (TWT), and 2) the geo-mechanical model used to simulate the vertical strain affected from pressure depletion.
As discussed in Section 5.2.1, the errors in the strain and/or time-shift have a large influence on the R coefficient. Another problem is to calibrate the results of the changes in the layer thickness with the measured difference in the 4D travel time. On one hand, there is the numerical solution to the geo-mechanical problem. The accuracy of the calculation depends on the density of the finite element mesh. On the other hand, the possibility to measure the time-shift depends strongly on the repeatability of the 4D data and

Vertical Strain	Time-Shift
Elastic properties of the rocks	The effect of noise on the signal
Geometry of the layers	Time-lapse repeatability
Value of the pressure depletion	Velocity model used for the PSDM
Finite Element Mesh used for the modelling	Cross-correlation time-window
The solution of the geo-mechanical problem	Cross-correlation smoothing lateral window
Depth of the reservoir	Offset of the data used for cross-correlation
	Time-sampling interval

Table 5.10: *Some of the main factors influencing the calculation of the vertical strain and 4D data time-shift.*

on the signal-to-noise ratio. To decrease the effect of noise on the measured time-shift, correlation windows are used. In addition, the cross-correlation between the reference and monitor surveys is applied using the stacked or partially stacked data. The use of these techniques decreases the accuracy, i.e., the measured time-shift at a specific interface will be influenced by the layers on both sides of the vertical/lateral boundary. To calibrate the precision in both of the results, in this section, the flow presented in Figure 5.25 is used.
The measured time-shift for the zero offset two-way vertical travel time is related to the relative time-lapse changes in the layer thickness and seismic velocity (Equation 2.28). From there the time-shift, can be split in two parts: 1) proportional to the changes in the seismic velocity but with opposite sign, and 2) proportional to the changes in the physical distance (vertical displacement). This approach (Figure 5.25) corresponds to the R coefficient assumption

$$\frac{\Delta t'}{t} = \frac{\Delta t}{t} - \frac{\Delta t''}{t} = R\frac{\Delta Z}{Z}. \tag{5.6}$$

The following approach is used to calculate the time-lapse changes in the seismic velocity:

[1] Δt is measured from the near offset (500 – 1300 m) time-lapse seismic data (source Shearwater). For inhomogeneous media, Δt can be expressed by the equation

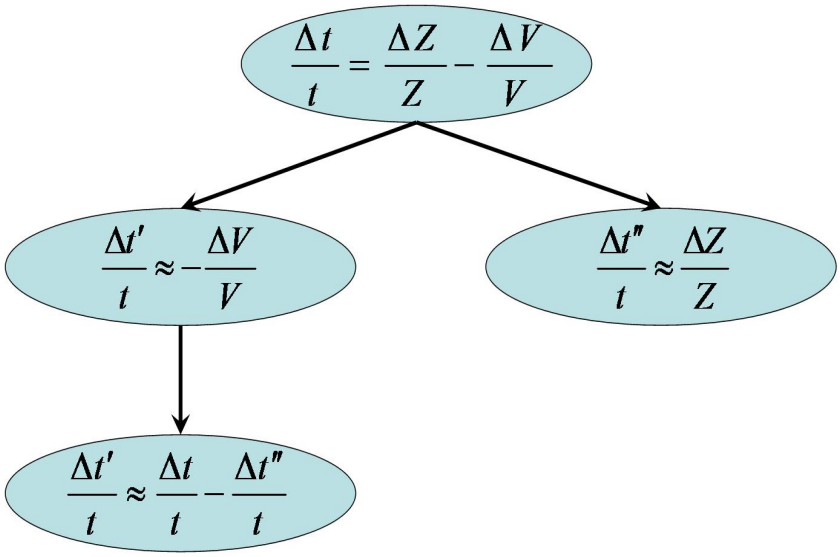

Figure 5.25: *Measured time-shift as a function of the seismic velocity, where the effect of changing the layer thickness is removed.*

$$\Delta t(z) \quad = \quad 2\int_0^z dz' \frac{\{1 + R(z')\}}{V(z')} e_{zz}(z'). \tag{5.7}$$

[2] $\Delta t''$ is calculated directly using the result of the geo-mechanical modelling (vertical displacement) using Equation 5.8,

$$\Delta t''(z) \quad = \quad 2\int_0^z dz' \frac{e_{zz}}{V(z')}(z'). \tag{5.8}$$

With Equation 5.7, the changes in the vertical strain are presented as changes in the two-way travel time.

[3] Further, $\Delta t''$ is processed using the same lateral and time windows used to measure Δt. Therefore the effect of strain is calibrated with the measured time-shift.

[4] The changes in the travel time $\Delta t'$ are calculated following the flow in Figure 5.26. Than the changes in the seismic velocity are calculated from $\Delta t'/t$.

$$\Delta t'(z) = -2 \int_0^z dz' \frac{\Delta V(z')}{V(z')^2}. \tag{5.9}$$

Using Equation 5.9, the time-lapse changes in the seismic velocity can be expressed:

$$\Delta V(z) = -\frac{V(z)^2}{2} \frac{\partial \Delta t'(z)}{\partial z}, \tag{5.10}$$

and the relative changes in the seismic velocity are

$$\frac{\Delta V(z)}{V(z)} = -\frac{V(z)}{2} \frac{\partial \Delta t'(z)}{\partial z}. \tag{5.11}$$

The calculated changes in the P-wave velocity are presented in Section 7.3.

5.3 Conclusions

The effect of pressure depletion on the time-lapse changes in vertical and horizontal stress, both inside the reservoir and in the surrounding media, was modeled using three different types of hydrocarbon reservoirs. It was demonstrated that the stress changes are strongly dependent on the geometry of the reservoir. In the particular case study of the Shearwater, because of the geometry of the gas reservoir, stress changes will be induced in the overburden over the entire reservoir. This stress distribution in the overburden explains the monitored changes in the seismic velocity in the previous Shearwater studies. The direct relation between changes in stress and time-lapse changes in the two-way travel time was explained. A method was proposed, how to use the results of the geo-mechanical modelling to remove from the measured time-shifts the effect of changes in the physical distance. Next the corrected time-shifts can be used directly to map the 4D changes in stress. This method is more direct and simplified compare to the R factor approach and allows the results of the geo-mechanical modelling to be scaled to the measured time-shifts from the seismic data.

In the first part, using a simple box model of the North Sea hydrocarbon reservoir, we demonstrated that the stress changes in the surrounding reservoir area are concentrated at the lateral edges of the reservoir (edge effect). The stress changes will also depend on the contrast of the elastic properties of the reservoir and surrounding media. The changes will increase with increasing contrast. With analytical modelling, it was demonstrated that changes in the acoustic velocity are linked to the stress changes and will be concentrated at the lateral boundaries of the reservoir.
With the second model the measured time-lapse changes in the seismic attribute (travel-time) were combined with the results of geo-mechanical modeling and the changes in the acoustic velocity were predicted. A method was proposed to decouple the time-shifts connected with stress changes from the time-shifts connected with compaction/elongation of the reservoir. The method was tested on a real North Sea gas reservoir in **Chapter 7**. It was also demonstrated that in a complex geometry, the stress changes are linked not only with the lateral edges of the reservoir, but also with the unconformities at the reservoir top and bottom. Each of these unconformities can be considered as a lateral boundary of the reservoir and cause an edge effect. Therefore, stress changes are detected not only at the lateral edges of the reservoir, but also above and below the entire reservoir body.

6

Forward modelling of the 4D seismic synthetic data: Monitoring the changes in the seismic travel time

In this chapter the calculated seismic velocities and density (**Chapter 5**) are used to create synthetic, seismic, time-lapse data. These data are further used in the time-lapse analysis, to quantify the changes in the seismic attributes as a result of hydrocarbon production. The physical principle of the 4D seismic method is illustrated in Figure 6.1 (Calvert [2005]). The seismic velocities and densities, labeled with V and ρ, are changing as a result of hydrocarbon production. Also, the variations in the seismic properties over time influences 4D effects in the seismic attributes, i.e. travel time (δt) and amplitude (δA). The time-lapse changes in the two-way travel time is presented in Section 6.1. Section 6.1 comprises the time shift in the reservoir as well in the overburden layers as a result of pressure depletion. In Section 6.2 the results of the geo-mechanical modelling are used, based on the North Sea gas reser-

voir (i.e. Section 5.2.1) to simulate time-lapse changes in the reservoir as well in the overburden. The results and the observations of the 4D seismic synthetic modelling are summarized and compared with the geo-mechanical effects in Section 6.3 of this chapter.

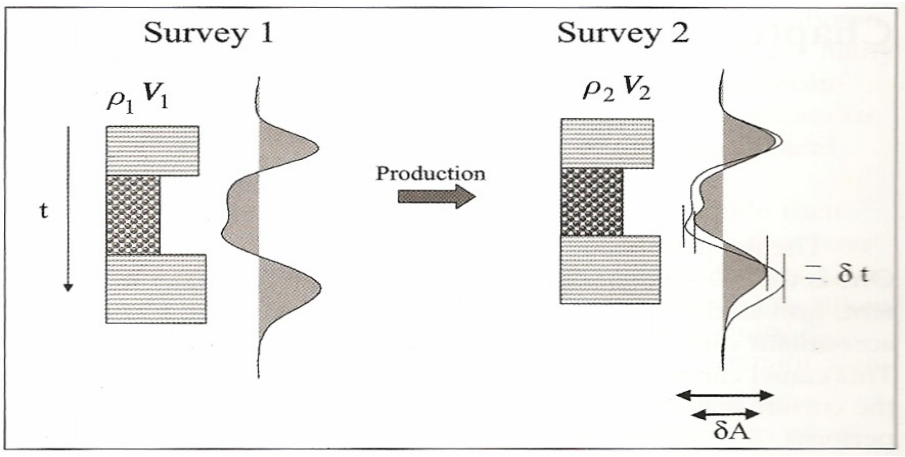

Figure 6.1: *The geophysics of time-lapse monitoring, Calvert [2005]; In the figure are illustrated the impedance model and the time-lapse seismic trace.*

6.1 Time - Shift

As mentioned by Calvert [2005], the time-shift measurements can be generalized to measure the spectral difference, Figure 6.2. First, the spectral ratio between monitoring and base line data is measured over an unchanged gate to determine the wavelet spectral differences. Next, by measuring the spectral ratio at the interface, where time-lapse changes as a result of hydrocarbon production occurred, and eliminating the effect of the wavelet spectral difference, the spectral ratio change resulting from the transmission through the reservoir and overburden layers is estimated. In Figure 6.3 the measured time-shift for the pre-stack data is illustrated. The correlated and measured

time-shift for the interface above the reservoir, i.e. between receivers r_{a1} and r_{a2}, can be expressed with the equation

$$\Delta T_{ai} \quad = \quad \Delta t_{W2-W1}, \tag{6.1}$$

where the ai is the gate between r_{a1} and r_{a2}.

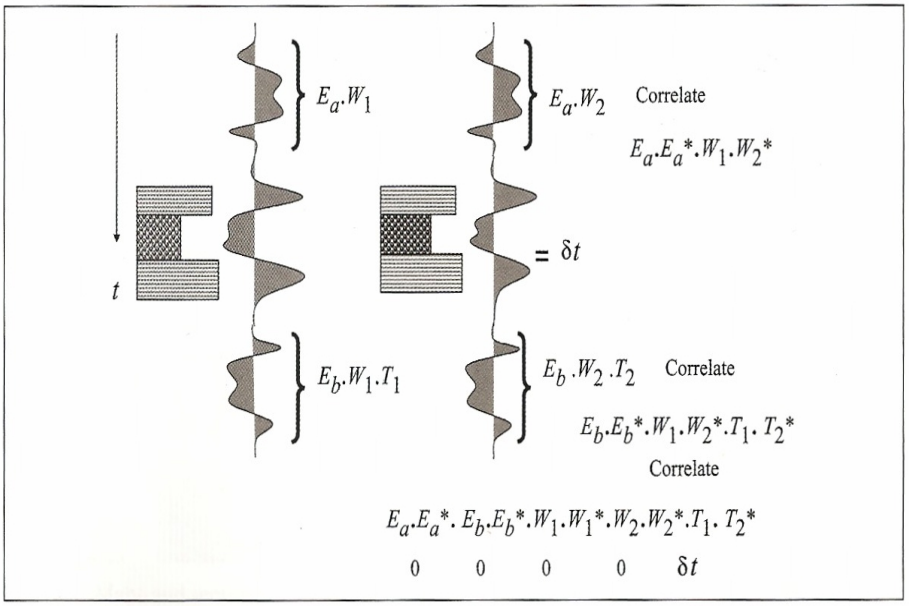

Figure 6.2: *Time-shift measurements over defined interval according to Calvert [2005]. E_a and E_b refer to the Earth response above and below the target interval. The wavelets used in the reference and monitor surveys are labeled respectively with W_1 and W_2. T is denoted to the transmission response, where δt represents the difference in the two way travel time between survey 1 and 2.*

For the part below the reservoir, receiver gate bi, the measured time shift is

$$\Delta T_{bi} \quad = \quad \Delta t_{W_2-W_1} + \delta t_i \cos\alpha_i + \delta t_j \cos\alpha_j, \tag{6.2}$$

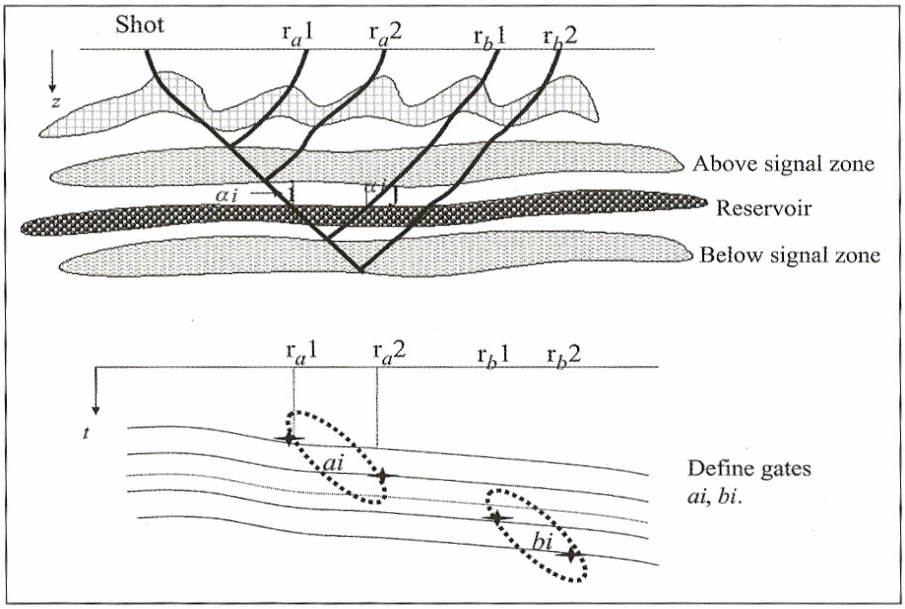

Figure 6.3: *Time-shift measured at the pre-stack data according to Calvert [2005]. α_i and α_j denote the incidence angle and the angle of reflection at the top of the reservoir.*

then the changes in the travel time inside the reservoir as result of production will be

$$\Delta T_{bi} - \Delta T_{ai} \quad = \quad \delta t_i \cos \alpha_i + \delta t_j \cos \alpha_j. \tag{6.3}$$

Time-shifts measured from the pre-stack 4D data can be further used to obtain quantitative results for the changes in the rock properties at the reservoir level. Several authors demonstrated how to measure the 4D changes in the two-way travel time from the time-lapse seismic data:

- Hatchell et al. [2003] monitored the 4D changes in the travel time for depleting gas fields. To measure the time-shifts they used the minimized objective function $\sum[M(t) - B(t)]^2$, where $M(t)$ and $B(t)$ are denoted to the monitor and the reference data.

- Mesdag et al. [2007] presented a full band-width simultaneous inversion performed on one base and two monitor surveys over the "Girassol" field, offshore Angola. The changes in the two way travel time between the base and the monitor survey are calculated by alignment of the near substack monitor data to the near substack base data.

In this thesis the time-shifts are measured, using the Volume Alignment tool implemented in the Jason Geoscience Workbench (JGW). This data alignment approach is similar to the one presented by Mesdag et al. [2007], and is illustrated in Figure 6.4. The time-shift are measured using the data alignment between the base and monitor near offset data (small angle of incidence). The small angle of incidence and almost vertical ray-paths, reduce the effect of lateral time-lapse changes in the seismic velocity. Røste et al. [2006] introduced α parameter to calculate the effect of AVO on the measured time-shift.
The time-shift is the one with the best correlation between the aligned data occurred.

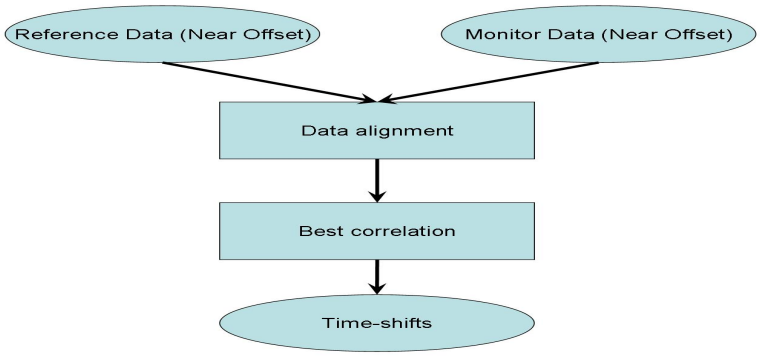

Figure 6.4: *The work flow used in this thesis to measure the 4D changes in the two-way travel time.*

6.2 Time - shift occurrence by using a simple 4D model of the North Sea reservoir

The time-shift is measured from the synthetic time-lapse data. The following steps are used in order to create the 4D data and to obtain the difference in the travel time.

[1] An acoustic finite difference code ("fdacmod"), product of the DELPHI consortium, is used to produce synthetic 4D seismic data. This software simulates the acoustic pressure response of a 2D gridded subsurface velocity and density model. The velocity and density models are discussed in Section 5.2.1. Time-lapse changes in the layer thickness, as an effect of pressure depletion, are not simulated. The reason for this is, that the relative small changes in the vertical displacement (in the order of [cm]) requires a quite dense finite different mesh and therefore it can be neglected.

[2] Further, pre-stack depth migration (PSDM) is applied on the reference and monitor synthetic data. The migration software is using one-way wavefield extrapolation operators in order to estimate the proper depth and amplitude of the reflectors (Wapenaar and Berkhout [1989]). For the migration of the monitor data, the reference velocity is used.

[3] Time-shifts are measured, where the monitor data are aligned to the reference ones. The correlation window size, used for the data alignment, must be considered, so that on the one hand it will not be influenced by noise (too small windows), and on the other hand it will not interfere with the time-shifts occurring at the neighboring interfaces (too large windows).

To control the effect of the migration procedure on the measured time-shifts, pre-stack zero-offset data are used. Next, these results are compared with the time-shifts measured from the migrated monitor and reference data.

Zero-offset non migrated data Zero-offset traces from the modeled time-lapse synthetic data are selected and sorted in the reference and monitor zero-offset gathers.

[1] A test model is developed, in order to test the resolution of the software (JGW), used to measure the time-shifts (Appendix C, Section C.1.1, Figure C.1). In this model the receivers are situated at the interfaces, therefore the interest is concentrated only on the first arrivals, and the effect of the complex trace is reduced. The measured time-shift is multiplied with a factor 2 in order to match the reflection results and plotted together with the expected time-shift values (Appendix C, Figure C.2 and C.3). We can conclude that the measured time-shifts correspond accurately to the expected ones. The vertical resolution obtained to detect the changes in the two-way travel-time is as high as half of a millisecond.

[2] Next the time-shifts are measured using the pre-migrated zero-offset reference and monitor gathers. For simplicity the reference and monitor trace going through the center of the reservoir is selected. The selected reference and monitor traces are repeated at all of the reservoir lateral positions. In addition to the JGW tool, two alternative algorithms are used for comparison to estimate the changes in the travel-time. The first one is suggested by Hatchell et al. [2003], whereas in the second one we measured the spectral ratio between the monitor and the reference data. JGW and Hatchell et al. [2003] are showing good agreement with the expected time-shifts, whereas the resolution of the spectral ratio method is poor (Figure C.4 - C.8).

Zero-offset migrated data The results of the PSDM are translated back to the time domain, using the reference interval velocity, where vertical ray-paths without reverberations are assumed. Further, zero-offset gathers are created and the time-shift is measured from the seismic data. The measured time-shift for the zero-offset data is illustrated in Figure 6.5. The next step is to estimate the misfit between the analytically calculated expected time shift and the measured time shift. According to the results as illustrated in Figure 6.6 – 6.10, the errors in the estimation of the cumulative time-shifts are minimal for the central part of the reservoir. The misfit at the top of the interfaces is relative small at the central part of the reservoirs and increases towards the reservoir edges (Table 6.1). There are two reasons for the edge effect: 1) one is the migration method, where a spatial convolution filter

is used, and each output point is depends of the neighbouring input points (Thorbecke et al. [2004]), 2) the large trace-sampling interval (2 [ms]) is adding numerical noise at the edges of the reservoir. Using the estimated time-shift and Equation 5.9 it is possible to estimate directly the changes in the average and interval acoustic velocities. The errors in the estimation are comparable with the values presented in Figures 6.6 - 6.10.

Top of the Interface	Vertical Correlation Window [ms]		
	60	80	120
Chalk - Hod	$2 \sim 22\%$	$2 \sim 22\%$	$2 \sim 22\%$
Chalk and Marl - Creta	$7 \sim 18\%$	$7 \sim 18\%$	$7 \sim 18\%$
Organic Claystone and Marl	$1 \sim 23\%$	$1 \sim 23\%$	$1 \sim 23\%$
Reservoir Top	$4 \sim 27\%$	$9 \sim 30\%$	$11 \sim 30\%$
Reservoir Bottom	$8 \sim 16\%$	$8 \sim 16\%$	$8 \sim 16\%$

Table 6.1: *Difference between the time-shifts measured from the zero-offset data, and analytically calculated time-shifts.*

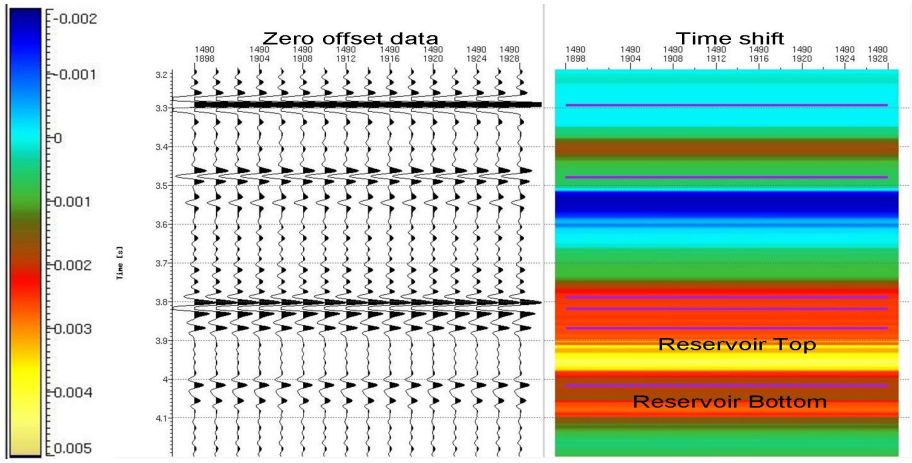

Figure 6.5: *Measured time shift for the zero-offset data.*

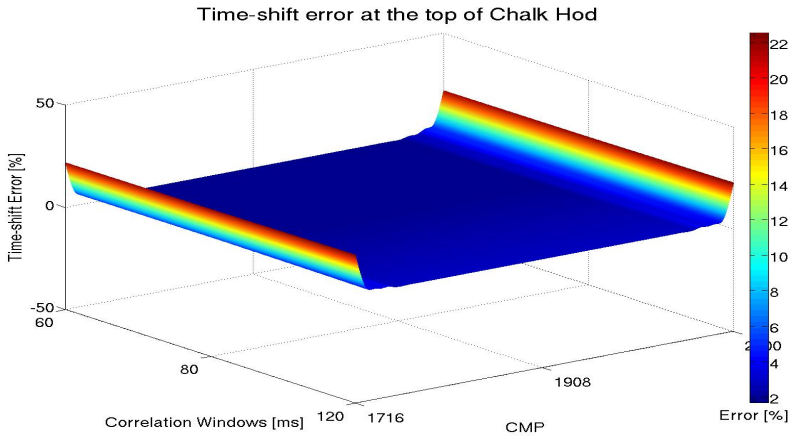

Figure 6.6: *Misfit between the measured and expected time-shifts in [%], measured at the top of the Chalk-Hod interval. The values in the central part of the reservoir are almost constant and around 2 [%].*

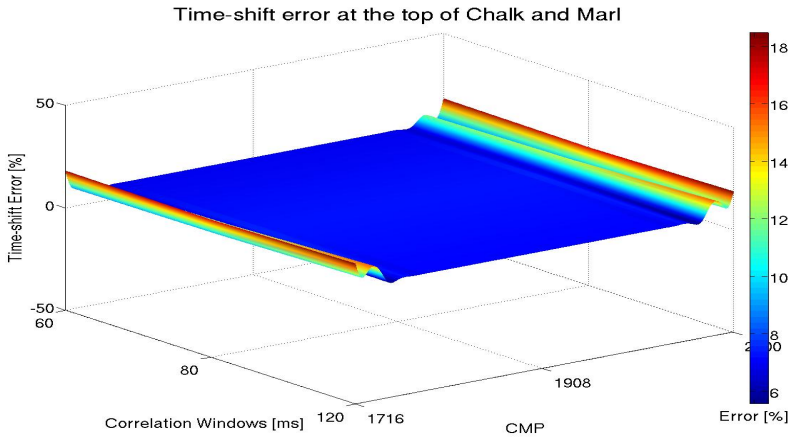

Figure 6.7: *Misfit between the measured and expected time-shifts in [%], measured at the top of the Chalk and Marl interval. The values in the central part of the reservoir are almost constant and around 7 [%].*

Migrated data - all offsets The time-shifts variations with the offset depend on the ray-path (Figure 6.3). 1D ray-tracing software, implemented in the JGW, is used to calculate the incident angles as a function of source-receiver offsets, and the results are plotted in Figure 6.11. The next step is to investigate the difference between the time-shifts, estimated from the different offsets. As illustrated in Figure 6.5 the error in the time-shift estimation will increase with the offset. The time shift as a function of offset is illustrated in Figures 6.12 and 6.13. As expected, the time shift increases with the offset because of the different ray-paths.

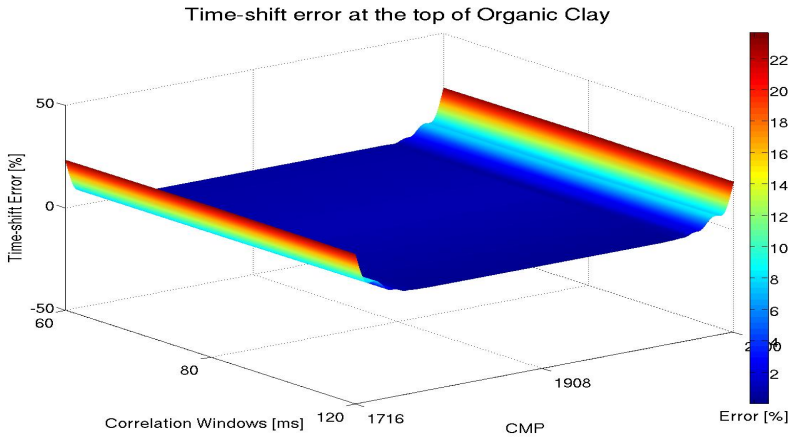

Figure 6.8: *Misfit between the measured and expected time-shifts in [%], measured at the top of the Organic Clay interval. The values in the central part of the reservoir are almost constant and around 1 [%].*

Time-shifts measured using the partial stacks To reduce the effect of noise and improve the overall data quality, the traces from the different processed seismic records were stacked together. The method is called stacking and the new record is called a stack. Stacking will reduce the changes of the seismic attributes with offset. If only part of the traces, which belong to specific offset ranges, are stacked together, then it is possible on the one hand to improve the seismic quality, and on the other hand to preserve the offset effect. This partial adding of seismic records is called partial stack. In this paragraph the time-shift is measured using partial stacks (Table 6.10). The partial stacks are separated in two groups:

[1] "small" partial stacks, where the fold consists of 4 to 5 offsets. The angle of incidence shows small variations, i.e. between 2 and 3 degrees, inside the fold, therefore it can be assumed that the AVO effect inside the single fold will be negligible. The "small" partial stacks are plotted in Figures 6.14 and 6.15.

[2] "large" partial stacks, where the fold consists of 9 offsets. The varia-

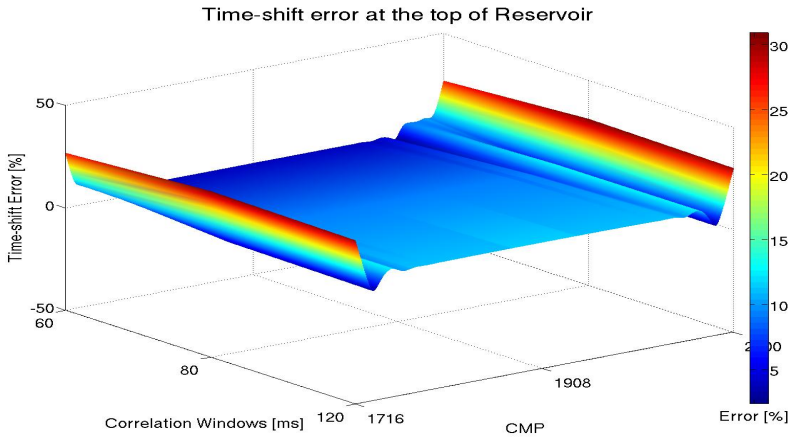

Figure 6.9: *Misfit between the measured and expected time-shifts in [%], measured at the top of the Reservoir. The values in the central part of the reservoir are between 4 and 11 [%].*

tion of the incidence angle inside the fold is around 5 degrees. These stacks can be used as representative for the near, mid, and far offsets. The large partial stacks are plotted in Figures 6.16 and 6.17.

The time-shifts measured from the partial stacks are close to the time-shifts measured from the offset gather. The near partial stack information can be further used to obtain the information about the changes in the layer thickness and in the acoustic velocity. The partial stacking will smear some local outliers appearing as a result of numerical noise and software limitations. In the real-data examples the partial stacking will hide the time-shifts as a result of low signal-to-noise ratio. The experiments in this section are showing that for the specific case study it is possible to use the time-shifts, measured from the near partial stacks instead of the zero-offset stacks in order to predict accurately the time-lapse changes in the seismic velocity.

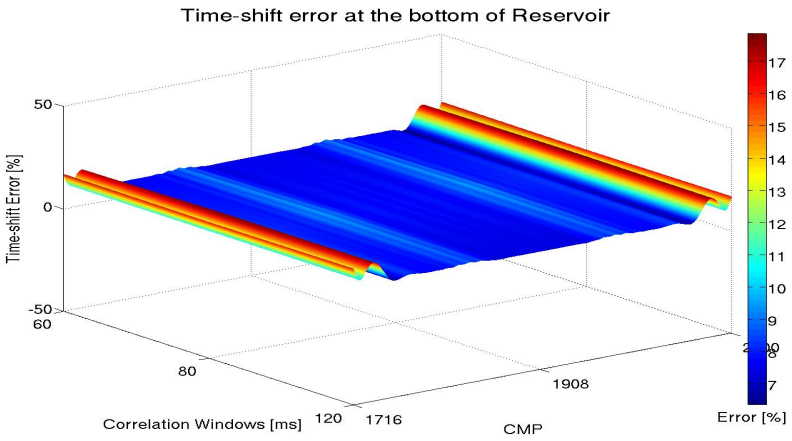

Figure 6.10: *Misfit between the measured and expected time-shifts in [%], measured at the bottom of the Reservoir. The values in the central part of the reservoir are almost constant and around 8 [%].*

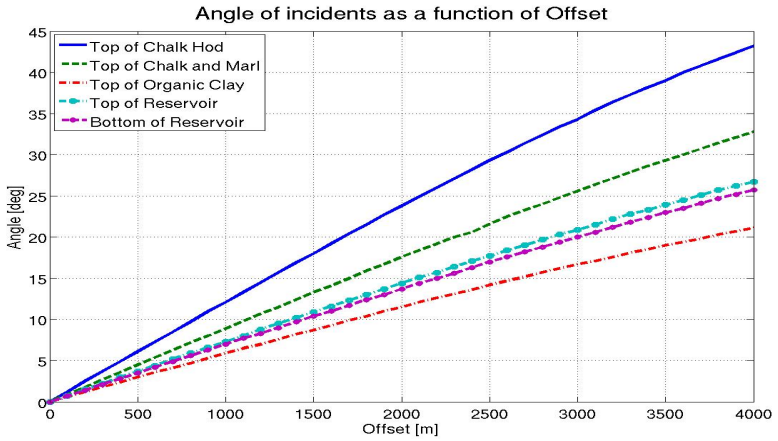

Figure 6.11: *Changes in the incidence angle as a function of offset.*

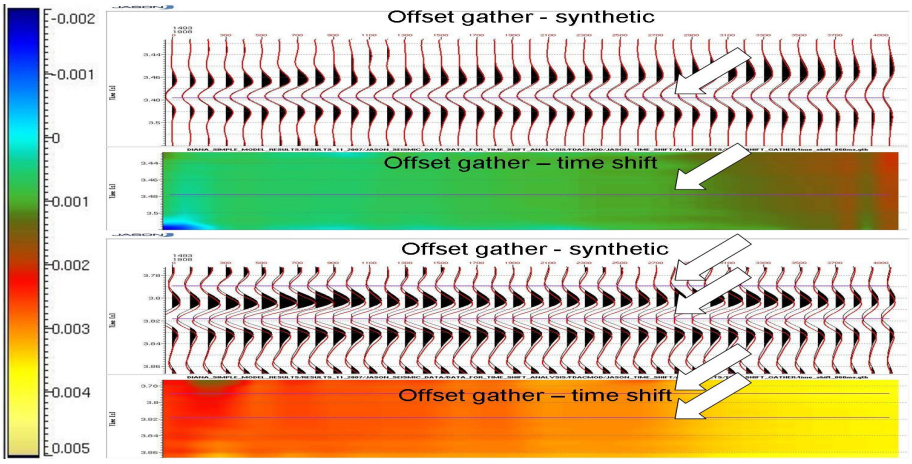

Figure 6.12: *Time-shifts (in seconds) as a function of offset, for the Chalk Tor and Chalk Marl and Organic Clay interval. The offset range is from 0 to 4000 m with a interval of 100 m between the different offsets.*

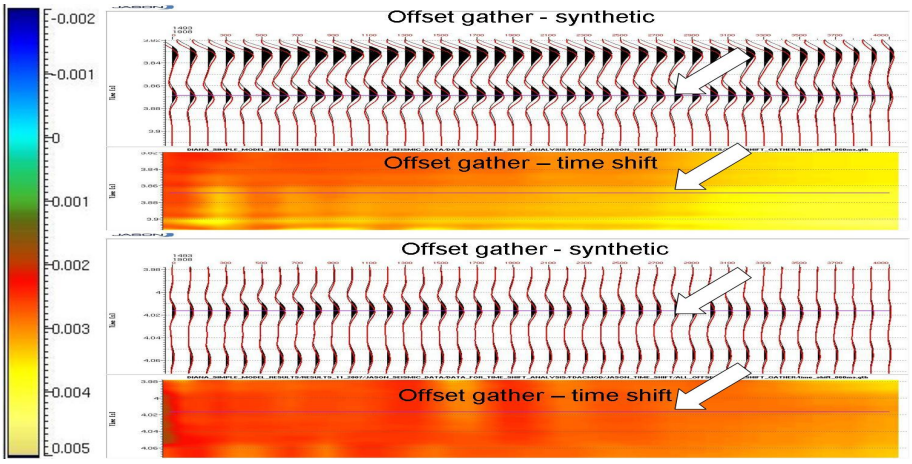

Figure 6.13: *Time-shifts (in seconds) as a function of offset, for the Top and Bottom of the Reservoir. The offset range is from 0 to 4000 m with a interval of 100 m between the different offsets.*

Partial Stacks - Small		
Source-Receiver Offset [m]	Incidence angle at the top [deg]	Incidence angle at the bottom [deg]
0 - 400	0.0 - 3.0	0.0 - 2.8
500 - 900	3.7-6.6	3.5-6.3
1000 - 1300	7.3-9.5	7.0-9.0
1400 - 1800	10.2-13.0	9.7-12.4
1900 - 2200	13.7-15.7	13.0-15.0
2300 - 2700	16.4-19.0	15.6-18.2
2800 - 3100	19.7-21.5	18.8-20.6
3200 - 3600	22.2-24.5	21.2-23.5
3700 - 4000	25.1-26.7	24.1-25.7
Partial Stacks - Large		
500 - 1300	3.7-9.5	3.5-9.0
1400 - 2200	10.2-15.7	9.7-15.0
2300 - 3100	16.4-21.5	15.6-20.6
3200 - 4000	22.2-26.7	21.2-25.7

Table 6.2: *Range of the chosen partial stacks together with the angles of incidence measured at the top and bottom of the reservoir.*

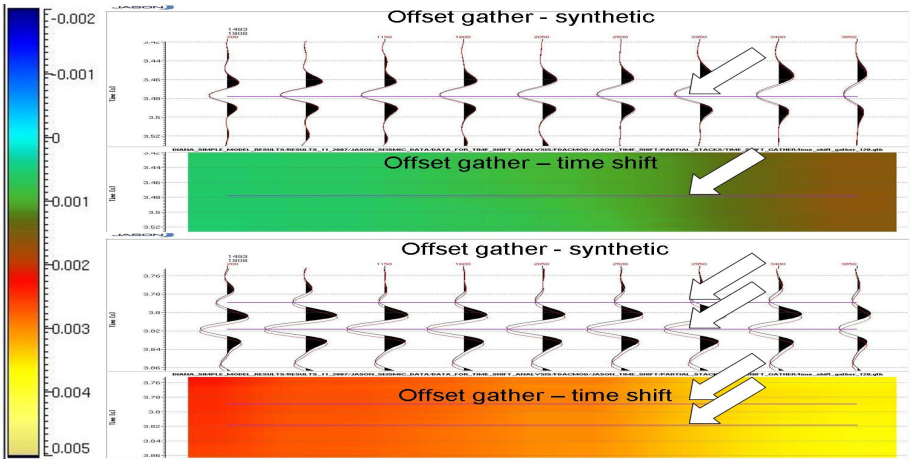

Figure 6.14: *Time-shifts (in seconds) as a function of offset, for the Chalk Tor and Chalk Marl and Organic Clay interval. Each trace represents a "small" partial stack. The partial stack ranges are: 0-400, 500-900, 1000-1300, 1400-1800, 1900-2200, 2300-2700, 2800-3100, 3200-3600, and 3700-4000 m.*

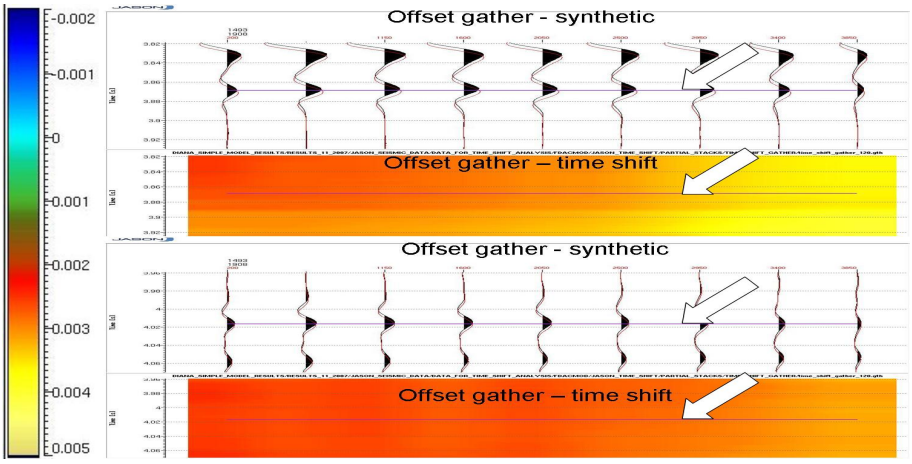

Figure 6.15: *Time-shifts (in seconds) as a function of offset, for the Top and Bottom of the Reservoir. Each trace represents a "small" partial stack. The partial stack ranges are: 0-400, 500-900, 1000-1300, 1400-1800, 1900-2200, 2300-2700, 2800-3100, 3200-3600, and 3700-4000 m.*

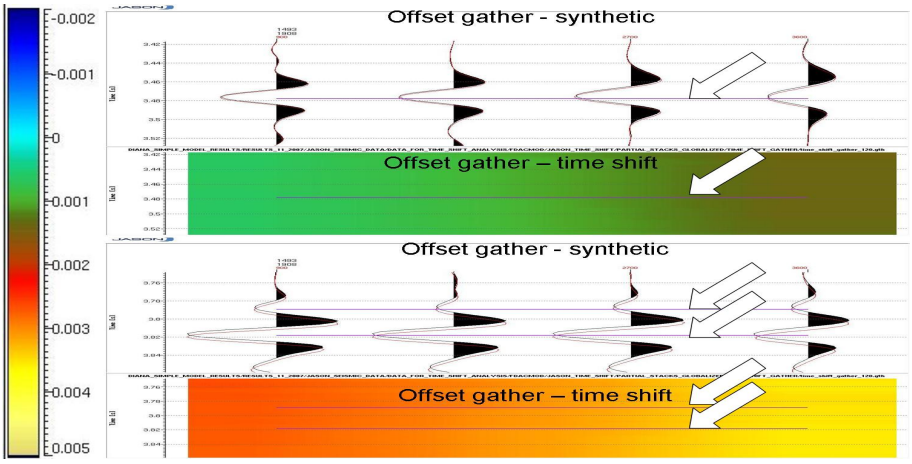

Figure 6.16: *Time-shifts (in seconds) as a function of offset, for the Chalk Tor and Chalk Marl and Organic Clay interval. Each trace represents a "large" partial stack. The partial stack ranges are: 500-1300, 1400-2200, 2300-3100, and 3200-4000 m.*

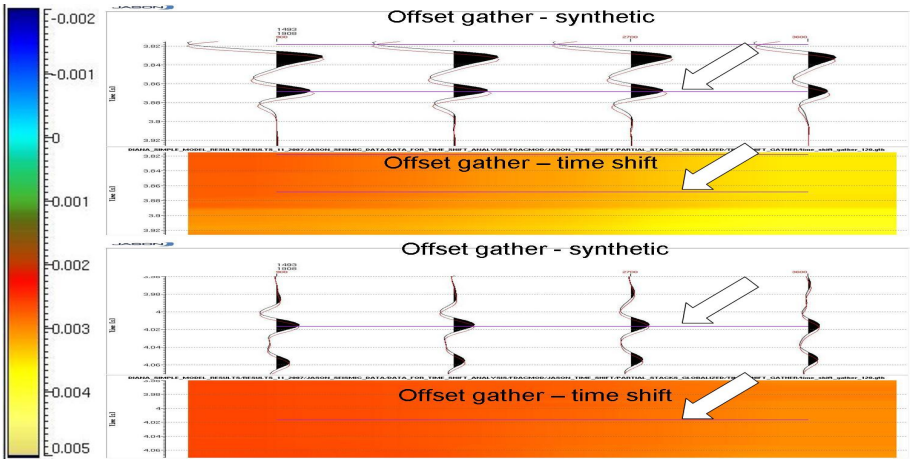

Figure 6.17: *Time-shifts (in seconds) as a function of offset, for the Top and Bottom of the Reservoir. Each trace represents a "large" partial stack. The partial stack ranges are: 500-1300, 1400-2200, 2300-3100, and 3200-4000 m.*

6.3 Conclusions

In this chapter, the time-lapse changes in the two-way travel time were used as a feasibility study of the real North Sea gas reservoir. The study was done on a simplified box model using synthetic modelling. The AVO effect on the measured time-shifts was monitored. It was demonstrated that in this particular case study the time-shifts, measured using near offset time-lapse data, can be considered as vertical time-shifts. Also, the time-shifts can be used to calculate the 4D changes in the acoustic velocity.

7

Case study of a North Sea gas reservoir

This chapter comprises a 4D time-lapse study of a North Sea gas reservoir. The reservoir is illustrated in Figure B.7 (**Appendix B**). The work flow is given schematically in Figure 7.1. Time-shifts, due to both stress induced velocity changes and subsidence displacements, are measured using the full stack and partial stack data. In combination with the changes in displacement predicted by geo-mechanical modelling, the changes in the acoustic velocity at a selected 2D line have been determined and quantified. For this case study the effect of subsidence displacements on the measured time-shifts appear to be negligible. Taking this into account, the time shifts have been used directly to calculate changes in the seismic velocity. In combination with the stress-velocity relation these results have been used to calculate the stress changes both at the reservoir level and in the overburden for the whole 3D area.

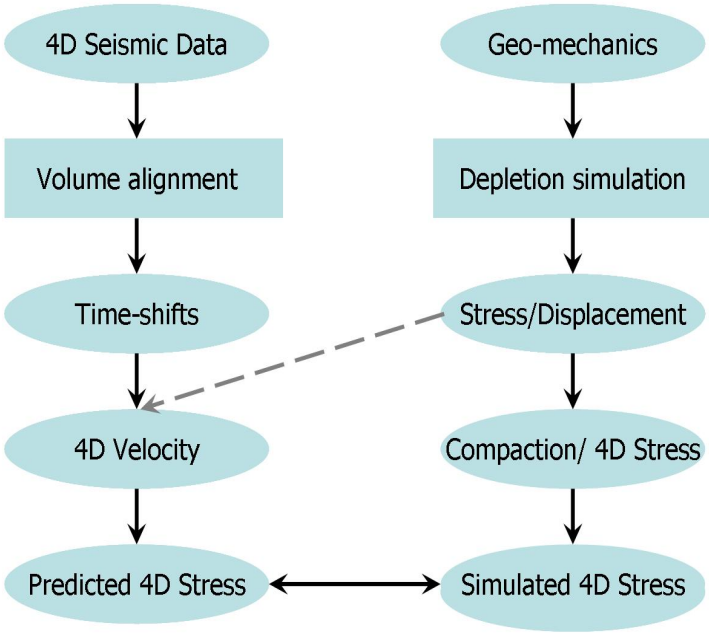

Figure 7.1: *Work flow used in this chapter. The calculated stress changes are compared with those simulated with the geo-mechanical modeling.*

7.1 Time - Shifts observation from the real data

The time-shifts are measured from the time-lapse data, representing a production period between the years 2002 and 2004. A pressure drop of 30 MPa was expected as a result of production which causes compaction at the reservoir level and overburden elongation. The compaction/elongation will affect the phase of the 4D data and as a result time-shift changes are expected. The provided data contain CMP gathers with an offset range of 500 to 4700 m, with steps of 100 m between the offsets. All the data are processed using the Kirchoff depth migration algorithm. After migration, the seismic data are

transformed back to the time domain using the migration velocity. In order to reduce the noise level the data are assembled in full and partial stacks. Partial stacks are calculated using "small" and "large" offsets stacks as in the synthetics time-lapse study from **Chapter 6**, see Table 7.1.

Partial Stacks - Small		
Source-Receiver Offset [m]	Incidence angle at the top [degr]	Incidence angle at the bottom [degr]
500 - 900	3.7-6.6	3.5-6.3
1000 - 1300	7.3-9.5	7.0-9.0
1400 - 1800	10.2-13.0	9.7-12.4
1900 - 2200	13.7-15.7	13.0-15.0
2300 - 2700	16.4-19.0	15.6-18.2
2800 - 3100	19.7-21.5	18.8-20.6
3200 - 3600	22.2-24.5	21.2-23.5
3700 - 4000	25.1-26.7	24.1-25.7
4100 - 4700	26.8-29.8	26.0-28.9
Partial Stacks - Large		
500 - 1300	3.7-9.5	3.5-9.0
1400 - 2200	10.2-15.7	9.7-15.0
2300 - 3100	16.4-21.5	15.6-20.6
3200 - 4000	22.2-26.7	21.2-25.7

Table 7.1: *Range of the chosen partial stacks together with the angles of incidence calculated at the top and bottom of the reservoir.*

The measured time-shifts are QC'ed and the near "0500-1300" partial stack is selected to determine the changes in the seismic velocity. This follows from chapter **Chapter 6** where synthetic modelling demonstrated that this partial stack can accurately represent the changes in the acoustic velocity. The effects of ray-path bending and processing (PSDM) are negligible at this offset range.

■ 7.1.1 Observing the time - shift of full stack data

The full stack is generated using the whole offset range, i.e. from 500 to 4700 [m]. Time-shifts are extracted as illustrated in Figure 7.2.

- As a QC the reference and monitor data are checked for inconsistency, as unrealistically high misalignment, different signatures of the mon-

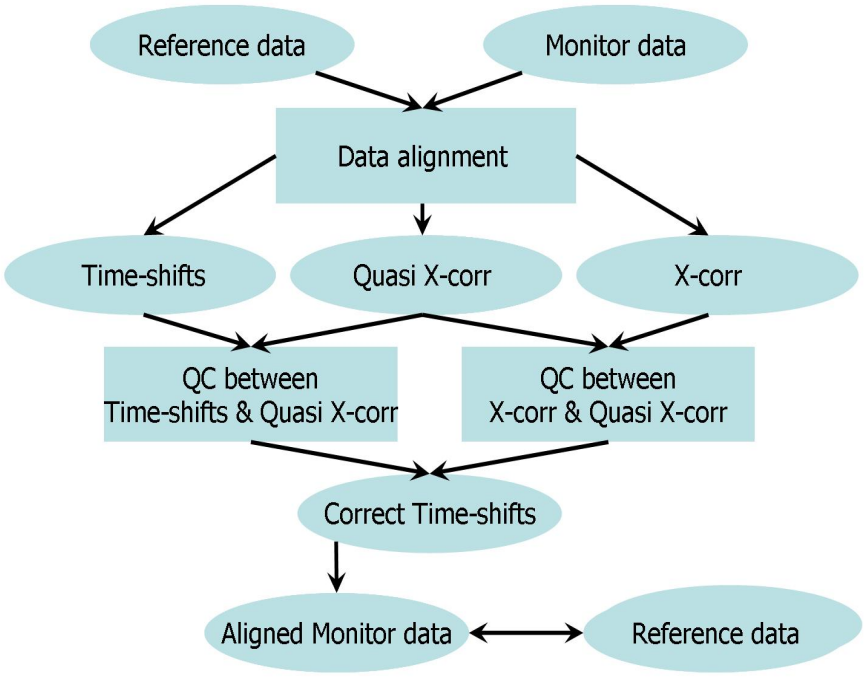

Figure 7.2: *Work flow used to measure the time-shifts. At the end the measured time-shifts were applied to the monitor data and the aligned data are compared with the reference data.*

itor and reference wavelet, missing data. A cross-section of the time-lapse data is plotted in Figure 7.3. In addition the amplitude spectra of both data sets are compared in Figure 7.4. From the feasibility study it can be concluded that the 4D data generally have good quality similar wavelet shapes and do not suffer from severe data misalignment, except the larger misalignment at the bottom of the reservoir between CMP's 1784 and 1862, Figure 7.3. The amplitude spectra of the time-lapse data are identical.

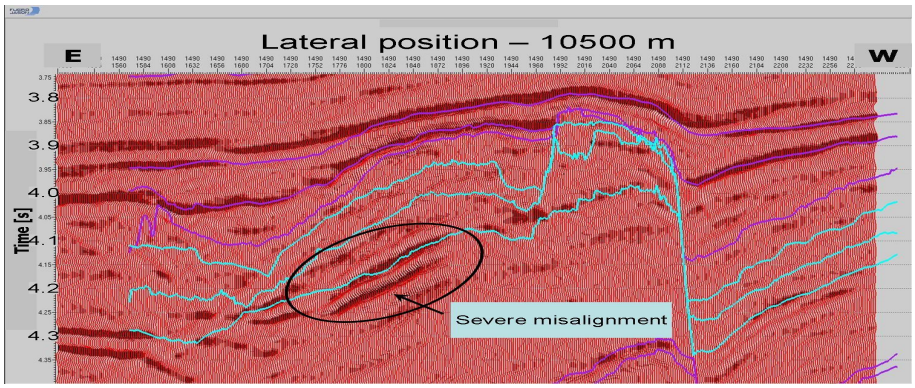

Figure 7.3: *Cross-section of the time-lapse seismic data. Black wiggles - data measured in 2002; Red wiggles - 2005 data. The original time-horizons (source Shearwater) are plotted on the data. The top, middle, and bottom of the reservoir are plotted in cyan color.*

- The reference and monitor data are cross-correlated. Next the time-shift is estimated at the point of the highest correlation. The cross-correlation is performed using the "Optimize T/D Volume Alignment" tool, part of the JGW. The settings of the performed volume alignment are given in Table 7.2 and Table 7.3. In the cross-correlation procedure the selected volume of the reference data is correlated with the selected volume of the monitor data. This is done for each time-sample point, where the sample point is the center of the selected volume. This way the changes in the travel time are estimated at each time-sample of

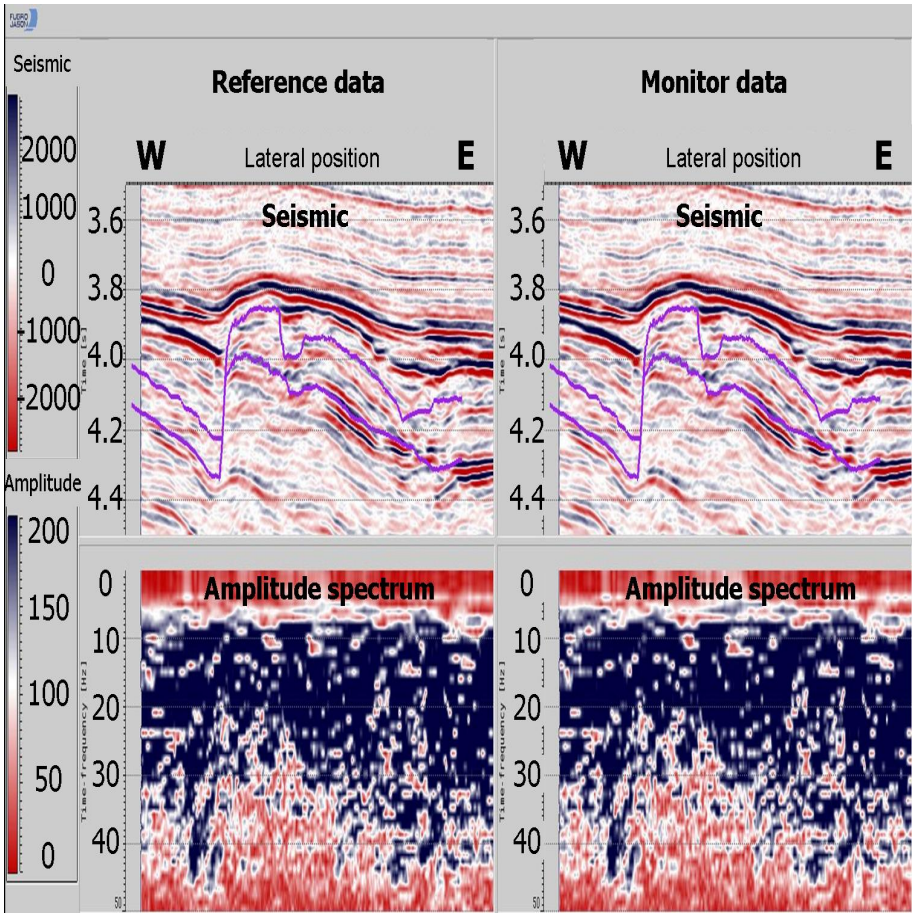

Figure 7.4: *Seismic and Amplitude spectra of the reference and monitor data. In the upper part of the figure are plotted the reference and monitor seismic at the reservoir level. The top and the bottom of the reservoir are delineated with the interpreted time-horizons (in pink color). The vertical axis present the two-way travel time in seconds. In the lower part of the figure is plotted the amplitude spectrum of the plotted above seismic. The vertical axis is the time-frequency in Hz.*

the data. The selected volume depends on the initial settings, and is given as an $Inline$, $Crossline$, and $Vertical\ sized$ window cube. The maximum allowed time-shift is given as a $Shift\ range$ parameter to avoid the loopshipping of the autocorrelation. The $Stretch/squeeze$ parameter represents the maximal stretch or squeeze factor applied on the data in order to find the highest correlation value. The minimum allowed Quasi-correlation (Equation 7.2) is set up, below this point no time-shift will be computed. The last parameter is the band-pass filter which is applied to the data before the alignment. The results of the volume alignment are in the form of time-shift, correlation and Quasi-correlation.

$Measurement$	$3D\ volume\ settings$		
$Number$	$Inline$	$Crossline$	$Vertical\ size$
1 – no filter	3	3	120 [ms]
2 – 6-4-30-10	3	3	120 [ms]
3 – 6-4-20-10	3	3	120 [ms]

Table 7.2: *Settings applied in the time-shift measurements. The measurements are done for each of the CDP locations and time-sample, using cross-correlation window defined by the $Inline$, $Crossline$, and $Verticalsize$.*

$Optimization\ settings$			$Filter$
$Shift\ range$	$Stretch/squeeze$	$Quasi-correlation$	$Filter\ settings$
12 [ms]	2	-1	none
12 [ms]	2	-1	6-4-30-10
12 [ms]	2	-1	6-4-20-10

Table 7.3: *Settings applied by the time-shift measurements. The numbers in the $Filtersettings$ represents the applied bandpass filter, i.e. 6-4-30-10 means bandpass filter from 6 to 30 Hz with overlaps of 4 and 10 Hz respectively.*

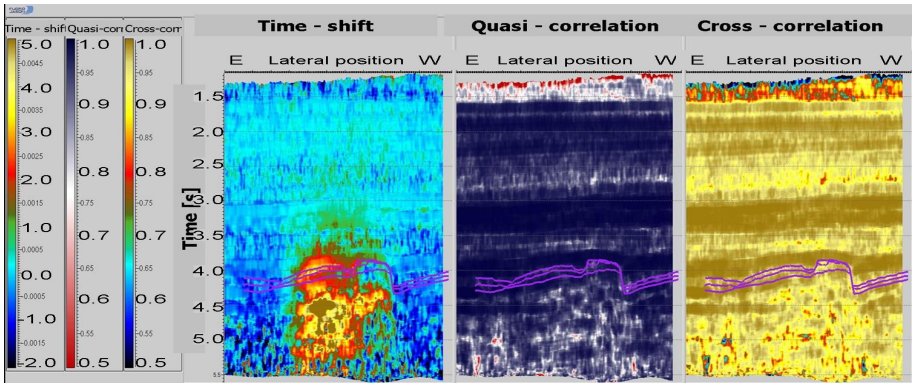

Figure 7.5: *Time-shift ms, Quasi-correlation and Cross-correlation. The result is generated with the settings of measurement 1 from Table 7.2.*

- Cross-plots between the time-shift, correlation and Quasi-correlation are used in order to QC the results and to remove the unreliable and irrelevant results.

  The first QC cross-plot is between the measured time-shift and Quasi cross-correlation, Figure 7.6. From the cross-plot the reliable results (in the black polygon) are selected. All the time-shifts, corresponding to a quasi-correlation less then 0.7 are not be taken into account. In addition some scatter values showing too low and too high time-shifts are also not included in the polygon. The second cross-plot is between the quasi-correlation and the correlation values. By definition the absolute quasi-correlation is always lower or equal to the absolutes value cross-correlation. All the absolute values of the quasi-correlation which are larger than the cross-correlation will be removed using the cross-plot technique. Quasi-correlation which is too low compared to the cross-correlation indicates that by estimating the optimal time-shift the amplitude of the monitor data sets needs to be scaled with an unrealistic large coefficient in order to match the reference data. This is not expected and such values will be disregarded. In Figure 7.7 the cross-plot between the cross-correlation and the quasi-correlation is shown.

The cross-correlation is calculated with the formula:

$$\begin{aligned} c(\bar{a},\bar{b}) &= \frac{(\bar{a},\bar{b})}{\|\bar{a}\| * \|\bar{b}\|}, \\ (a,b) &= \sum_{i=1}^{n} a_i b_i, \\ \|a\| &= \sqrt{a_1^2 + ... + a_n^2}, \\ \bar{a} &= (a_1 - mean(a), ..., a_n - mean(a)). \end{aligned} \tag{7.1}$$

The quasi cross-correlation is calculated with the formula:

$$\sigma(\bar{a},\bar{b}) = \frac{2(\bar{a},\bar{b})}{\|\bar{a}\|^2 + \|\bar{b}\|^2}. \tag{7.2}$$

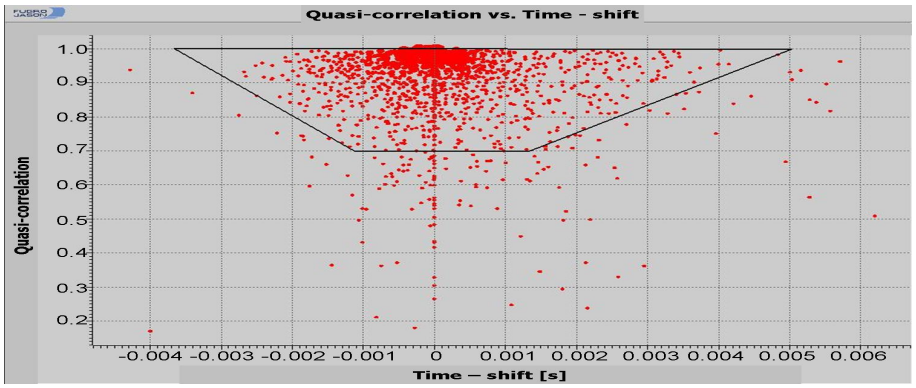

Figure 7.6: *Cross-plot between the time-shift and the Quasi-correlation. The result is generated with measurement 1 from Table 7.3.*

- The unreliable time-shifts are removed and the time-shifts are smoothed using a lateral filter consisting of 11x11 in-lines and cross-lines, and

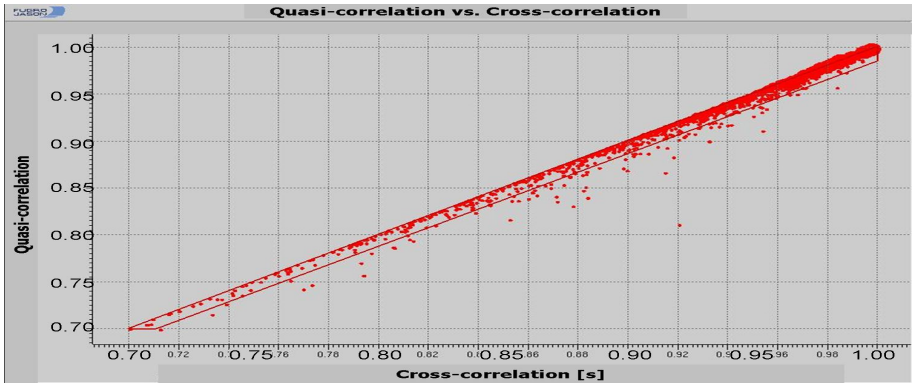

Figure 7.7: *Cross-plot between the cross-correlation and the Quasi-correlation. The result is generated with measurement 1 from Table 7.3.*

a vertical time-window of 10 ms. The smoothing filter is applied together with an interpolation method to reduce noise and to interpolate data gaps. In Figure 7.8, the measured time-shifts, time-shifts with removed unreliable parts, and the smoothed corrected time-shifts are shown. A cross-plot between the applied and measured time-shift is created to review the performance, see Figure 7.9.

- The corrected time-shift is applied to the monitor data and the monitor data are compared with the reference data in Figure 7.10. This demonstrates that the monitor data are accurately aligned to the reference and that the measured and corrected time-shifts are consistent. The amplitude spectrum of the data is presented in Figure 7.11.

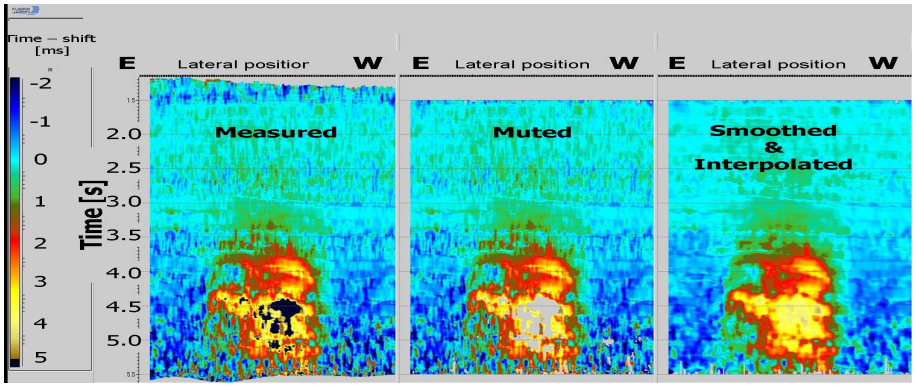

Figure 7.8: *Left – measured time-shifts; Middle – time-shifts with muted unreliable values; Right – the smoothed corrected time-shifts.*

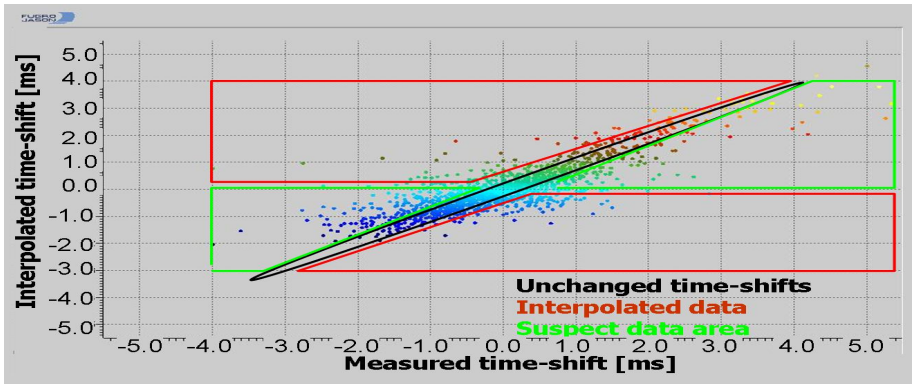

Figure 7.9: *Cross-plot between the measured and smoothed data. In the black polygon are enclosed the non muted time-shifts; the time-shifts enclosed in the red polygons represents the interpolated time-shifts after the muting; the time-shifts in the green polygon represents the muted (suspect) time-shifts.*

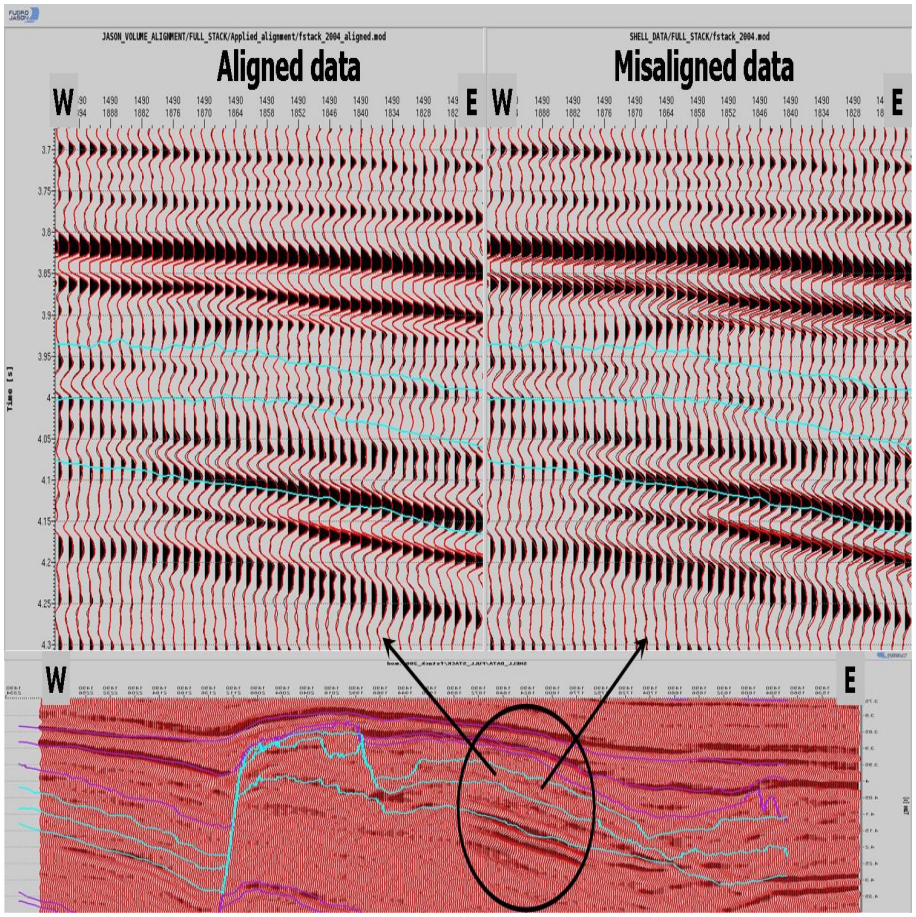

Figure 7.10: *QC of the measured time-shift; Left – reference with aligned monitor data; Right – reference with not aligned monitor data. The reference data are plotted as black wiggles where the aligned monitor data are plotted as red wiggles.*

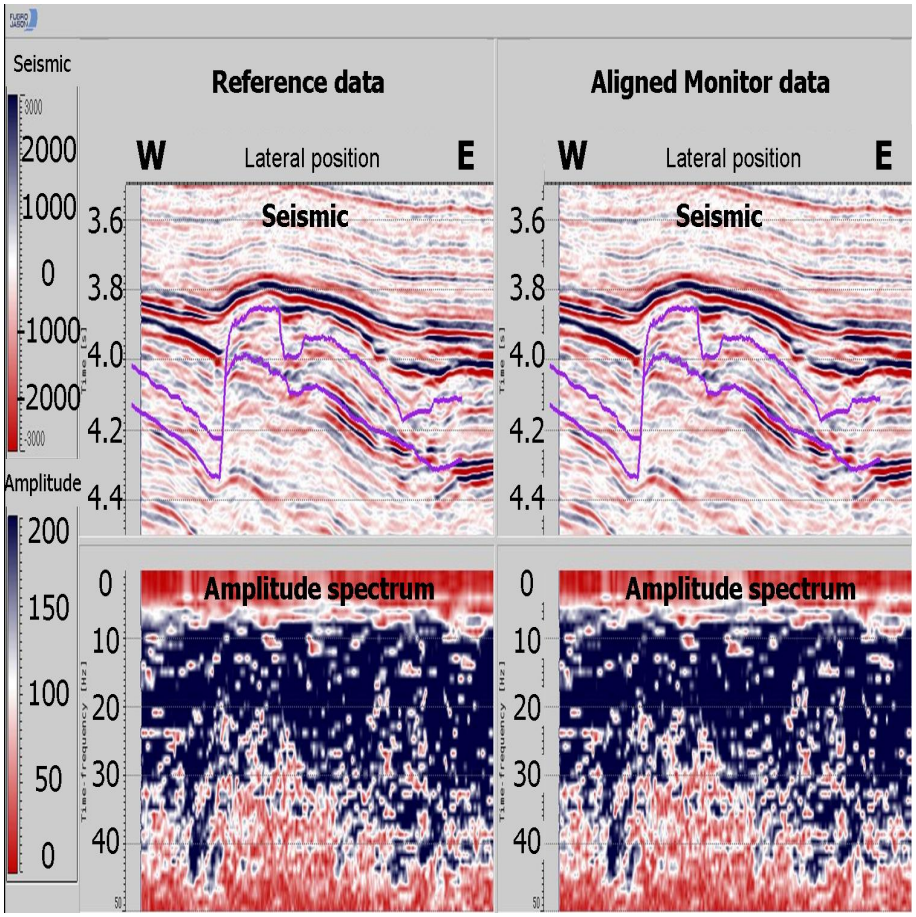

Figure 7.11: *Seismic and Amplitude spectra of the reference and aligned monitor data. In the upper part of the figure are plotted the reference and aligned monitor seismic at the reservoir level. The top and the bottom of the reservoir are delineated with the interpreted time-horizons (in pink color). The vertical axis present the two-way travel time in seconds. In the lower part of the figure is plotted the amplitude spectrum of the plotted above seismic. The vertical axis is the time-frequency in Hz.*

- Different band-pass filters are applied to the data before time-shift estimation. The measured time-shifts are compared to the time-shifts measured without applying a band-pass filters to the data, Figure 7.12. The similarity of the results leads to the conclusion that the measured time-shifts are present in the whole spectrum and are not correlated to high-frequency noise. Additionally, histograms of the time-shifts are computed and plotted in Figure 7.13. The normal distribution of the computed histogram time-shifts with a maximum point around zero suggests that the measured time-shifts are not correlated with some particular event, i.e. there are no outlier peaks.

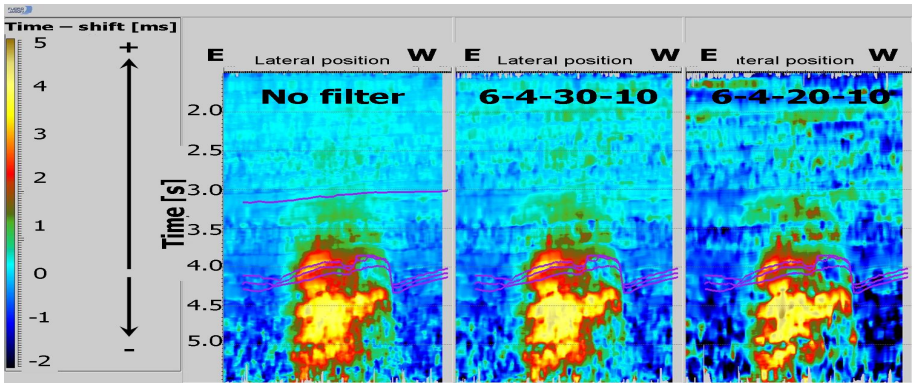

Figure 7.12: *Measured time-shift; Left – no band-pass filter is applied to the seismic data; Middle – band-pass filter 6-4-30-10 is applied to the seismic data; Right – band-pass filter 6-4-20-10 is applied to the seismic data.*

- Smoothed and corrected time-shifts at the top, in the middle and at the bottom of the reservoir and overburden layers, are extracted over time-horizons and the results are presented in Figures 7.14 - 7.19. The results are smoothed using a 250x250 m linear uniform and a non linear median filter - to remove the spikes. The non singular negative time-shift around the reservoir area has been removed (note that the removed parts are not a part of the side-burden effect). A feasibility study has been done, to determine whether the measured time-shift in-

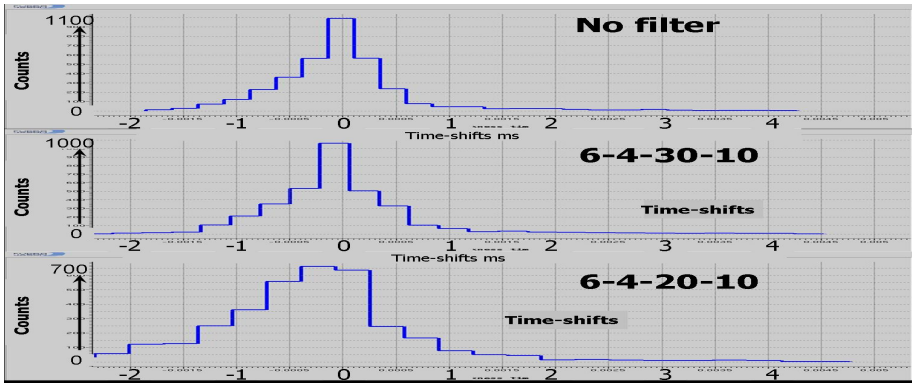

Figure 7.13: *Histograms of the time-shifts distribution; Top – no band-pass filter was applied to the seismic data; Middle – band-pass filter 6-4-30-10 was applied to the seismic data; Bottom – band-pass filter 6-4-20-10 was applied to the seismic data.*

formation can be used to distinguish the production zone from the rest of the reservoir. The study is presented in the next section. Using the time-shifts, measured from the full-stack data, it has been proven possible to detect the changes in the overburden and at the reservoir level. In the next subsection the time-shifts are measured from the partial stacks which will allow a more quantitative analysis of the effect of production.

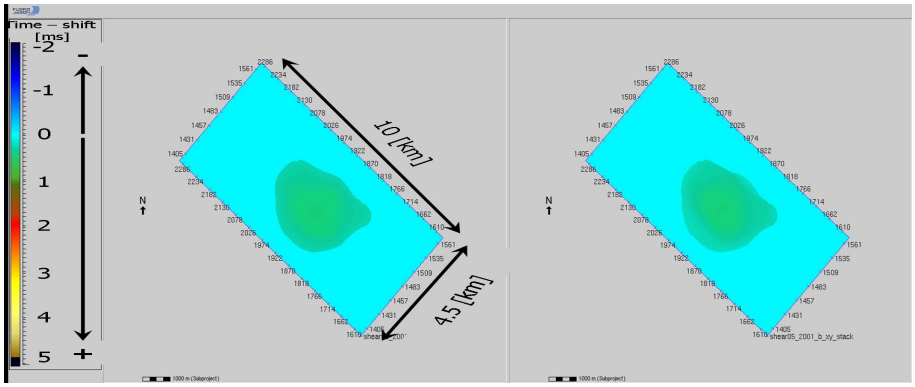

Figure 7.14: *Measured time-shift at the top of the claystone interval (Appendix C, Figure C.09). Left – no filter is applied. Right – band-pass filter 6-4-30-10 is applied. Three time-shift horizons are extracted from the measured time-shift, around the top of the layer (± 60 ms) using the original time-horizons(Shearwater source). The horizons are smoothed and the noise outliers are removed. The average of the top, bottom and middle horizons is taken.*

The feasibility study shows if it is possible to map the production drainage area using the measured time-shifts information. The feasibility study gives an answer where further to investigate the selected area. The interval time-shifts in the overburden and at the reservoir level are plotted in Figure 7.20 and 7.21. The depleted part of the reservoir can be delineated using the cross-plots presented in Figure 7.22 and 7.24. Selected interval time-shifts are plotted in Figure 7.23 and Figure 7.25. From Figure 7.22 to 7.25, one can conclude that it is possible to map the depleting part of the reservoir using the measured time-shifts. This has also been confirmed after comparing the time-shifts with the 4D changes in the seismic amplitude, see Figure 7.26, 7.27. The measured 4D changes in the travel-time and amplitude match the stress-changes map presented by Hawkins et al. [2007], Figure 7.28. The zones of negative differential time-shift correspond accurately to the locations of stress compression, given by Hawkins et al. [2007], where the zones of positive differential time-shift correspond accurately to zones of stress decreases. However, this will give us a quantitative analysis of the reservoir

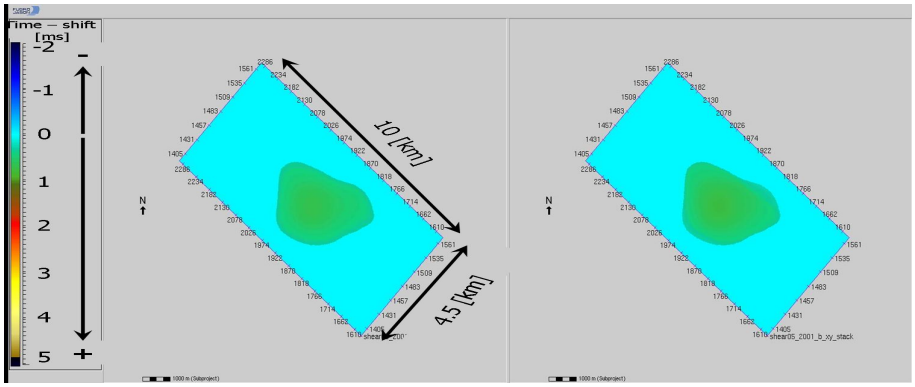

Figure 7.15: *Measured time-shift at the top of the chalk interval (Appendix C, Figure C.09). Left – no filter is applied. Right – band-pass filter 6-4-30-10 is applied. Three time-shift horizons are extracted from the measured time-shift, around the top of the layer (± 60 ms) using the original time-horizons(Shearwater source). The horizons are smoothed and the noise outliers are removed. The average of the top, bottom and middle horizons is taken.*

depletion. To do the qualitative analysis and estimate the real absolute values of the measured time-shifts it is required to use the partial stack information - see Figure 6.3, **Chapter 6**.

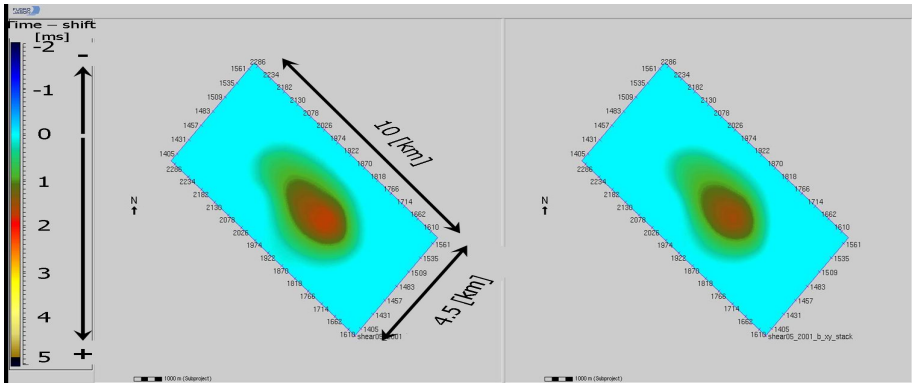

Figure 7.16: *Measured time-shift at the base of the chalk interval (Appendix C, Figure C.09). Left – no filter is applied. Right – band-pass filter 6-4-30-10 is applied. Three time-shift horizons are extracted from the measured time-shift, around the top of the layer (± 60 ms) using the original time-horizons(Shearwater source). The horizons are smoothed and the noise outliers are removed. The average of the top, bottom and middle horizons is taken.*

7.2 Calculate the differential time-shifts for vertical ray-path

To calculate the time-shifts which correspond to the normal incidence case, the two near partial stacks “500-900” and “500-1300” were generated. From the synthetic results obtained in **Chapter 6**, it was concluded that for the given case the time-shift measured from the near offsets stacks will be comparable to the results measured from the normal-incidence data. The differential time-shifts (Landrø and Stammeijer [2004]) in the near overburden and at the reservoir level are plotted in Figures 7.29 and 7.30. The time-shifts measured from the “500-900” are very noisy, whereas the time-shifts measured from the “500-1300” offset stack are less noisy and more consistent. The time-shifts measured from “500-1300” are used in Section 7.3 to predict the relative changes in the acoustic velocity. To calculate the differential time-shifts it is assumed that the vertical time-shift variations inside the layer will be a linear interpolation between the top and the bottom of the

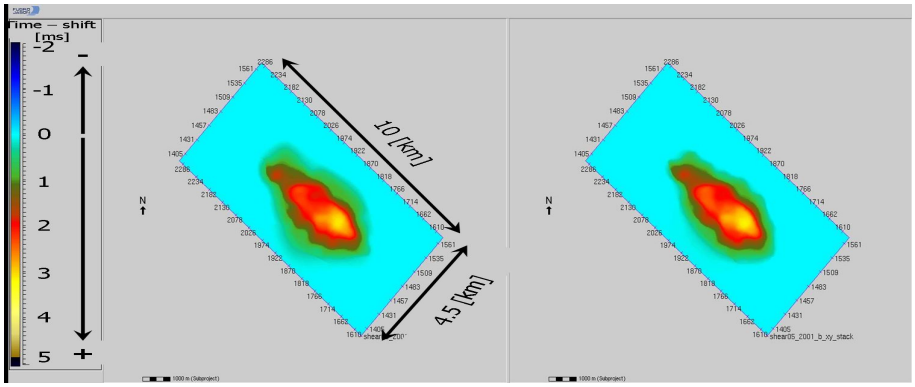

Figure 7.17: *Measured time-shift at the top of the reservoir (Appendix C, Figure C.09). Left – no filter is applied. Right – band-pass filter 6-4-30-10 is applied. Two time-shift horizons are extracted from the measured time-shift, above (+ 60 ms) and at the top of the layer using the original time-horizons(Shearwater source). The horizons are smoothed and the noise outliers are removed. The average of the top, bottom and middle horizons is taken.*

reservoir. The differential time-shift is calculated by subtracting the measured time-shift at the top of the reservoir from the measured time-shift at the bottom of the reservoir and dividing the result by the, calculated from the interpreted time-horizons, time-thickness of the layer (see Landrø and Stammeijer [2004]). In a first-order approximation the relative changes in the seismic velocity can be presented as relative changes in the two-way travel time by neglecting the effect of compaction/elongation of the geological layers on the measured time-shifts. This approach is used as a first pass test to assess if the relative changes in the seismic velocity can be accurately extracted from the differential time-shifts. In this first-order approach we contribute the changes in the two-way travel time to changes in the seismic velocity. The next step is to validate the first-order approach by calculating the effect of layers compaction/elongation on the 4D changes in the two-way travel time and removing this effect from the total time shift. Neglecting the effect of compaction/elongation appears justified by the results of the geomechanical modelling in Section 7.3, showing only a minor effect.

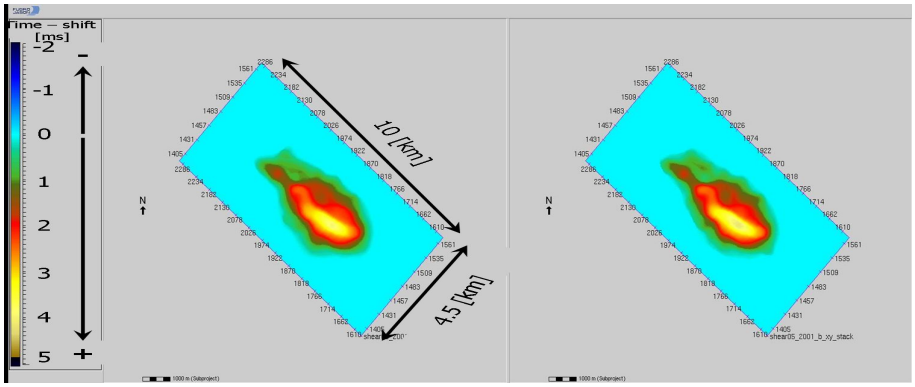

Figure 7.18: *Measured time-shift in the middle of the reservoir (Appendix C, Figure C.09). Left – no filter is applied. Right – band-pass filter 6-4-30-10 is applied. Three time-shift horizons are extracted from the measured time-shift, around the top of the layer (± 60 ms) using the original time-horizons(Shearwater source). The horizons are smoothed and the noise outliers are removed. The average of the top, bottom and middle horizons is taken.*

7.3 Link between changes in the seismic velocity and the changes in the stress field

The measured changes in the travel times are compared with the results from the geo-mechanical modelling on a 2D line crossing the reservoir presented in **Chapter 5**. The results of the 2D geo-mechanical model presented as changes in vertical stress and vertical displacement are plotted in Figure 7.33. The effect of the layer compaction/elongation on the 4D change in travel time is calculated using the approach presented in Section 5.2. Next, the calculated time shift, induced from layer compaction/elongation, is substracted from the total time shift to decouple the effect of the layers stretch from the 4D changes in the seismic velocity only. The calculated result presents the differential time-shift which is directly linked to the changes in the seismic velocity only. The measured and calculated differential time-shifts are presented in Figure 7.34. From the results presented in Figure 7.34 it is concluded that in this particular case the layers com-

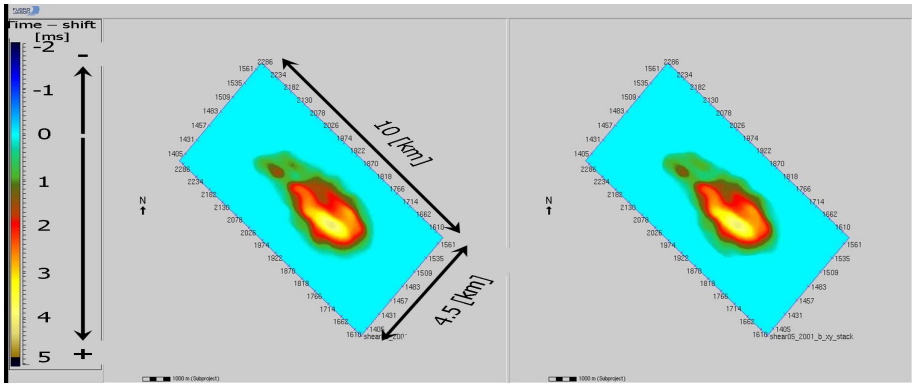

Figure 7.19: *Measured time-shift at the bottom of the reservoir (Appendix C, Figure C.09). Left – no filter is applied. Right – band-pass filter 6-4-30-10 is applied. Two time-shift horizons are extracted from the measured time-shift, above (+ 60 ms) and at the top of the layer using the original time-horizons(Shearwater source). The horizons are smoothed and the noise outliers are removed. The average of the top, bottom and middle horizons is taken.*

paction/elongation effects on the measured total time-shift are negligible and the time-lapse changes in the two-way travel time can essentially be attributed to 4D changes in the seismic velocity. As a next step the relative changes in the compressional velocity are calculated using the fact that $\Delta t/t \approx -\Delta V_P/V_P$. The relative changes in the seismic velocity are presented in Figure 7.35. The monitored relative changes in the P-wave velocity (Figure 7.35) are in the order of 0.3% in the reservoir and -0.5% in the near overburden. Note that, the absolute value of the velocity inside the reservoir is 50% larger compared to the values in the near overburden. The relative changes in the seismic velocity are compared with the modelled time-lapse changes in the vertical and horizontal stress with the geo-mechanical modelling (Figure 7.36). From Figure 7.36, it can be concluded, that the changes in the compressional velocity both in the reservoir and in the overburden are following accurately the changes in the vertical and horizontal stresses.

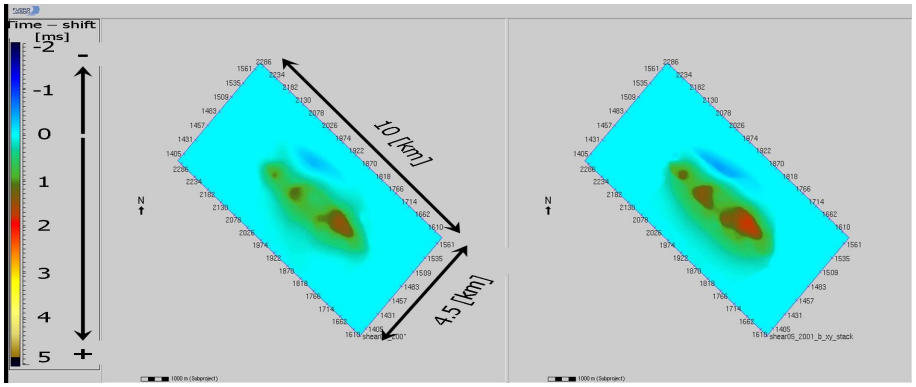

Figure 7.20: *Difference between the measured time-shift at the top of the reservoir and at the bottom of the Chalk interval. The results illustrates the changes in the two-way travel-time in the "near" overburden.*

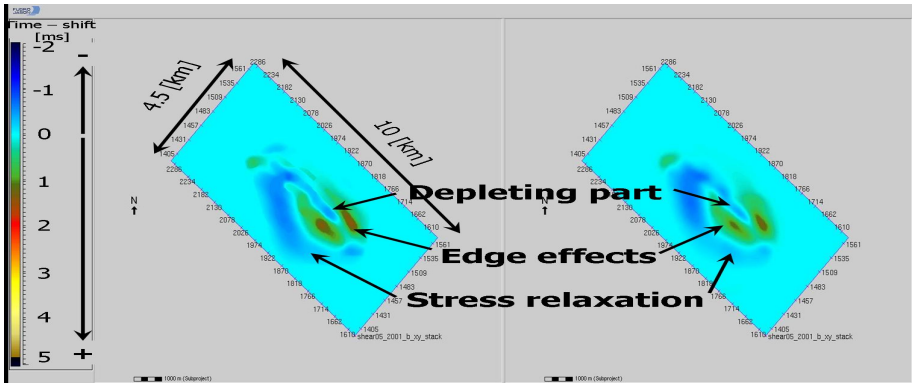

Figure 7.21: *Difference between the measured time-shifts at the bottom and at the top of the reservoir. The results illustrates the changes in the two-way travel-time at the reservoir level. With "Edge effect" are denoted the zones where the reservoir body pushes on the side-burden. The "Stress relaxation" zone delineates the stress compression a side from the depleting part as a result of stress arching.*

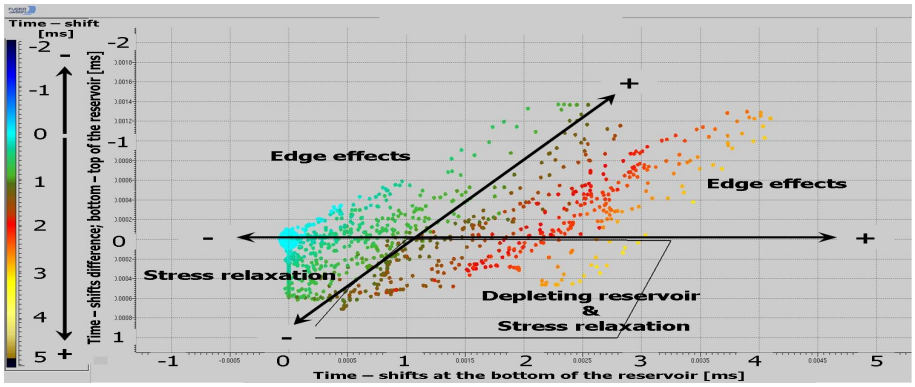

Figure 7.22: *Cross-plot between the time-shifts difference, top-bottom of the reservoir (Figure 7.21), and the time-shifts measured at the bottom of the reservoir (Figure 7.19). The depleting part of the reservoir is where the time-shifts difference are negative and the measured time-shifts, at the top of the reservoir has higher values. It is expected that the effect of stress relaxation will be smaller compare to the effect of depletion.*

7.4 3D stress changes

In this section we extrapolated the calculated stress changes for the selected 2D line stress changes over the whole 3D project area. The extrapolation is controlled using the correlation between the results of the geo-mechanical modelling and the measured time-shift (see Figure 7.37). The whole time-shifts are contributed to the 4D stress changes, neglecting the effects of compaction/elongation as it was already discussed in Section 7.3 based on the 2D modelling results.
The extrapolation is performed using the following steps:

- The model is divided into geological bodies (layers) using a structural model obtained from the well log information. Each of the layers is subdivided in polygon areas. Each of the polygons correspond to an area where the influence of one of the different stress effects on the time-shifts (as presented in Figure 7.31) is dominant: overburden effect, pressure depletion, edge effects and stress relaxation. The goal is

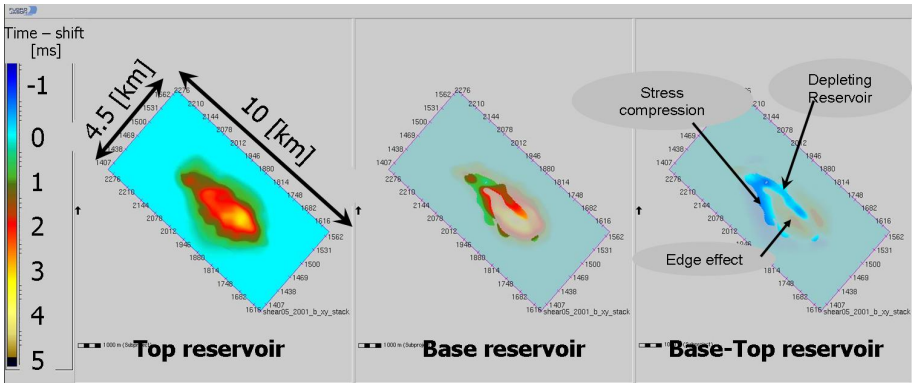

Figure 7.23: *Delineating the reservoir zone, using the cross-plot technique from Figure 7.22. Note that the plotted time-shifts corresponds from left to right to the: Figure 17, Figure 19, and Figure 21.*

to find single time-shifts-stress relations for each of these areas.

- For each of the areas a stress-time-shifts relation is created, calibrated to the measured time-shifts and to the output of the geo-mechanical modelling based on the modeled 2D-line. The stress-time-shift relation is estimated at the top and at the bottom of each layer.

- The created stress-time-shift relationships are used as a function to extrapolate the modeled 2D stress changes in the whole 3D project area as a horizon at the top and at the bottom of each layer.

- A simple kriging method with a spherical variogram, implemented in Jason Geoscience Workbench, is used to extrapolate the values at the top and at the bottom of the layers.

- Linear interpolation is applied between the created top and bottom stress-horizons to create a stress 3D stress volume.

In Figures 7.38-7.39 the extrapolated 3D volume of the time-lapse changes in the vertical stress as a result of pressure depletion in the reservoir is plotted

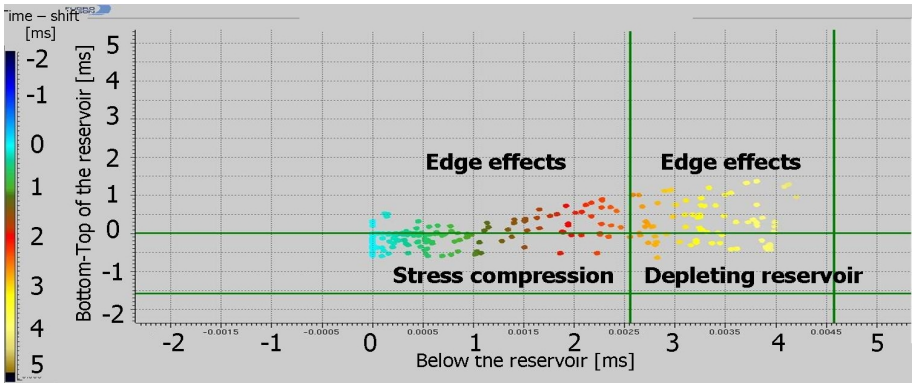

Figure 7.24: *Cross-plot between the time-shifts difference, top-bottom of the reservoir (Figure 7.21), and the time-shifts measured below the reservoir. The difference between the time-shifts measured at the bottom and at the top of the reservoir gives the time-shifts decrease or increase at the reservoir level. The decrease of the time-shifts delineate the zones of depletion and stress compression. The two zones can be distinguish by cross-plott between the interval time-shifts and the time-shifts measured below the reservoir. The highest time-shifts below the reservoir will be mostly concentrated below the depleting zone. Note that the plotted time-shifts in the left plot correspond to Figure 7.19, where the plotted time-shift in the right plot correspond to Figure 7.21. In the middle plot are presented the time-shifts measured below the reservoir.*

The distribution of the lateral stress changes (pressure depletion, edge effect, stress relaxation and overburden effect), can be detected both at the reservoir and in the overburden.

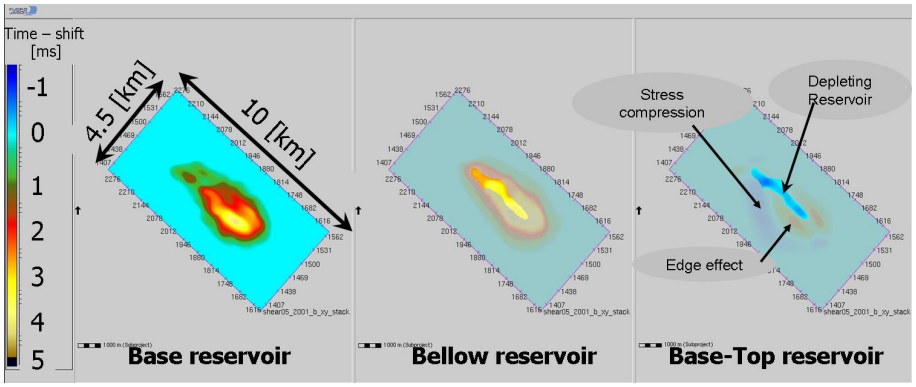

Figure 7.25: *Delineating the depleting zone of the reservoir using the cross-plot from Figure 7.24.*

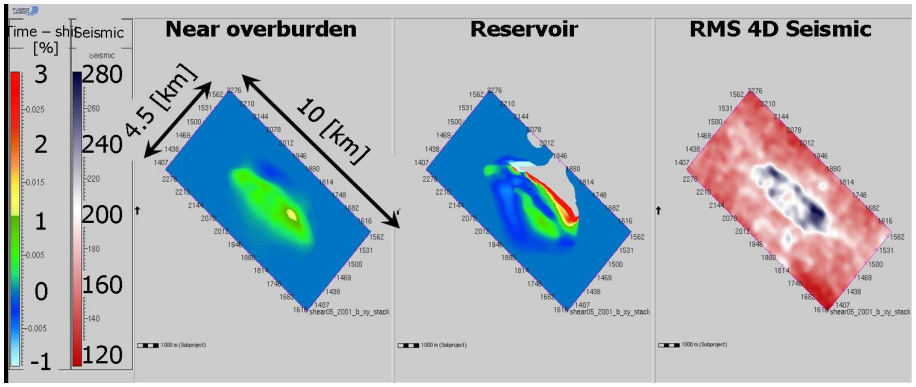

Figure 7.26: *The differential time-shifts at the top and at the bottom of the reservoir with the rms of the 4D amplitude changes across the reservoir (top and bottom).*

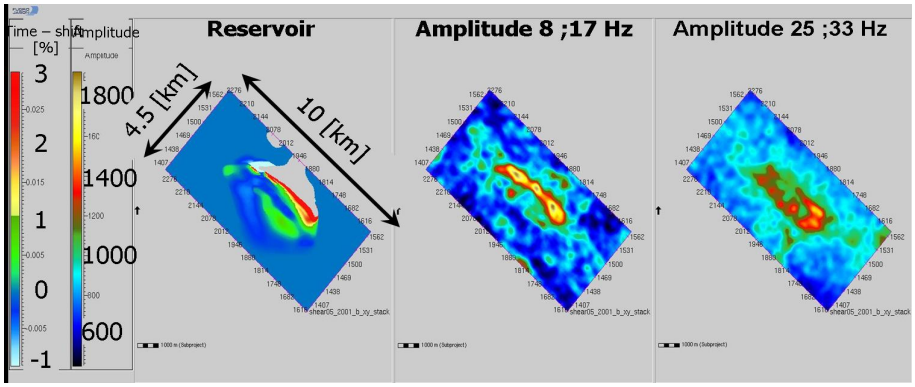

Figure 7.27: *The differential time-shifts at the bottom of the reservoir with the stacked amplitude: 1) decomposed at 8 Hz and decomposed at 17 Hz, and 2) decomposed at 25 Hz and decomposed at 33 Hz.*

7.5 Results and Observations

In this Chapter the real-data time-shifts measured from the full stack and from the near-offset stacked data are used together with the results of the synthetic geomechanical modelling to predict the time-lapse changes in the vertical stress as a result of pressure depletion at the reservoir layer. We demonstrated that the time-shifts measured in the overburden using Shearwater 4D data are real, and they are induced by the stress field changes. Further, we used the measured time-shifts in combination with the modeled 4D stress changes to predict the time-lapse changes in the vertical stress both in the reservoir and in the surrounding rock.

- The time-shifts measured from the full-stack data are used as an indicator to investigate where the pressure depletion effects are detectable.

- The differential time-shifts calculated from the measured time-shifts (derived from the full-stack data), are compared to 4D amplitude changes. The results confirm that the calculated results are real and not only a noise effect.

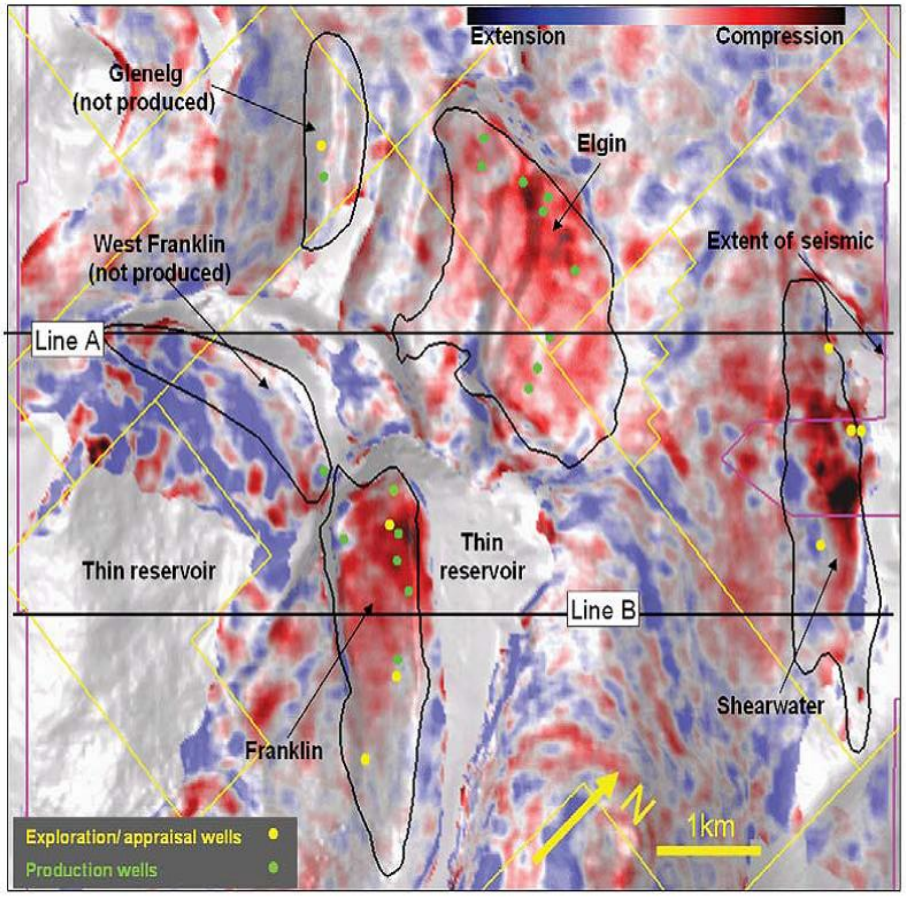

Figure 7.28: *The magnitude of the 4D stress changes within the reservoir generally correlate to the locations of the production wells at top reservoir, Hawkins et al. [2007]*

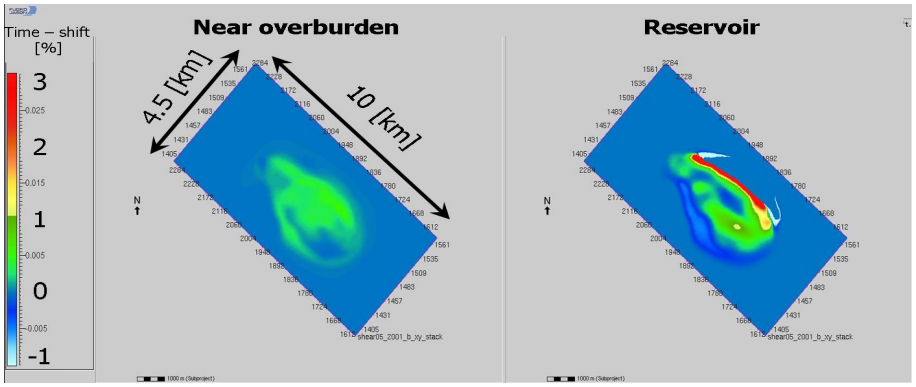

Figure 7.29: *Differential time shift in the near overburden and at the reservoir level, measured using "500-900" stack.*

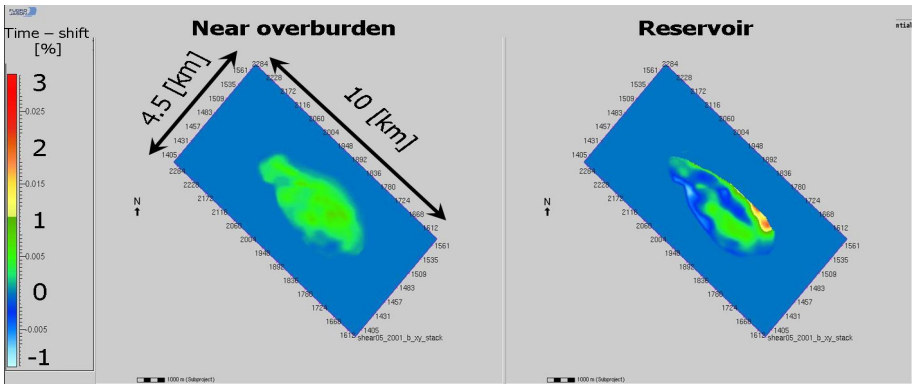

Figure 7.30: *Differential time shift in the near overburden and at the reservoir level, measured using "500-1300" stack.*

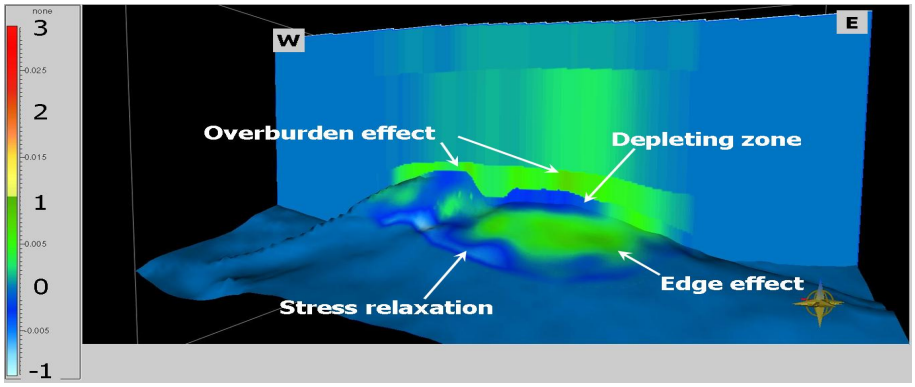

Figure 7.31: *3D-view of the differential time-shift. The horizontal slice follows the horizon between the upper and the lower part of the reservoir.*

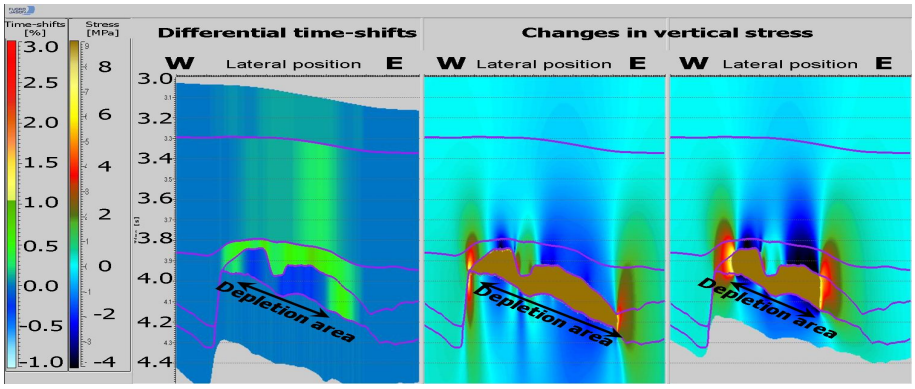

Figure 7.32: *Measured differential time-shifts and modeled changes of vertical stress. The depletion area of the initial geo-mechanical model, in the middle, is updated in order to match the measured time-shifts. The updated model is plotted in the right panel.*

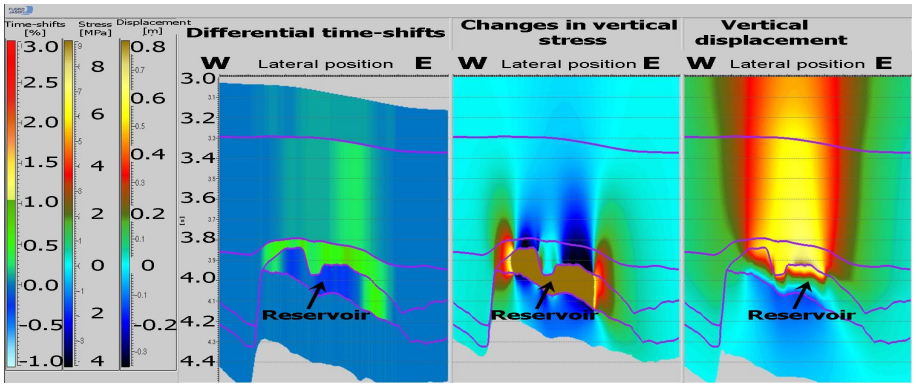

Figure 7.33: *Left - differential time-shifts; Middle - changes in vertical stress; Right - vertical displacement.*

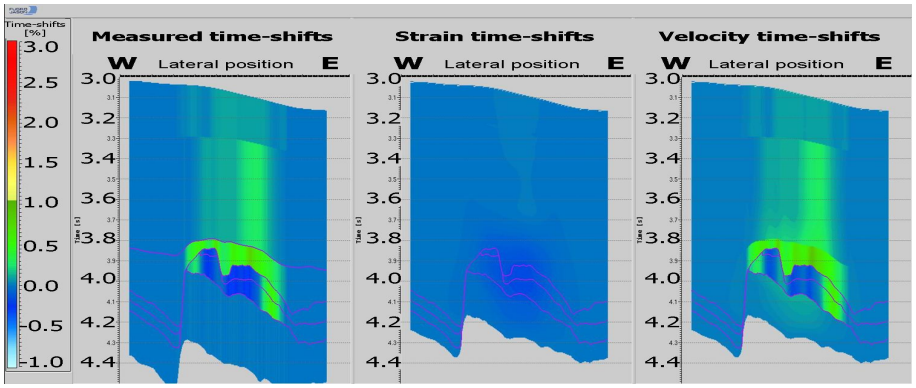

Figure 7.34: *Left - measured differential time-shifts ($\Delta t/t$, Equation 5.7); Middle - differential time-shifts as a result of vertical displacement ($\Delta t''/t$, Equation 5.8); Right - time-shifts caused by changes in the seismic velocity ($\Delta t'/t$, Equation 5.8).*

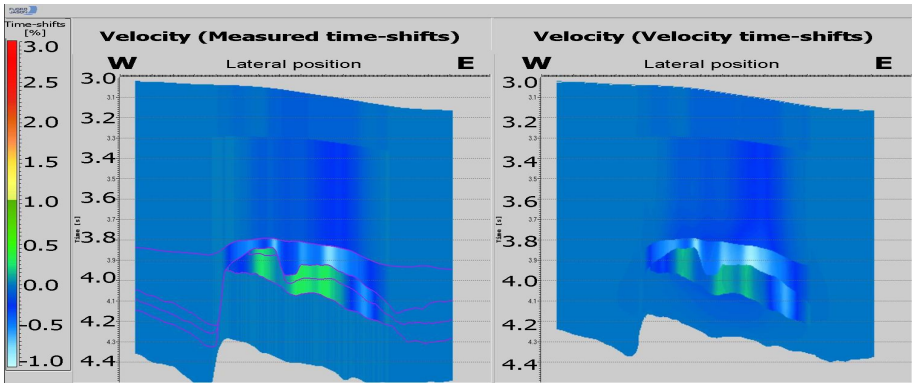

Figure 7.35: *Left - the relative changes in the compressional velocity, calculated from the measured time-shifts ($\Delta t/t$). Right - the relative changes in the compressional velocity calculated from ($\Delta t''/t$).*

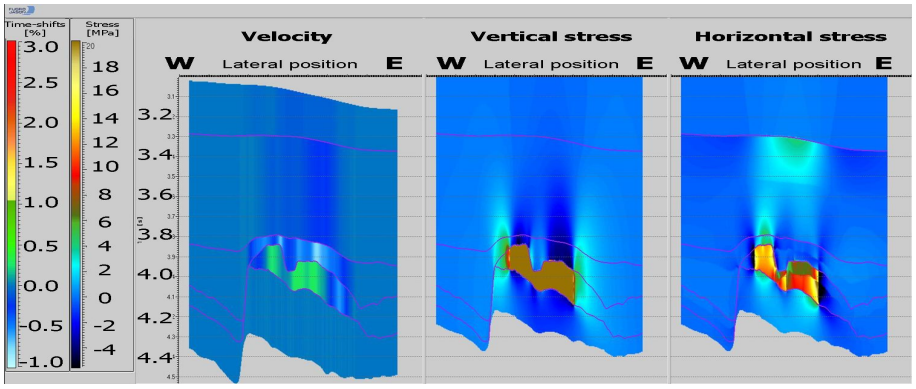

Figure 7.36: *Left - the relative changes in the compressional velocity, calculated from the measured time-shifts ($\Delta t/t$). Middle - changes in the vertical stress (geo-mechanical model), Right - changes in the horizontal stress (geo-mechanical model).*

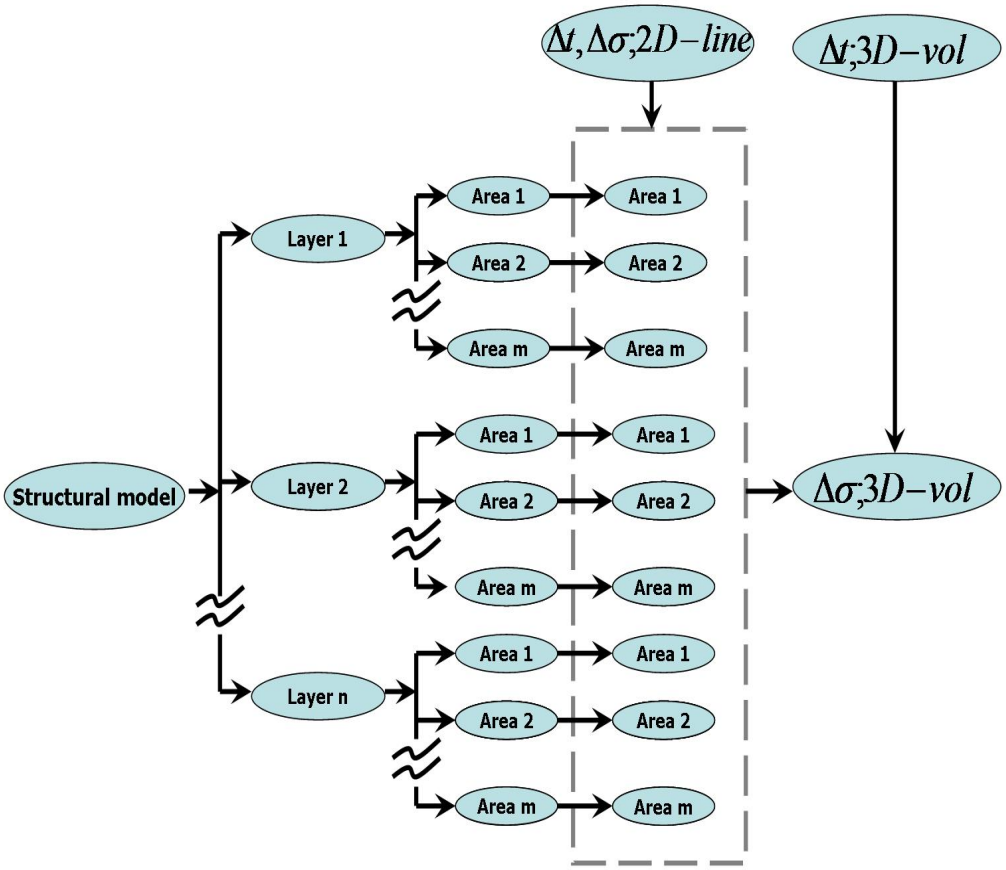

Figure 7.37: *Work-flow used to extrapolate the calculated stress from the modeled 2D line to the whole 3D project area using the measured time-shifts and the estimated stress-time-shifts relation.*

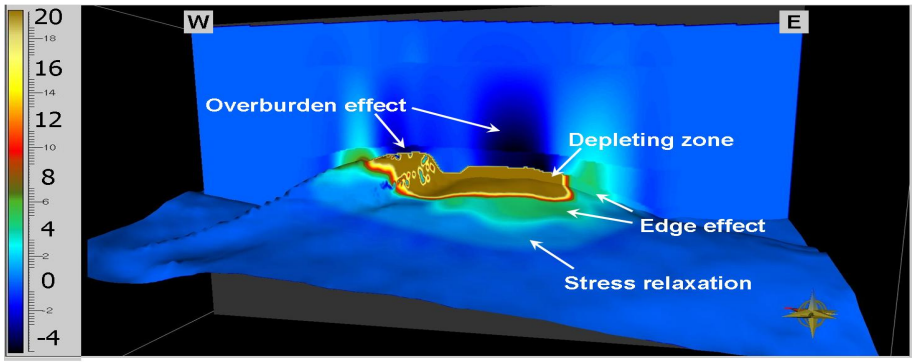

Figure 7.38: *Extrapolate changes in the vertical stress in MPa. The horizontal slice follows the horizon between the upper and the lower part of the reservoir.*

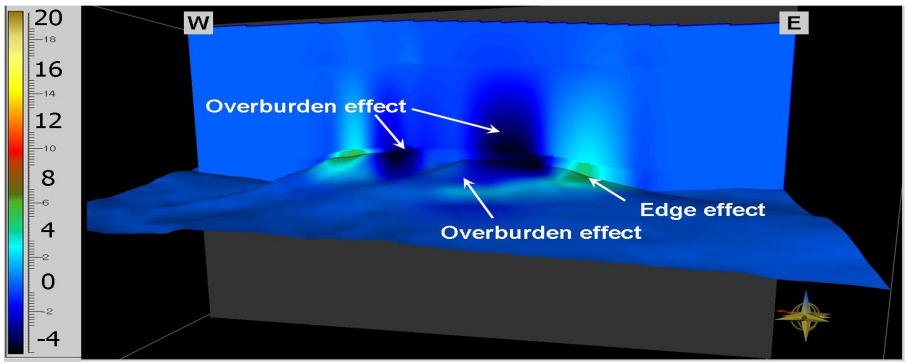

Figure 7.39: *Extrapolate changes in the vertical stress in MPa. The horizontal slice follows the horizon between the top and the bottom of the near overburden.*

- In addition, the calculated differential time-shifts (full-stack data) are compared with independent studies of the Shearwater field, obtained from the literature (Hawkins et al. [2007]) and reservoir simulations (Shearwater source). The independent studies confirm that the differential time-shifts correlate well with the expected effects of pressure depletion.

- The differential time-shifts were also calculated from the measured near-offset data time-shifts. The near-offset time-shifts will be less affected than the full stack time-shifts by the ray-path and PSDM effects as explained in **Chapter 6**.

- The calculated differential time-shifts follow accurately the 4D stress-changes produced with the geo-mechanical modelling.

- The near-offset differential time shifts are used to calculate the relative changes in the acoustic velocity using the method presented in **Chapter 5**. It is demonstrated that in this particular case, the effect of physical compaction/elongation on the 4D time-shifts will be negligible compared to the effect of 4D changes in stress.

- A 4D volume of stress changes volume is created using the calculated near-offset differential time-shifts and the result of the 2D geo-mechanical modelling. The created stress-changes volume can be used to improve the 4D reservoir characterization. Once combined with the rock physics, the stress-changes model can be used to update the inverted seismic and rock properties. The stress changes model can also be used to detect the zones in the overburden undergoing stress concentrations in order to improve the design of the future wells.

8

Conclusions

This thesis describes a methodology to separate the effect of compaction and of stress-induced elastic parameter changes on seismic reservoir characterization using 4D seismic attributes (i.e. time-shifts) in combination with geo-mechanical modeling.
This integrated approach helps to improve the prediction of the distribution of time-lapse stress changes both in the overburden and at the reservoir level as a result of hydrocarbon production by establishing a stress-seismic-attributes relation. The predicted stress distribution can be used to optimize the design of future wells by avoiding locations with high-stress concentration in the overburden.
In more detail, this research has led to the following conclusions:

- The influence of the rock properties on the seismic properties is demonstrated using an analytical rock physics model, showing that the stress changes will influenced directly the seismic velocity. Furthermore, it has been demonstrated that the 4D changes in the stress field can be inverted from the measured time-lapse changes in the seismic attributes. (**Chapter 3**)

- The effect of pressure depletion on the time-lapse changes in vertical and horizontal stress, both inside the reservoir and in the surrounding media, is modeled using three different types of hydrocarbon reservoirs. Stress arching is observed. Furthermore, different scenarios have been tested to investigate the distribution of the 4D changes in the vertical and lateral stresses. Main factors influencing the stress distribution appear to be the distribution and magnitude of the pressure drop in the reservoir due to depletion, the geometrical shape of the reservoir and of the overburden (especially the presence of faults) and the elastic properties of the layers. (**Chapter 5**)

- A relation between changes in stress and time-lapse changes in the two-way travel time is elaborated upon. A method is proposed, in which the results of the geo-mechanical modelling are used to eliminate the effect of compaction (i.e. physical displacement of the layers) from the measured time-shifts. (**Chapter 5**)

- The AVO effect on the measured time-shifts is investigated including pulse distortion as a result of the applied NMO/DMO and ray-bending along the travel paths. As one intuitively might suspect, time-shifts derived from near-offset data are least distorted by these effects, since these resemble most the vertical travel path. The signal-to-noise ratio of partial stack is however lower than that of the full-stack data. (**Chapter 6**)

- Analysis of the Shearwater field shows that the time-lapse amplitude effects in the seismic data induced by production are small. However, a clear relation exists between the measured time-shifts and the 4D changes in the seismic amplitudes. (**Chapter 7**)

- Based on the results of the geo-mechanical modelling (vertical displacement), it is demonstrated that for Shearwater the effects of compaction (i.e. physical displacements of the layers) on the observed differential time-shifts is negligible. Therefore, the relative changes in the acoustic velocity can be directly calculated from the differential time-shifts. (**Chapter 7**)

- The observed differential time-shifts in the surrounding reservoir rock correspond accurately to the modeled 4D changes in the stress filed, using geo-mechanical modelling. These time-lapse changes in stress are result of: stress relaxation, edge effects and negative stress concentration in the overburden. (**Chapter 7**)

- For Shearwater it is demonstrated that the 4D changes in the acoustic velocity (derived from the differential time-shifts) follow accurately the modeled 4D stress changes. In this thesis the inverse relationship has been used to predict the stress changes both in the reservoir and in the surrounding rocks. (**Chapter 7**)

A

Appendix A

A.1 The effect of various oil/gas production operations on the reservoir conditions and seismic properties

Process description	**Effect on reservoir conditions**	**Effect on seismic properties**
Primary depletion with weak aquifer	Decrease pore pressure, increase effective stress. Uniform increase in gas saturation when reservoir pressure falls below bubble point. Gas segregation upward if saturation exceeds critical value. Water saturation relatively constant.	Initial velocity increase with increasing effective stress; decrease in velocity and density as free gas phase forms.
Primary depletion with strong aquifer	Pore pressure and effective stress relatively constant. If pressure remains above bubble point, no gas saturation. Increasing of water saturation.	Velocity and density increase as water saturation increases.
Water flood of formation with weak aquifer	Increase in pore pressure and decrease effective stress. Decrease gas saturation spreading from injectors. Increase water saturation	Increasing velocity and density with increased water saturation and loss of gas. Possible velocity decrease near injector.
Pressure maintenance with gas	Pore pressure and effective stress relatively constant. Increasing gas saturation spreading from injectors.	Velocity and density decrease with expanding gas cap. Oil-water contact relatively constant
CO_2 flood	Increase pore pressure, decrease effective stress. Increase CO_2 saturation from injectors.	Velocity and density decrease near injectors depending on pressure and temperature.
Steam flood	Increase pore pressure, decrease effective stress. Increase formation temperature. Liquid water bank propagates ahead of steam.	Velocity drops with temperature rise and steam saturation. Slight velocity increase in water bank.

Table A.1: *General recovery processes and their effects, Batzle et al. [1998]*

A.2 The analysis of the technical risk of the 4D project

Row Parameters	Ideal	Indonesia	Gulf of Mexico	West Africa	North Sea
Reservoir					
depth (ft)	shallow	650	7000-8000	4000-6000	9200 - 10400
effective stress (psi)	low	530	7000-8000	4000-6000	6500 - 7500
pore pressure (psi)	high	100-350	3100-3300	2200	6500 - 5250
bubble point (psi)	—	110	3100	4500	1250
temperature (F)	high	100-430	176-180	175	215
unit thickness (ft)	high	100	100-150	50-150	15-40
Rocks					
dry bulk modulus [GPa]	low	2-3	3-5.8	5-8	10-30
dry density [g/cc]	low	1.54-1.67	1.7-2.1	1.76	2.07-2.23
porosity [%]	high	30-38	21-34	26-30	16-23
Oil					
GOR [scf/stb]	high	0	250-350	350-400	$>$300
gravity [API]	high	22	25	22-28	36
density [g/cc]	low	0.9	0.85	0.77	0.75
bulk modulus [GPa]	low	1.5	1.2-1.5	1.0	0.92
Water					
salinity [ppm]	high	40000	190000	40000	200000
density [g/cc]	high	1	1.1	1.0	1.08
bulk modulus [GPa]	high	2.25	3.35	2.25	3.0
Gas					
density [g/cc]	low	0.1	0.1	0.1	0.12
bulk modulus [GPa]	low	0.1	0.1	0.1	0.12
4-D Fluids					
fluid saturation [%]	high	90→10	90→10	75→25	75→40
fluid compression contrast [%]	high	$>$100	150-200	125	200
Seismic					
dominant frequency [Hz]	high	125	50	30	25
average resolution [ft]	low	15	50	85	100
image quality (1-5)	5	4	5	4	3
repeatability (1-5)	5	5	4	4	3
fluid contact visibility (1-5)	5	4	4	4	2
time-shift	$>$4	20	0	0-4	0
impedance changes [%]	$>$4	55	8-10	4-6	3-7

Table A.2: *4-D fact sheet, Lumley et al. [1997]*

	Score	5	4	3	2	1	0
Dry rock bulk modulus	GPa	<3	3-5	5-10	10-20	20-30	30+
Fluid compress contrast	%	250+	150-250	100-150	50-100	25-50	0-25
Fluid saturation	%	50+	40-50	30-40	20-30	10-20	0-10
Porosity	%	35+	25-35	15-25	10-15	5-10	0-5
Impedance change	%	12+	8-12	4-8	2-4	1-2	0
Travel-time change	#samples	10+	6-10	4-6	2-4	1-2	0

Table A.3: *Reservoir scorecard, Lumley et al. [1997]. The highest score, giving the most favorable conditions for the time-lapse interpretation is* 5.

	Ideal	Indonesia	Gulf of Mexico	West Africa	North Sea
Reservoir					
dry rock bulk modulus	5	5	4	3	2
fluid compress contrast	5	5	4	3	4
fluid saturation change	5	5	5	4	3
porosity	5	5	4	4	3
impedance changes	5	5	4	3	3
reservoir total	25	25	21	17	15
Seismic					
image quality	5	4	5	4	3
resolution	5	5	4	3	1
fluid contacts	5	4	4	4	2
repeatability	5	5	4	4	2
seismic total	20	18	17	15	8
Total Score	45	43	38	32	23

Table A.4: *4-D technical risk spreadsheet, Lumley et al. [1997].*

A.3 Herz-Mindlin contact theory; Hashin-Strickman bounds

A brief review of the Herz-Mindlin contact theory and the Hashin-Strikman bounds is given below. The contact theory in general is a modelling of the porous rock by a random packing of identical solid spherical particles (granular materials). In rock physics, these granular materials are referred to as unconsolidated sands, Wang and Nur. [1992]. The normal stiffness of two identical spheres is defined as the ratio of a confining force increment to the shortening of a sphere radius, Figure A.1 - left part. The tangential stiffness of two identical spheres is the ratio of a tangential force increment to the increment of the tangential displacement of the center, relative to the contact region, Figure A.1 - right part. Both the normal and tangential stiffness are

$$S_n = \partial \mathbf{F}/\partial \delta, S_\tau = \partial \mathbf{T}/\partial \tau. \tag{A.1}$$

Where S_n and S_τ are denoted to the normal and the tangential stiffness, $\mathbf{F}$ and $\mathbf{T}$ represent the normal and the tangential forces; finally the normal and the tangential displacements are respectively δ and τ. Further, the effective bulk and shear modulus are expressed through porosity (ϕ), the average numbers of contact per grain/sphere (C), sphere radius (R) and normal and tangential stiffness of a two sphere situation

$$\begin{aligned} K_{eff} &= \frac{C(1-\phi)}{12\pi R} S_n, \\ G_{eff} &= \frac{C(1-\phi)}{20\pi R}(S_n + 1.5 S_\tau). \end{aligned} \tag{A.2}$$

Hertz, as described by Mavko et al. [1998] presented the normal stiffness using the shear modulus (G) and the Poisson ratio (ν) of the grain material

$$S_n = \frac{4Ga}{1-\nu}, \tag{A.3}$$

where a is the contact area of two identical spheres as a result of normal compression. According to Hertz (Wang and Nur. [1992] and Mavko et al.

[1998]), the contact area of the two spheres is related to the radius (R), the applied forces (**F**), the Poisson ratio (ν) and the Young modulus. The applied forces and the Young modulus could be replaced by using the Poisson ratio, the shear modulus, and the displacement ($\delta = 2a^2/R$) between the spheres, therefore the contact area a is

$$a = R\sqrt[3]{\frac{3\pi(1-\nu)}{2C(1-\phi)G}\sigma_{eff}}, \tag{A.4}$$

where σ_{eff} is the effective stress applied to a random identical sphere packing. Than the effective bulk modulus of a dry random identical sphere packing is:

$$K_{eff} = \sqrt[3]{\frac{C^2(1-\phi)^2G^2}{18\pi^2(1-\nu)^2}\sigma_{eff}}. \tag{A.5}$$

Mindlin [1949], showed that if the tangential force is applied after the spheres were pressed together, the effective shear modulus of a dry random identical sphere packing is

$$G_{eff} = \frac{5-4\nu}{5(2-\nu)}\sqrt[3]{\frac{3C^2(1-\phi)^2G^2}{2\pi^2(1-\nu)^2}\sigma_{eff}}. \tag{A.6}$$

Mindlin [1949] assumed the same normal displacement and contact stiffness as given in Equation A.3, where the tangential forces affect neither the distribution of the σ_{eff}, nor the area of the contact.
Hashin and Strickman [1963] showed how to predict the effective elastic modulus of a mixture of grains and pores, where the geometric details of how the phases are arranged relative to each other are unknown. They used the fact that for a given volume fraction of constituents the effective modulus will fall between two bounds, but its precise value depends on the geometric details, Hashin and Strickman [1963], see Figure A.2. The Hashin-Strickman bounds are expressed in the Equation A.7.

$$K^{HS\pm} = K_1 + \frac{f_2}{(K_2 - K_1)^{-1} + f_1(K_1 + \frac{4}{3}\mu_1)^{-1}}, \tag{A.7}$$
$$\mu^{HS\pm} = \mu_1 + \frac{f_2}{(\mu_2 - \mu_1)^{-1} + \frac{2f_1(K_1+2\mu_1)}{5\mu_1(K_1+\frac{4}{3}\mu_1)}},$$

where the bulk and shear modulus of the individual phases are denoted with $K_{1,2}$ respectively $\mu_{1,2}$. With $f_{1,2}$ are labeled the two volume fractions.

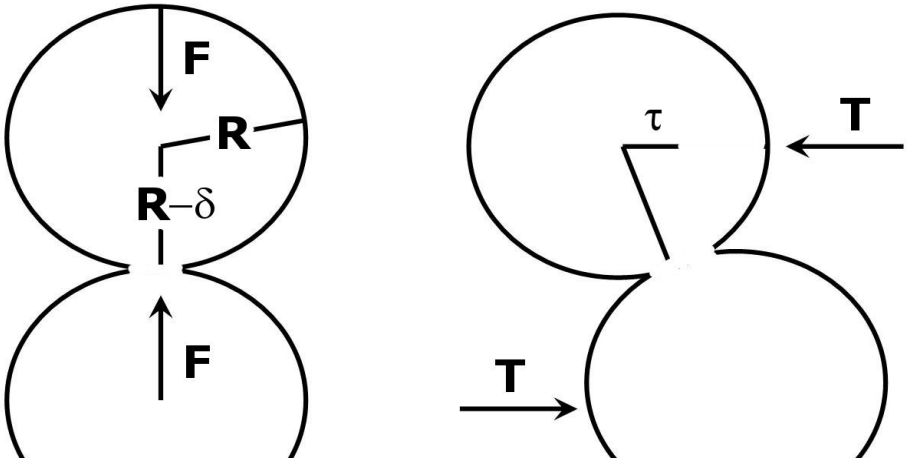

Figure A.1: *Normal and tangential contact stiffness of a two-particle combination, Mavko et al. [1998].*

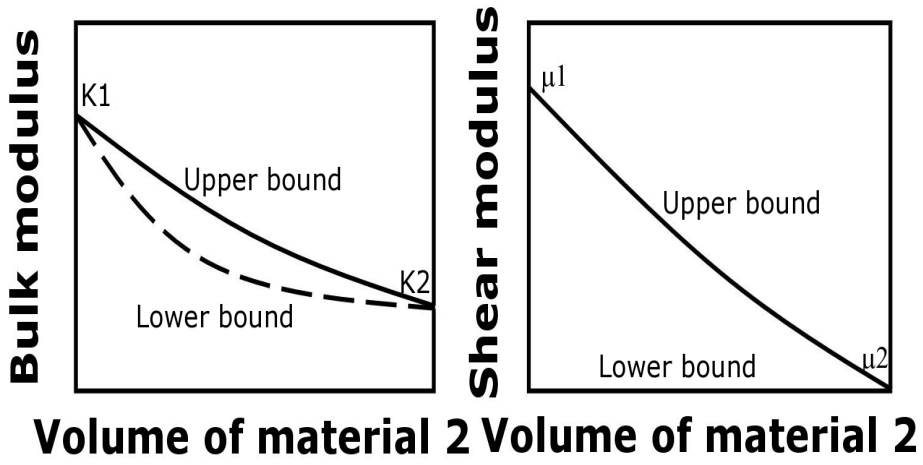

Figure A.2: *Schematic representation of the upper and lower bounds on the elastic bulk and shear modulus, Mavko et al. [1998].*

A.4 Gassmann theory assumptions

The basic assumption in the Gassmann [1951] theory are:

- The rock is macroscopically homogeneous. It is assumed that the wavelength is longer than the grain and pore size.
- All the pores are connected or communicating. There are no isolated or poorly connected pores in the rock. This conjunction will ensure a full equilibrium of the pore fluid flow, induced by the passing wave. For seismic waves only poorly consolidated sand can meet this assumption because of the sand's high porosity and permeability.
- The pores are filled with frictionless fluid (liquid, gas or mixture). To ensure the full equilibrium of the pore fluid flow the viscosity of the fluid must be zero. If the viscosity is zero the pore fluid will easily equilibrate.
- The rock-fluid system under study is closed (undrained). For laboratory rock samples the rock-fluid system is sealed at the boundaries.

- The pore fluid does not interact with the solid in a way that would soften or harden the dry frame. This assumption eliminates any effect of chemical/physical interactions between the rock matrix and the pore fluid.

A.5 The effect of 4D changes in the rock properties on the seismic parameters

In general, the seismic velocities and impedances increase when the effective stress increases. The relationship between the seismic properties and the effective stress is not linear as it is presented in Figure A.3. A rapid increase in the lower stress areas is followed by a minimal increase and even lack of change in the seismic velocity in higher-stress regions, Schoen [1996], Bourbie et al. [1987], Holt et al. [2005] and Prasad [2002]. The increase of the velocity depends on the type of the rock. By increasing the effective stress, the cracks in the rock are closing. The closure increases the rigidity of the material, respectively the elastic modulus will increase. The increase of the elastic modulus will increase the seismic velocity (Equation 2.28). The increase of the elastic modulus depends on the type of the applied stress, on the stress orientation, and on the orientation of the cracks. There is a number of publications reporting the behavior of cracks and pores under the effective stress, Walsh [1965], Walsh [1969] and Wu [1966]. As reported by Bourbie et al. [1987], the increase in P-velocity as a function of the effective stress is much smaller for a saturated sample than for a dry sample. The reason for this is that the bulk modulus and density of the saturated rock is influenced by the bulk modulus and density of the fluid (Equation 3.8 and 3.9), Murphy et al. [1992]. On the other hand, the S-wave velocity is unaffected by the presence of liquids in the pores.
As suggested by Wang [1997], the fluid substitution leads to a high contrast in pore fluid compressibility in the following situations: 1) live oil from/to water/brine; 2) liquid from/to gas; 3) oil from/to high salinity brine; 4) live oil from/to dead oil. Whenever a liquid changes phase to (or is displaced by) a gas, its compressibility increases dramatically, due to the fact that the pore fluid is much less compressible than the gas/steam. By higher GOR (gas-to-oil ratio) the live oils are much more compressible than water. When the live oil is substituted by water/brine, the compressibility of the pore fluid decreases (Equation 3.6). The liquid saturation increases the P-wave velocity of dry sandstones, however, as it was shown by Wang and Nur [1990], the value of this increase depends on the rheology of the rock. Gregory [1976] suggested that the fluid saturation effects on the compressional velocity are larger in low-porosity than in high-porosity rocks. Parallel to the increase of

the elastic modulus, the water(brine)/oil and liquid/gas substitution is also increasing the bulk density of the rock. This increase will decrease the seismic velocities.

Rock properties	Fluid properties	Environment
Compaction	Viscosity	Frequency
Consolidation history	Density	Stress history
Age	Wettability	Depositional environment
Cementation	Fluid composition	Temperature
Texture	Phase	Reservoir process
Bulk density	Fluid type	Production history
Clay content	Gas-oil, gas-water ratio	Layer geometry
Anisotropy	Saturation	Effective stress
Fractures		
Porosity		
Lithology		
Pore shape		

Table A.5: *Factors influencing seismic properties of sedimentary rocks (with increasing importance from top to bottom), Wang [2001].*

Figure A.4 depicts the measurements of the compressional velocity in porous sandstone, where the dry rock was saturated with water, Gregory [1976] and Bourbie et al. [1987]. From Figure A.4 it is obvious that at lower porosity the compressional velocity will increase by substituting the air with water. This could be explained by the fact that the changes in the bulk density are smaller than the changes in the elastic modulus of the saturated rock. In rocks with porosity between 10 and 25 $\%$ no changes in the seismic velocity are monitored until 70 $\%$ of water saturation, this means that the effect of changes in the bulk density is equal to the effect of changes in the bulk modulus. After this threshold of 70 $\%$, the velocity increased with increas-

ing water saturation. In case of high porosity sandstones the P-wave velocity is decreasing, where the maximum of this decrease occurr at about 20 - 30 % of water saturation. Wang et al. [1991] presented the combined effect of changes in the effective stress and saturation with different kind of liquids on Ottawa 30-50% saturated unconsolidated sands. The results are reproduced in Figure A.5.

The seismic velocities are decreasing with increasing porosity, as presented by Bourbie et al. [1987], Schoen [1996], Han et al. [1986], Kuster and Toksöz [1974a], Kuster and Toksöz [1974b], Zimmer et al. [2007a], Zimmer et al. [2007b] and Zimmer et al. [2002]. Porosity is defined as the ratio of the volume of void or pore space to the total volume of the rock. From Figure A.4 it flollows that by increasing porosity the bulk modulus decreases which causes a decrease in the seismic velocity. This can be also confirmed by investigating the Gassmann equation 3.9. Based on laboratory measurements, Han et al. [1986] shown an empirical relation between the porosity and seismic velocity in sandstones. Similar results were shown by Castagna et al. [1985], Wang [2002a] and Wang [2002b], the last two including the effect of the weak anisotropy.

Wang and Nur [1990] presented laboratory experiments of dry sandstones and liquid saturated sandstones, where the compressional and shear velocities were measured by different temperatures. Generally there are speeddowns in the seismic velocities as a function of temperature, Mavko et al. [1998]. Wang and Nur [1990], Nur et al. [1984] and Timur [1977] showed that the seismic velocities and impedances decrease only slightly in rocks saturated with gas and water as the temperature increases. When the rock is saturated with oil, the seismic velocity may decrease by large amounts with increasing temperature, especially in the case of heavy oils and unconsolidated sands. According to Tosaya et al. [1987] and Wang and Nur [1990], the decrease of the seismic velocity in the heavy oil sands is a consequence of temperature increase. The factors that caused the velocity to vary with temperature are the changes in the compressibility of the liquid, changes in the viscosity of the saturating fluid, and changes in the phase, Bourbie et al. [1987]. Carmichael [1982] showed that for low porosity rocks the decrease in velocity with temperature is nearly 5% for a temperature increase of about 100 C. According to Timur [1977] and Jones and Nur [1983] the velocity variations as a result of temperature changes can be significant for

high-porosity sandstones.

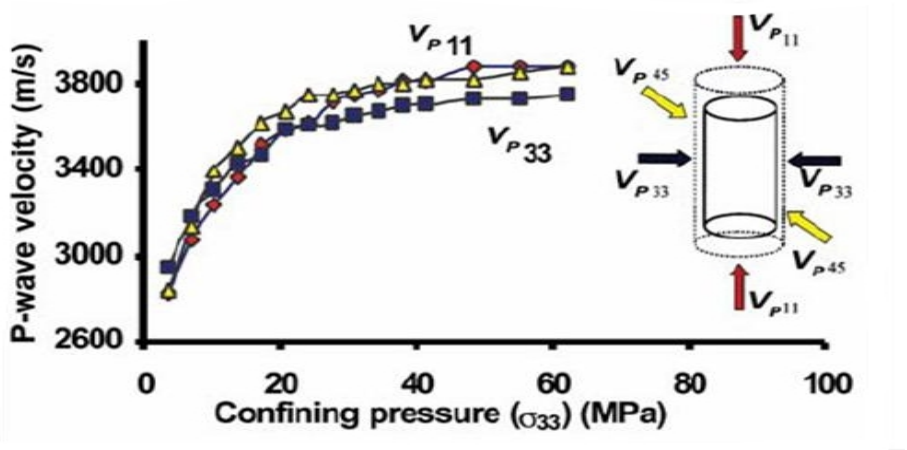

Figure A.3: *Alternations in the P-velocities induced by increasing the effective stress (confining pressure). The hydrostatic compression test was applied on Berea sandstone, Scott [2007].*

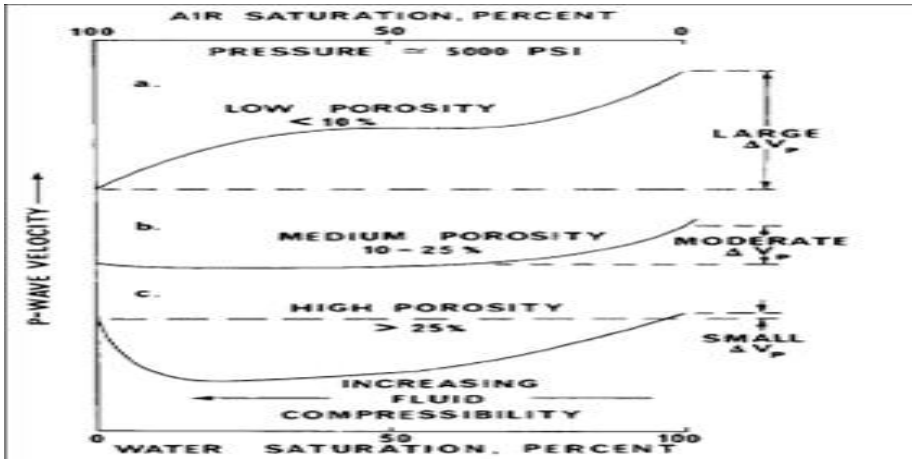

Figure A.4: *"Characteristic" behavior of velocity as a function of water saturation for consolidated sediments and a confining pressure of 35 MPa, Gregory [1976].*

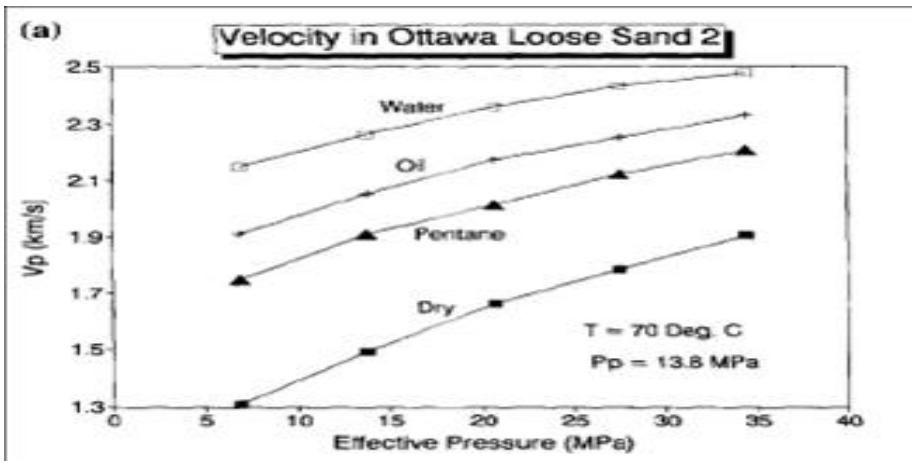

Figure A.5: *Compressional velocity in Ottawa unconsolidated sands, Wang et al. [1991].*

A.6 Limitations of the analytical model of the North Sea reservoir

The limitations of the used analytical model are:

- The effect of static and dynamic modulus. The initial elastic properties used for the reservoir modelling are derived from the wave speeds and bulk density. The wave-derived elastic modula are the dynamic properties, while the in-situ reservoir rocks are deformed statically. The wave-derived or laboratory-measured dynamic elastic modulus needs to be converted to static a elastic modulus, representing the in-situ application. This conversion is not straightforward for the reservoir rocks. Several authors presented empirical relations between dynamic and elastic modulus, Simmons [1965], Cheng [1981], van Heerden [1987], Eissa and Kazi [1988], Yale and Jamieson [1994] and Wang and Nur [2000], which can be used to convert the dynamic to static modulus. This kind of corrections should be applied to the estimated dynamic modulus. After that, the calculated static modulus can be used in the reservoir model.

- Another problem, related to the estimation of the elastic modulus from the log data, is the reliability of the core data study, discussed by Holt et al. [2000], Nes et al. [2000] and Charlez [1997]. Core samples retrieved from deep boreholes may be damaged as a result of the stress release occurring during the drill-out. A primary concern is to quantify and correct for core damage effects, which significantly enhances the stress dependency of wave velocities. Careful laboratory procedures and modeling efforts may reduce such effects.

- The used reservoir model is applicable for isotropic solids. However, the cracks, faults, flat pores, fine-layered medium, and fluid substitution are introducing anisotropy in the elastic properties and in the seismic velocity in the reservoir rock. The anisotropy induced by the inhomogeneity of the dry rock was discussed in several papers Backus [1962], Thomsen [1986], Sayers and van Munster [1991], Schoenberg and Sayers [1995] and Thomsen [2002]. The effect of fluid phase on the seismic anisotropy was presented by Gelinsky and Shapiro [1997],

Mukerji and Mavko [1994] and Thomsen [1995]. Vernik and Nur [1992] and Vernik and Liu [1997] presented a number of measurements on saturated rocks from various sources, the results confirm that the anisotropy is strongly affected by the kerogen contents.

- The limitations of the Gassmann theory were already discussed in Section A.4.

B

Appendix B

B.1 2D Box-model of North Sea live-oil reservoir

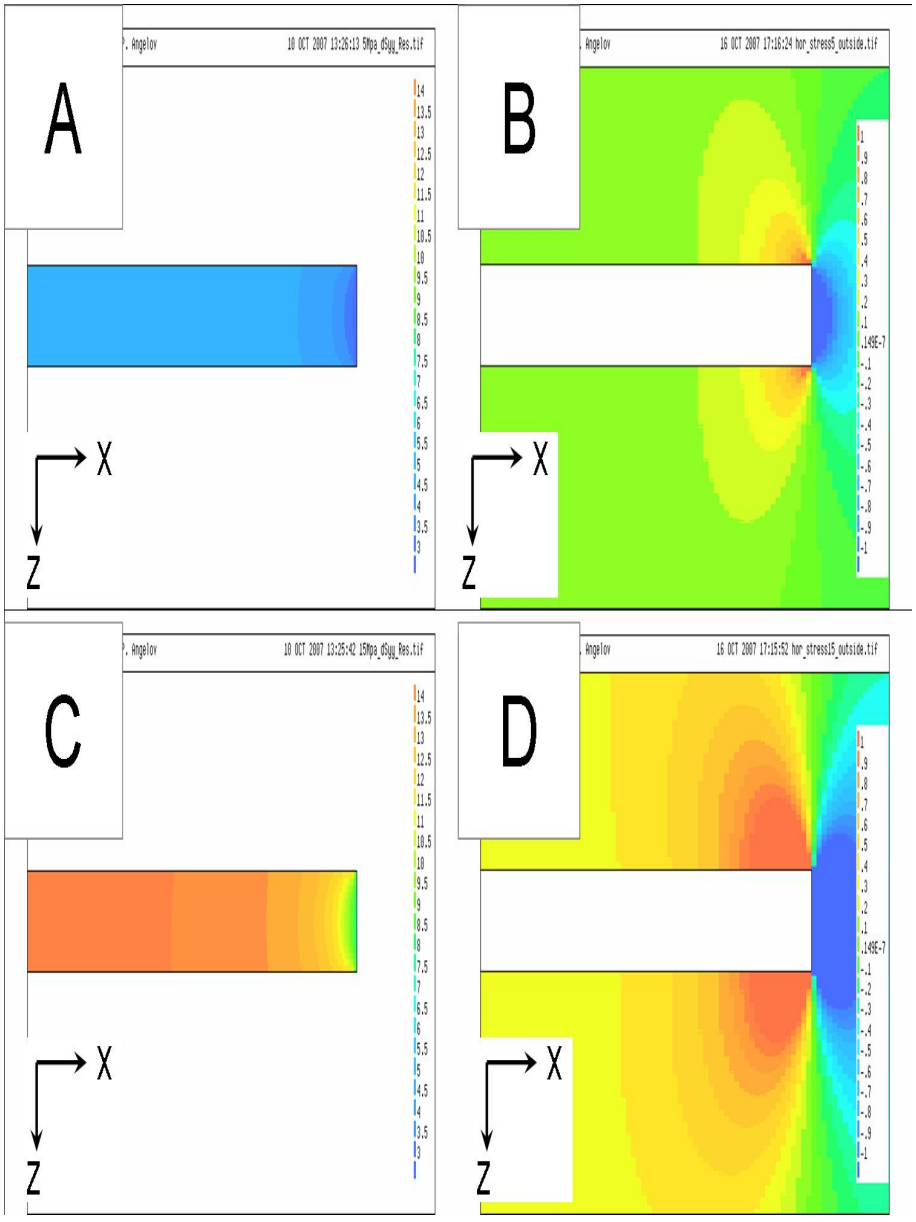

Figure B.1: *Time-lapse changes in the vertical stress as result of pressure depletion at the reservoir level. A, B - changes in the reservoir and in the overburden after pressure drop of 5 MPa. C, D - changes in the reservoir and in the overburden after pressure drop of 15 MPa. The range of the color map used on A and C is between -1 and 1 MPa, and for B and D is from 3 to 15 MPa. The stress changes are increasing from "cold" to "hot" color. The place, outside the reservoir, where the stress field remain unchanged are colored in green.*

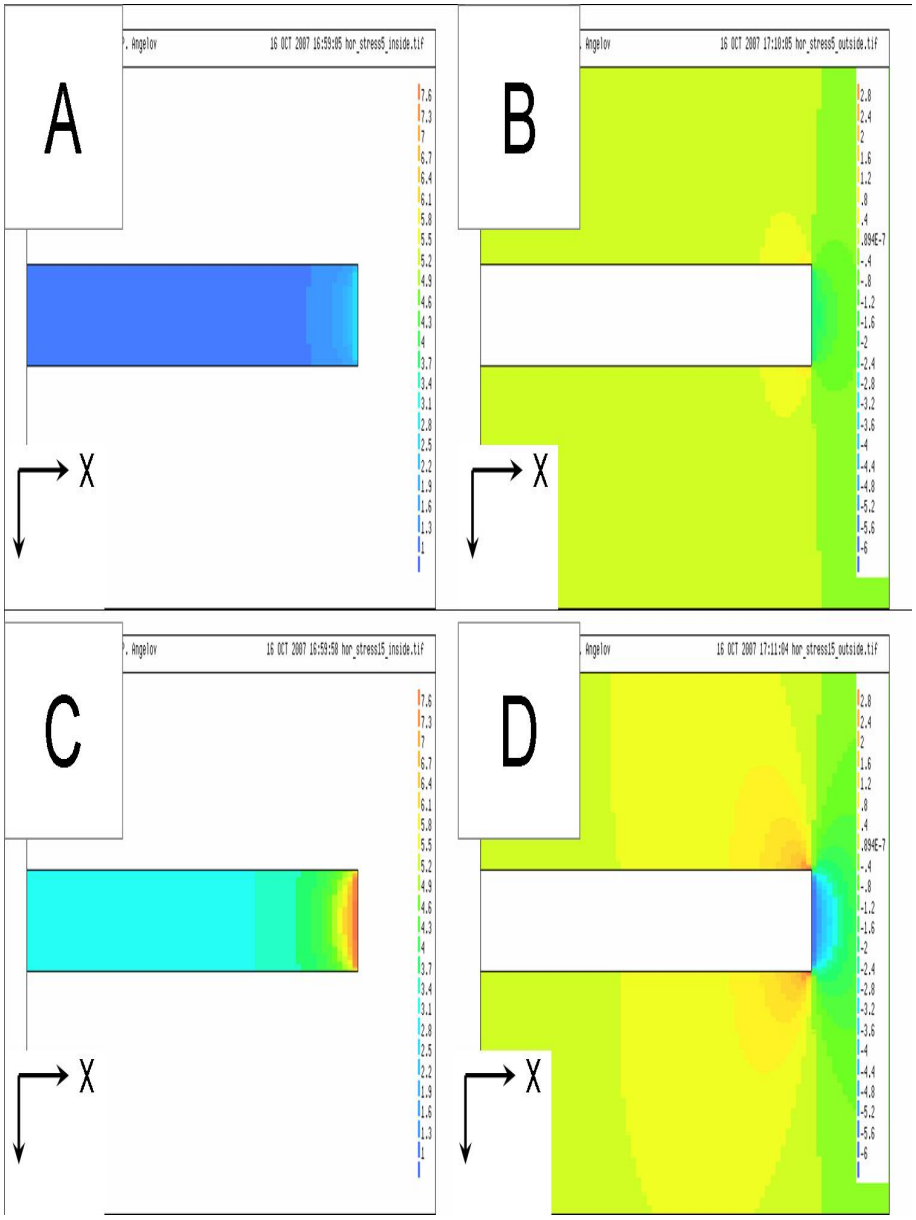

Figure B.2: *Time-lapse changes in the horizontal stress as result of pressure depletion at the reservoir level. A, B - changes in the reservoir and in the overburden after pressure drop of 5 MPa. C, D - changes in the reservoir and in the overburden after pressure drop of 15 MPa. The range of the color map used on A and C is between -1 and 1 MPa, and for B and D is from 1 to 8 MPa. The stress changes are increasing from "cold" to "hot" color. Places outside the reservoir, where the stress field remain unchanged, are colored in green.*

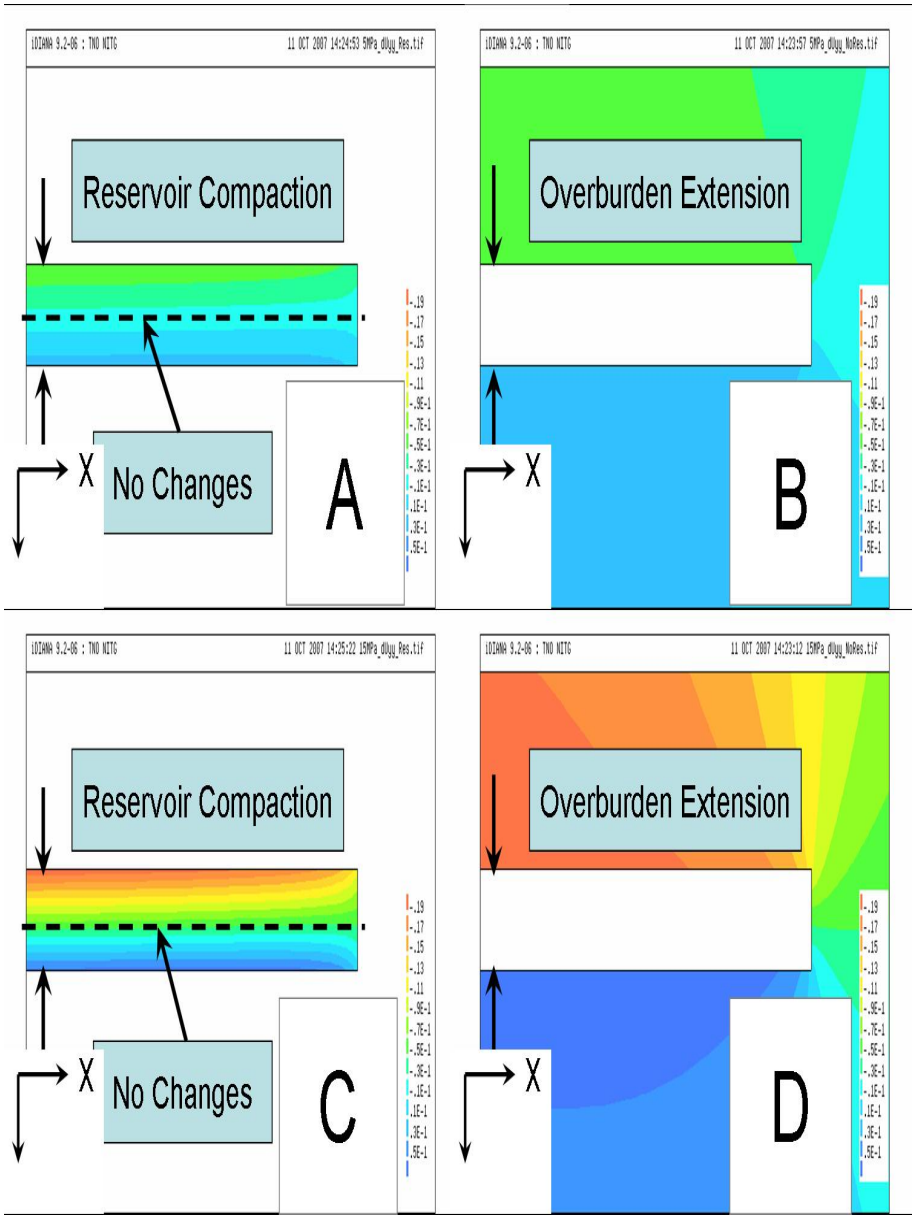

Figure B.3: *Vertical displacement as result of pressure depletion at the reservoir level. A, B - changes in the reservoir and in the overburden after pressure drop of 5 MPa. C, D - changes in the reservoir and in the overburden after pressure drop of 15 MPa. The range of the color map is between -20 and 5 cm. The "hot" colors are used to map the displacement in the direction from the surface to the reservoir top, where the "cold" colors are presenting the pushup of the under-burden in the direction of the Earth surface. The displacement is negligible or zero at places that are painted in light-blue.*

Figure B.1 illustrates the changes in the vertical stress inside the reservoir and in the overburden resulting from depletion of 5 and 15 MPa at the reservoir level. In Figure B.1 A and C, there are no significant lateral and vertical variations in the changes of the vertical stress inside the reservoir, except very close to the lateral boundaries with the side-burden. Outside the reservoir, Figure B.1 B and D, the stress changes are concentrated near the edges of the reservoir, on the top and on the bottom, as well in the side-burden close to the reservoir. The observed changes in the reservoir are between 2.5 and 5 MPa for the pressure depletion of 5 MPa, and from 8 to 15 MPa for a pressure drop of 15 MPa. Outside the reservoir the values are between -1 and 3 and -4 and 9 MPa respectively. The decrease of the vertical stress is monitored at the top and the bottom of the reservoir, whereas in the side-burden, in the vicinity of the reservoir, the vertical stress increases slightly . Figure B.2 presents the calculated changes of the horizontal stress, using the same assumption as described for the vertical stress. As discussed in Section 4.3 (equations 4.15 and 4.16), the changes in the horizontal and vertical stress are related. The time-variations in σ_h are approximately $1/3$ of the changes in σ_v, because of the K_0 value. The reservoir compaction, caused by the hydrocarbon production, is plotted in Figure B.3. The sign of the vertical displacement show, that the reservoir top and bottom are displaced in the direction towards the center of the reservoir. The value of the overburden elongation is much larger than the under-burden push-up. This is because the subsidence of the top of the reservoir is supported from the whole weight of the overburden. The expected maximum of the compaction is positioned at the center of the reservoir. In the direction towards the reservoir edges the stress arching is protecting the reservoir from the overburden load. This causes the lateral variations (reduction) of the vertical compaction in direction from the center to the lateral boundaries of the reservoir. Therefore, to understand the stress variations illustrated in Figure B.1 to Figure B.3, the stress arching must be considered. The stress arching (γ) is often referred to the coordinate system used, so that for instance for an, x,z-coordinate system the terms γ_x and γ_z would apply instead of γ_h and γ_v. Figure B.4, B.5 and B.6 depict the changes in the effective stress per unit depletion, for the horizontal and the vertical monitoring lines, Figure 5.5. The drop in pore pressure has a direct influence on the effective stress inside the reservoir, equation 4.18. As can be estimated, from equation 4.17 the changes

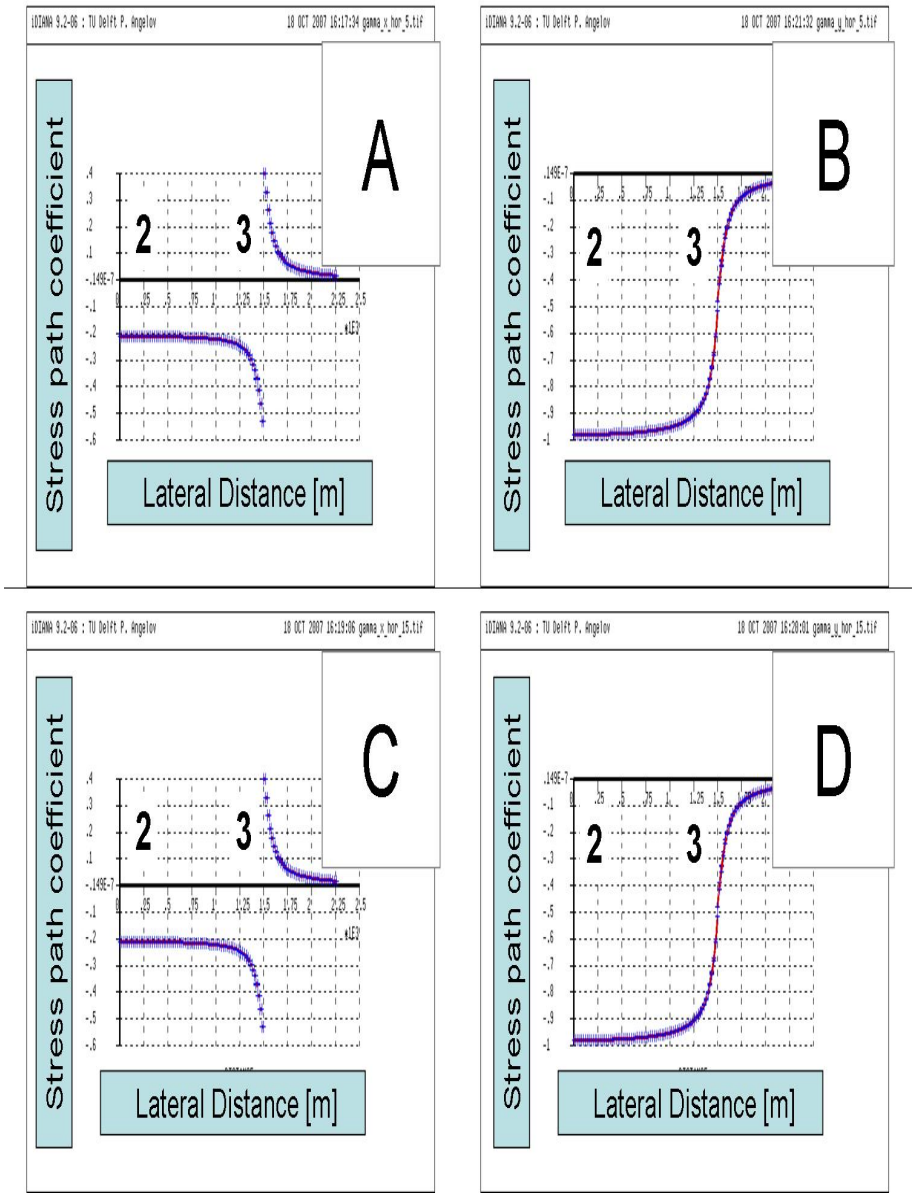

Figure B.4: *Changes in the effective stress per unit of depletion. A, B - γ_x and γ_z after pressure drop of 5 MPa. C, D - γ_x and γ_z after pressure drop of 15 MPa. The horizontal observation line, Figure 5.5, is used.*

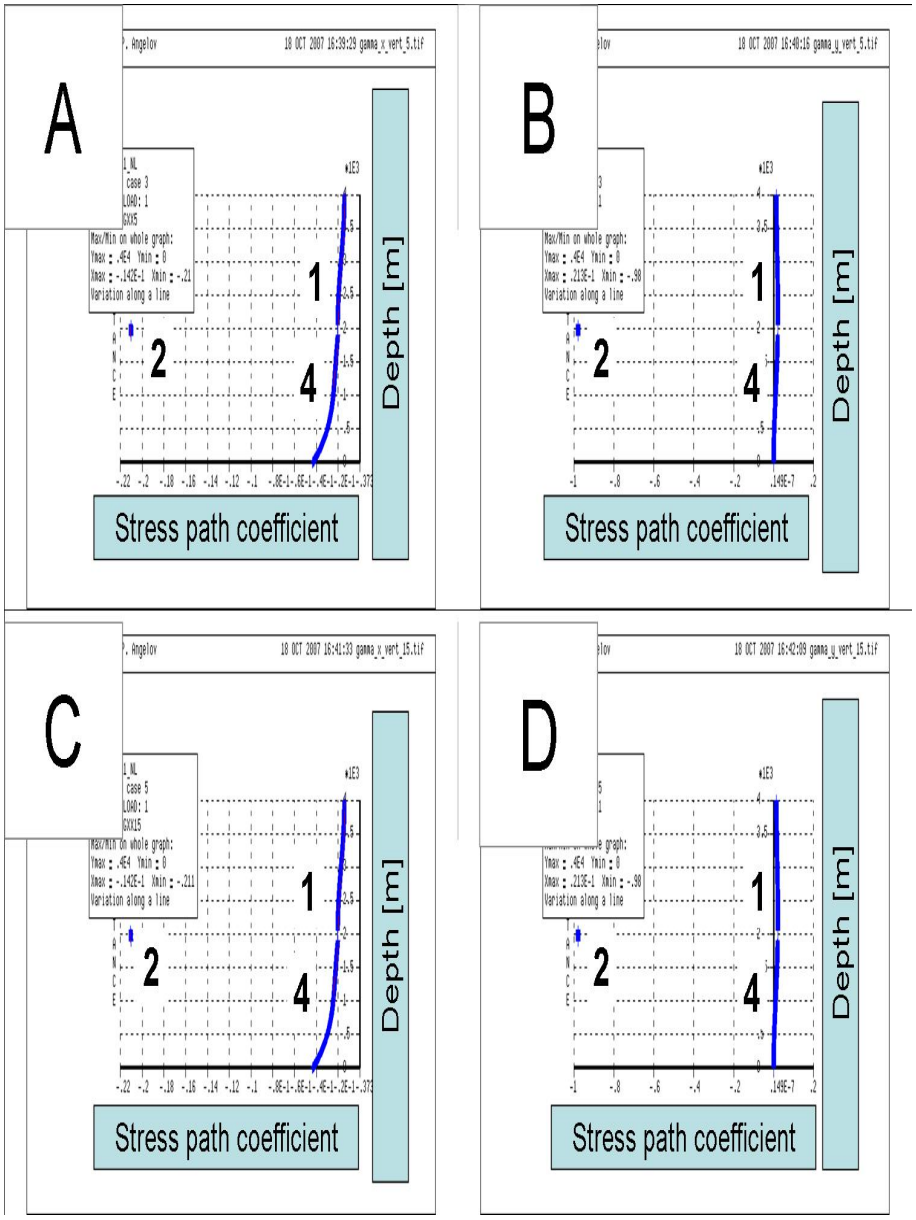

Figure B.5: *Changes in the effective stress per unit of depletion. A, B - γ_x and γ_z after pressure drop of 5 MPa. C, D - γ_x and γ_z after pressure drop of 15 MPa. The vertical observation line, Figure 5.5, is used.*

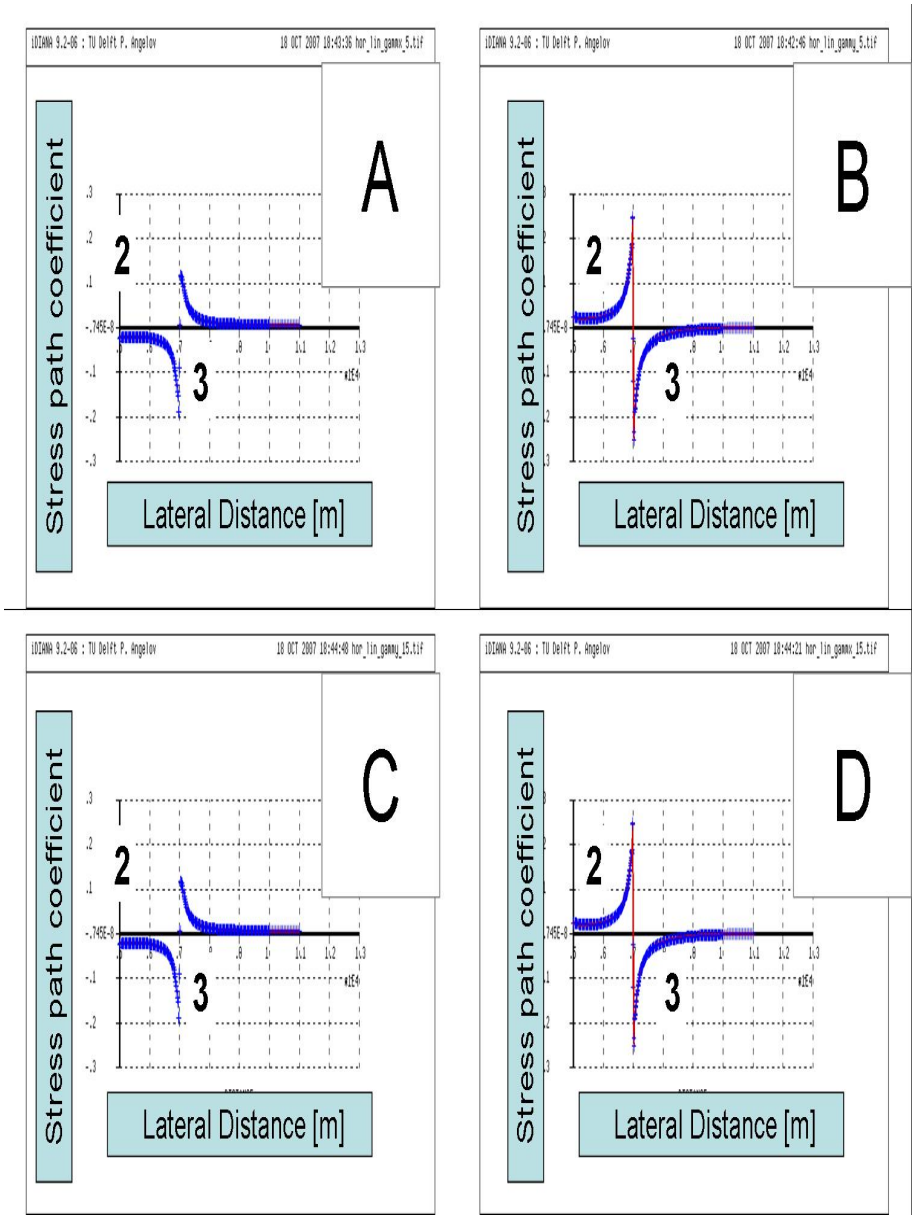

Figure B.6: *Changes in the effective stress per unit of depletion. A, B - γ_x and γ_z after pressure drop of 5 MPa. C, D - γ_x and γ_z after pressure drop of 15 MPa. The horizontal observation line is situated just above the top of the reservoir, and it is parallel to the horizontal line presented on Figure 5.5.*

in the vertical stress will be larger than the changes in the horizontal stress ($K_0 < 1$). Inside the reservoir the largest changes occur in the vertical effective stress. Significant alternations in the horizontal component of the effective stress are monitored only near the lateral edges of the reservoir. This effect is most likely due to the forces occurring at the boundary between the reservoir and the side burden, resulting from the lateral compaction of the reservoir. The changes in the vertical stress are almost constant throughout the whole reservoir and decrease at the lateral boundary of the reservoir. To understand the effect of pressure depletion on the effective stress in the overburden, the horizontal monitoring line is situated just above the reservoir top. The stress variations are positioned at the lateral edges above the reservoir is result from stress arching. The stress arching is protecting the compacted top of the reservoir from the overburden load. In the other parts of the model, above the reservoir the stress changes are negligible.

B.2 2D model of North Sea gas reservoir; Shearwater field

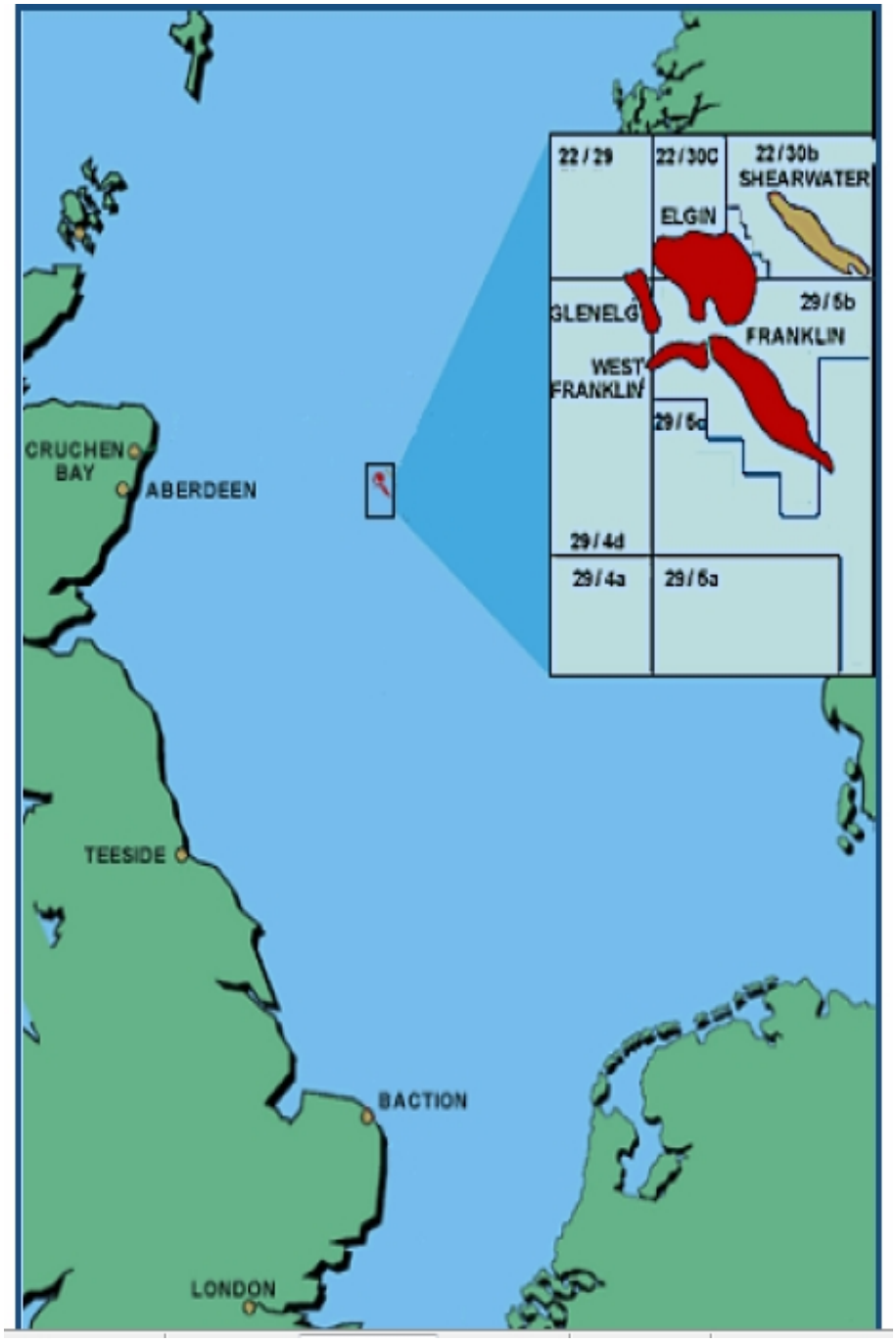

Figure B.7: *Map of the North Sea showing the Shearwater field (in yellow color), Holm et al. [2005].*

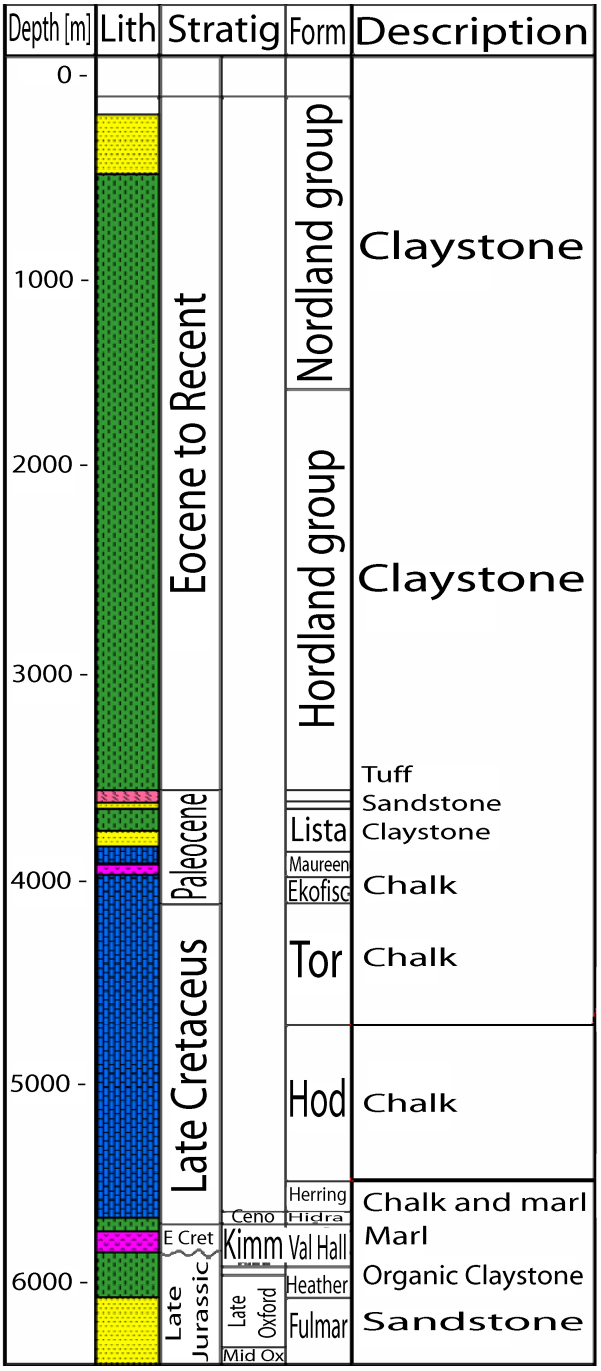

Figure B.8: *Generalized stratigraphy of Elgin/Franklin/Shearwater are, Holm et al. [2005].*

■ B.2.1 2D box-model

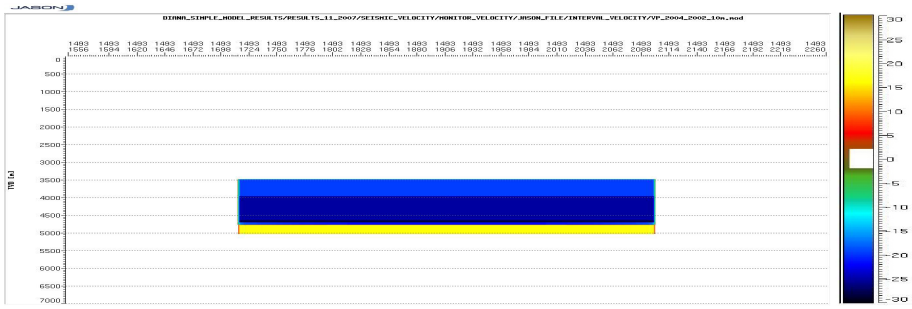

Figure B.9: *Time-lapse changes in the P-wave velocity as result of pressure depletion at the reservoir level. The "hot" colors are presenting increase in the seismic velocity, where the "cold" colors are denoted to velocity decrease. The color bar is in m/s.*

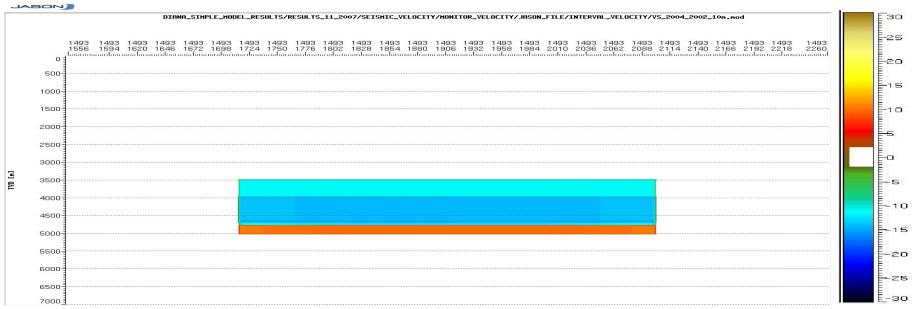

Figure B.10: *Time-lapse changes in the S-wave velocity as result of pressure depletion at the reservoir level. The "hot" colors are presenting increase in the seismic velocity, where the "cold" colors are denoted to velocity decrease. The color bar is in m/s.*

■ B.2.2 Complex 2D Model

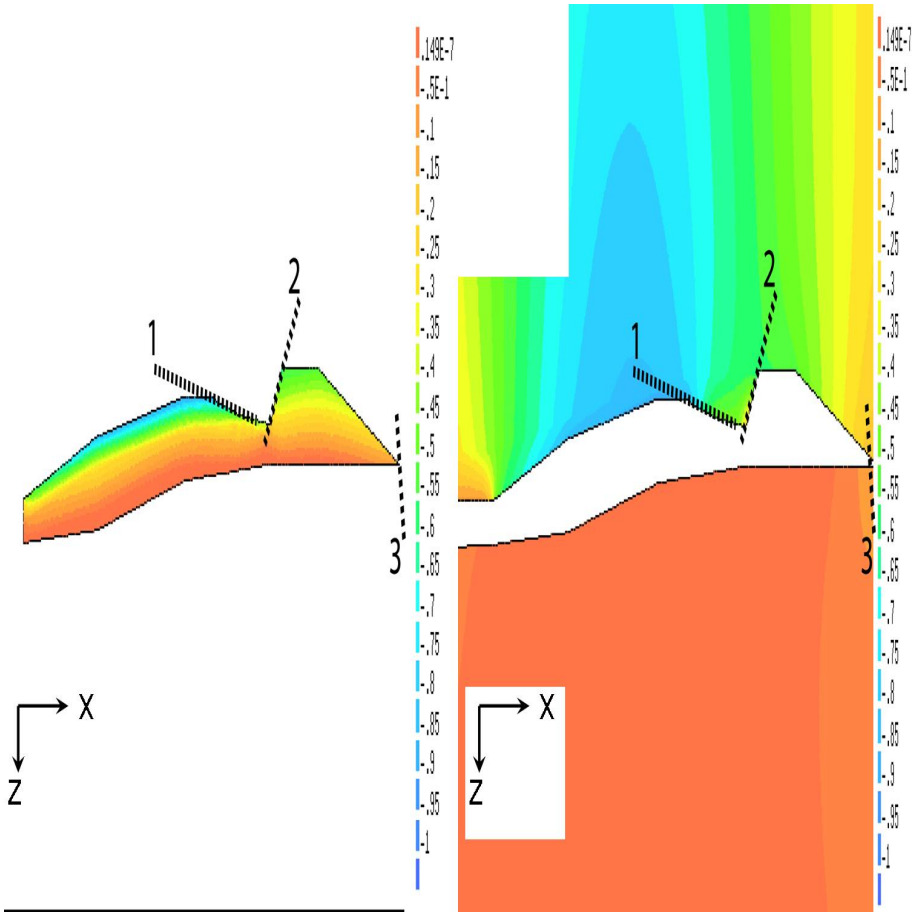

Figure B.11: *The vertical displacement as result of pressure depletion. Left - vertical displacement at the reservoir, right - vertical displacement in the surrounding layers. The elongation of the overburden is laterally decreasing from the central part to the edges of the reservoir, from "cold" to "hot" colors. The push-up of the underburden is laterally constant through the whole part of the reservoir. The color bar is in m. The the three known faults are labeled by 1,2 and 3.*

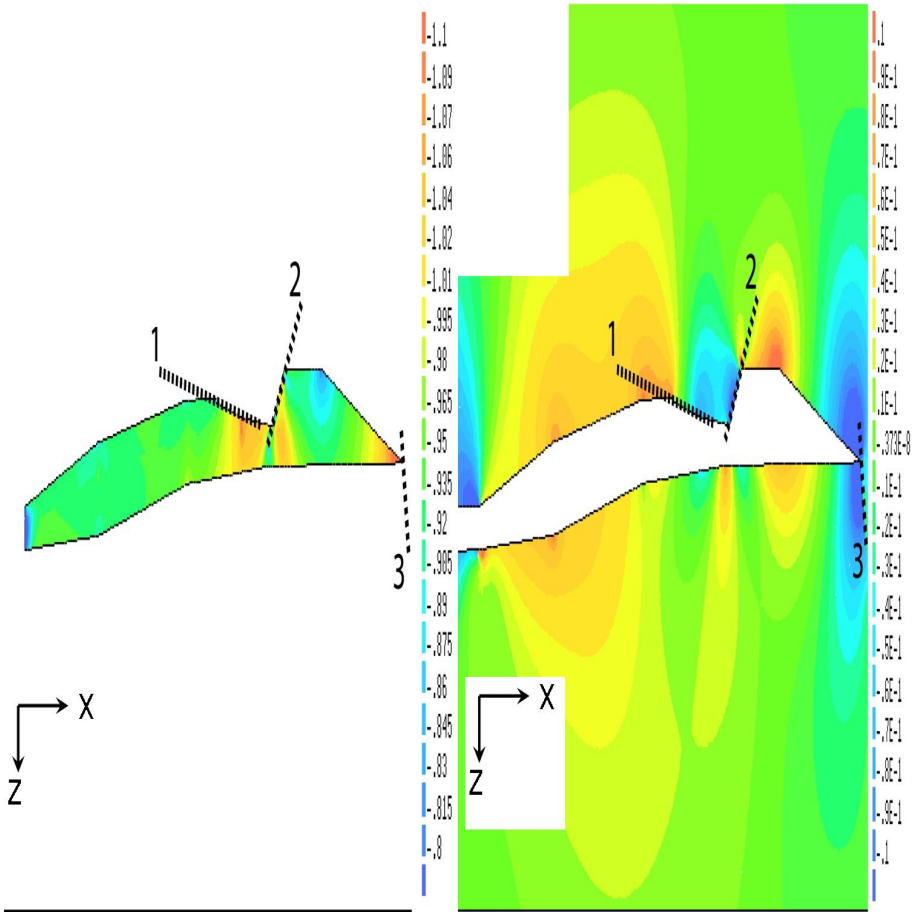

Figure B.12: *The vertical stress path (γ_z) at the reservoir level - left, and i the surrounding layers - right. With 1, 2 and 3 are labeled the three known faults. The maximum absolute value of the stress-path coefficient is monitored near the faults 2 and 3. The stress path absolute value is increasing from "cold" to "hot" colors.*

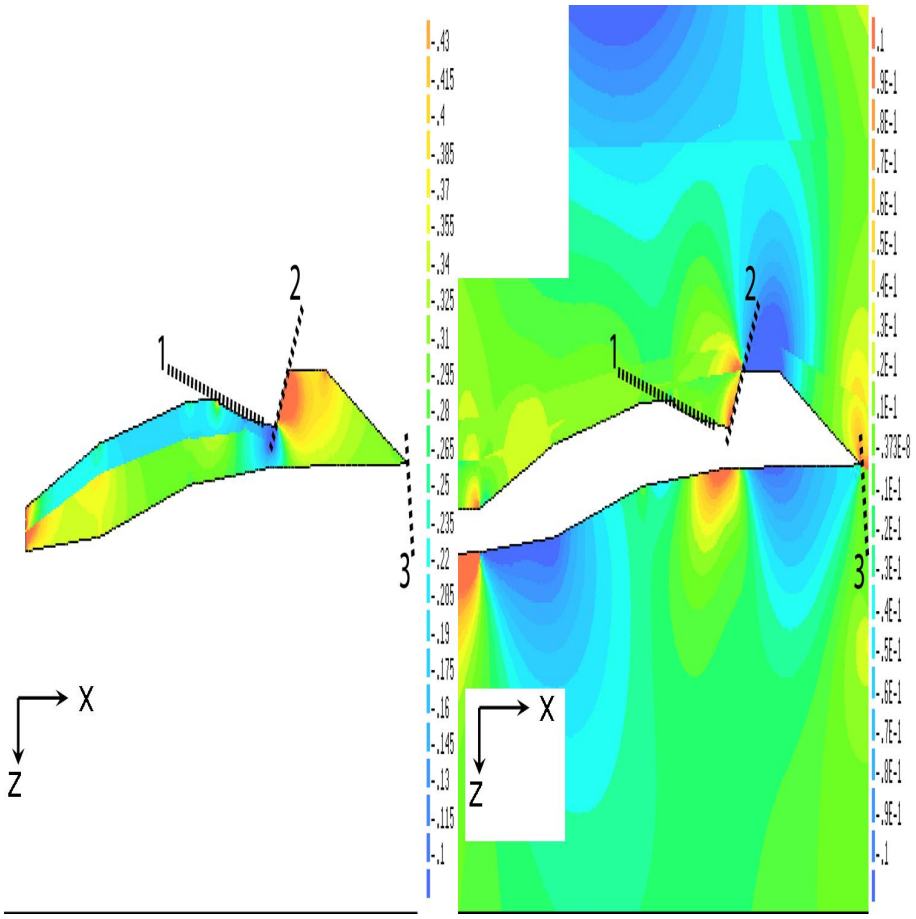

Figure B.13: *The horizontal stress path (γ_z) at the reservoir level (left), and in the surrounding layers (right). The three known faults are labeled with 1, 2 and 3. The maximum absolute value of the stress path coefficient is monitored near the faults 2 and 3. The stress path absolute value is increasing from "cold" to "hot" colors.*

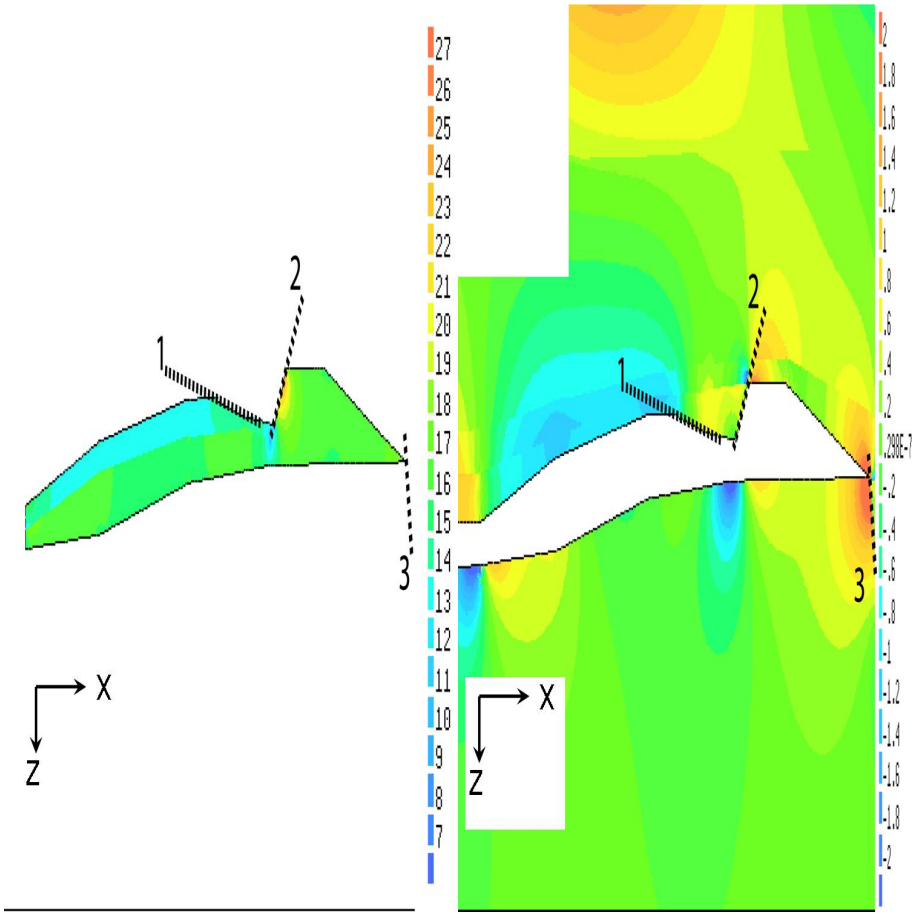

Figure B.14: *The mean effective stress changes at the reservoir level (left), and in the surrounding layers (right) as result of pressure depletion.*

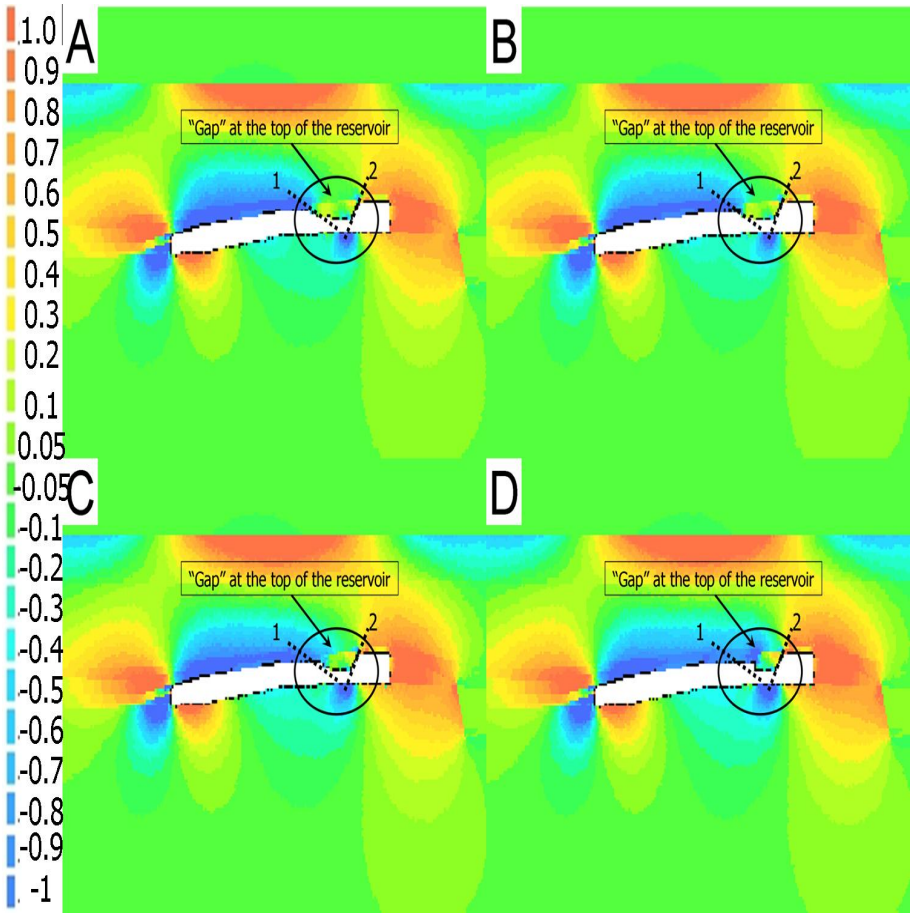

Figure B.15: *The mean effective stress changes in MPa below and beneath the reservoir level as result of pressure depletion. A sequence of models is calculated for which the gap in the top of the reservoir between 1 and 2 is smoothly closed. This is done by replacing the overburden with the reservoir with a step of 100 m (from A to D). The white part of the model represents the reservoir. Note that the results are clipped between -1 and 1 MPa.*

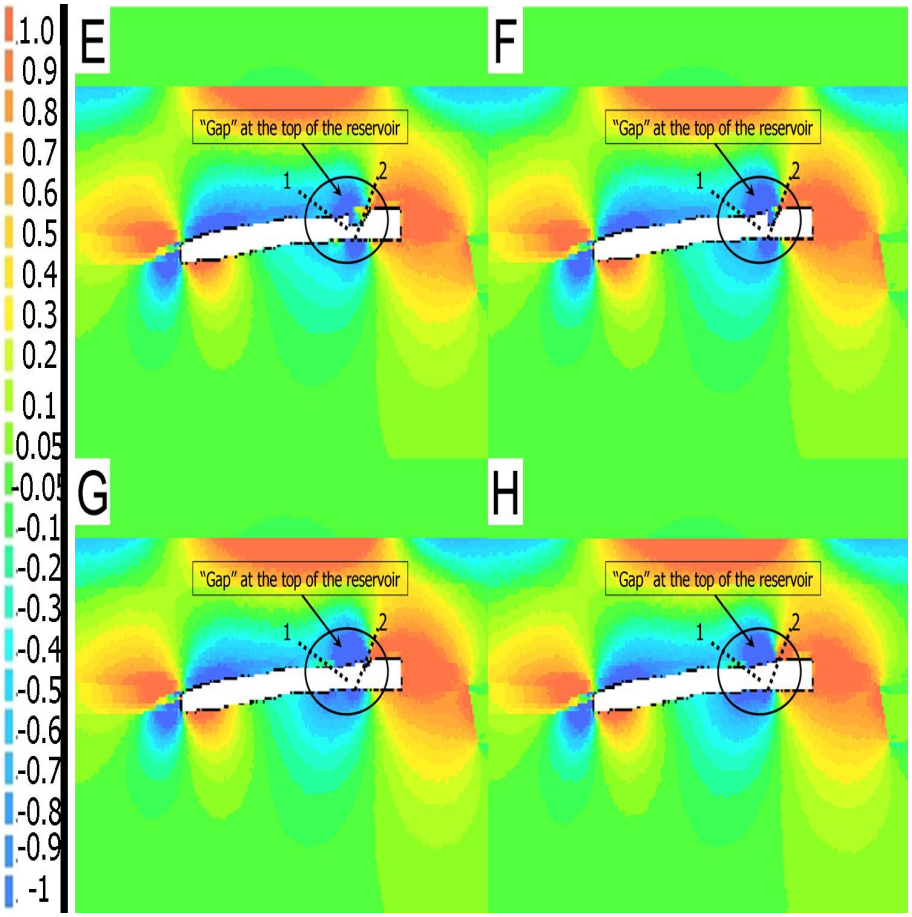

Figure B.16: *The mean effective stress changes in MPa below and beneath the reservoir level as result of pressure depletion. A sequence of models is calculated for which the gap in the top of the reservoir between 1 and 2 is smoothly closed. This is done by replacing the overburden with the reservoir with a step of 100 m (from E to H). The white part of the model represents the reservoir. Note that the results are clipped between -1 and 1 MPa*

C

Appendix C

C.1 Time-shift Shearwater

C.1.1 Transmission models

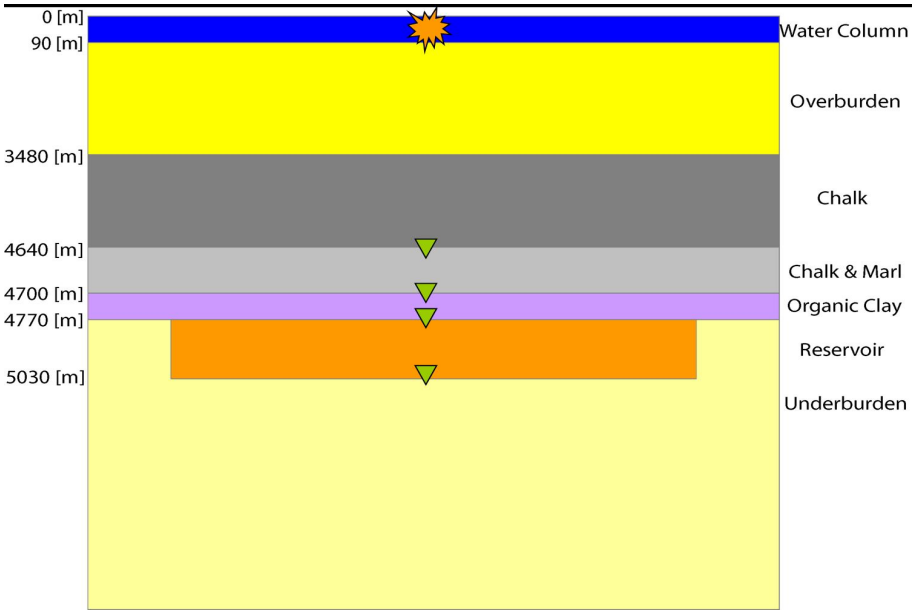

Figure C.1: *Transmission model. The receivers are situated at the interfaces, where time-shifts are expected. The source is positioned 5 [m] below the sea level. The length of the reservoir is 4000 [m].*

C.1.2 Pre-migrated zero offset gather

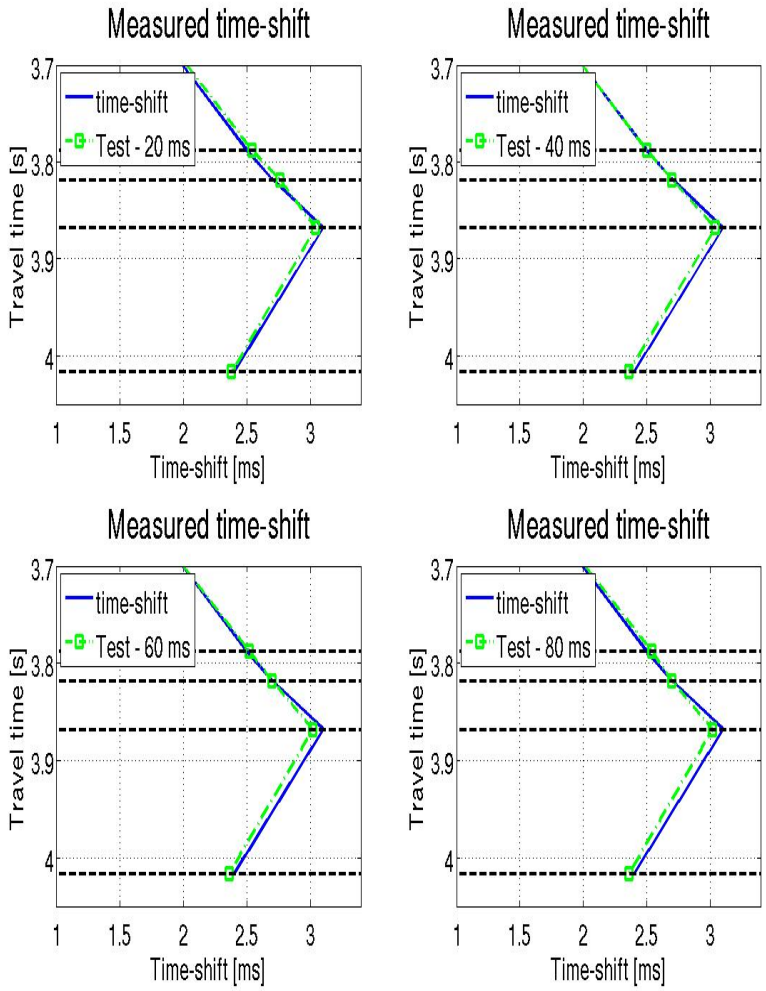

Figure C.2: *Expected and measured time-shifts for models 1 and 4. The expected results are presented with blue solid line, where the measured time-shifts are presented with green dashed line. Vertical correlation window used to produce the measured time-shifts vary from 20 to 80 [ms].*

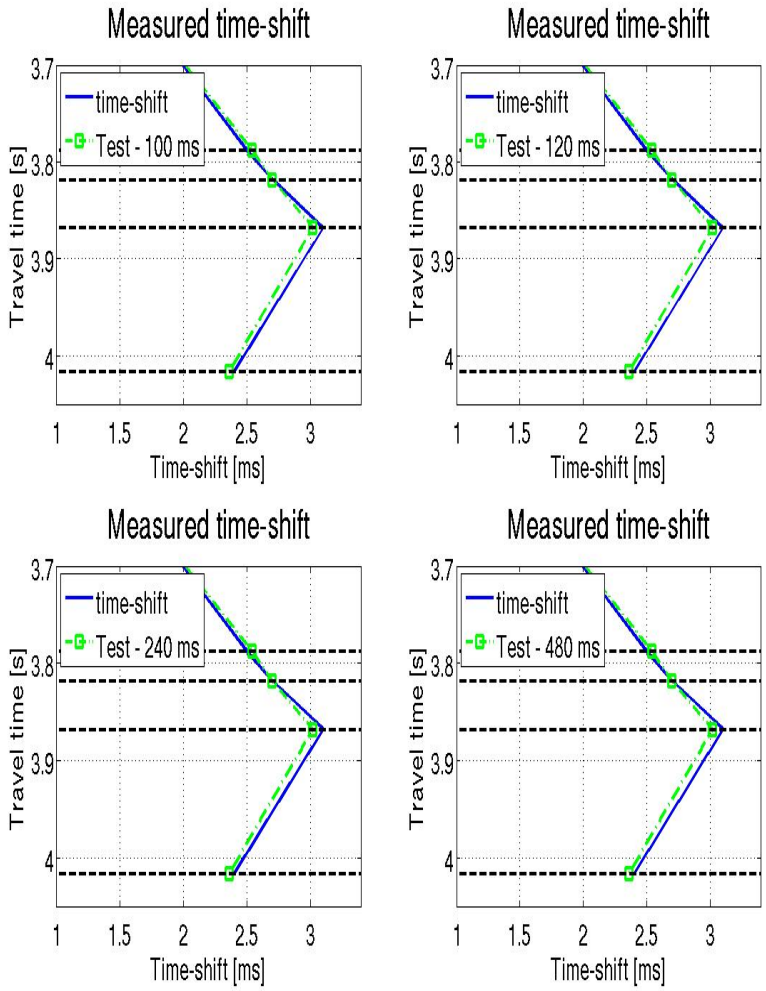

Figure C.3: *Expected and measured time-shifts for models 1 and 4. The expected results are presented with blue solid line, where the measured time-shifts are presented with green dashed line. Vertical correlation window used to produce the measured time-shifts vary from 100 to 480 [ms].*

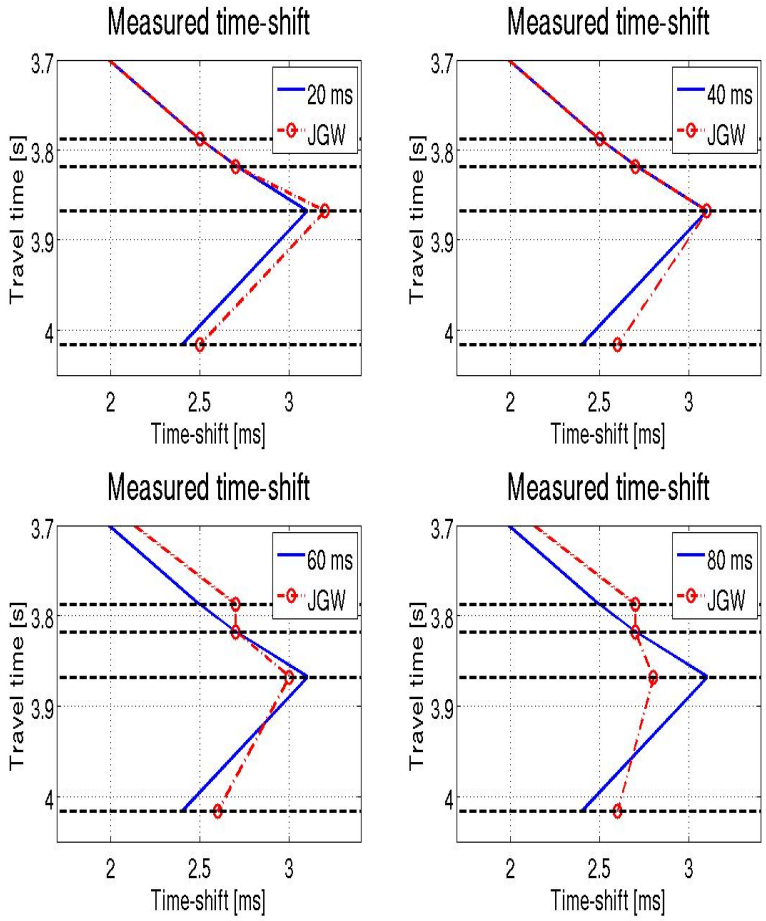

Figure C.4: *Measured time-shift for the zero-offset data at the center of the reservoir. Blue - expected time-shift, red - time-shift measured using JGW. Correlation windows from 20 to 80 [ms] are used.*

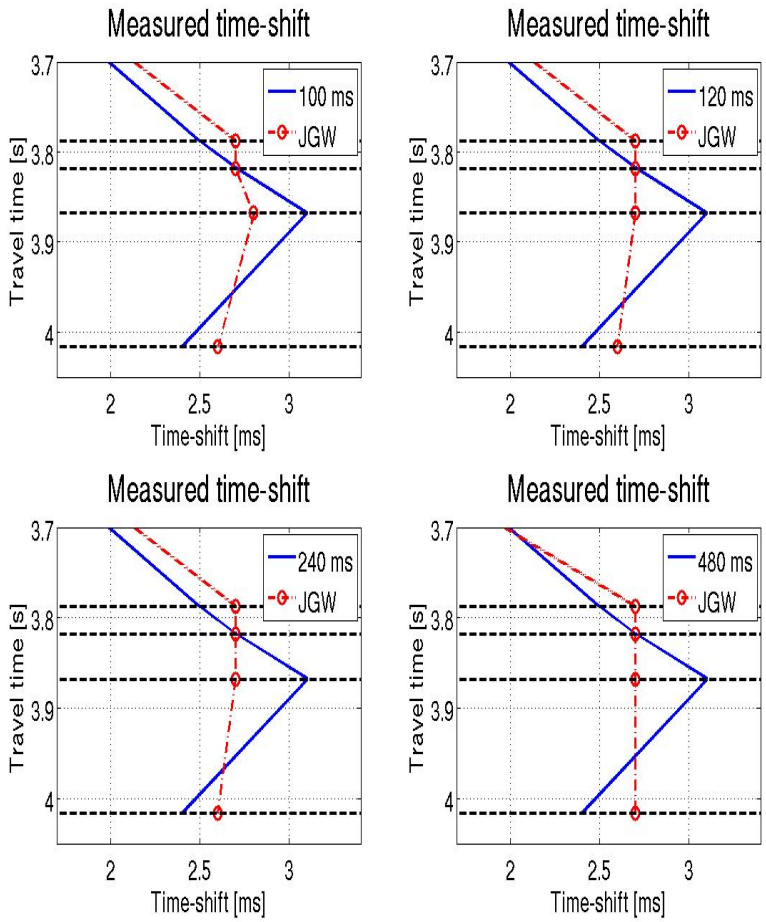

Figure C.5: *Measured time-shift for the zero-offset data at the center of the reservoir. Blue - expected time-shift, red - time-shift measured using JGW. Correlation windows from 100 to 480 [ms] are used.*

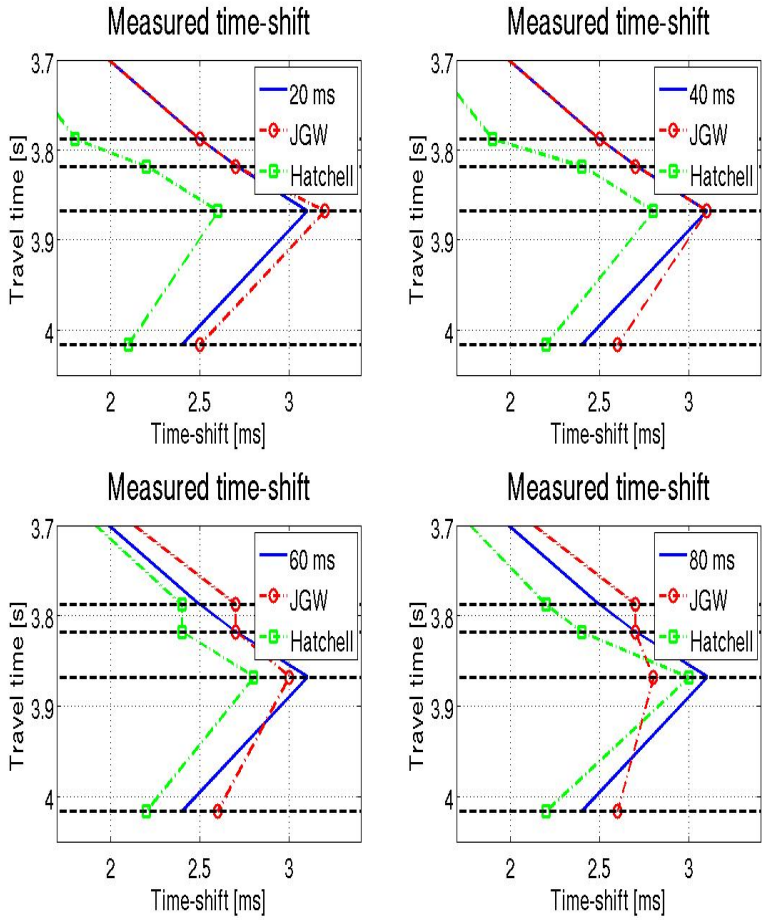

Figure C.6: *Measured time-shift for the zero-offset data at the center of the reservoir. Blue - expected time-shift, red - time-shift measured using JGW. Green - time-shift measured using the Hatchell approach. Correlation windows from 20 to 80 [ms] are used.*

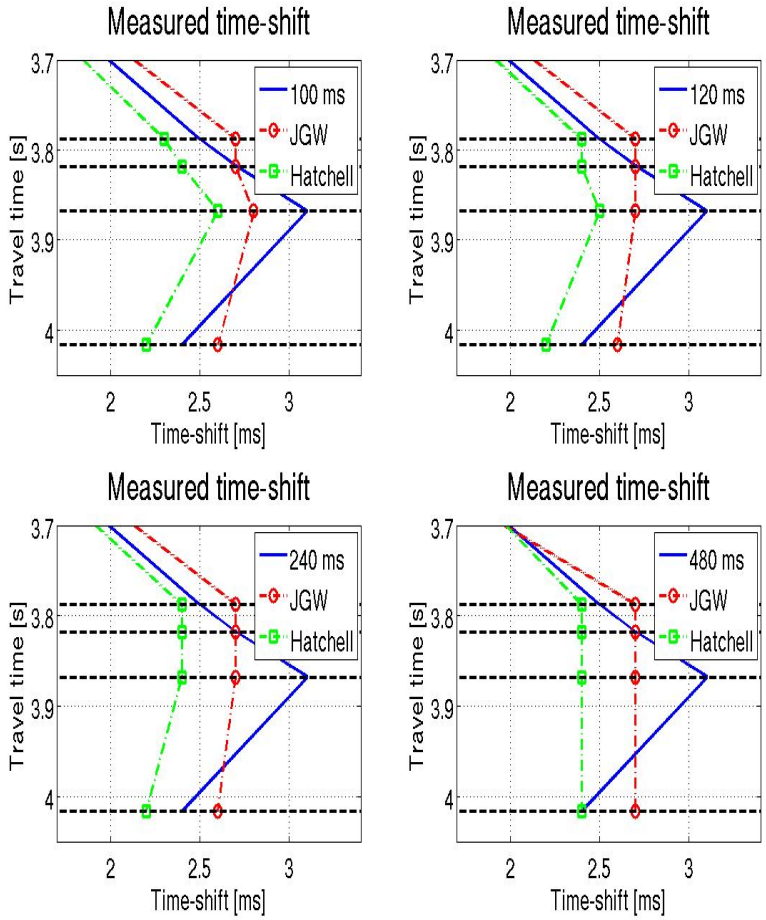

Figure C.7: *Measured time-shift for the zero-offset data at the center of the reservoir. Blue - expected time-shift, red - time-shift measured using JGW. Green - time-shift measured using the Hatchell approach. Correlation windows from 100 to 480 [ms] are used.*

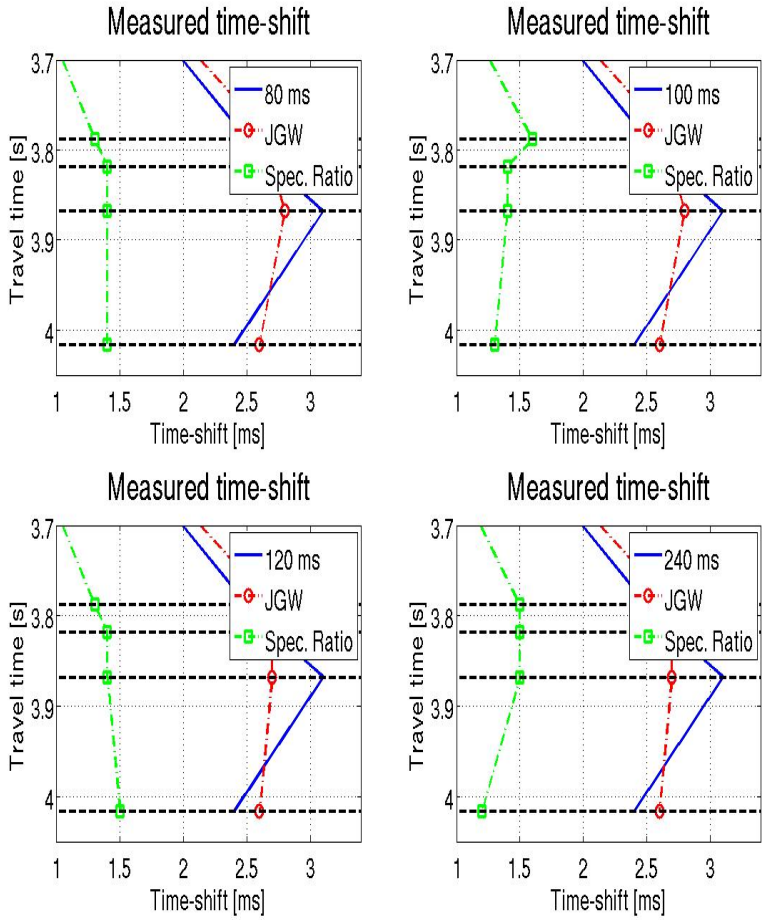

Figure C.8: *Measured time-shift for the zero-offset data at the center of the reservoir. Blue - expected time-shift, red - time-shift measured using JGW. Green - time-shift measured using the spectral ratio. Correlation windows from 80 to 240 [ms] are used.*

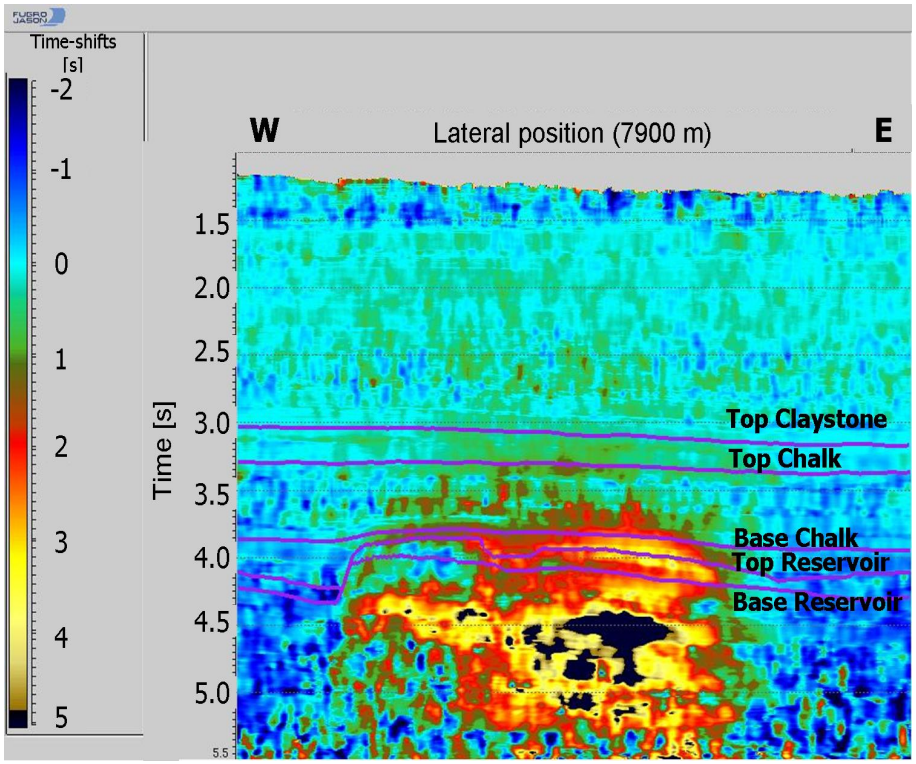

Figure C.9: *Measured time-shift from the full-stack data (Shearwater). The interpreted time-horizons are plotted in pink color.*

Acknowledgments

The research presented in this thesis was supported by the Technology Foundation STW, applied science division of NWO and the technology program of the Ministry of Economic Affairs (grant DAR.5763). The research was carried out at the department of Applied Geophysics and Petrophysics, section of Geotechnology, Faculty of Civil Engineering and Geosciences at Delft University of Technology. I would like to thank all colleagues at the department for the support and discussions during my time in Delft. Especially, I would like to thank my two promoters Prof. Kees Wapenaar and Prof. Rob Arts for all their input and advice. I also would like to thank Dr. Jesper Spetzler who was my daily supervisor in the first two years of my research.

I also would like to acknowledge Dr. Bogdan Orlic from TNO who was guiding me in my first and last steps in the geo-mechanical modelling. Dr. Bogdan Orlic was always ready to help me technically and with scientific advices.

I would like to acknowledge Dr. Peter Mesdag from "Fugro-Jason". I am much indebted to Dr. Peter Mesdag for helping me to start using the "Fugro-Jason" software and all the technical and scientific advices in the past few years.

I also would like to acknowledge Dr. Ir. D. W. van der Burg from PGS for his vital help in translating the summary and the propositions part of the the-

sis in Dutch.
Especialy, I would like to acknowledge Shell U.K. Limited, BP and XOM for allowing me to work with real 4D data from the Shearwater field and for the permission to publish the results in this thesis. In "Shell" I would like to acknowledge Dr. Paul Hatchell ("Shell") and Dr. John Verbeek ("NAM") for all their scientific advice. Dr. John Verbeek also fhelped with the organization of obtaining the real seismic data and getting permission to publish the results in this thesis. I would like also to thank Dr. Rob Staples for his help in obtaining and analyzing the seismic data for Shearwater filed and for the technical and scientific feedback how to measure and interpret the 4D changes in the travel time. In "Shell" I also would like to thank Peter van Loevenzijn, and Ben Hull-Bailey for the great help in obtaining permissions to publish the Shearwater results in my thesis.
I would like to thank all my colleagues in "Fugro-Jason" BV, especialy the QATT team (Beth, Pleun, Maartje, Sarah, and David), for the warm welcome and for the moral support at the last stage of my PhD.
In Delft I am indebted to Deyan Draganov who convienced me to start the PhD study. During my first year in Delft, Deyan helped me a lot to integrate in The Netherlands and in my work environment. I also would like to thank Gerrit (the small boss) and Dennis (the hooligan) for showing me Koeniginnennach in Den Haag and visiting Feyenoord games. I would like to thank Deyan, Dennis, and Daria for amassing trip in USA. Bobby and Tristan for the best EAGE conference I ever had. My roommates in the TU from the "Balkan" room, Aletta and Daniela. I also thank to Jan, Martijn, Sevgi, Florance, Antonio, Ainoha, Ranajit, Evert, Guus, Guy, Wim, Lily, Nihet, Joost, Elmer, Karel, Jurg, Ali, Christian, Bouko, Menne, Wiebke, and the rest of my colleagues in TU-Delft. I also would like to thank the bulgarian group in Delft for their moral support and for the nice time there: Kuzi (The Shearwater); Sasho, Paco, and Dessie (the Paris trip was fabulous); Vankata and Dessie; Ivo H. (for my first pilot experience); Blago and Nadja; Vlado (The animal from Kostenec); Chorbar Buchvarov.
I would like to thank Dessie Koleva and Gencho for the nice parties and a lot of help.
Especialy, I would like to thank the "Leiden" goup for the moral and alcoholical support in the past 6 years and for the great time together: Prodi (The Playboy), Dr. Stoykov and Venci (for the trips in Amsterdam and Brussels),

Keti and Kuncho (the last of thr Mahicans in Leiden), Stelugi (snowboarding is the best!!!) and Kateto.
I also would like to thank Pesho Kashchiev for the nice time in Madrid.
I would like to thank Hélène Rees for the nice time in Bansko, Strassbourg, Leiden and Amsterdam.
I would like to acknowledge some of my friends in Vienna: Svetla and her familly, dr. Ilić and Simonida, Mitacheto (Hudozhnika) and Adriana, Plamen, Lexe and Helmut.
I am much indebted to my family for the moral support in all the years of my PhD study: My parents - Sofia and Vlado Angelovi; My brother - Boris Angelov and his family (Rossi, Krum, Tervel and Meglena).

Curriculum Vitae

Petar Vladov Angelov was born in the charming city of Pernik, Bulgaria on 10^{th} of April 1974. The city of Pernik is well known with it's romantics and intelligent citizens as well with the vast population of grasshoppers locally known as "skakauez". Pernik is also known as the "The vale of the VW Golf" and it is the only place in the World your car could be crashed from behind while driving in the opposite traffic. Petar is imbedded to his parents for living this city when he was three years old and settle down in Sofia, Bulgaria. In Sofia he attended secondary school at the 4^{th} ("The jolly") school of Sofia. In 1992 Petar graduated the "National high school with mathematics and nature science" in Sofia. In the same year he started his study in the "Mining and Geology" University, Sofia, Bulgaria. In 1998 he obtained his M.Sc. degree in the same University with a final assignment topic : "Calculation of the 3D Magnetic Anomalies; Numerical finite element simulation of a 3D magnetic anomaly". In the period 1999-2003 he was employed as software developer and tester at SQS AG, Cologne, Germany. In 2003 he started with his Ph.D. research in the section of Applied Geophysics and Petrophysics in the department of Geotechnology, faculty of Civil Engineering and Geoscience at the Delft University of Technology. In the first year the project was under supervision of dr. J. Spezler, Delft University of Technology. After that till the end the project was supervised by prof. dr. ir. R.J. Arts and prof. dr. ir. C.P.A. Wapenaar at the Delft University of Technol-

ogy. The research progress was presented at several conferences in Europe, USA and Canada. In 2008 he became one of the Fugro-Jason argonauts and is still on his way to Kolkhis looking for the Golden Fleece and definitely preferring to deal with the sorceress Medea than with the Harpies.

Bibliography

Aki, K. and Richards, P. G. (2002). Quantitative Seismology. Univercity Science Books.

Amadei, B. and Stephansson, O. (1997). Rock stress and its measurement. Chapman and Hall, London.

Angelov, P. V., Spetzler, J., Arts, R. and Wapenaar, K. (2005). Modelling seismic time-lapse changes in the overburden and in the reservoir as a result of reservoir depletion. SEG, pp. 2516–2519.

Arts, R., Chadwick, A., Eiken, O., Thibeau, S. and Nooner, S. (2008). Special topic on underground co_2 storage. First Break, 26, pp. 1383–1392.

Arts, R., Eiken, O., Chadwick, A., Zweigel, P., van der Meer, B. and Kirby, G. (2004a). Seismic monitoring at the sleipner underground co_2 storage site (north sea). S.J. Baines R.H. Worden (Eds): Geological storage of CO_2 for emissions reduction. Geological Society, London, Special Publications, 233, pp. 181–191.

Arts, R., Eiken, O., Chadwick, A., Zweigel, P., van der Meer, L. and Zinszner, B. (2004b). Monitoring of co_2 injected at sleipner using time-lapse seismic data. Energy, 29, pp. 1383–1392.

Avseth, P., Mukerji, T. and Mavko, G. (2005). Quantitative Seismic Interpretation. Cambridge University Press.

Backus, G. E. (1962). Long-Wave Elastic Anisotropy Produced by Horizontal Layering. Jurnal of Geophysical Research, 67, pp. 4427–4440.

Batzle, M., Christiansen, R. and Han, D. (1998). Reservoir recovery processes and geophysics. The Leading Edge, 17, pp. 1444–1447.

Batzle, M. and Wang, Z. (1992). Seismic properties of pore fluids. Geophysics, 57, pp. 1396–1408.

Berryman, J. G. (1987). Long-wavelength propagation in composite elastic media. J. Acoust. Soc. Am., 68, pp. 1809–1831.

Blangy, J., Strandenest, S., Moos, D. and Nur, A. (1993). Ultrasonic velocities in sands-revisited. Geophysics, 58, pp. 344–356.

Bourbie, T., Coussy, O. and Zinszner, B. (1987). Acoustics of porous media. Editions Technip.

Brandt, H. (1955). A study of the speed of sound in porous granular media. Journal of Applied Mechanics, 22, pp. 479–486.

Calvert, R. (2005). Insights and Methods for 4D Reservoir Monitoring and Characterization. Distinguished Instructor Series, 8.

Carcione, J. M. C. (2006). Detemining the Dilatation Factor in 4D Monitoring of Compacting Reservoirs by Rock-Physics Models. EAGE, p. Extended abstracts A020.

Carmichael, R. S. (1982). Handbook of physical properties of rocks; Vol II. CRC Press.

Castagna, J. P., Batzle, M. L. and Eastwood, R. L. (1985). Relationships between compressional-wave and shear-wave velocities in clastic silicate rocks. Geophysics, 50, pp. 571–581.

Charlez, P. A. (1991). Rock Mechanics; volume 1; Theoretical Fundamentals. Editions Technip.

Charlez, P. A. (1997). Rock Mechanics; volume 2; Petroleum Applications. Editions Technip.

Cheng, C. . H. (1981). Dynamic and Static Moduli. Jurnal of Geophysical Research, 8, pp. 39–42.

Dutta, N. C. (1998). Geopressure prediction using seismic data: Current status of the road ahead. Geophysics, 67, pp. 2012–2041.

Dvorkin, J., Mavko, G. and Nur, A. (1991). The effect of the cementation on the elastic proprties of granular material. Mechanics of Materials, 12, pp. 207–217.

Dvorkin, J. and Nur, A. (1996). Elasticity of high-porosity sandstones: Theory for two North Sea data sets. Geophysics, 61, pp. 1363–1370.

Dvorkin, J., Nur, A. and Yin, H. (1994). Effective properties of cemented granular materials. Mechanics of Materials, 18, pp. 351–366.

Eissa, E. A. and Kazi, A. (1988). Relation between Static and Dynamic Young's Moduli of Rocks. International Journal of Rock Mineral Science and Geomechanical Abstracts, 25, pp. 479–482.

Eshelby, J. D. (1957). The determination of the elastic field of an ellipsoidal inclusion, and related problems. Proc. R. Sos., pp. 376–396.

Fokker, P. A. and Orlic, B. (2006). Semi-Analytic Modelling of Subsidence. Mathematical Geology, 38, pp. 565–589.

Gassmann, F. (1951). Ueber die elastizitaet poroeser medien. Vier. der Natur. Gesellschaft in Zuerich, 96, pp. 1–23.

Geertsma, J. (1973). A Basic Theory of Subsidence due to Reservoir Compaction: The Homogeneous Case. Verhandelingen Kon. Ned. Geol. Mijnbouwk. Gen., 28, pp. 43–62.

Geertsma, J. and van Opstal, G. (1973). A Numerical Technique for Predicting Subsidence above Compacting Reservoirs, based on the Nucleus of Strain Concept. Verhandelingen Kon. Ned. Geol. Mijnbouwk. Gen., 28, pp. 63–78.

Gelinsky, S. and Shapiro, S. A. (1997). Poroelastic Backus averaging for anisotropic layered fluid- and gas-saturated sediments. Geophysics, 67, pp. 1867–1878.

Goulty, N. R. (1998). Relationships between porosity and effective stress in shales. First Break, December, pp. 413–419.

Grasso, J. R. and Wittlinger, G. (1990). 10 years of seismic monitoring over a gas field area. Bull. Seismol. Soc. Am., 76, pp. 450–473.

Gregory, A. R. (1976). Fluid saturation effects on dynamic elastic properties of sedimentary rocks. Geophysics, 41, pp. 895–921.

Guilbot, J. and Smith, B. (2002). 4-D constrained depth conversion for reservoir compaction estimation: Application to Ekofisk Field. The Leading Edge, 21, pp. 302–308.

Han, D., Nur, A. and Morgan, D. (1986). Effects of porosity and clay content on wave velocities in sandstones. Geophysics, 51, pp. 2093–2107.

Hashin, Z. and Strickman, S. (1963). A variational approach to the elastick bahavior of multiphase materials. Journal Mechanics of Phys. Solids, 11, pp. 127–140.

Hatchell, P. J., van den Beukel, A., Molenaar, M., Maron, K., Kenter, C., Stammeijer, J., Van der Velde, J. and Sayers, C. (2003). Whole earth 4D: reservoir monitoring geomechanics. SEG, pp. 1330–1333.

Hatchell, P. J. and Bourne, S. (2005). Rock under strain: Strain-induced time-lapse time shifts are observed for depleting reservoirs. The Leading Edge, 24, pp. 1222–1225.

Hatchell, P. J., Kawar, R. S. and Savitski, A. A. (2005). Integrating 4D seismics, geomechanics, and reservoir simulation in the Valhall field. EAGE, p. Extended abstracts C012.

Hawkins, K., Howe, S., Hollingworth, S., Conroy, G., Ben-Brahim, L., Tindle, C., Taylor, N., Joffroy, G. and Onaisi, A. (2007). Production-induced stresses from time-lapse time shifts: A geomechanics case study from Franklin and Elgin fields. The Leading Edge, 26, pp. 655–662.

van Heerden, W. L. (1987). General Relations Between Static and Dynamic Moduli of Rocks. International Journal of Rock Mineral Science and Geomechanical Abstracts, 24, pp. 381–385.

Hill, R. (1963). Elastic properties of reinforced solids: Some theoretical principles. Journal Mechanics of Phys. Solids, 11, pp. 357–372.

Holm, G., Owens, J., Page, G. and Ritchie, A. (2005). The Hod Geohazard: A Unique Overpressured Interval - Cooperation in Its Recognition, Evaluation and Risk Mitigation. Society of Petroleum Engineers, 96383.

Holt, R. M., Brignoli, M. and Kenter, C. J. (2000). Core quality: quantification of coring-induced rock alternation. Rock Mechanics and Mining Science, 37, pp. 889–907.

Holt, R. M. and Fjaer, E. (2003). Wave velocities in shales - a rock physics model. EAGE, C-13.

Holt, R. M., Nes, O.-M. and Fjaer., E. (2005). In-situ stress dependence on wave velocities in reservoir and overburden rocks. The Leading Edge, 24, pp. 1268–1274.

Hoversten, G. M., Cassassuce, F., Gasperikova, E., Newman, G. A., Chen, J., Rubin, Y., Hou, Z. and Vasco, D. (2006). Direkt reservoir parameter estimation using joint inversion of marine seismic AVA and CSEM data. Geophysics, 71, pp. C1–C13.

Johnson, D. L., Schwartz, L. M. and Elata, D. (1998). Linear and nonlinear elasticity of granular media: stress-induced anisotropy of random sphere pack. ASME, 65, pp. 380–388.

Johnston, D., McKenny, R., Verbeek, J. and Almond, J. (1998). Time-lapse seismic analysis of Fulmar Field. The Leading Edge, 17, pp. 286–293.

Jones, T. D. (1986). Pore fluids and frequency-dependent wave propagation in rocks. Geophysics, 51, pp. 1939–1953.

Jones, T. D. and Nur, A. (1983). Velocity and attenuation in sandstone at elevated temperatures and pressures. Geophysical Research Letters, 10, pp. 140–143.

Kawar, R., Hatchell, P. J., Calvert, R. and Khan, M. (2003). The Workflow for 4D Seismic. Society of Petroleum Engineers, 81527.

Kenter, C. J., Blanton, T. L., Schreppers, G. M. A., Baaijens, M. N. and Ramos, G. G. (1996). Compaction Study for Shearwater Field. Society of Petroleum Engineers, 47280.

Kenter, C. J., Van den Beukel, A. C., Hatchell, P. J., Maron, K. P., Molenaar, M. M. and Stammeijer, J. G. F. (2004). Geomechanics and 4D: Evaluation of reservoir characteristics from timeshifts in the overburden. American Rock Mechanics Association, pp. ARMA/NARMS 04–627.

Koesoemadinata, A. P. and McMechan, G. A. (2001). Empirical estimation of viscoelastic seismic parameters from petrophysical properties of sandstone. Geophysics, 66, pp. 1457–1470.

Kuster, G. T. and Toksöz, M. N. (1974a). Velocity and Atenuation of Seismic Waves in Two-Phase Media: Part I. Theoretical Formulations. Geophysics, 39, pp. 587–606.

Kuster, G. T. and Toksöz, M. N. (1974b). Velocity and Atenuation of Seismic Waves in Two-Phase Media: Part II. Experimental Results. Geophysics, 39, pp. 607–618.

Landrø, M. (2001). Descrimination between pressure and fluid saturation changes from time-lapse seismic data. Geophysics, 66, pp. 836–844.

Landrø, M. (2002). Uncertainties in quantitative time-lapse seismic analysis. Geophysical Prospecting, 50, pp. 527–538.

Landrø, M. and Amundsen, L. (2009). Estimating velocity and thickness changes of compacting reservoirs combining 4d seismic and gravimetric measurements. SEG, pp. 3785–3789.

Landrø, M. and Stammeijer, J. (2004). Quantitative estimation of compaction and velocity changes using 4D impedance and travel time changes. Geophysics, 69, pp. 949–957.

Lehner, F. K. (2002). Stress changes associated with reservoir depletion - Plane strain solutions of Goodier and Nowacki. Lecture 5 of CISM Course No 254, Udine.

Lumley, D. E., Behrens, R. A. and Wang, Z. (1997). Assesing the technical risk of a 4-D seismic project. The Leading Edge, 16, pp. 1287–1291.

Mase, G. T. and Mase, G. E. (1999). Continuum Mechanics for Engineers. CRC Press.

Mavko, G., Mukerji, T. and Dvorkin, J. (1998). The Rock Physics Handbook: Tools for Seismic Analysis in Porous Media. Cambridge University Press.

Meadows, M. A. (2001). Enahacements to Landrø's method for separating time-lapse pressure and saturation changes. SEG, pp. 1652–1655.

Mesdag, P. R., Feroci, M., Barens, L., Prat, P. H. and Pillet, W. (2007). Full Bandwidth Inversion for Time Lapse Reservoir Characterization on the Girassol Field. EAGE, p. Extended abstracts A032.

Mindlin, R. D. (1949). Compliance of elastic bodies in contact. Journal of Applied Mechanics, 16, pp. 259–268.

Molenaar, M. M., Hatchell, P. J., Van den Beukel, A. C., Jenevy, N. J. ., Stammeijer, J. G. F., Van der Velde, J. J. and de Haas, W. O. (2004). Applying Geo-mechanics and 4D: "4D In-situ Stress" as a complimentray tool for optimizing field managment. American Rock Mechanics Association, pp. ARMA/NARMS 04–639.

Morita, N., Whitfill, D. L., Nygaard, O. and Bale, A. (1989). A Quick Method to Determine Subsidence, Reservoir Compaction, and In-Situ Stress Induced by Reservoir Depletion. Journal of Petroleum Technology, pp. 71–79.

Mukerji, T. and Mavko, G. (1994). Pore fluid effects on seismic velocity in anisotropic rocks. Geophysics, 50, pp. 233–244.

Mulders, F. M. M. (2003). Modelling of stress development and fault slip in and around a producing gas reservoir. Ph.D. thesis, Delft University of Technology.

Murphy, W., Reischer, A. and Hsu, K. (1992). Modulus decomposition of compressional and shear velocities in sand bodies. Geophysics, 58, pp. 227–239.

Nes, O. M., Holt, R. M. and Fjaer, E. (2000). The Reliability of Core Data as Input to Seismic Reservoir Monitoring Studies. Society of Petroleum Engineers, p. SPE 65180.

Norris, A. N. and Johnson, D. L. (1997). Nonlinear elasticity of granular media. ASME J. Appl. Mech., 64, pp. 39–49.

Nowacki, W. (1986). Thermoelasticity, 2nd edition. Pergamon.

Nur, A. (1989). Four-dimensional seismology and (true) direct detection of hydrocarbons: The petrophysical basis. The Leading Edge, 8, pp. 30–36.

Nur, A., Tosaya, C. and Vo-Thanh, D. (1984). Seismic monitoring of thermal enhanced oil recovery processes. SEG, pp. 337–341.

Pande, G. N. and Pietruszczak, S. (1992). Seismic Data Analysis, volume 1. A.A.Balkema, Rotterdam, The Netherlands.

Pennington, W. D., Davis, S. D., Carlson, S. M., DuPree, J. D. and Ewing, T. E. (1986). The evolution of seismic barriers and asperities caused by the depressuring of fault planes in oil and gas fields of south Texas. Bull. Seismol. Soc. Am., 76, pp. 939–948.

Petterson, O., Storli, A., Ljosland, E. and Massie, I. (1990). North Sea oil and gas reservoirs II; Field Review 4; The Gullfaks Field: Geology and Reservoir Development. The Norwegian Institute of Technology, pp. 67–90.

Prasad, M. (2002). Acoustic measurements in uncosolidated sands at low effective pressure and overpressure detection. Geophysics, 67, pp. 405–412.

Ranalli, G. (1995). Rheology of the Earth. Chapman and Hal.

Røste, T., Stovas, A. and Landrø, M. (2005). Estimation of layer thickness and velocity changes using 4D prestack seismic data. EAGE.

Røste, T., Stovas, A. and Landrø, M. (2006). Estimation of layer thickness and velocity changes using 4D prestack seismic data. Geophysics, 71, pp. S219–S234.

Rudnicki, J. W. (1999). Alteration of regional stress by reservoirs and other inhomogeneities: stabilising or destabilising? 9th International Congress on Rock Mechanics -Case Studies, Paris.

Sams, M. S., Neep, J. P., Worthington, M. H. and King, M. S. (1997). The measurements of velocity dispersion and frequency-dependent intrinsic attenuation in sedimentary rocks. Geophysics, 62, pp. 1456–1464.

Sayers, C. M. and van Munster, J. G. (1991). Microcrack-Induced Seismic Anisotropy of Sedimentary Rocks. Jurnal of Geophysical Research, 96, pp. 16529–16533.

Schoen, J. H. (1996). Physical Properties of Rocks. Pergamon.

Schoenberg, M. and Sayers, C. M. (1995). Seismic anisotropy of fractured rock. Geophysics, 60, pp. 204–211.

Schutjens, P. M. T. M., Hanssen, T. H., Hettema, M. H. H., Merour, J., de Bree, J. P., Coremans, J. W. A. and Helliesen, G. (2004). Compaction-induced porosity/permeability reduction in sandstone reservoirs: Data and model for elasticity-dominated deformation. Society of Petroleum Engineers, 71337.

Scott, T. E. (2007). The effects of stress paths on acoustic velocities and 4D seismic imaging. The Leading Edge, 26, pp. 602–609.

Segall, P. (1983). Stress and Subsidence Resulting From Subsurface Fluid Withdrawal in the Epicentral Region of the 1983 Coalinga Earthquake. Jurnal of Geophysical Research, 90, pp. 6801–6816.

Segall, P. (1989). Earthquakes triggered by fluid extraction. Geology, 17, pp. 942–946.

Segall, P. and Fitzgerald, S. D. (1998). A note on induced stress changes in hydrocarbon and geothermal reservoirs. Tectonophysics, 289, pp. 117–128.

Segall, P., Grasso, J.-R. and Mossop, A. (1994). Poroelastic stressing and induced seismicity near the Lacq gas field, southwestern France. Jurnal of Geophysical Research, 99, pp. 15423–15438.

Settari, A. (2002). Reservoir Compaction. Society of Petroleum Engineers, 76805.

Sheriff, R. A. (2002). Encyclopedic Dictionary of Applied Geophysics. SEG.

Simmons, G. (1965). Comparison of Static and Dynamic Measurements of Compressibility of Rocks. Jurnal of Geophysical Research, 70, pp. 5649–5656.

Spencer, A. J. M. (2004). Continuum Mechanics. Dover Publications.

Stammeijer, J. G. F., Van Der Felde, J. J., Hatchell, P. J., Van Den Beukel, A. and Molenaar, M. M. (2004). Integrating 4d seismic and geomechanics: a case study. EAGE, p. Extended abstracts A038.

Staples, R., Ita, J., Burrell, R. and Nash, R. (2007a). Monitoring pressure depletion and improving geomechanical models of the Shearwater Field using 4D seismic. The Leading Edge, 26, pp. 636–642.

Staples, R., Ita, J., Burrell, R., Nash, R., Hague, P. and Burrell, R. (2007b). Using 4D Seismic Data and Geomechanical Modelling to Understand Pressure Depletion in HPHT Fields of the Central N Sea. EAGE, 69, pp. A025.

Teufel, L. W., Rhett, D. W. and Farrell, H. E. (1991). Effect of reservoir depletion and pore pressure drawdown on in situ stress and deformation in the Ekofisk field, north sea. Rock Mechanics as a Multidisciplinary Science, pp. 63–72.

Thomsen, L. (1986). Weak elastic anisotropy. Geophysics, 51, pp. 1954–1966.

Thomsen, L. (1995). Elastic anisotropy due to aligned cracks in porous rock. Geophysical Prospecting, 43, pp. 805–829.

Thomsen, L. (2002). Understanding Seismic Anisotropy in Exploration and Exploitation. SEG.

Thorbecke, J. W., Wapenaar, K. and Swinnen, G. (2004). Design of one-way wavefield extrapolation operators, using smooth functions in wlsq optimization. Geophysics, 69, pp. 1037–1045.

Tiğrek, S. (2004). Seismic Evidence of Tectonic Stresses: Implications for basin reconstruction. Ph.D. thesis, Delft University of Technology.

Timur, A. (1977). Temperature dependence of compressional and shear wave velocities in rocks. Geophysics, 42, pp. 950–956.

Tosaya, C., Nur, A., Vo-Thanh, D. and Da Prat, G. (1987). Laboratory seismic method for remote monitoring of thermal EOR. Society of Petroleum Engineers, 12744.

Tura, A., Barker, T., Cattermole, P., Collins, C., Davis, J., Hatchell, P., Koster, K., Schutjens, P. and Wills, P. (2005). Monitoring primary depletion reservoirs using amplitudes and time shifts from high-repeat seismic surveys. The Leading Edge, 24, pp. 1214–1221.

Tura, A. and Lumley, D. E. (1999). Estimating pressure and saturation changes from time-lapse AVO data. SEG, pp. 1655–1658.

Vernik, L. and Liu, X. (1997). Velocity anisotropy in shales: A petrophysical study. Geophysics, 62, pp. 521–532.

Vernik, L. and Nur, A. (1992). Ultrasonic velocity and anisotropy of hydrocarbon source rocks. Geophysics, 57, pp. 727–735.

Vidal, S., Huguet, F. and Mechler, P. (2002). Characterizing reservoir parameters by integrating seismic monitoring and geomechanics. The Leading Edge, 21, pp. 295–301.

Vidal-Gilbert, S., Huguet, F., Assouline, L. and Longuemare, P. (2005). Hydromechanical modeling of reservoir behavior during underground gas storage exploration. EAGE, p. Extended abstracts C051.

Vidal-Gilbert, S. and Tisseau, E. (2006). Sensitivity Analysis of Geomechanical Behavior on Time-Lapse Seismic Velocity. Society of Petroleum Engineers, 100142.

Walsh, J. B. (1965). The effect of the compressibility of rocks. Jurnal of Geophysical Research, 70, pp. 381–385.

Walsh, J. B. (1969). New analysis of attenuation of partially melted rock. Jurnal of Geophysical Research, 14, pp. 4333–4337.

Walton, K. (1987). The effective elastic moduli of a random packing of spheres. Journal Mechanics of Phys. Solids, 35, pp. 213–226.

Wang, Z. (1997). Feasibility of time-lapse seismic reservoir monitoring: The physical basis. The Leading Edge, 16, pp. 1327–1329.

Wang, Z. (2001). Y2K tutorial: Fundamentals of seismic rock physics. Geophysics, 66, pp. 398–412.

Wang, Z. (2002a). Seismic anisotropy in sedimentary rocks, part1: A single-plug laboratory method. Geophysics, 67, pp. 1415–1422.

Wang, Z. (2002b). Seismic anisotropy in sedimentary rocks, part2: Laboratory data. Geophysics, 67, pp. 1423–1440.

Wang, Z., Hirsche, W. K. and Sedgwick, G. (1991). Seismic monitoring of water floods? - A petrophysical study. Geophysics, 56, pp. 1614–1623.

Wang, Z. and Nur, A. (1990). Wave velocities in hydrocarbon-saturated rocks: Experimental results. Geophysics, 55, pp. 723–733.

Wang, Z. and Nur., A. (1992). Seismic and Acoustic Velocities in Reservoir Rocks, volume 2. SEG.

Wang, Z. and Nur, A. (2000). Seismic and Acoustic Velocities in Reservoir Rocks, volume 3. SEG.

Wapenaar, C. P. A. and Berkhout, A. J. (1989). Elastic Wave Field Extrapolation. ELSEVIER.

Winkler, K. (1985). The measurements of velocity dispersion and frequency-dependent intrinsic attenuation in Berea sandstone. Geophysical Research Letters, 90, pp. 6793–6800.

Winkler, K. (1986). Estimates of velocity dispersion between seismic and ultrasonic frequencies. Geophysics, 51, pp. 183–189.

Wu, B., Addis, M. A. and Last, N. C. (1998). Stress Estimation in Faulted Regions: The Effect of Residual Friction. SPE, p. 47210.

Wu, T. T. (1966). The effect of inclusion shape on the elastic moduli of two phase materials. International Journal of Solids Structures, 2, pp. 1–10.

Xu, S. and White, R. E. (1996). A physical model for shear-wave velocity prediction. Geophysical Prospecting, 44, pp. 687–717.

Yale, D. P. and Jamieson, W. H. (1994). Static and dynamic mechanical properties of carbonates. Rock Mechanics, pp. 463–471.

Yerkes, R. F. and Castle, R. O. (1976). Seismicity and Faulting Attributable to Fluid Extraction. Engineering Geology, 10, pp. 151–167.

Yilmaz, O. (2001a). Seismic Data Analysis, volume 1. SEG.

Yilmaz, O. (2001b). Seismic Data Analysis, volume 2. SEG.

Yin, S., Dusseault, M. B. and Rothenburg, L. (2007). Analytical and numerical analysis of pressure drawdown in a poroelastic reservoir with complete overburden effect considered. Advances in Water Resources, 30, pp. 1160–1167.

Zimmer, M. A., Prasad, M. and Mavko, G. (2002). Pressure and porosity influences on $V_p - V_s$ ratio in unconsolidated sands. The Leading Edge, 21, pp. 178–183.

Zimmer, M. A., Prasad, M., Mavko, G. and Nur, A. (2007a). Seismic velocities of unconsolidated sands: Part 1 - Pressure tends from 0.1 to 20 MPa. Geophysics, 72, pp. 1–13.

Zimmer, M. A., Prasad, M., Mavko, G. and Nur, A. (2007b). Seismic velocities of unconsolidated sands: Part 2 - Influence of sorting- and compaction-induced porosity variation. Geophysics, 72, pp. 15–25.